Invasive growth in a human fungal pathogen : mechanical forces and cellular reorganization

Charles Puerner

UNIVERSITÉ CÔTE D'AZUR

ÉCOLE DOCTORALE
SCIENCES DE LA VIE ET DE LA SANTÉ

THÈSE DE DOCTORAT

Croissance invasive d'un champignon pathogène de l'Homme: forces mécaniques et réorganisation cellulaire

Charles Thomas Smart PUERNER

Institut de Biologie Valrose (iBV)

Présentée en vue de l'obtention du grade de docteur en Sciences de la vie et la sante Interactions moléculaires et cellulaires
d'Université Côte d'Azur
Dirigée par : Dr. Robert ARKOWITZ
Soutenue le : 25 Septembre, 2020

Devant le jury, composé de :
Dr. Robert ARKOWITZ, CNRS DR, Université Côte d'Azur
Dr. Martine BASSILANA, CNRS DR, Université Côte d'Azur
Dr. Judith BERMAN, Tel Aviv University, IL
Dr. Jim KRONSTAD, University of British Columbia, CA
Dr. Aaron MITCHELL, University of Georgia, USA
Dr. Agnese SEMINARA, CNRS HDR, Université Côte d'Azur

PolarNet Principles of Polarity
HORIZON 2020
MARIE CURIE ACTIONS
AGENCE NATIONALE DE LA RECHERCHE ANR

Croissance invasive d'un champignon pathogène de l'Homme: forces mécaniques et réorganisation cellulaire

Jury:

Président du jury
Dr. Martine BASSILANA, CNRS DR, Université Côte d'Azur

Rapporteurs
Dr. Judith BERMAN, Tel Aviv University, IL
Dr. Jim KRONSTAD, University of British Columbia, CA

Examinateurs
Dr. Aaron MITCHELL, University of Georgia, USA
Dr. Agnese SEMINARA, CNRS HDR, Université Côte d'Azur

Résumé

Croissance invasive d'un champignon pathogène de l'Homme: forces mécaniques et réorganisation cellulaire

Candida albicans est un champignon pathogène de l'Homme qui provoque des infections potentiellement mortelles chez les patients immunodéprimés. J'ai étudié la croissance filamenteuse invasive de *C. albicans,* en collaboration avec des physiciens, - en particulier les forces mécaniques lors de ce processus -, et quantifié les effets de ces forces sur la morphologie cellulaire. En outre, j'ai examiné la fonction d'un cluster de vésicules à l'apex du filament, appelé Spitzenkörper, dans la régulation de la croissance et de la morphologie cellulaire.

Les forces physiques générées par la croissance filamenteuse de *C. albicans* sont critiques pour pénétrer les tissus de l'hôte et pour échapper aux cellules immunitaires. Nous avons utilisé le polymère polydiméthylsiloxane (PDMS) pour générer des micro-chambres de rigidité différente, similaire à celle des tissus de l'hôte. J'ai examiné la croissance filamenteuse de *C. albicans* dans ces chambres confinées, afin de déterminer les propriétés biophysiques de la croissance invasive. En utilisant la microscopie en temps réel, j'ai montré que le pourcentage de filaments invasifs diminuait avec une augmentation de la rigidité du PDMS, et déterminé un seuil de rigidité pour lequel les filaments sont incapables d'envahir - probablement la « growth-stalling force ». Pendant la croissance invasive, la vitesse d'extension du filament est réduite, par rapport à une croissance en surface non invasive, en fonction de la rigidité du PDMS. De plus, au cours de ce processus, j'ai observé un changement de morphologie cellulaire, avec une augmentation significative du diamètre et une diminution concomitante de la longueur du compartiment cellulaire, résultant en un volume similaire à celui des cellules en croissance non invasive. Ce changement de morphologie est associé à une augmentation dramatique du taux de Cdc42 activé, régulateur clé de la polarité, à l'apex du filament et à une dépolarisation de Rho1 activé, régulateur de la glucan-synthase. Ces résultats indiquent que les changements de morphologie cellulaire pendant la croissance invasive ne sont pas dus à la dépolarisation ou à la déstabilisation de Cdc42 activé. Au contraire, des analyses complémentaires suggèrent que des forces mécaniques, en particulier la compression, sont largement responsables de ces changements morphologiques.

Le Spitzenkörper, cluster de vésicules situé à l'apex du filament, est observé chez une variété de champignons filamenteux. Chez *C. albicans*, des études de microscopie électronique ont

révélé que le Spitzenkörper est composé d'une population uniforme de vésicules, mais la fonction de cette structure pendant la croissance filamenteuse est peu connue. J'ai montré que ce Spitzenkörper est entièrement composé de vésicules de sécrétion et étudié sa fonction en utilisant des mutants et des approches d'interactions forcées. Perturber cette structure entraîne une modification de la morphologie du filament et de la vitesse de croissance; l'augmentation du diamètre du filament est associée à une augmentation concomitante de la vitesse de croissance. En outre, la délétion d'un des composants du Spitzenkörper réduit considérablement la croissance invasive. Dans l'ensemble, ces résultats indiquent que cette structure régule la région d'insertion de nouveau matériel membranaire, donc focalise la croissance, et suggèrent qu'une augmentation du flux de vésicules de sécrétion compense pour une moindre focalisation de l'ajout de matériel membranaire. Dans l'ensemble, mes études révèlent que les forces mécaniques affectent la morphologie de *C. albicans* et sa capacité d'invasion, et que le Spitzenkörper est le lien central entre morphologie du filament d'une part et vitesse de croissance et invasion filamenteuse, d'autre part.

Mots clés

Candida albicans, croissance invasive, forces mécaniques, morphologie, polarité cellulaire, Spitzenkörper, Cdc4

Abstract

Invasive growth of a human fungal pathogen: mechanical forces and cellular reorganization

The dimorphic fungi *Candida albicans* is a major human pathogen that causes life-threatening infections for immunocompromised patients. I have investigated *C. albicans* invasive filamentous growth, in collaboration with physicists. In particular, I have studied the mechanical forces during this process, and quantitated the effects of these forces on cell morphology. Furthermore, I have examined the function of a filament tip cluster of vesicles, known as a Spitzenkörper, in the regulation of growth and cell morphology.

Physical forces generated by *C. albicans* filamentous growth are likely to be critical for host tissue penetration, as well as escape from host immune cells. We have used the polymer polydimethylsiloxane (PDMS) to generate microchambers with different stiffness, similar to that of host cells and tissues. I have examined *C. albicans* filamentous growth in these confined chambers in order to determine the biophysical properties of growth and substrate invasion. Using time-lapse microscopy, I showed that the percentage of invasive hyphae decreased with an increase in PDMS stiffness and determined a stiffness threshold, in which hyphae are unable to invade - likely the growth-stalling force. Compared to surface growth, there was a striking reduction in filament extension rate during invasive growth, which was dependent on PDMS stiffness. Furthermore, during this process, I observed a cell morphology change, *i.e.* a significant increase in cell diameter and a concomitant decrease in cell compartment length, resulting in cell volumes that were largely indistinguishable from that of surface growing cells. This morphology change was associated with a striking increase in the level of active Cdc42, the master regulator of polarity, at the hyphal tip and a concomitant depolarization of active Rho1, the glucan-synthase regulator, during invasive growth. These results indicate that changes in cell morphology during invasive growth are not due to depolarization or destabilization of active Cdc42. Rather, additional analyses suggest that mechanical forces, *i.e.* compression, are largely responsible for these morphological changes.

The Spitzenkörper, which is a cluster of vesicles located at the filament apex adjacent to the plasma membrane, has been observed in a range of filamentous fungi. In *C. albicans*, electron microscopy studies have revealed that the Spitzenkörper is comprised of a uniform population of vesicles; however, little was known regarding the function of this structure during filamentous growth. I have shown that the *C. albicans* Spitzenkörper is composed entirely of secretory vesicles. I have investigated the function of the Spitzenkörper using mutants and

synthetic physical interaction approaches. Perturbation of the Spitzenkörper resulted in altered filament morphology and growth rate, strikingly an increase in filament diameter and concomitant increased growth rate was observed. Furthermore, deletion of a Spitzenkörper component dramatically reduced invasive growth. Together these results indicate that the Spitzenkörper regulates the region of new plasma membrane insertion, *i.e.* the ability to focus growth, and suggest that an increase in the flux of secretory vesicles compensates for less focused membrane addition. In summary, my studies reveal that mechanical forces affect *C. albicans* morphology and substrate invasive ability, and that the Spitzenkörper is the central link between filament morphology and growth rate, as well as substrate invasion.

Key Words
Candida albicans, invasive growth, mechanical forces, morphology, cell polarity, Spitzenkörper, Cdc42

Contents

List of Abbreviations

The following table is a list of abbreviations and acronyms, with their respective meanings, that are the most common throughout this thesis.

Abbreviation	Meaning
Bni1	Spitzenkörper formin
Bem1	Bud emergence protein 1 (scaffold)
BWP 17	Wild-type Candida albicans strain
Cdc24	GEF for Cdc42
Cdc42	Cell division control protein 42 (master polarity regulator)
Cla4	Serine/threonine-protein kinase
DIC	Differential interference contrast (transmission image)
F-actin	Filamentous actin
FCS	Fetal calf serum
FM4-64	An amphiphilic styryl dye
FRAP	Fluorescence recovery after photobleaching
GAP	GTPase-activating protein
GDP	Guanosine diphosphate
GEF	Guanine nucleotide-exchange factor
GFP	Green fluorescent protein
GNB	GFP nanobody
GTP	Guanosine triphosphate
GTPase	GTP binding/hydrolyzing protein

Abbreviation	Meaning
miR	miRFP670 far-red fluorescent protein
Mlc1	Myosin light chain 1
mSc	mScarlet red fluorescent protein
PAK	p21 activated kinase – effector protein for Cdc42
PDMS	Polydimethylsiloxane
PfV	40 nm GEM
PI	Phosphatidylinositol
PIP	Phosphatidylinositol phosphate
PI(4)P	Phosphatidylinositol-4- phosphate
PI(4,5)P2	Phosphatidylinositol 4,5- bisphosphate
PM	Plasma membrane
PS	Phosphatidylserine
Sec2	GEF for Sec4
Sec4	GTPase secretory vesicle marker
VSC	Vesicle supply center
YEDP+Uri	Yeast extract peptone dextrose media with uridine

Introduction

Chapter 1

The goal of this introduction is to provide an overview of the fundamental principles of cell polarity with a particular focus on the establishment and maintenance of polarity during hyphal tip growth of the human fungal pathogen *Candida albicans*. I will first discuss the fundamental principles of polarity, followed by the mechanisms involved in symmetry breaking. Next, I will address the mechanisms of polarity establishment and maintenance during hyphal tip growth. In order to examine the polarity mechanisms of *C. albicans*, it will be necessary to review the well-studied filamentous fungi models *Aspergillus nidulans* and *Neurospora crassa*, in addition to the model yeasts *Saccharomyces cerevisiae* and *Schizosaccharomyces pombe* as these organisms are often used as comparisons with *C. albicans*. Lastly, I will analyze how hyphal tip growth results in the invasion of host tissue and the known effects of resistive forces on polarized growth in fungi.

It is important to briefly review the medical relevance of *C. albicans* in order to put into perspective the importance of this organism's biology. Candidiasis is a major global disease and *Candida sp.* causes topical infections on mucosal membranes such as the mouth and vagina, as well as systemic infections of the blood, candidemia, and internal organs (Pappas et al., 2018). The latter is termed invasive candidiasis and is of great medical importance due to its much higher mortality rate (Fig. I-1). *C. albicans* and other *Candida* species are commensal organisms of the human gut and skin flora in approximately 60% of the adult population (Kullberg and Arendrup, 2015; McCarty and Pappas, 2016; Pappas et al., 2018). Fungal proliferation that ultimately leads to infection is frequently observed in immunocompromised individuals. Although a number of *Candida* species cause human disease, *C. albicans* is globally the most prevalent (Moyes et al., 2015; Pappas et al., 2018).

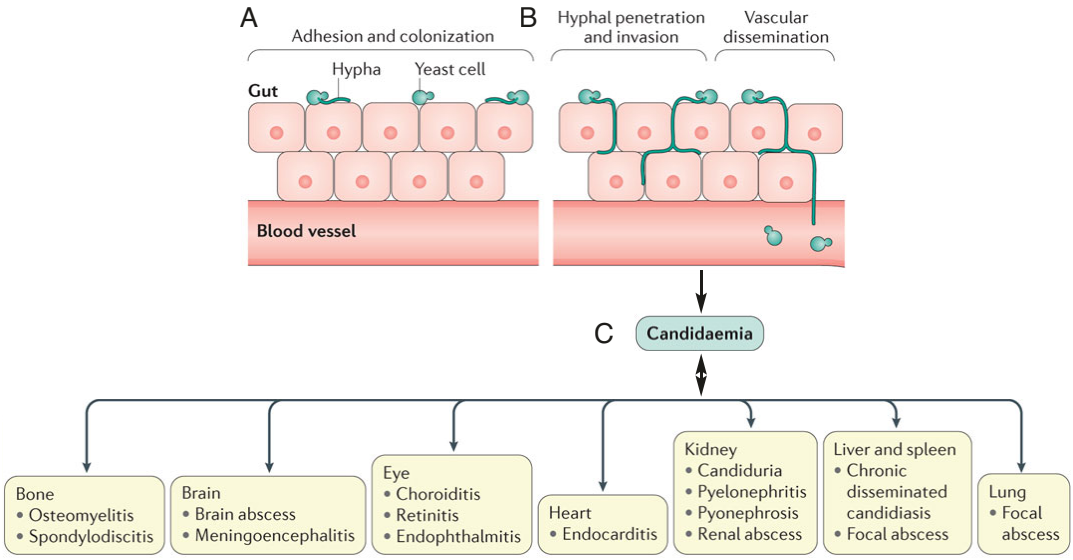

Figure I-1: ***Candida albicans* causes major systemic infections upon crossing mucosal barriers.** A) In normal conditions, *C. albicans* can survive as a commensal organism on host mucosal membranes. B) Upon immunosuppression, *C. albicans* is able to cross the mucosal barriers and enter the blood stream leading to candidemia. C) Once in the blood, *C. albicans* is disseminated to various organs leading to major infection. Figure adapted from Pappas *et al.*, 2018.

Invasive candidiasis is the result of a translocation of *C. albicans* from a mucosal surface through the epithelium to the blood stream where it is disseminated to different organs. The ability of *C. albicans* to transition between the yeast and filamentous form is important for its pathogenicity because strains that cannot filament are avirulent (Lo et al., 1997; Murad et al., 2001; Pappas et al., 2018). Specifically, the ability of *C. albicans* to transition between budding and filamentous forms is important for its ability to translocate and cause invasive candidiasis (Cleary et al., 2016; Pappas et al., 2018; Saville et al., 2003, 2006). This was observed by the use of the tetracycline induced promotor to control the expression of *NRG1*, a negative regulator of filamentation, or *TUP1*, a transcriptional repressor with a role in cellular morphology. The absence of expression results in constitutive pseudohyphal growth (Cleary et al., 2016). The medical importance of the yeast to hyphal transition highlights the importance of studying *C. albicans* polarity during filamentous growth.

I – Cell polarity and polarized growth

Cell polarity is a process fundamental for a cell's ability to grow in a defined direction, necessary for the development of three-dimensional shapes, and critical for intracellular organization. Polarity is also required for cells to organize into organs and other structures. Many cell types develop polarized domains to perform a specific function, such as intestinal epithelial cells (Riga et al., 2020). Additionally, some non-motile microorganisms, such as budding yeast and filamentous fungi, use site-directed growth in order to find mating partners, forage for nutrients and, in pathogenic organisms, penetrate host tissue (Bassilana et al., 2020; Riquelme et al., 2018). Filamentous fungi undergo polarized tip growth, where membrane and cell wall material are directed to the apex of the extending hyphae. This type of polarized growth requires the organization of the membrane traffic network to focus the delivery of material to a specific site or region in the cell, thereby directing growth to the tip (Riquelme et al., 2018).

Model filamentous fungi such as *A. nidulans* and *N. crassa* have provided a wealth of information that can be extrapolated in some cases to other fungi such as *C. albicans*; however, there are important differences such as growth rate, cytoskeleton requirements, and Spitzenkörper composition. The growth rate of *C. albicans* is substantially slower than that of other well-studied filamentous fungi with an extension rate ~ 0.3 µm/min (Silva et al., 2019), while *A. nidulans* extends at 1.8 µm/min (Takeshita et al., 2017) and *N. crassa* extends even faster at a rate of 12 µm/min (Takeshita et al., 2017). Differences in growth rates mean that dramatically different amounts of membrane and cell wall material need to be delivered to the tip to maintain growth. Therefore, it is likely that large differences in growth rates can be attributed to fundamental differences in growth mechanisms. One such example is Spitzenkörper organization, which will be discussed later in detail.

Hyphal tip growth in filamentous fungi is largely dependent on the intracellular organization to direct growth to a unique site. This type of growth, once established, can be maintained for long periods of time, assuming environmental nutrient conditions are sufficient to sustain it. The cytoskeleton is a key structure that allows for material to be delivered to the filament tip. In rapidly growing fungi, such as *A. nidulans,* microtubules and actin filaments have roles in the transport of membrane material *via* secretory vesicles (Riquelme et al., 2018; Takeshita, 2016). Additionally, in these multinucleated fungi, the microtubules aid in the spatial organization of nuclei in the filament (Takeshita, 2016). Although microtubules are involved in hyphal tip growth of this organism, filamentous actin (F-actin) appears to be more crucial since growth is immediately arrested when F-actin is compromised (Takeshita, 2016).

F-actin is important for three processes in filamentous fungi: septin ring formation, endocytosis and transport of secretory vesicles. Actin patches are involved in endocytosis which, in extending filaments, is localized to a collar just behind the site of growth at the filament tip (Araujo-Bazán et al., 2008; Ghugtyal et al., 2015; Peñalva, 2010; Takeshita, 2016). In *C. albicans* the endocytic collar remains at a fixed distance from the tip, irrespective of the filament length (Ghugtyal et al., 2015). In *A. nidulans* there is a transfer of secretory vesicles from microtubule-dependent transport to actin-dependent trafficking that occurs in the tip (Riquelme et al., 2018). However, the requirements of this process are debated because growth can occur for some time in the absence of microtubules and there are endoplasmic reticulum (ER) and Golgi that are located close to the filament tip throughout growth. This suggests there is some short-range traffic occurring (Pinar et al., 2013; Takeshita, 2016; Zhang et al., 2011). This type of short traffic is analogous to what has been observed in *C. albicans* when the tip organization was investigated by electron microscopy (Weiner et al., 2019).

Another significant difference between these fungi is the utilization and requirement for microtubule-based transport during hyphal tip growth. In more rapidly growing fungi,

microtubules are required for long-range transport. In *C. albicans* microtubules are not required for filamentous growth (Rida et al., 2006). F-actin is required for filamentous growth in all the fungi, where it is thought to play a role in the short-range transport between the Spitzenkörper and the exocyst in the filament tip (Riquelme et al., 2018; Takeshita, 2016). In *C. albicans* F-actin dependent transport is the major form of membrane transport; this may be due to the presence of endoplasmic reticulum and Golgi located close to the filament tip, which results in localized secretory vesicle production (Weiner et al., 2019). This organization reduces the necessity for long-range transport of secretory vesicles, consistent with microtubule-independent growth.

Filamentous growth in *C. albicans* is also strikingly different than other filamentous fungi because the septa that form lack a pore or connection between the two resulting compartments (Sudbery, 2011b). Therefore, unlike *N. crassa* or *A. nidulans*, there is unlikely to be the passage of material between subapical compartments once cell division occurs. One electron microscopy study suggested that a 25 nm pore existed in *C. albicans* septa. However, the existence and functionality of such a pore has yet to be confirmed by other means (Odds, 1984). In *N. crassa* and *A. nidulans* the septal pore allows for the passage of material to transit to the filament tip. Therefore, material from further back in the filament can be transported long-range *via* microtubules to the Spitzenkörper, after which it is then transferred to actin cables to be delivered to the growing tip (Jedd and Pieuchot, 2012; Pieuchot et al., 2015). This type of long-range transport is not possible in long *C. albicans* hyphae that have formed septa.

II – Symmetry breaking

Symmetry breaking is the process in which a symmetrical cell undergoes changes to become a polarized, asymmetric cell (Goryachev and Leda, 2017). In the case of fungi, it occurs

when an isotopically growing cell transitions to bud formation. This process has been extensively studied in the budding yeast *S. cerevisiae*, and more recently in the fission yeast *S. pombe* (Arkowitz and Bassilana, 2011; Goryachev and Leda, 2017; Martin, 2015; Singh et al., 2017). Many of the mechanisms that were discovered in these model yeast form the framework of our understanding of *C. albicans* budding growth and, by extension, its switch to filamentous growth (Arkowitz and Bassilana, 2011; Goryachev and Leda, 2017; Singh et al., 2017). There is, however, an important distinction to be made between symmetry breaking in budding yeast and the yeast to hyphal transition in *C. albicans*. The former is in response to an internal cue, while the latter occurs in response to external cues. The main regulator of polarized growth, and hence symmetry breaking, in both of these model yeasts is the small Rho GTPase Cdc42. This protein was initially described in *S. cerevisiae* (Johnson and Pringle, 1990) and is highly conserved with its mammalian counterparts, with 80% similarity in amino acid sequence between budding yeast and human forms (Etienne-Manneville, 2004; Johnson, 1999; Park and Bi, 2007; Ziman et al., 1991). First, the mechanisms of symmetry breaking in *S. cerevisiae* will be discussed and then how this can be extrapolated to the yeast to hyphal transition in *C. albicans*.

In budding yeast, symmetry breaking is the change from isotropic growth to polarized growth that results in the formation of a bud and ultimately a daughter cell (Arkowitz and Bassilana, 2011; Goryachev and Leda, 2017). When a budding cell separates from the mother cell, it enters G1 and isotropic symmetrical growth follows. During this time a cortical patch of activated Cdc42 forms, which exhibits small fluctuations in its localization and levels, and is enhanced *via* a Bem1-dependent positive feedback loop to locally activate additional Cdc42 at this incipient bud site (Butty et al., 2002; Irazoqui et al., 2003; Kozubowski et al., 2008; Ozbudak et al., 2005; Woods and Lew, 2017). The localization of the Cdc42 cluster is normally determined by cortical spatial cues. However, in the absence of these cues, polarity sites are

still spontaneously established (Irazoqui et al., 2003; Johnson et al., 2011). This ability to undergo spontaneous symmetry breaking implies that cells have feedback mechanisms to amplify small stochastic asymmetries of polarity proteins in order to establish a polarity site in the absence of spatial cues (Woods and Lew, 2017).

The scaffold protein Bem1 was originally identified in genetic screens for proteins involved in bud emergence and mating projection formation (Bender and Pringle, 1991). It was later investigated for the role it plays in symmetry breaking (Chant and Herskowitz, 1991; Irazoqui et al., 2003). Bem1 is a scaffold protein that binds active Cdc42, Cdc42 effectors including p21 activated kinases (PAKs), and the Cdc42 GEF, Cdc24 (Bose et al., 2001; Endo et al., 2003; Ito et al., 2001; Peterson et al., 1994; Winters and Pryciak, 2005). The binding of Cdc24 to Bem1 and GTP-Cdc42 results in a feedback mechanism wherein neighboring GDP-Cdc42 is activated by this complex (Woods and Lew, 2017). This results in the formation of a new complex, and this process is iteratively repeated, thereby forming a polarized patch of GTP-Cdc42. Bem1 is particularly important for this feedback mechanism because GTP-Cdc42 does not directly bind to Cdc24; therefore, Bem1 provides a scaffold to mediate this interaction (Woods and Lew, 2017).

The requirement for Bem1 in Cdc42 localization was shown by disrupting the interactions between Bem1 and Cdc24 or Cdc42 effector proteins, which resulted in severe polarity defects (Irazoqui et al., 2003). Additionally, disrupting the localization of Bem1 or Cdc24 resulted in the inhibition of polarity, an important outcome because both Bem1 and Cdc24 accumulate with Cdc42 at the polarity site (Woods et al., 2015). Cells can successfully polarize without Bem1 if the Cdc24 and a PAK, such as Cla4, are fused. It is thought that this fusion performs a similar role as Bem1, where the Cdc24 is localized in proximity to GDP-Cdc42 due to the interaction between the effector and Cdc42 (Kozubowski et al., 2008).

Polarized localization of anionic lipids, specifically phosphatidylserine (PS), is required for the proper localization of active Cdc42 and Bem1 (Fig. I-2) (Fairn et al., 2011; Sartorel et al., 2018). In both budding and fission yeast, PS is enriched at the growth site (Fairn et al., 2011; Haupt and Minc, 2017). This contributes to an asymmetric charge distribution on the membrane, where the apex of the gradient at the growth site is the most negatively charged (Fairn et al., 2011; Haupt and Minc, 2017). Using super-resolution microscopy, it was shown that Cdc42 forms nanoclusters at the cell cortex, which are regulated by PS and dependent on Bem1 (Fig. I-2) (Sartorel et al., 2018). Cdc42 nanoclusters were largest at the cell poles and increased in size in cells expressing constitutively active Cdc42 (Sartorel et al., 2018). Further investigation showed that Cdc42 nanoclustering was driven by Bem1 interaction with anionic lipids on the plasma membrane (PM) through basic rich domains (Meca et al., 2019). The interaction between Bem1 basic rich domains and anionic lipids drives the nanoclustering of the Cdc42 module that consists of Bem1-PAK-Cdc24, which results in the local activation of Cdc42 and can facilitate nanoclustering through a positive feedback loop (Fig. I-2) (Meca et al., 2019).

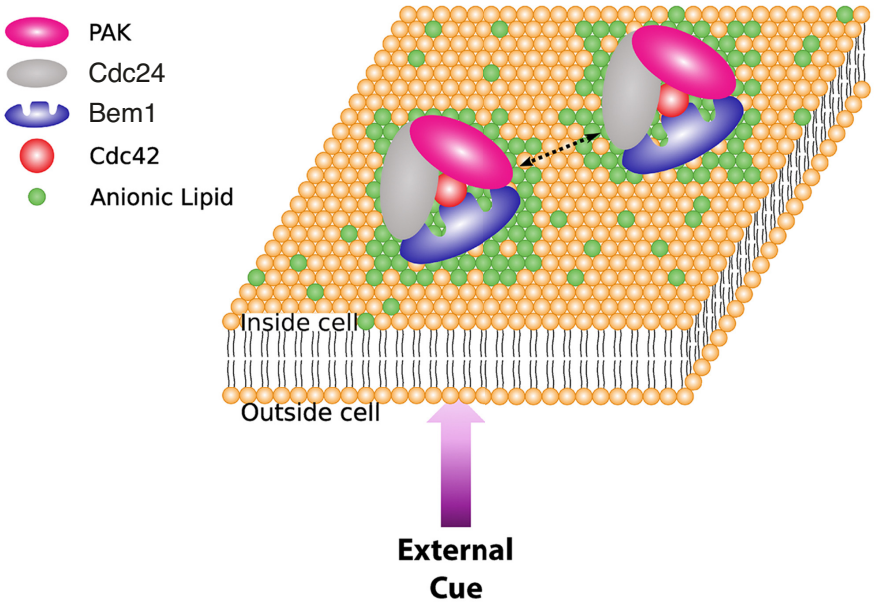

Figure I-2: **Anionic plasma membrane lipids drive active Cdc42 nanoclustering.** Interactions between Bem1 and anionic lipids drives nanoclustering of active Cdc42. The Bem1 scaffold brings Cdc42 in proximity to its GEF Cdc24 and effectors such as p21-activates kinases. The dashed lines demonstrate there are additional interactions between clusters. Figure adapted from Bassilana *et al.*,2020

III – Polarization in response to external cues

In addition to budding growth, *S. cerevisiae* can also grow in a pseudohyphal morphology and form a mating projection in response to an external pheromone. Here, I will be focusing on mating projection formation as an example of morphology change in response to an external cue. In response to mating pheromone, a pear-shaped cell, referred to as a shmoo, forms and, during the mating process, cells of the opposite mating type grow towards each other (Fig. I-3A) (Arkowitz, 2009) . The response to an internal signal, such as those required for budding, results in the clustering of active Cdc42, which is dependent on the scaffold protein Bem1 and lipid composition at the polarization site (Meca et al., 2019; Rapali et al., 2017; Sartorel et al., 2018). In external mediated responses, such as shmoo formation, Bem1 is also localized to the growth site (Butty et al., 2002; Fairn et al., 2011). At the mating and

budding growth site, Bem1 interacts with Cdc42, Cdc24, and Cla4 (Butty et al., 2002). The binding of Bem1 to Cdc24 activates Cdc24, which then activates Cdc42 *via* its GEF activity. GTP bound Cdc42 then recruits additional Bem1. This process results in a positive feedback loop to enhance active Cdc42 localization to the growth site (Butty et al., 2002). Additionally, Cdc42 binding to Bem1 enhances the binding of the PAK protein kinase Ste20 to Bem1, which enforces a strong pheromone signaling response (Bassilana et al., 2020; Martin and Arkowitz, 2014; Yamaguchi et al., 2007).

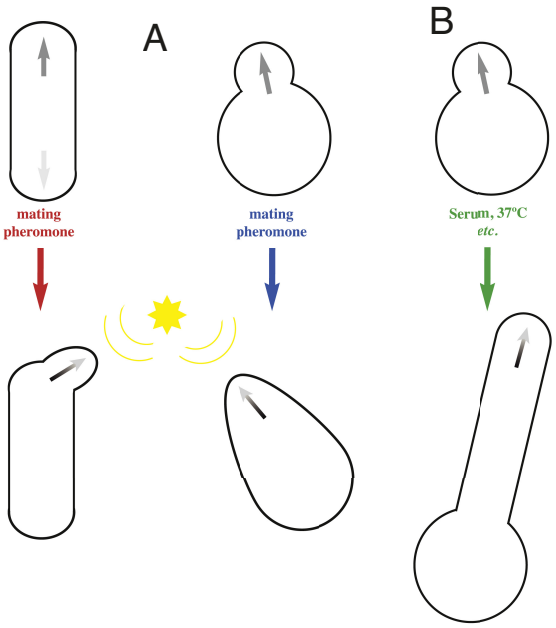

Figure I-3: **External signals lead to changes in polarized growth.** A) When mating pheromone is sensed with *S. cerevisiae* and *S. pombe*, there is an alteration of growth from vegetative growth to the formation of a shmoo. B) For *C. albicans,* external signals, such as serum and 37°C, result in the switch from budding growth to polarized tip growth. Figure adapted from Bassilana *et al*., 2020.

In response to both internal budding and external signals, there is an increase in PS enrichment at the growth site in both *S. cerevisiae* and *S. pombe* (Fairn et al., 2011; Haupt and Minc, 2017). Disruption of this localization using mutants lacking PS synthase lead to defects in shmoo formation that were recovered by the addition of exogenous lysophosphatidylserine (Fairn et al., 2011). It is still unknown whether the formation of lipid-dependent nanoclustering is also required for the enhancement of the polarized patch during shmoo formation through

external signal response. In addition to PS enrichment, shmoo tips are also enriched in phosphatidylinositol phosphate (PIP), phosphatidylinositol 4,5- bisphosphate ($PI(4,5)P_2$), whereas phosphatidylinositol-4- phosphate (PI(4)P) is enriched in budding tips (Garrenton et al., 2010; Guillas et al., 2013; Wild et al., 2004). These PIPs are likely to be important for the localization of polarity proteins, such as PAK kinases, Cdc42 effectors, such as Gic2 (Orlando et al., 2008; Takahashi and Pryciak, 2007); septins (Bertin et al., 2010), and exocyst components, such as Sec3 and Exo70, in budding and fission yeast (He et al., 2007; Zhang et al., 2008). For example, the PAK kinase Cla4 is localized by PI(4)P *via* its pleckstrin homology (PH) domain to growth sites, and $PI(4,5)P_2$ polarization is responsible for the proper localization of the MAPK scaffold Ste5 during mating projection formation *via* a PH domain located within the Ste5 protein (Garrenton et al., 2006, 2010; Wild et al., 2004). Additionally, the PAK kinase Ste20 is recruited to both budding and shmooing growth sites *via* a basic-rich domain that is not specific to a particular PIP but does require membrane binding and Cdc42 binding to initiate the downstream MAP kinase cascade (Takahashi and Pryciak, 2007).

Work from *S. pombe* has also shown the requirement for the homologs of *S. cerevisiae* Cdc42, Cdc24 and Bem1 in polarization during pheromone response (Bendezú and Martin, 2013; Chang et al., 1994). The Cdc24 and Bem1 homologs Scd1 and Scd2 are required for both vegetative growth and mating growth site formation (Chang et al., 1994). Scd1 and Scd2, in addition to Cdc42, localize to sites of active growth in cell tips and in mating projections. Additionally as observed in *S. cerevisiae* mating projections, fission yeast also have a PS gradient emanating from the growth site in a mating projection, which forms a negative charge gradient and has a role in regulating polarized growth (Haupt and Minc, 2017).

Analogous to *S. cerevisiae* discussed above, *C. albicans* polarity establishment occurs during bud formation (Arkowitz and Bassilana, 2011). Additionally, polarization in response to external stimuli can occur when *C. albicans* cells initiate germ tube emergence (Fig. I-3B)

(Arkowitz and Bassilana, 2011, 2019). The signals that lead to hyphal growth in *C. albicans* are extensive and include elevated temperature (37ºC), changes in pH, the presence of carbon dioxide, nutrient starvation, the presence of GlcNAc, and the presence of serum (Sudbery, 2011b). A robust trigger for filamentation is the exposure to 37ºC and fetal calf serum (FCS) (Arkowitz and Bassilana, 2011; Sudbery, 2011b).

The external stimuli that lead to the transition to the hyphal form are transduced through several signaling pathways, which result in the activation of different transcription factors that are responsible for the control of hyphal growth specific genes (Fig. I-4) (Chen et al., 2020; Kornitzer, 2019; Sudbery, 2011b). Hyphal formation in response to liquid media containing serum, carbon dioxide, neutral pH or GlcNAc, and solid spider media require the transcription factor Efg1. Efg1 appears to have a more substantial effect on the regulation of hyphal transition regulation in many conditions, while the transcription factor Cph1 is only required for solid spider media (Braun and Johnson, 2000; Leberer et al., 1996; Liu et al., 1994; Lo et al., 1997; Stoldt et al., 1997). Each of these two transcription factors are activated by specific upstream pathways, a mitogen-activated protein kinase (MAPK) pathway that is activated *via* Ras1 for Cph1 and a cyclic AMP (cAMP) dependent pathway for Efg1, which is also activated *via* Ras1 (Chen et al., 2020; Kornitzer, 2019). Cyr1, also referred to as Cdc35, is the sole adenylyl cyclase in *C. albicans*, and it regulates the cAMP pathway culminating in Efg1 activation (Davis-Hanna et al., 2008; Hall et al., 2011; Rocha et al., 2001). Cyr1 is also responsible for transducing environmental cues from a variety of sources, such as serum and carbon dioxide, and is negatively regulated by the quorum sensing molecule farnesol (Davis-Hanna et al., 2008; Hall et al., 2011; Rocha et al., 2001).

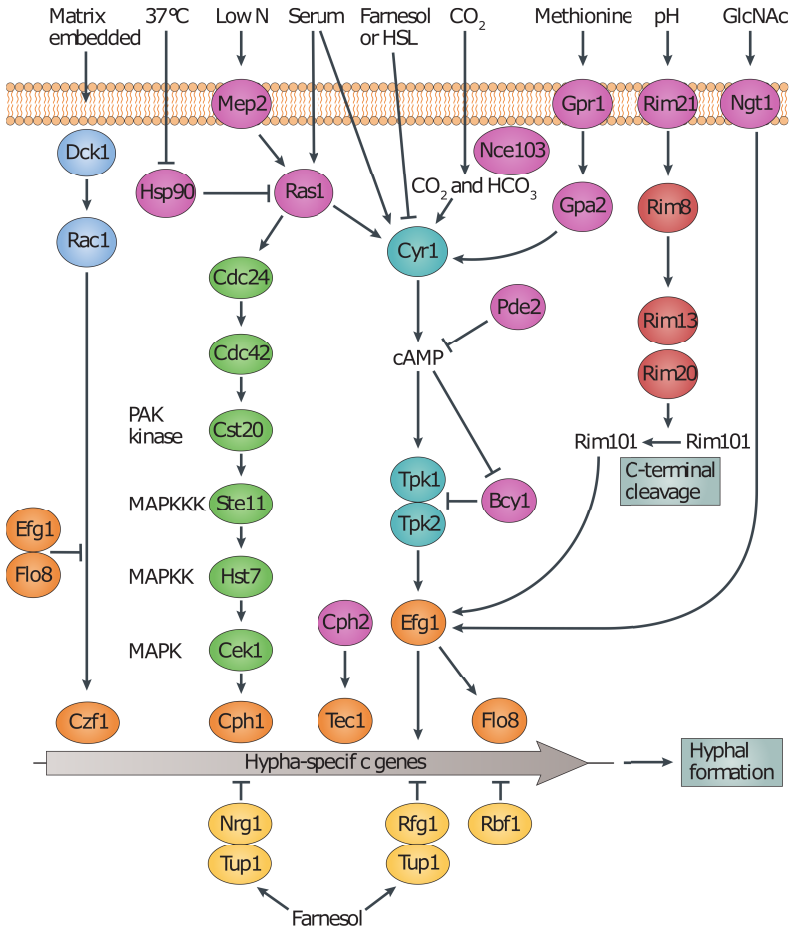

Figure I-4 **Hypha-specific gene expression is induced by external signals through signaling cascades.** Signals are perceived by receptor molecules and are then transformed through a corresponding signaling cascade, which results in the activation of hypha specific transcription factors. This set of transcription factors act on hypha-specific genes that results in the transition from budding to filamentous growth. The quorum sensing molecule, farnesol, acts through Tup1 to negatively regulate hyphal specific gene expression; therefore, at a high concentration of farnesol the yeast to hypha transition does not occur. Figure adapted from Sudbery, 2011

Serum induction of filamentation stimulates Cyr1 through two mechanisms: first through Ras1, which interacts with Cyr1 *via* a Ras-association domain; and second through a direct activation by bacterial peptidoglycan-like molecules that are present in serum (Fang and Wang, 2006; Xu et al., 2008). The activation of Cyr1 by bacterial peptidoglycans occurs through direct binding by a Cyr1 leucine-rich-repeat domain (Xu et al., 2008). Response to these signals leads to the transcription of hyphal specific genes that encode secreted aspartyl protease (SAP) proteins Sap4, Sap5, and Sap6; the adhesion protein Als3, the cell wall protein Hwp1, and the cytolytic toxin protein Ece1 (Allert et al., 2018; Kadosh and Johnson, 2005;

Nantel et al., 2002). Hyphal induction signals also rapidly lead to the establishment and maintenance of a polarity site, resulting in hyphal tip growth (Corvest et al., 2013).

Hyphal growth in response to an external stimulus occurs in a cell cycle independent fashion (Hazan et al., 2002). A hypha can form from an already polarized budding cell by maintaining apical polarity. Additionally, a hypha can form from an isotopically growing cell at any point during the cell cycle (Arkowitz and Bassilana, 2011). Once established, tip growth is maintained regardless of the cell cycle stage. Hyphal initiation leading to filamentous growth in *C. albicans* requires cortical clustering of active Cdc42 to the growth site (Corvest et al., 2013; Silva et al., 2019). In *cdc42* or *cdc24* mutants, *C. albicans* cells are defective in forming hyphal filaments (Bassilana et al., 2003; Corvest et al., 2013; Ushinsky et al., 2002; VandenBerg et al., 2004). Bem1 is also required for hyphal formation (Bassilana et al., 2003), and Cdc24 recruitment to the growth site is important for hyphal growth (Bassilana et al., 2005). Interestingly, mutants for the Arf-like small GTPase Arl1 are defective in establishing a stable polarity patch, most likely due to a defective regulation of membrane trafficking (Labbaoui et al., 2017).

In addition to the polarized localization of proteins needed for tip growth, there is also a polarization of membrane lipids during the yeast to hyphal transition. In *C. albicans* the phospholipids PS and PIPs form gradients with the highest concentration at the growth site, at the filament apex (Arkowitz and Bassilana, 2014; Ghugtyal et al., 2015; Labbaoui et al., 2017; Vernay et al., 2012). The transition from budding growth to hyphal growth requires both a PM PI(4)P and PI(4,5)P_2 gradient (Ghugtyal et al., 2015; Vernay et al., 2012). These gradients are generated by the PM specific PI(4)-kinase Sst4 (Ghugtyal et al., 2015) and the tip localized PI(4)P-5-kinase Mss4 (Vernay et al., 2012), respectively. Stt4 is localized throughout the PM, and a combination of modeling and experimentation revealed that hydrolysis of PI(4)P by the PI(4)P phosphatase Sac1 is critical for the steep PI(4)P PM gradient (Ghugtyal et al., 2015).

The PI(4,5)P_2 gradient requires tip localized Mss4, sufficient PI(4)P production by Stt4, and the actin cytoskeleton, which is critical for PI delivery to the hyphal apex and Mss4 localization (Vernay et al., 2012).

Golgi PI(4)P is also involved in secretory vesicle trafficking during the transition from budding growth to filamentous growth (Ghugtyal et al., 2015). A reduction in Golgi PI(4)P, by repression of the essential Golgi-specific PI(4)-kinase, results in a decrease in secretory vesicle traffic (Ghugtyal et al., 2015). Additionally, a reduction in Golgi PI(4)P results in an increase in the number of Golgi particles that have a reduced movement (Ghugtyal et al., 2015). These phospholipid gradients may also be involved in the clustering of active Cdc42 in *C. albicans*, as many proteins that are involved in the establishment and maintenance of polarized tip growth, such as PAK kinases, Cdc42 effectors, septins, and components of the exocyst complex, have been shown to bind to PI(4,5)P_2 in *S. cerevisiae* (Bassilana et al., 2020). However, it should be noted that the reduction of PM PI(4,5)P_2 levels did not alter Cdc42 localization in *C. albicans* (Vernay et al., 2012).

IV – Hyphal growth initiation and maintenance in *C. albicans*

Septin ring formation, assembly, and subsequent cell separation are important for the initiation of polarized tip growth. Septin disassembly occurs *via* the Cdc28/Hgc1-dependent phosphorylation of a variety of proteins involved in cell polarity and cell separation (González-Novo et al., 2008; Wang et al., 2009; Zheng et al., 2007). The cyclin dependent kinase, Cdc28, regulates the activity of the cyclin Hgc1 (Zheng et al., 2004). At the onset of hyphal development, the Cdc42 GAP Rga2 is hyperphosphorylated by Cdc28/Hgc1, which results in Rga2 instability (Zheng et al., 2007). This maintains active Cdc42 at the tip growth site (Zheng et al., 2007). Cells expressing a Cdc28 analog-sensitive mutant are unable to form long hyphae when Cdc28 activity is inhibited, similar to the situation in *hgc1*Δ cells (Zheng et al., 2007).

The filamentation defect of *hgc1*Δ cells can be rescued by deleting *RGA2*, resulting in elongated budding cells, but apparently normal filaments (Zheng et al., 2007). Additionally, Cdc28/Hgc1 prevents cell separation by phosphorylating the Sep7 septin, resulting in the instability of Cdc10 and the septum ring, and the inability of Cdc14 to associate to the septum ring (Clemente-Blanco et al., 2006; González-Novo et al., 2008). Cdc28/Hgc1 also phosphorylates the transcription factor Efg1, which associates with Ace2 to target and prevent the expression of genes encoding septum degradation enzymes that are required for the degradation of the septum and cell separation (Wang et al., 2009).

The maintenance of hyphal tip growth requires a steady influx of membrane and cell wall material, and the maintenance of polarity proteins restricted to the tip (Arkowitz and Bassilana, 2011). This maintenance of tip growth occurs *via* mechanisms, including polarized exocytosis, site-specific endocytosis that is localized to a collar behind the growth site, restricted or reduced diffusion, and the inactivation of GTPases by GAPs and phospholipids by hydrolysis (Caballero-Lima et al., 2013; Ghugtyal et al., 2015; Zheng et al., 2007). The initial high flux of secretory vesicles, relative to their limiting rate of fusion with the PM, is likely to result in a vesicle cluster at the tip referred to as the Spitzenkörper (Crampin et al., 2005; Weiner et al., 2019). The composition and properties of this structure will be discussed in further detail below.

Exocytosis of vesicles to the filament tip is thought to bring phosphatidylinositol (PI) to the tip, where it is locally converted to PI(4)P (Ghugtyal et al., 2015). PI(4)P forms a steep gradient emanating from the tip that is largely maintained by hydrolysis and, to a lesser extent, uptake by endocytosis (Ghugtyal et al., 2015). In fission yeast it has also been shown that GAP proteins help to restrict the localization of active Cdc42 to the cell tip; however, in this organism, GAPs do not affect response to mating pheromone (Castro and Martin, 2018). Additionally, cells lacking the GAP Rga4, which localizes to the fission yeast cell side, have

an increased diameter but are still able to polarize during vegetative growth (Kelly and Nurse, 2011; Revilla-Guarinos et al., 2016). In *C. albicans* filamentation occurs even in the absence of the Cdc42 GAPs Rga2 and Bem3, which suggests GAPs do not play a significant role in the maintenance of hyphal growth (Court and Sudbery, 2007).

The endocytic collar, which is approximately 2 μm wide and located behind the Spitzenkörper (1-3 μm from the tip), aids in the recycling of polarity and cell wall building proteins, and regulating hyphal extension by removing excess membrane material (Caballero-Lima and Sudbery, 2014; Ghugtyal et al., 2015; Knafler et al., 2019). Endocytosis during filamentous growth is regulated by the endocytic protein Sla1 (Zeng et al., 2012). The dephosphorylation of Sla1 promotes its interaction with the Arp2/3 complex activator Pan1 (Zeng et al., 2012). Cells lacking Sla1, or with a phosphomimetic version of Sla1, have problems maintaining polarized growth, do not uptake FM4-64, and do not exhibit an endocytic collar indicated by actin patches (Zeng et al., 2012). The endocytic collar in *C. albicans* functions to provide cell shape by removal of excess material and cell wall building proteins, and has a minor role in regulating the asymmetrical distribution of the phospholipid PI(4)P (Caballero-Lima et al., 2013; Ghugtyal et al., 2015). Additionally, endocytosis has a function in the regulation of the rate of hyphal elongation. Cells lacking *AKL1,* a kinase implicated in endocytosis regulation through phosphorylation of the scaffold protein Pan1, have an increased elongation rate, whereas over expression of *AKL1* results in a reduced elongation rate (Bar-Yosef et al., 2018).

Ultimately the process of polarized growth is driven by the constant presence of activated Cdc42 at the filament tip by its GEF Cdc24 (Bassilana et al., 2005; Corvest et al., 2013; Silva et al., 2019). The site-specific localization of active Cdc42 promotes the formation of actin cables and the clustering of polarity proteins. The persistent localization of activated Cdc42 and Cdc24 in the hyphal tip indicates that Cdc24 is critical for maintaining active Cdc42

at the tip in *C. albicans* (Bassilana et al., 2005; Corvest et al., 2013; Hazan and Liu, 2002). Additionally, it was shown in budding yeast that the phospholipid-dependent nanoclustering that occurs due to Bem1 and active Cdc42 interaction results in reduced diffusion of active Cdc42 at the growth site (Meca et al., 2019; Sartorel et al., 2018).

Polarized growth in *C. albicans* hyphae is an unidirectional process; however, some responses to external cues can result in altered filament orientation, a process likely to be regulated by the small GTPase Rsr1 (Brand et al., 2008). Cells lacking the Ras like GTPase Rsr1 are unable to respond to external stimuli *via* thigmotropism, physical barriers or galvanotropism, which is the response to an electric field (Brand et al., 2008; Thomson et al., 2015). Wild-type hyphae often reorient their growth when they come in contact with a relatively short physical barrier, like ridges, on a quartz slide or microfabricated, stiff polydimethylsiloxane (PDMS) (Brand et al. 2008; Thomson et al. 2015). In contrast, the *rsr1* mutant does not appear to detect physical barriers; rather, the growth of this mutant remains directionally persistent despite barriers (Brand et al., 2008; Thomson et al., 2015). It has been proposed that Rsr1 has a role in the orientation of the Spitzenkörper.

V – Molecular composition of the filament tip

The filament tip can be divided into three zones: the Spitzenkörper, the tip, and the endocytic collar (Fig. I-5) (Jones and Sudbery, 2010; Martin et al., 2007). Each region has a specific set of proteins that localize to it (Sudbery, 2011a). Proteins found in the Spitzenkörper include the Rab8 homolog Sec4 and its GEF Sec2, the myosin light chain Mlc1, the formin Bni1, and the Rab11 homolog Ypt31 (Crampin et al., 2005; Jones and Sudbery, 2010; Silva et al., 2019). The role of these proteins in the Spitzenkörper will be later discussed in depth. The apical polarity cluster is characterized by a crescent at the extreme apical curvature of the tip and contains proteins that are components of the exocyst and polarisome (Fig. I-5, zone 1).

Additionally, the PM of this region contains a high concentration of PI(4)P (Ghugtyal et al., 2015) and ergosterol (Martin and Konopka, 2004). The polarisome complex, which aids in the targeting of actin filaments from Bni1 to the filament tip, consists of Bud6 (Amberg et al., 1997) and Spa2 (Sheu et al., 1998), both of which have been fluorescently labeled and visualized as a crescent in the filament tip (Crampin et al., 2005; Sudbery, 2011a). The polarisome complex is responsible for actin nucleation in *S. cerevisiae* in order to direct vesicle traffic to the bud tip (Xie et al., 2019). In *C. albicans* the polarisome is important for polarized hyphal growth, and its localization is dependent on the Cdc28 dependent phosphorylation of Spa2 (Wang et al., 2016). Cells lacking *SPA2* or cells containing a non-phosphorylatable mutant are unable to form proper hyphae (Wang et al., 2016).

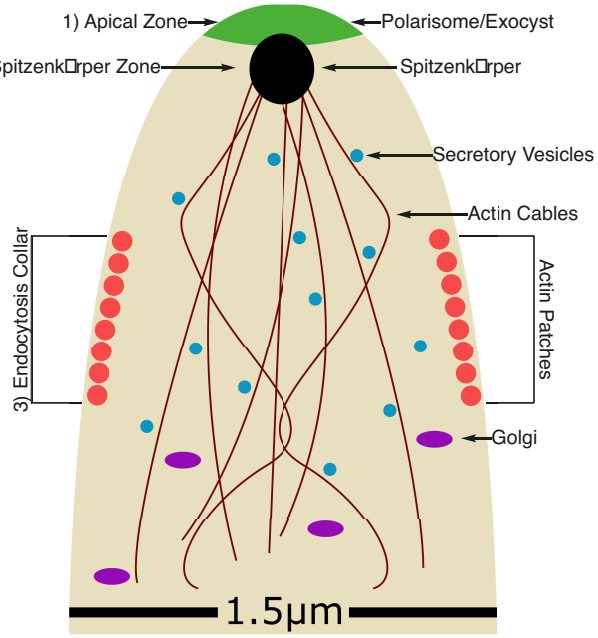

Figure I-5: **The three zones of the hyphal tip.** The hyphal tip can be separated into three general zones. 1) The apical zone –where components of the polarisome and exosome are localized to the PM and where secretory vesicles are incorporated for growth to continue. 2) The Spitzenkörper zone –where the formin Bni1 is localized and where there is an accumulation of vesicles. Vesicles are trafficked from the Spitzenkörper to the apical zone for incorporation at the filament tip. Vesicles are transported into the Spitzenkörper on F-actin. 3) The endocytosis collar –an accumulation of actin patches located 1-3µm sub-apically from the apex. The location of this collar is stable during filament extension.

The exocyst complex, which aids in directing secretory vesicles to the tip (Boyd et al., 2004), was originally discovered in budding yeast (TerBush et al., 1996) and is composed of Exo70, Exo84, Sec15, Sec3, Sec6 and Sec8 (Bowser and Novick, 1991; Guo et al., 1999; Sudbery, 2011a; TerBush and Novick, 1995; Wiederkehr et al., 2003). This complex stabilizes incoming secretory vesicles, which allows docked vesicles to fuse with the PM *via v*-snare and *t*-snare interactions (Novick et al., 2006). In *C. albicans* the exocyst protein Sec15 has been shown to interact with the small GTPase Rsr1, which is required for Sec15 localization (Guo et al., 2016). As previously discussed, polarized active Rho GTPases are localized to this apical polarity cluster, with active Cdc42 localized as a tight cap at the tip and active Rho1 more spread out (Corvest et al., 2013).

Also located towards the tip, the endocytic collar is found just behind the tip, where it is located consistently between 1-3 μm from the hyphal tip (Fig. I-5, zone 3) (Ghugtyal et al., 2015). The endocytic collar is the location of endocytic recycling of membrane material and bound polarity proteins; however, modeling showed that it is not important for the maintenance of polarized PI(4)P distribution (Caballero-Lima and Sudbery, 2014; Ghugtyal et al., 2015). The endocytic collar is composed of proteins involved in clathrin mediated endocytosis such as the actin binding protein Abp1 (Epp et al., 2013; Martin et al., 2007). Regulation of endocytosis is important for the regulation of hyphal elongation rates as cells lacking the Akl1 kinase results in increased elongation rates, while overexpression of this regulatory kinase results in a reduction in hyphal elongation rate.

VI – The Spitzenkörper

The Spitzenkörper is a fungal specific structure found in the hyphal tip (Riquelme and Sánchez-León, 2014). The Spitzenkörper was first described in the early 20th century in fixed *Coprinus narcoticus* and *Coprinus sterquilinus* hyphae as an iron hematoxylin stained apical

body (Brunswick, 1924). Using phase contrast microscopy, the Spitzenkörper was initially observed as a dense region in the filament tip of *Polystictus versicolor* (Girbardt, 1957). Developments in electron microscopy facilitated ultrastructural analyses of a large variety of filamentous fungi; the most recent of which is *C. albicans* (Bourett and Howard, 1991; Fisher and Roberson, 2016; Fisher et al., 2018; Girbardt, 1969; Grove and Bracker, 1970; Harris et al., 2005; Howard, 1981; Lang et al., 2010b, 2010a; Quindós, 2014; Rico-Ramírez et al., 2018; Riquelme et al., 2002; Roberson et al., 2011; Schmied et al., 2014; Vargas et al., 1993; Weiner et al., 2019). These ultrastructural studies revealed the Spitzenkörper to be an accumulation of vesicles (Fig. I-6) (Bourett and Howard, 1991; Girbardt, 1969; Grove and Bracker, 1970; Howard, 1981; Vargas et al., 1993; Weiner et al., 2019).

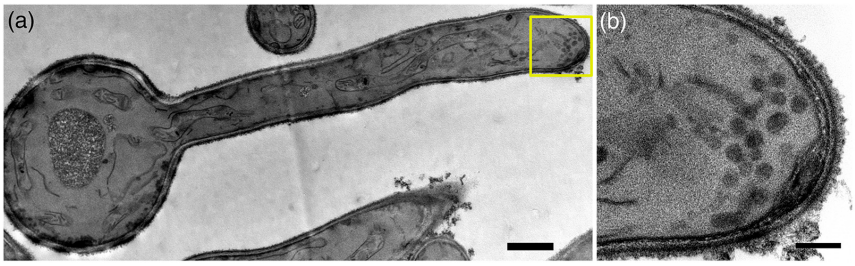

Figure I-6: **The *C. albicans* Spitzenkörper is an accumulation of vesicles.** As in other filamentous fungi, in *C. albicans* an accumulation of vesicles can be observed in the filament tip by scanning electron microscopy. This accumulation of vesicles is the Spitzenk□rper. Figure adapted from Weiner *et al.*, 2019.

The function of the Spitzenkörper has been studied through mathematical modeling to investigate the role it plays in hyphal morphogenesis; much of this pioneering work was done by Bartnicki-Garcia and colleagues. Early on, the Spitzenkörper was proposed to be a vesicle supply center (VSC), a body from which vesicles moved into and then were directed to the PM to contribute to growth (Fig. I-7) (Bartnicki-Garcia et al., 1989). A two-dimensional VSC model was developed to explain the importance of the location of the Spitzenkörper for tubular hyphal growth and morphogenesis (Bartnicki-Garcia et al., 1989). This model demonstrated that alterations in the location of the Spitzenkörper resulted in altered morphologies and

changes in hyphal directionality (Bartnicki-Garcia et al., 1989; Riquelme et al., 1998). Additionally, this model showed the importance for the directed traffic of vesicles from the Spitzenkörper or VSC to the PM since absence of directed movement resulted in spherical growth (Bartnicki-Garcia et al., 1989). This model was additionally used to analyze, by computer simulation, the morphological effects of a Spitzenkörper disturbance phenomenon observed in the fungi *Rhizoctonia solani* and *Aspergillus niger* (Bartnicki-Garcia et al., 1995; Reynaga-Peña et al., 1997). Disturbance of the Spitzenkörper in the former fungi resulted in a permanent bulge from which growth was redirected (Bartnicki-Garcia et al., 1995) and apical branching occurred in *A. niger* (Reynaga-Peña et al., 1997).

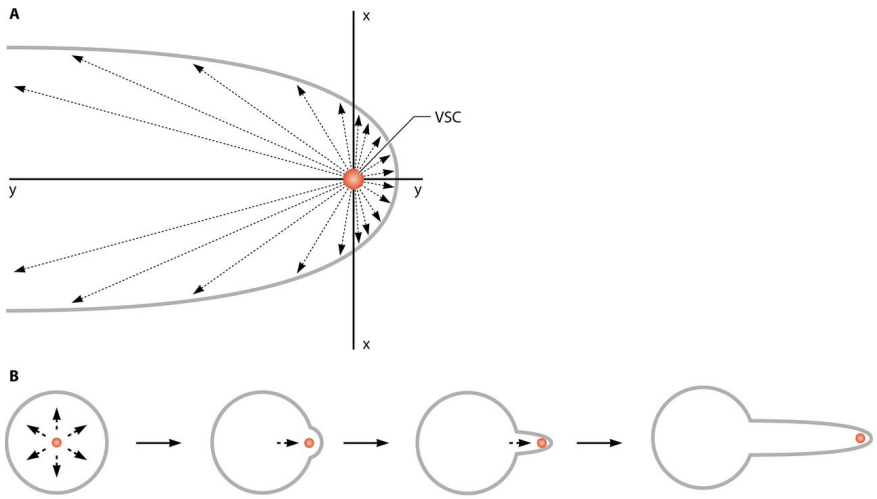

Figure I-7: **The vesicle supply center (VSC) model drives polarized growth of a hyphae.** A) A computer simulation model of a hyphae generated by the addition on material from the VSC plotted on Cartesian coordinates. The vesicle supply center is a model representation of the function of the Spitzenk□rper. The model takes into consideration the rate of material adding vesicles that are moved from the VSC to the plasma membrane and the rate at which the VSC progresses forward. Alterations in the speed of advancement result in different cell diameters. B) Moving the VSC from the central position in a round cell, such as a spore towards the cortex with continual advancement, results in a bulge and ultimately a filament from this point. Figure adapted from Riquelme *et al.,* 2018.

In addition to the modeling of the vesicle supply center, observations were made that the addition of smaller Spitzenkörper like clusters, called satellite Spitzenkörpers, into the main Spitzenkörper correlates with temporary pulses in hyphal extension rates in the relatively rapid

growing fungi *Fusarium culmorum* and *Trichoderma viride* (López-Franco et al., 1994). The mechanism behind these pulses has yet to be fully explained; however, there has been some evidence that pulses of Ca^{2+} correlate with pulsed growth in *A. nidulans* through oscillation in actin depolymerization and polymerization in the hyphal tip (Takeshita, 2018; Takeshita et al., 2017).

The VSC model was later adapted to a three-dimensional model of growth that attempted to incorporate the cell wall expansion during extension (Gierz and Bartnicki-Garcia, 2001). This model was unable to distinguish between three outcomes of cell wall expansion: rotational, orthogonal, or isometric expansion (Gierz and Bartnicki-Garcia, 2001). This model was tested by tracking markers on the inner PM surface and the outer cell wall surface over time during the hyphal extension of *Rhizoctonia solani* (Bartnicki-Garcia et al., 2000). Observations of these markers lead to the conclusion that a single location of the cell wall undergoes orthogonal expansion as the tip proceeds forward (Bartnicki-Garcia et al., 2000). The discovery of the orthogonal expansion of the cell wall provided support for turgor pressure driven cell wall expansion (Bartnicki-Garcia et al., 2000).

Recently it was reported that the Spitzenkörper in *N. crassa* is assembled through a cascade of protein-protein interactions that place two scaffolds in the Spitzenkörper region, which are important for polarity effector recruitment (Zheng et al., 2020). The scaffolds are Leashin-2 (LAH-2) and a complex of Janus-1 (JNS-1) and SPA-2, a polarisome protein (Zheng et al., 2020). The LAH-2 scaffold recruits the glycolysis enzyme GPI-1 and the signaling kinase COT-1 to the Spitzenkörper, while SPA-2 recruits CCP-1, a calponin domain-containing F-actin effector (Zheng et al., 2020). Both scaffold proteins are transported to the Spitzenkörper by MYO-5 *via* the coiled-coil cargo adaptor protein SPZ-1. The JNS-1/SPA-2 scaffold is analogous to the GIT/PIX in metazoans and Pea2/Spa2 complex in *S. cerevisiae* (Zheng et al.,

2020). In both *S. cerevisiae* and metazoans, these complexes are important for polarized growth (Zheng et al., 2020).

The Spitzenkörper was further investigated in a variety of fungi, including *N. crassa* and *A. nidulans,* using the amphiphilic styryl dye FM4-64, which is initially endocytosed and then accumulates in the Spitzenkörper due to membrane recycling (Fischer-Parton et al., 2000). From this work a simple model was proposed for endocytosis and exocytosis during filamentous growth (Fischer-Parton et al., 2000). The accumulation of FM4-64 at the Spitzenkörper has been observed in several fungi including *C. albicans* (Crampin et al., 2005; Fischer-Parton et al., 2000). In *C. albicans,* myosin light chain 1, Mlc1, was proposed as a Spitzenkörper marker by colocalization with the apically accumulated FM4-64 (Crampin et al., 2005). The polarisome components Spa2 and Bud6 were observed as localized to a crescent that only partially colocalized with a FM4-64 accumulation (Crampin et al., 2005). It was also observed that the formin Bni1 and the small GTPase secretory vesicle marker Sec4 and its GEF Sec2 also localize to the Spitzenkörper region (Bishop et al., 2010; Crampin et al., 2005; Jones and Sudbery, 2010; Li et al., 2007; Silva et al., 2019; Wakade et al., 2017; Weiner et al., 2019).

The composition of the Spitzenkörper has been analyzed in several fungi. *N. crassa* was the first fungal model used to study this in detail. It was revealed using transmission electron microscopy that the Spitzenkörper of *N. crassa* consists of two populations of vesicles, macrovesicles and microvesicles (Grove and Bracker, 1970; Howard, 1981). It was later revealed by fluorescence microscopy that the macrovesicle layer contains members of the β-1,3-glucan synthase complex, such as GS-1 (Verdín et al., 2009). When GS-1 was fluorescently labeled, a clear ring at the Spitzenkörper was observed (Verdín et al., 2009). The inner population of microvesicles contain chitin synthases, which when examined with GS-1 are observed at the center of the GS-1 ring (Riquelme et al., 2007; Verdín et al., 2009). This structure is substantially different from what has been observed in *C. albicans*.

The Spitzenkörper of *C. albicans* is comprised of approximately 60 vesicles that have a diameter of 70 nm, as observed by serial section transmission electron microscopy (Weiner et al., 2019). Immuno-gold labeling of Mlc1-GFP unequivocally revealed that Mlc1 is localized to this vesicular cluster at the Spitzenkörper. Additionally, the mechanism of vesicle delivery to the Spitzenkörper appears to be different in *C. albicans* compared to other filamentous fungi.

Analysis of the intracellular organization, by transmission electron microscopy and focused ion beam scanning electron microscopy, revealed the presence of parallel sheets of endoplasmic reticulum extending from the nucleus throughout the germ tube. Near the hyphal tip, these membrane sheets are not stacked and appear less organized (suggested to be the Golgi), ultimately resulting in a cluster of vesicles at the tip apex, presumably by vesicles budding off the late Golgi (Weiner et al., 2019). From these observations, and the fact that *C. albicans* undergoes filamentous growth independent from microtubules (Rida et al., 2006), Weiner *et al.* proposed a model where the majority of the vesicular transport occurs within a short range (within the subapical zone), being that the membrane compartments of the secretory pathway are localized close to the active growth site in the filament tip (Weiner et al., 2019). These electron microscopy images also reveal that the vesicles are tightly packed with > 25% in close proximity (< 70 nm) to the PM (Weiner et al., 2019).

Early investigations of the Spitzenkörper in *C. albicans* using fluorescent proteins claimed that the Spitzenkörper could be distinguished from the polarisome and exocyst complex (Jones and Sudbery, 2010). However, given its proximity, this distinction is technically not possible due to light resolution limits when measured by electron microscopy. Nonetheless, electron microscopy revealed that 75% of Spitzenkörper vesicles are located between 70 nm and 500 nm from the hyphal tip, which provides a region where a highly concentrated of vesicles can be distinguished from tip localized proteins (Weiner et al., 2019). The eight components of the exocyst, Sec3, Sec5, Sec6, Sec8, Sec10, Sec15, Exo70 and Exo84,

localize to a crescent in the filament tip (Jones and Sudbery, 2010). Additionally, the polarisome components Spa2 and Bud6 have been observed as forming a crescent in the filament tip (Jones and Sudbery, 2010). The small GTPase Sec4, an established secretory vesicle marker (Li et al., 2007), was originally observed localized to the hyphal tip as a spot (Jones and Sudbery, 2010; Li et al., 2007). Observing the localization of double labeled strains for Sec4 and the exocyst component Exo70 by confocal microscopy appeared to show Sec4 localized in a spot behind the exocyst crescent; however, the GFP fluorescent tag on Sec4 had some bleed-through to the YFP channel for Exo70-YFP, which makes the localization results difficult to interpret (Jones and Sudbery, 2010). Both Sec4 and Mlc1 have similar localizations in the tip at the Spitzenkörper (Crampin et al., 2005; Jones and Sudbery, 2010; Li et al., 2007). It has been reported that, at times, the localization of Mlc1 and Sec4 can also become crescent like, which was suggested as possibly being due to changes in growth rates or other environmental factors (Jones and Sudbery, 2010), as has been observed in *Ashbya gossypii* (Köhli et al., 2008).

A fluorescence recovery after photobleaching (FRAP) approach was carried out to probe the dynamics of the Spitzenkörper, exocyst complex, and polarisome complex (Jones and Sudbery, 2010). From these studies, it was observed that Sec4 and Mlc1 have relatively fast fluorescence recoveries, with Mlc1 recovering somewhat slower with a half-time ($t_{1/2}$) of ~12 sec than Sec4, which recovered with a $t_{1/2}$ of ~7 sec (Jones and Sudbery, 2010). Both Mlc1 and Sec4 had faster fluorescence recovery than polarisome and exocyst proteins, with the fastest being Spa2 with a recovery $t_{1/2}$ of ~21 sec and the slowest being Bud6 with a recovery $t_{1/2}$ ~48 sec (Jones and Sudbery, 2010).

While FRAP measures the rate of new protein addition compared to that of proteins leaving, a fluorescence loss in photobleaching (FLIP) experiment was used to measure the rate at which Sec4 and Spa2 enter the Spitzenkörper and polarisome (Jones and Sudbery, 2010).

The experiment was performed by the continuous bleaching of a subapical strip and measuring the loss of fluorescence in the tip. In this experiment the fluorescence of Sec4 showed a rapid exponential decline suggesting Sec4 is moved from the bleached region to the Spitzenkörper, while the Spa2 signal decreases only slightly suggesting this protein is not actively transporting through the bleached region (Jones and Sudbery, 2010).

Turnover rates of Spitzenkörper vesicles were determined using vesicle surface area measured by electron microscopy and filament extension rates with several assumptions (Weiner et al., 2019). Qualitatively, the fluorescence signal of the Spitzenkörper appears constant during growth and the number of vesicles in the Spitzenkörper, determined by electron microscopy, did not depend on filament length; therefore, it was assumed that the Spitzenkörper has a constant number of vesicles. This results in the rate of vesicles going into and out of the Spitzenkörper (presumably fusing with the PM) also being constant. From these experiments it can be assumed that the vesicle population in the Spitzenkörper remains constant during filamentous growth (Weiner et al., 2019).

VII – The Spitzenkörper marker protein, Mlc1

The myosin light chain protein, Mlc1, has been localized to the Spitzenkörper in *C. albicans* by immune-gold labeling (Weiner et al., 2019). Fluorescently labeled Mlc1 forms a bright, distinctive spot at the apex (the Spitzenkörper) and colocalizes with FM4-64 staining (Crampin et al., 2005). Additionally, Mlc1 localizes to the region of cell division (cytokinesis) in budding, pseudo-hyphal growth and filamentous growth (Crampin et al., 2005). However, its function has only been studied in the model yeast *S. cerevisiae*, where Mlc1 is a haplo-insufficient essential protein (Stevens and Davis, 1998). In *S. cerevisiaie* Mlc1 regulates the activity of the myosin motor proteins Myo2 and Myo1 (Stevens and Davis, 1998). In budding yeast Mlc1 is found at two locations: the site of growth, also known as the bud site, and the

cytokinetic ring. Mlc1 is found at the incipient bud site during G1 and remains associated with the bud tip during S and G2, where associates with Myo2 (Luo et al., 2004; Pennestri et al., 2007).

The majority of studies on the function of Mlc1 in *S. cerevisiae* have focused on its role during cytokinesis. Mlc1 is recruited to the cytokinetic ring during cytokinesis, where it is associated with Myo1 (Boyne et al., 2000). At the cytokinetic ring, Mlc1 is also responsible for the recruitment of Iqg1, an IQGAP-like protein involved in the assembly and contraction of the actomyosin ring and is also known as Cky1 (Feng et al., 2015; Shannon and Li, 2000). Iqg1 contains eleven IQ repeats that are responsible for binding to Mlc1, which anchors Iqg1 to the cytokinesis site (Epp and Chant, 1997; Lippincott and Li, 1998; Shannon and Li, 1999, 2000; Tian et al., 2014). After recruitment of Iqg1, the complex then recruits Myo1 and the F-BAR-domain containing protein Hof1 to promote the formation of the cytokinetic ring complex (Boyne et al., 2000; Luo et al., 2004; Shannon and Li, 2000). Hof1 also has a role in polarized growth through the regulation of actin cable formation by regulating the activity of the Bnr1 formin (Luo et al., 2004; Tian et al., 2014). Mlc1 arrives first to the cytokinetic ring where it is recruited by septins (Graziano et al., 2014). After localization to the cytokinetic ring, Mlc1 recruits Iqg1 (Feng et al., 2015). In depletion experiments cells exhibit cytokinesis defects upon the depletion of Mlc1 (Shannon and Li, 2000). Although the localization of Mlc1 in *C. albicans* has been described, its function in this pathogen has yet to be examined.

VIII – Invasive growth mechanisms and their role during infection

Not all *Candida* species require filamentation for their ability to infect a host. For example, filamentation has yet to be observed in *Candida glabrata* despite the ability of this organism to invade and infect its host (Boyne et al., 2000). Filamentation of *C. albicans* is

important during infection, which has been studied during active penetration and induced endocytosis (Allert et al., 2018; Goyer et al., 2016; Wächtler et al., 2012). The role of filamentation in crossing epithelial barriers has been examined using *in vitro* epithelial models, such as buccal mucosa and intestinal epithelium (Pappas et al., 2018). These models facilitate the investigation of adhesion, induced endocytosis, and active penetration mechanisms during *C. albicans* infection (Fig. I-8).

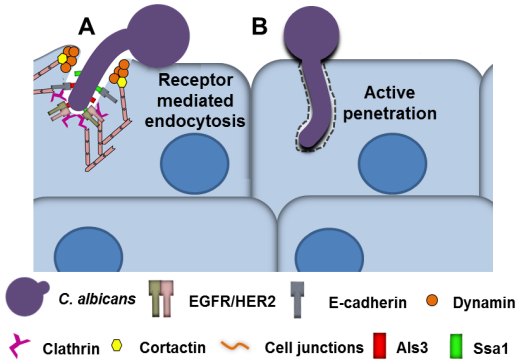

Figure I-8: **Host cell invasion occurs through both host cell mediated endocytosis and active penetration.** A) Endocytosis by the host cell occurs through interactions between the fungal cell wall proteins Als3 and Ssa1 and the host cell receptors EGFR/HER2 complex and E-cadherin. This is a clathrin mediated process. B) Active penetration requires the hyphae to overcome the tension of the host cell membrane, this is likely achieved by the adhesion of the fungi to the host cell surface prior to penetration occurring. This adhesion provides the anchor for the filament to push against during active penetration. Figure adapted from Swidergall and Filler, 2017

Adhesion of *C. albicans* hyphae to the PM of epithelial cells is important for induced endocytosis and active penetration (Allert et al., 2018; Goyer et al., 2016; Wächtler et al., 2012). Additionally, this step initiates host-cell signaling cascades leading to responses to the fungi by the host. Adhesion largely occurs through the interaction between the fungal agglutinin-like protein Als3 and the host surface adhesion protein E-cadherin (Goyer et al., 2016; Moyes et al., 2015; Pappas et al., 2018; Wächtler et al., 2012). Nevertheless, the absence of either Als3 in the fungi or E-cadherin on the host results in a reduction, but not abolition, of adherence of *C. albicans* to an epithelial cell surface (Moyes et al., 2015; Wächtler et al., 2012).

This suggests other adhesive interactions are involved, which occur *via* Hwp1, Iff4 and Eap1. The first of which, Hwp1, covalently binds an unknown host surface protein (Goyer et al., 2016; Wächtler et al., 2012). The latter two were discovered as mutants that resulted in reduced adhesion to plastic and polystyrene (Wächtler et al., 2012).

The interaction between Als3 and E-cadherin is the major contributor to the ability of *C. albicans* to adhere to host cells (Moyes et al., 2015). This has been shown by testing adhesion with Hela cells lacking E-cadherin compared to TR-146 oral epithelial cells that express E-cadherin on their surface (Wächtler et al., 2012). An overall reduction in the invasion of Hela cells was observed compared to TR-146 cells (Wächtler et al., 2012). In the same study, the ability of the *als3*Δ mutant to invade cells lacking E-cadherin was examined, and a further reduction in invasion was observed (Wächtler et al., 2012). It has also been shown that pre-incubating *C. albicans* cells with soluble E-cadherin protein resulted in a reduction of adhesion (Wächtler et al., 2012). Interestingly, in intestinal epithelial cells, blocking the Als3 interaction with E-cadherin didn't result in a reduction in invasion (Wächtler et al., 2012). It is likely that different cell types and locations have different adhesive requirements or adhesion may occur by other mechanisms, or both may be true. Invasion can occur once hyphal *C. albicans* cells are adhered to the epithelial surface. Adhesion is required to take advantage of the forces generated by the hyphae for penetration. In other words, if the fungi were not adhered to the host cell surface, the forces generated by the hyphae during attempted invasion would simply push the hyphae backwards rather than utilizing the force to penetrate the PM of the host cell.

Invasion of *C. albicans* cells into host tissue has been shown to occur *via* two mechanisms: induced endocytosis (Fig. I-8A), which is a passive process for the fungi and an active processes for the host, and active penetration (Fig. I-8B), which is an active process for the fungi yet a passive process for the host (Goyer et al., 2016). Induced endocytosis is a process by which hyphal *C. albicans* cells are actively endocytosed in a clathrin-mediated

fashion by the host cell. Observations of this process by electron microscopy have shown hyphae in the process of being endocytosed by the epithelial cell, which is characterized by the host membrane tightly associated with the hyphae and ruffling filipodia on the epithelial cell surface (Moyes et al., 2015). This process is facilitated by surface interactions between proteins on the hyphae and signaling proteins located on the surface of the host cell. In oral epithelial cells, endocytosis is mediated by the interaction of Als3 with the EGFR/Her3 complex and E-cadherin (Wächtler et al., 2012). This interaction leads to cytoskeleton rearrangement and the formation of filipodia, which engulf and endocytose the hyphae in a clathrin-mediated fashion (Moyes et al., 2015). This process is also tissue specific; it is the prevalent means of invasion for oral epithelial cells yet is rarely observed with intestinal epithelial cells (Moyes et al., 2015). Active penetration appears to be the dominant means of translocation across the epithelial layer in the intestinal epithelium.

Active penetration occurs when a hypha enters an epithelial cell from the cell surface, or when a hyphae bursts through of an endocytic envelope into the interior of a cell. Both processes require force generation from hyphae to penetrate and to adhere to the host cell PM in order to fully utilize the generated hyphal forces (Allert et al., 2018; Goyer et al., 2016; Moyes et al., 2015). In oral epithelial cells, this is most likely the dominant form of invasion in the early stages of an infection since the fungus needs to first penetrate differentiated cell layers that are unlikely to endocytose the fungus (Moyes et al., 2015; Naglik et al., 2011). Later in this type of infection, induced endocytosis becomes more dominant in the lower layers. When observed with electron microscopy, active penetration is visually different from induced endocytosis, which is characterized by a greater space between the host cell membrane and the hyphae, and a lack of ruffling at the cell surface (Naglik et al., 2011). Nonetheless, such observations are somewhat biased because they are based on situations in which only induced endocytosis or active penetration has occurred. As both induced endocytosis and active

penetration occur during an infection, it is challenging to distinguish them from one another (Wächtler et al., 2012).

In intestinal epithelium, active penetration appears to be the major form of invasion, unless there is disruption of the cell junctions that leads to an increase in induced endocytosis (Wächtler et al., 2012). Additionally in cultured intestinal epithelial cells, the ability of *C. albicans* to actively penetrate is reduced as a function of time during the differentiation process (Goyer et al., 2016). In this same study, where the epithelial layers were treated with mycotoxin patulin, it was observed that if tight junctions were disrupted by chemical treatment then induced endocytosis could occur (Goyer et al., 2016). This was the first instance where induced endocytosis was observed in intestinal epithelia (Goyer et al., 2016).

Following the treatment of the epithelial layer with mycotoxin patulin, tight junctions were relaxed, which exposed the adherens junctions located below. This potentially provides access for Als3 on the fungal hyphae to bind with E-cadherin, which leads to induced endocytosis. However, the increase in endocytic uptake was not attributed to the Als3 interaction with E-cadherin because immunoblocking E-cadherin did not affect invasiveness in patulin treated cells (Goyer et al., 2016). It is likely that the interaction between Als3 and the EGFR/Her2 complex has a role in signaling that leads to induced endocytosis, as was observed with oral epithelial cells (Goyer et al., 2016). Additionally, the authors observed less invasion with the *als3*Δ mutant compared to wild-type *C. albicans*, similar to what was observed in oral epithelial cells (Zhu et al., 2012).

Often, the end result after attachment and invasion is the translocation of the fungi across the epithelial layer or layers. Invasion is accompanied by host cell damage, weakening of the epithelium, and an increase in the likelihood of translocation (Goyer et al., 2016; Wächtler et al., 2012). The process and characteristics of translocation have been well studied for intestinal epithelium (Moyes et al., 2015). The mechanism of translocation into the gut is

important to understand because of the constant presence of *C. albicans* as a commensal in humans (Allert et al., 2018). Allert *et al.* proposed four possible mechanisms of translocation across the intestinal epithelia: apoptosis of the host cell, paracellular, transcellular with necrotic damage, and transcellular without damage (Allert et al., 2018). The dominant mechanism that resulted in the greatest potential for translocation was transcellular with necrotic damage. This was observed in endpoint assays where nearly 40% of intestinal epithelial cells had undergone necrotic cell death after 24 hr of exposure to *C. albicans* (Allert et al., 2018).

Necrotic cell death occurs due to fungal secreted enzymes and toxins, of which the cytolytic toxin candidalysin, encoded by *ECE1*, has the most significant effect (Allert et al., 2018). Others include SAP proteins, which have been shown to disrupt tight junctions (Allert et al., 2018). The *ECE1* gene was first described as having a significant effect on the invasive ability of *C. albicans* due to its protein product candidalysin (Allert et al., 2018; Moyes et al., 2015). In an *in vivo* oropharyngeal mouse model, the *ece1*Δ/Δ strain was cleared from most mice (Moyes et al., 2016). In the few mice where the fungus was still detected, no mucosal tissue damage was observed (Moyes et al., 2016). In a second mucosal model using zebrafish swim bladders, a significant reduction in neutrophil recruitment and cell damage was observed (Moyes et al., 2016). This was also observed in the *in vitro* intestinal epithelium model. The *ece1*Δ/Δ mutant displayed a significant reduction in cell damage and translocation; however, some cells were still able to translocate (Moyes et al., 2016). This suggests that there are other factors that also facilitate invasion, such as other toxic or degradative secreted proteins that can cause cell damage or facilitate induced endocytosis or both. Additionally, there is likely a physical component where *C. albicans* hyphae are capable of generating the physical forces necessary to overcome the epithelia cell membrane and advance either in an intra-cell or inter-cell fashion to translocate through the membrane.

The studies into the mechanism of *C. albicans* invasion, specifically active penetration, have thus far been limited to end point experiments. The effects of infection were observed after the host and pathogen had been in contact for some time. To further understand the process of host invasion, it would be necessary to move from endpoint experiments, which provide a snapshot of the process, to observing invasion of host tissue in real-time. This would likely be possible by the live cell imaging of *C. albicans* cells added to the surface of cultured tissues. Labeling both the host cells and *C. albicans* could provide a comprehensive assessment of the mechanisms of invasion and the host cell response to this pathogen.

IX – Biophysical properties of fungal growth

Fungal cells are highly turgid similar to plant and bacterial cells, which is only possible due to the presence of a cell wall. Without a cell wall, the high turgor pressures in fungi would not be contained by a cell membrane and the cells would lyse. In filamentous fungi, membrane traffic provides material for cellular extension, while turgor pressure provides the forces needed to extend growth at the tip (Fig. I-9). This occurs in filamentous fungi, fission yeast and budding yeast, both bud and shmoo forms, where the cell wall at the growth site is thinner and less stiff than the cell wall along the length of the cell (Altenburg et al., 2019; Baba et al., 1989; Cassone et al., 1979; Davì et al., 2018; Goldenbogen et al., 2016; Lew, 2011; Martínez-Núñez and Riquelme, 2015). This difference in stiffness allows the growth site to expand due to pressure, thus providing extension (Chang, 2017). The cell wall continues to stiffen and modified as the growing tip moves away through the addition of new material (Fig. I-9). Turgor

pressure, which provides the force for growth, has been measured indirectly using the fission yeast model *S. pombe* and its effect on growth (Haupt et al., 2018; Knapp et al., 2019; Minc et al., 2009).

Turgor pressure has been shown to have a large effect on the cell shape of fission yeast

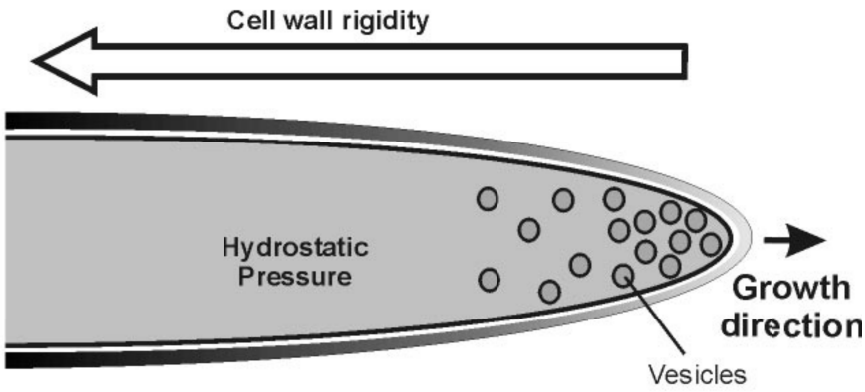

Figure I-9: **Turgor pressure provides force for growth.** Internal hydrostatic pressure (turgor pressure) provides the necessary force for growth to occur. This pressure, in combination with a softer cell wall at the growth site, where directed secretory vesicle traffic occurs, results in filament extension and a tubular shape. Figure adapted from Bastmeyer *et al.*, 2002.

and budding yeast, where the internal pressure provides the pressure to inflate the cell membrane and the cell wall (Atilgan et al., 2015; Minc et al., 2009; Schaber et al., 2010). The cell wall is an elastic material that can be deformed by strong internal pressure (Atilgan et al., 2015; Julien and Boudaoud, 2018). When this pressure is reduced by cell lysis or by hyperosmotic treatment, the cell wall shrinks (Minc et al., 2009). By releasing cell pressure and examining the cell wall, the elastic modulus of the fission yeast cell wall has been estimated to be approximately 50 MPa with an effective turgor pressure estimated at 1.5 MPa (Abenza et al., 2015; Atilgan et al., 2015). The turgor pressure value was estimated using two different methods, firstly by using PDMS microchambers of known stiffnesses as force sensors (Atilgan et al., 2015; Chang, 2017; Minc et al., 2009) and secondly by measuring shrinkage of the cell wall after osmotic shock (Minc et al., 2009). The cell wall properties for *S. cerevisiae* was first

estimated by mathematical modeling to have an elastic modulus of approximately 14.3 MPa (this estimation had a standard deviation of 10.4) with an estimated turgor pressure of 0.6 MPa (Schaber et al., 2010). Later, the cell wall elastic modulus was directly measured by atomic force microscopy (AFM) to be approximately 2.6 MPa, from which the internal turgor pressure was estimated to be approximately 0.21 MPa (Goldenbogen et al., 2016).

Filamentous fungi use tip growth generated by turgor pressure to explore their environment or penetrate host tissue while foraging or producing fruiting bodies (Bastmeyer et al., 2002). For example, an early experiment observing the forces generated by the fungi *Coprinus sterquilinus* demonstrated that the fruiting body of this fungi was capable of lifting 200 grams, which was later estimated to be due to growth with a turgor pressure of 0.07 MPa (Bastmeyer et al., 2002; Buller, 1931). This type of force by a fruiting body is sufficient enough to crack through asphalt paving (Bastmeyer et al., 2002).

In order to penetrate host tissue, fungi use a variety of mechanisms. One remarkable example of the use of turgor pressure to penetrate very rigid host tissue is the formation of an appressorium in the rice blast plant fungal pathogens *Magnaporthe grisea* (Bastmeyer et al., 2002; Howard and Valent, 1996; Howard et al., 1991; Wilson and Talbot, 2009). This is an extreme example in which this fungus forms a specialized cell that acts as a high-pressure chamber referred to as an appressorium. The appressorium, which can generate turgor pressures up to 8 MPa through cell wall melanization and glycerol production, focuses pressure into a small germ tube or penetration peg in order to penetrate the very stiff leaf cuticle of the plant host (Jong et al., 1997; Ryder et al., 2019). Penetration of host tissue by other plant and animal fungal pathogens often does not result in dramatic changes in fungal morphology; although, some increased cell diameter upon invasion has been reported, such as with the tomato pathogen *Cladosprium fulvum* (Van den Ackerveken et al., 1994; Bastmeyer et al., 2002; Mendgen et al., 1996).

The turgor pressure driven process of growth leading to invasion is a form of growth under resistive forces. The cellular effects of growth under extreme resistive forces have been studied in the rod-shaped *S. pombe.* Cells were grown under confined conditions in PDMS microfluidic chambers, and the effects on polarized proteins were investigated (Haupt et al., 2018). Completely confined growth resulted in wandering Cdc42 patches and eventually the complete dispersion of polarized Cdc42, which indicates that active Cdc42 patches disperse under growth arrest (Haupt et al., 2018). This observation was confirmed by slowing growth *via* osmotic shock using a strain that is incapable of osmoregulation (Haupt et al., 2018). Hyperosmotic shock, which lead to transient cell shrinkage, resulted in a dramatic reduction in growth rate, as previously observed, (Minc et al., 2009) and the dispersion of active Cdc42 domains, which remained stable for 1 hr post-treatment (Haupt et al., 2018). Additionally, oscillations of hyperosmotic shocks to disrupt growth rate over longer time scales (multiple hours) lead to the accumulation of cytosolic proteins (Knapp et al., 2019). Once released from these oscillations, cells exhibited a higher-than-normal growth rate, or supergrowth, which functions to dilute the cytosolic protein concentration to normal levels (Knapp et al., 2019).

The disruption of growth rate by cell swelling also resulted in the disruption of active Cdc42 patches (Haupt et al., 2018). Using a slow growing mutant that can be restored to wild type-like growth rates by adding 50 mM KCl to the media showed an increase in active Cdc42 signaling after the addition of 50 mM KCl (Haupt et al., 2018). These results suggest that active Cdc42 activity at the polarized growth site is tightly linked to growth rate but not cell shape as active Cdc42 localization does not determine cell shape (Abenza et al., 2015). Additionally, growth arrest by osmotic and physical means resulted in the disorganization of actin cytoskeleton, polarisome and exocyst components (Sec6 and Sec8), and the mis-localization of the beta-glucan synthase subunit Bgs4, which suggests that these perturbances also disrupt membrane traffic (Haupt et al., 2018).

In terms of shape determination, the localization of active Cdc42 appears to be less important (Abenza et al., 2015). Rather, it appears that the localization of exocytosis related proteins, specifically the exocyst component Sec6, in combination with cell wall mechanical properties can be used as effective determinates of cell shape (Abenza et al., 2015). In fact forcing a wider exocytosis domain resulted in proportional changes to cell morphology (Abenza et al., 2015). This was done by utilizing a GFP binding protein that was targeted to the PM. This resulted in an increase in an altered localization of the GFP labeled exocytic protein Syb1, leading to cells with an increased tip curvature and cell diameter (Abenza et al., 2015).

Furthermore, growth rate disruption by inhibiting actin polymerization also resulted in a dramatic reduction in active Cdc42 polarization (Haupt et al., 2018). These experiments and results highlight a feedback mechanism between membrane transport (providing growth material) and polarity domains that direct material to growth sites. Polarity domains cannot be maintained when membrane traffic is disrupted, such as the disruption of actin cables; and conversely, membrane traffic cannot be maintained if polarity domains are disrupted by growth inhibition. Interestingly, upon the release of confinement by the ablation of a cell, polarized growth was resumed in neighboring cells to fill the gap of the missing cell (Haupt et al., 2018).

The effects of growing against a substrate have been studied in *C. albicans* during *in vitro* studies on abiotic surfaces, such as PDMS and polyacrylamide hydrogels (Desai et al., 2015; Thomson et al., 2015). Biofilm formation on hydrogels resulted in hyphal invasion in an Rhr2 dependent fashion (Desai et al., 2015). Rhr2 is protein responsible for glycerol accumulation, which is responsible for the transcription of adhesion protein genes, such as *ALS1*, in substrate invasion (Bonhomme et al., 2011; Desai et al., 2013). When *ALS1* or the transcription factors *BRG1* or *UME6* were over expressed in the *rhr2* mutant, biofilm formation was restored but not invasive growth of the hydrogel substrate (Desai et al., 2015). This

highlights an additional role for Rhr2 in glycerol accumulation to provide turgor pressure for biofilm substrate invasion (Desai et al., 2015).

Mathematical modeling of the role of turgor pressure in substrate invasion showed the amount of invasion directly depends on the proportion of hyphal turgor pressure to substrate elastic modulus (Desai et al., 2015). This model was confirmed by using hydrogels of different stiffnesses, which resulted in a linear relationship between substrate stiffness and depth of biofilm hyphal invasion (Desai et al., 2015). From these observations the effective turgor pressure was estimated to be 0.7-1.0 mPa for biofilm-derived hyphae (Desai et al., 2015). Additionally, the turgor pressure of planktonic *C. albicans* hyphae was estimated based on the magnitude of deformation that occurred when a hyphal tip encountered a low PDMS ridge (Thomson et al., 2015). The force of indentation was estimated by using a force of indentation standard curve generated by AFM (Thomson et al., 2015). These experiments revealed that *C. albicans* is capable of generating a minimal tip force of ~ 8.7 μN with an effective turgor pressure of ~1.2 MPa (Thomson et al., 2015). The minimal force generated by this fungus is more than sufficient to penetrate host-cell membranes solely using mechanical force (Thomson et al., 2015).

This idea of growth arrest, or stalling, due to a substrate resistive force was previously introduced as a force threshold where the turgor pressure, also known as outward force, is equal to the resistive force, or inward force, experienced by the cell (Haupt et al., 2018). Circular microchambers fabricated from PDMS of a variety of stiffnesses from 0.1 to 1.5 MPa were developed as a tool to study the mechanical forces involved in fission yeast growth and to estimate turgor pressure (Minc et al., 2009). This novel method has a number of advantages compared to previously developed methods to measure forces in fungi, such as the utilization of an oil filled pressure probe (Bastmeyer et al., 2002).

In these experiments, Minc *et al*. observed *S. pombe* during growth under the confinement of the microchambers and noted that stress response pathways did not appear to be activated by the confinement conditions *via* monitoring the stress reporters Sty1 and Pap1 (Minc et al., 2009). This model was used to measure the parameters needed to estimate the cell wall elastic modulus, turgor pressure, and how external mechanical force affects growth rates. The elastic properties of the cell wall were estimated using PDMS growth chambers through observing the deformation of the chamber by growing yeast and the force required for cell buckling. By varying the chamber stiffness and size, the surface modulus was obtained and subsequently used with previously measured cell wall thicknesses to estimate the Young's elastic modulus of the cell wall to be ~101 MPa (Minc et al., 2009). This value is within the same order of magnitude as a recent estimation that used changes in cell wall size induced by osmotic shock, cell lysis, and tracking cell shape over time to estimate the elastic modulus of the cell wall (Abenza et al., 2015; Atilgan et al., 2015; Minc et al., 2009).

Microchamber force sensors were also used to study the effects of mechanical forces on growth rates (Minc et al., 2009). In these experiments, cells were allowed to grow within the microchambers and, once long enough, the cells began to deform the chamber or buckle depending on the chamber's stiffness (Minc et al., 2009). Observing the relationship between chamber deformation and growth rates resulted in the ability to estimate the growth stalling forces for *S. pombe* (Minc et al., 2009). The force was derived from a linear extrapolation of the growth rate and chamber deformation because actual stalling could not be observed due to buckling, which resulted in a stalling force of approximately 11 μN (Minc et al., 2009). Turgor pressure was confirmed to be the required force for chamber deformation because when cells defective in osmoregulation were exposed to osmotic stress, it resulted in a significantly lower stalling force (Minc et al., 2009). Additionally, cells that lacked actin cables still produced a wild type-like stalling force (Minc et al., 2009). The results from osmotic stress and actin cable

disruption highlight the requirement for turgor pressure, and not microfilaments, to provide the force necessary for growth.

The buckling of cells grown in stiff microchambers occurred after a brief pause in the growth rate. The buckling force is positively correlated to this delay, and these results were used to validate a theoretical model that utilized the parameters estimated from the osmotic stress experiments, cell wall elastic modulus, and the stalling force determined from chamber deformation experiments (Minc et al., 2009). Using the derived parameters of cell wall elastic modulus and stalling force, the effective turgor pressure was estimated to be approximately 0.85 MPa (Minc et al., 2009). During the active penetration of host cells, *C. albicans* hyphae also experience resistive force. As a result, it is critical to study the effects of resistive force on the filamentous growth of *C. albicans* hyphae. This has been studied with biofilms (Desai et al., 2015) and at the single cell level, but this has only been studied in non-invasive conditions (Thomson et al., 2015), thus highlighting the need to study the effects of mechanical forces of growth during invasion at the single cell level.

X – Thesis objective

Filamentous fungal growth requires the establishment and maintenance of polarized tip growth. Much of the mechanisms of polarity have been extensively studied in the model yeast organisms *S. cerevisiae* and *S. pombe*, and in well-studied model filamentous fungi, such as *N. crassa* and *A. nidulans*. However, the medical importance of major pathogenic fungi like *C. albicans* signifies the need to study polarized growth and the way in which host invasion occurs in order to better understand and treat infection by these organisms. Here I present two studies regarding the polarized invasive growth of *C. albicans*. The first study investigates the effect of mechanical force on polarized growth during invasion at the single cell level. The second

study examines the role of the Spitzenkörper regulating growth by perturbing the Spitzenkörper and its dynamics, and quantifying the effects.

Chapter 2

External signal–mediated polarized growth in fungi

Martine Bassilana, **Charles Puerner**, and Robert A. Arkowitz

Bassilana, *et al.,* 2020, Current Opinion in Cell Biology 62,150–158

This section of the introduction will include an in-depth review on the recent advances in external signal-mediated polarity in fungi. As a coauthor, I contributed to this work through background research on the recent advances in *S. pombe* as related to the scope of this article. Additionally, I created the schematics presented in Figure 3 on GTPase cycle and polarity protein clustering on the plasma membrane. I also participated in the editing of the final document before submission. This section is meant to be an expansion on the introduction section III – Polarization in response to external cues.

Available online at www.sciencedirect.com

ScienceDirect

Current Opinion in Cell Biology

External signal–mediated polarized growth in fungi

Martine Bassilana, Charles Puerner and Robert A. Arkowitz

Abstract

As the majority of fungi are nonmotile, polarized growth in response to an external signal enables them to search for nutrients and mating partners, and hence is crucial for survival and proliferation. Although the mechanisms underlying polarization in response to external signals has commonalities with polarization during mitotic division, during budding, and fission growth, the importance of diverse feedback loops regulating external signal–mediated polarized growth is likely to be distinct and uniquely adapted to a dynamic environment. Here, we highlight recent advances in our understanding of the mechanisms that are crucial for polarity in response to external signals in fungi, with particular focus on the roles of membrane traffic, small GTPases, and lipids, as well as the interplay between cell shape and cell growth.

Addresses

Université Côte D'Azur, CNRS, INSERM, Institute of Biology Valrose (iBV), Parc, Valrose, Nice, France

Corresponding authors: Arkowitz, Robert A (arkowitz@unice.fr); Bassilana, Martine (Martine.BASSILANA@univ-cotedazur.fr)

Current Opinion in Cell Biology 2020, **62**:150–158

This review comes from a themed issue on **Cell architecture**

Edited by **Sandrine Etienne-Manneville** and **Robert Arkowitz**

For a complete overview see the Issue and the Editorial

Available online 23 December 2019

https://doi.org/10.1016/j.ceb.2019.11.001

Keywords

Fungi, Polarized growth, Membrane traffic, Acidic phospholipids, GTPases, Cell shape.

Introduction

Polarized growth in fungi occurs by insertion of new material into the plasma membrane *via* the secretory pathway and concomitant remodeling of the cell wall. Such growth can be triggered by internal cues, for example, cell cycle progression or external cues, including changes in the environment or the presence of peptide mating pheromone. During external signal–mediated polarized growth in fungi, growth is either directed toward a source of attractant or occurs in a random direction. The presence of an external signal initiates polarized growth and typically overrides or masks growth dictated by an internal signal. Primary examples of fungal external signal–mediated polarized growth are mating projection formation in *Saccharomyces cerevisiae* and *Schizosaccharomyces pombe*, and hyphal cells in filamentous and dimorphic fungi, including *Neurospora crassa*, *Aspergillus nidulans*, and *Candida albicans* (Figure 1). In fungi, polarized growth occurs in the presence of an internal hydrostatic pressure (turgor), which is in the order of 0.5–1.5 MPa for the aforementioned species, that is 0.1 mg-force/μm^2 [1–8]. In each of these fungi, an initial asymmetry is triggered in response to an external signal. This limited asymmetry, which is typically observed as a cluster of an activated small GTPase, is reinforced by feedback loops and ultimately directs site-specific membrane traffic. Here, we will focus on new findings with respect to external signal–mediated polarized growth in fungi, more specifically regarding membrane traffic, small GTPases, and lipids, as well as the interplay between cell shape and polarized growth (Figures 2 and 3). We will not discuss chemotropism and cell fusion in *S. cerevisiae* and *S. pombe*, which have been extensively reviewed recently [9].

Membrane traffic

For polarized growth in fungi, new material has to be inserted into the plasma membrane at a spatially restricted location. Site-specific exocytosis is not sufficient to generate localized growth, as diffusion in the plane of the plasma membrane would result in an ever-extending zone of growth. Hence, it is critical to limit the zone of insertion of the new membrane material, and several studies have revealed that endocytosis fulfills this function in budding and filamentous fungi [10–14]. Recent work on *S. cerevisiae* suggests that exocytosis is directly coupled to endocytosis *via* an interaction between the Rab8 homolog Sec4 and the WASp protein homolog Las17/Bee1 at the plasma membrane [15]. Although this molecular link between an exocytic Rab GTPase and a protein that promotes cortical actin patch formation and is required for endocytosis is intriguing, it remains to be seen whether this is a common theme in other fungi. In filamentous fungi, the endocytic collar is several microns back from the filament tip [16,17] in a region where homologs of Sec4 have yet to be observed. Nonetheless, endocytosis is clearly important for polarized growth in hyphal filaments, as well as in budding and fission yeast [13,16,18,19]. Indeed, membrane traffic is critical for morphogenesis in filamentous fungi, such as *N. crassa* and *A. nidulans* [16,20], and for the maintenance of polarized hyphal growth in *C. albicans*

Figure 1

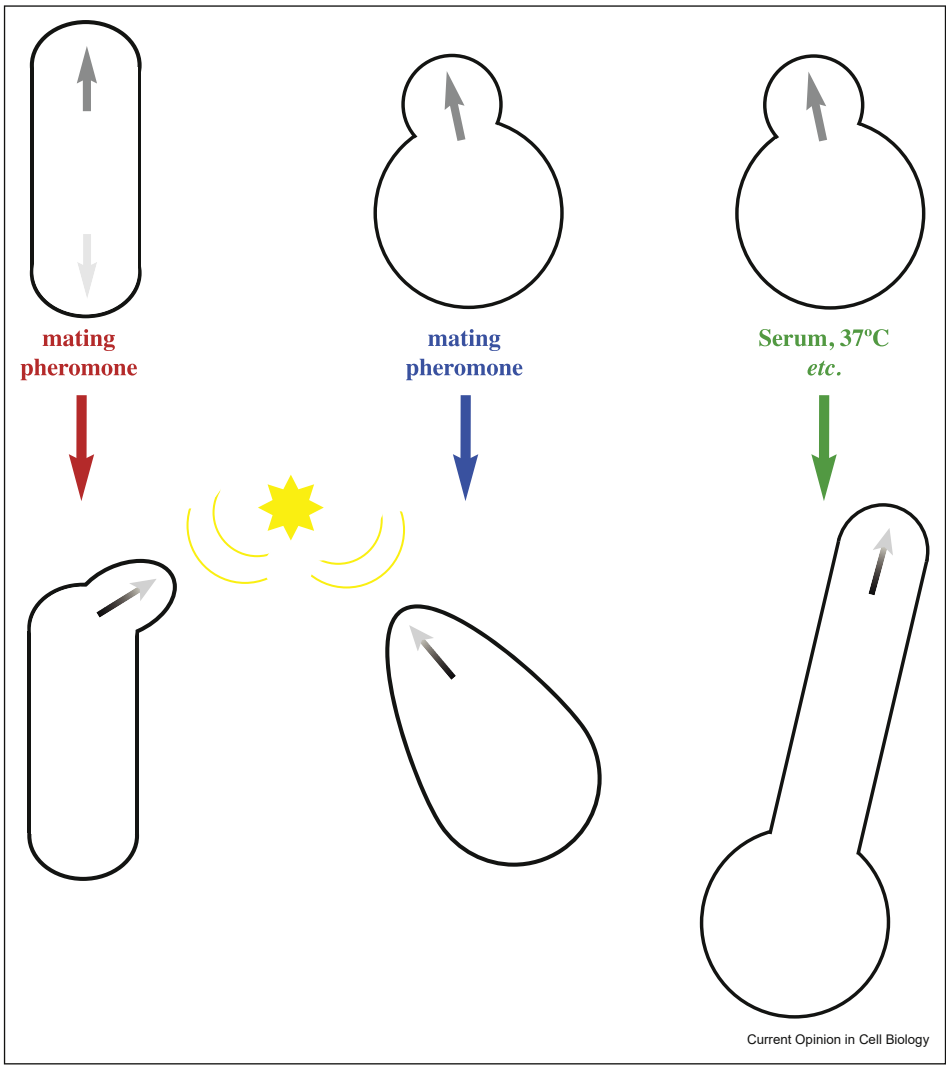

Fungal polarized growth in response to external stimuli. Polarized growth in response to mating pheromone in *Schizosaccharomyces pombe* (left panel) and *Saccharomyces cerevisiae* (middle panel), as well as in dimorphic fungi such as *Candida albicans* in response to a range of external cues including serum (right panel). The upper row depicts cells that are polarized in response to internal stimuli with gray arrows indicating where new growth is directed. The yellow star indicates a source and gradient of mating pheromone and the graded black arrow (lower row) depicts location of growth in response to external stimuli.

[21], and is regulated, in addition to Rab GTPases, by Arf GTPases. Recent studies investigating how membrane traffic regulates hyphal growth focused on Arf GTPases, as well as the AP-2 adapter complex.

In *S. cerevisiae*, Arf3 (the homolog of the human Arf6) specifically interacts with cell polarity proteins and endocytosis factors [22,23] and the *A. nidulans* homolog ArfB, as well as the *Magnaporthe oryzae* homolog Arf6, s regulate endocytosis and maintain polarized hyphal growth [24,25], yet surprisingly in *C. albicans* and *Ashbya gossypii*, *arf3* mutants are unaffected for endocytosis and hyphal growth [26,27]. In contrast, in *C. albicans,* the Arf-like protein Arl1 is important for hyphal growth, with an *arl1* mutant exhibiting shorter hyphae and multiple germ tubes, indicating that Arl1 is required for maintaining growth to a single site [26]. Together, these studies highlight the importance of Arf GTPases in polarity maintenance in different fungi.

The heterotetrameric complex AP-2 has been shown to be critical for relocalization of the cell wall stress sensor Mid2 to the tip of a mating projection in *S. cerevisiae* [28] and, in *S. pombe*, the AP-2 alpha subunit Apl3 is important for cell wall synthesis and morphogenesis [29]. Although dispensable for fungal endocytosis in general,

Figure 2

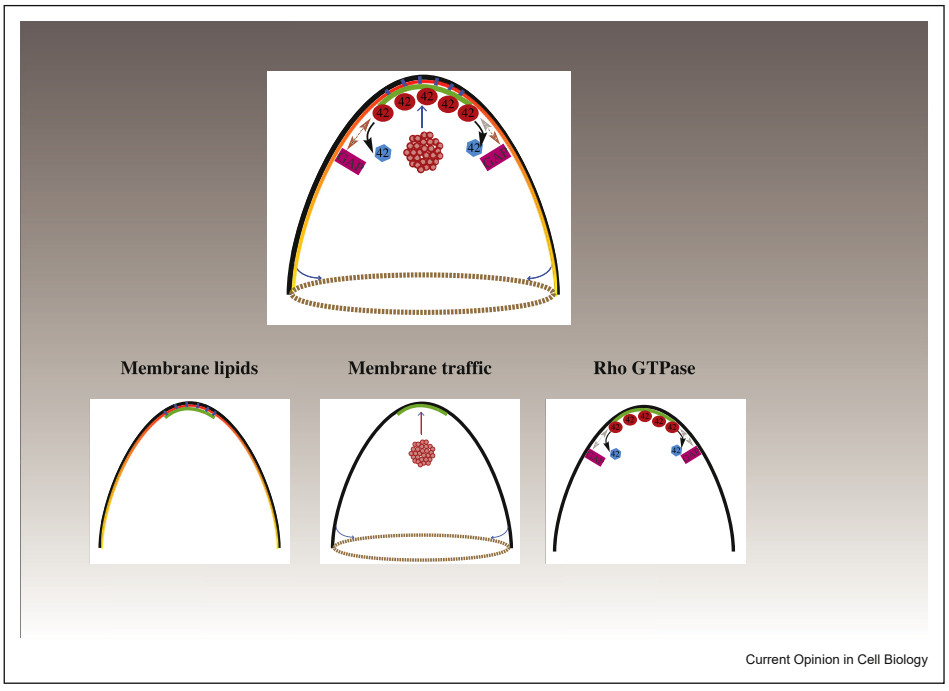

Contribution of membrane lipids, membrane traffic, and Rho GTPases to polarized growth in response to external stimuli. Schematic shows the different processes critical for initiation and maintenance of polarity in response to an external signal (top panel). The left panel highlights the asymmetric distribution of membrane lipids, depicted by a red to yellow gradient at the plasma membrane, for example of PS, PI(4)P, or PI(4,5)P_2. The green patch at the tip depicts polarity factors, including targeted membrane insertion and GTPases with lipid nanoclusters indicated in blue. The middle panel shows directed membrane traffic, with a cluster of vesicles (Spitzenkörper), which is typically found in filamentous fungi, and green patch indicating zone of membrane insertion. Note the brown dashed ring depicts the endocytic collar, which is several microns back from the growth site. The right panel shows the distribution of a Rho GTPase, such as Cdc42, with the active form indicated in red. The gray arrows indicate diffusion in the plane of the membrane and GAP proteins limiting the cluster of active Cdc42, with Cdc42 inactive form shown in blue. PI(4)P, phosphatidylinositol-4-phosphate; PI(4,5)P2, phosphatidylinositol-4,5-bisphosphate.

AP-2 was very recently shown to be essential for the maintenance of hyphal polarity in *A. nidulans* [30], *Fusarium graminearum* [31], and *C. albicans* [18] *via* the regulation of lipid polarization and cell wall deposition. In *A. nidulans* and *F. graminearum*, AP-2 interacts with lipid flippases (DnfA and DnfB) [30,31], and it maintains ergosterol polarization specifically at the *C. albicans* hyphal tip [18]. Furthermore, in *C. albicans*, the AP-2 mu subunit (Apm4) was shown to be critical for the recycling of the cell wall biosynthesis enzyme, chitin synthase 3 (Chs3), resulting in elevated chitin synthesis, associated with morphological defects in the *apm4* deletion mutant [18]. Together, these studies point to a critical role of AP-2 in lipid polarization, necessary to sustain fungal polarized growth.

Lipids

Phosphatidylethanolamine, phosphatidylserine (PS), and phosphatidylinositol phosphates (PIPs) are the major phospholipids of the yeast plasma membrane, together comprising more than 80% of phospholipids [32], and the sterol ergosterol comprises ~ half of the lipids in the inner leaflet of the plasma membrane [33]. In yeast, more than 80% of the phospholipids are found on the inner leaflet of the plasma membrane [34], and it is likely that the negative charge of PS and PIPs is important for protein localization and clustering. PS is enriched at sites of growth, such as *S. cerevisiae* and *S. pombe* tip of mating projections [35,36] and *C. albicans* hyphae [26], and is critical for polarized growth in response to an external signal, during shmoo and hyphal formation [35,37]. Upon perturbation of PS levels, defects in Cdc42 localization in *S. cerevisiae* shmoos and *S. pombe*, as well as in *C. albicans* hyphae, and Rho1 localization in *S. pombe* and *C. albicans* [35,36,38] were observed, indicating that this negatively charged lipid is important for Rho GTPase distribution. In these fungi, PS forms a gradient from the growth site [26,35,36]. Interestingly, PS appears to regulate the size of Cdc42 nanoclusters in *S. cerevisiae* budding cells, dependent on the Bem1 scaffolding protein [39]. Recent work on this organism indicates that multivalent anionic lipid interactions are crucial for establishing polarity and occur *via* the Bem1–Cdc42 GEF (guanine nucleotide exchange factor) complex at the site of bud growth [40]. This lipid–polarity protein association affects

Figure 3

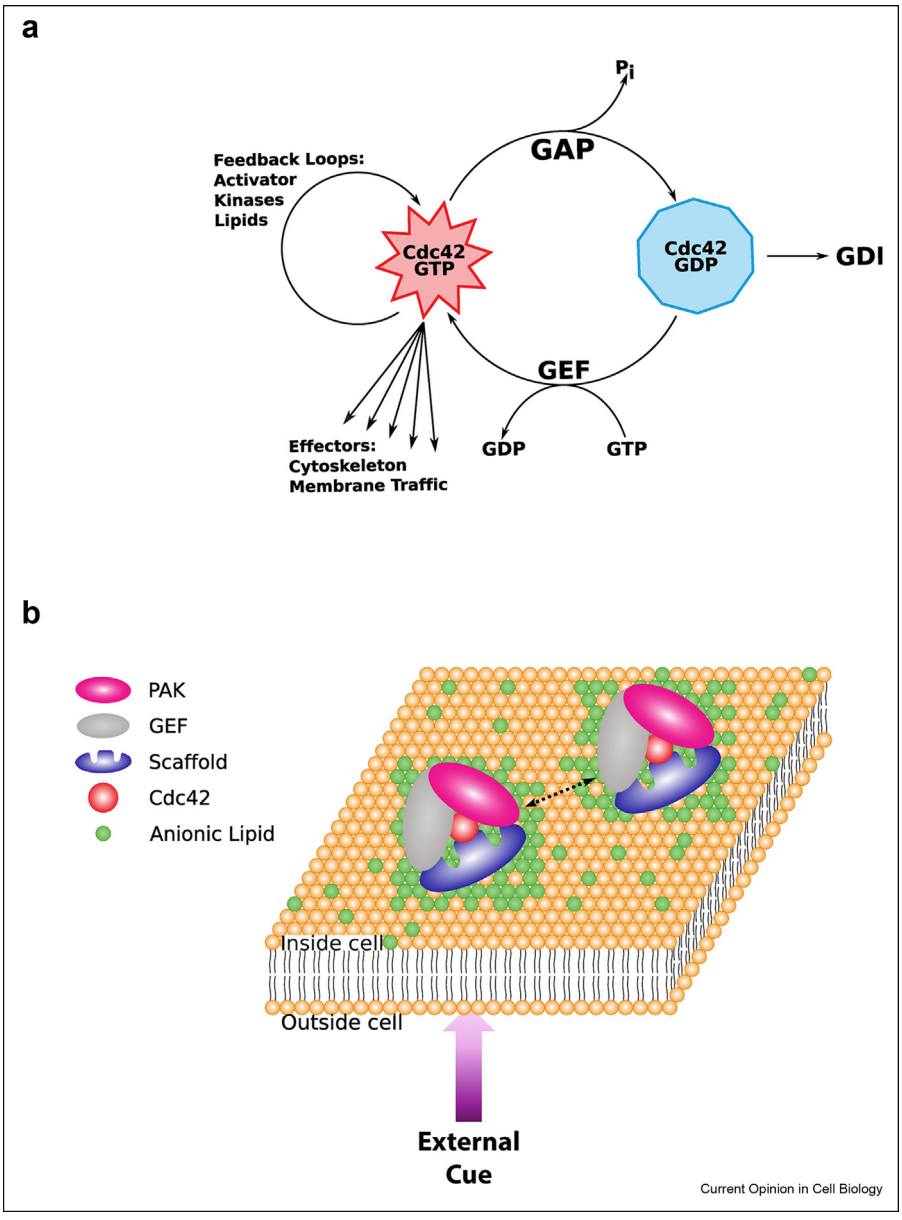

Mechanisms critical for Cdc42 membrane recruitment, Cdc42 activation, and formation of a polarity cluster. (a) Cdc42 GTPase cycle. GAPs include Rga and Bem3 proteins and their homologs, GEFs include Cdc24, Gef1 and Scd1 and their homologs and guanine nucleotide dissociation inhibitor (GDI) homologs. **(b)** Clustering of polarity proteins and lipids on the inner face of the plasma membrane. PAKs include Ste20 and Cla4 proteins and their homologs, scaffold proteins include Bem1 and Scd2 and their homologs, and anionic phospholipids include phosphatidylserine and phosphatidylinositol phosphates. Dashed arrow indicates higher order interactions between polarity clusters (nanoclusters) to generate larger signaling platforms. Figure based upon that of [40] which investigated internal signal–mediated polarity in *Saccharomyces cerevisiae*. Note that the transduction of an external cue to the inner leaflet could be *via* proteins and/or lipids.

membrane rigidity in a sterol-dependent fashion and limits the diffusion of Cdc42. Intriguingly, it was recently shown that PS similarly stabilizes nanoclusters of the Rho GTPase Rho of Plants (ROP) in plants [41]. Whether such lipid dependent clustering is critical for cell polarity in response to external signals in shmoos and hyphae is not yet known.

PIPs are also important for polarized growth in fungi. In particular, plasma membrane phosphatidylinositol-4-phosphate (PI(4)P) and phosphatidylinositol-4,5-bisphosphate ($PI(4,5)P_2$) are critical for external signal–mediated polarized growth in *S. cerevisiae*, *C. albicans*, and *N. crassa* [17,42–45]. $PI(4,5)P_2$ is enriched at the tip of the mating projection in *S. cerevisiae* [46] and forms a

long-range gradient in the *C. albicans* hyphal filament emanating from the apex [45], whereas PI(4)P forms a steep gradient in *C. albicans* hyphae [17]. It is likely that such polarized distributions of these PIPs play a critical role in reinforcing cell polarity by binding small GTPases and their effectors. For example, the polybasic region of Rho GTPases binds acidic phospholipids, and PIPs, including PIP_2, are important for targeting these GTPases to the plasma membrane [47]. In addition, a number of proteins with varied roles in polarized growth bind $PI(4,5)P_2$, including the PAK kinase Ste20, the Cdc42 effector Gic2, septins [48–50], and exocyst subunits Exo70 [51] and Sec3 [52,53]. Interestingly, studies on mammalian cells show that protein targeting to the plasma membrane requires both PI(4)P and $PI(4,5)P_2$, and suggest that PI(4)P has functions at the plasma membrane independent of its role as a $PI(4,5)P_2$ precursor [54]. Indeed, in *S. cerevisiae*, PI(4)P is required to localize the PAK kinase Cla4 to bud growth sites [55].

In *S. cerevisiae* budding cells, Osh proteins, which are homologs of the oxysterol-binding proteins are important for polarized exocytosis [56,57], and recent work on *S. pombe* shows that endoplasmic reticulum–plasma membrane contact sites spatially confine regions of exocytosis [58]. Either Osh4 or Osh6 is sufficient for polarized exocytosis in *S. cerevisiae*, suggesting that PI(4)P (which binds both of these Osh proteins) has a critical role in this process [59]. It remains to be seen whether plasma membrane PI(4)P has a specific function in external signal–mediated polarized growth, and whether endoplasmic reticulum–plasma membrane contact sites, which play a crucial role in regulating this phospholipid [60], are important for such growth responses.

Small GTPases

The highly conserved Rho GTPase Cdc42 is critical for cell polarity in a range of systems and a small asymmetry in the distribution of this activated GTPase, which is subsequently amplified by positive feedback that includes local activation, typically defines sites of growth [61]. Two key characteristics of the feedback are that active Cdc42 recruits additional activators to growth sites and that the various polarity components exhibit different mobilities in the membrane [62]. The association of active Cdc42 with Bem1 increases the activation of additional Cdc42 *via* the sole Cdc42 activator, the GEF Cdc24 [63]. In addition, Bem1 increases Cdc24 phosphorylation *via* the PAK kinase Cla4, which ultimately results in Cdc24 becoming insensitive to stimulation by Bem1. Bem1 interactions with anionic lipids are also critical for Cdc42 nanoclustering and reduced mobility of active Cdc42 at sites of growth [39,40]. A recent optogenetic study on *S. cerevisiae* budding cells revealed that local recruitment of either Cdc24 or Bem1 is sufficient to trigger cell polarization, yet the specific response depends on whether Cdc24 or Bem1 was recruited, the cell cycle stage, and preexistent polarization sites [64]. How site-specific recruitment of these proteins affects cell polarity in response to an external signal, such as mating pheromone, is currently unknown. Very recent studies on *C. albicans* show that recruitment of constitutive active Cdc42 all over the plasma membrane resets polarity in highly asymmetric hyphal cells [65]. Increasing the level of active Cdc42 on the plasma membrane disrupts the localization of Sec3 and results in a striking *de novo* clustering of secretory vesicles, which is highly dynamic until it settles down at a new growth site. These results highlight that even in the absence of directional growth, membrane traffic retains some organization.

GTPase-activating proteins (GAPs) play an important role in restricting the distribution of active Cdc42. During vegetative growth, Cdc42 GAPs prevent *S. cerevisiae* budding within the previous division site [66] and restrict active Cdc42 to *S. pombe* cell tips [67,68], yet the role of these GAPs in external signal–mediated growth is less clear. For example, *C. albicans* cells can form hyphae even in the absence of the GAPs Rga2 and Bem3 [69], and *S. pombe* cells lacking all three Cdc42 GAPs (*RGA3, RGA4, and RGA6*) were able to polarize in response to pheromone [70]. Nonetheless, in the absence of Rga4, which localizes to cell sides, *S. pombe* cells are somewhat wider [67,71]. In *S. cerevisiae* and *C. albicans*, there is a sole GEF for Cdc42 at the growth site, whereas, in *S. pombe*, there are two Cdc42 GEFs, one localized at the growth site (Scd1) and one broadly distributed in the cytoplasm (Gef1) that is normally antagonized by Rga4, which may provide an additional level of regulation of Cdc42 activation [72]. Although deletion of *RGA3* does not result in morphological defects during *S. pombe* vegetative growth during mating, strains had longer shmoos, which appear to be less well oriented towards a mating partner [70]. Together, these results indicate that GAP activity would only play a minor role in external signal–mediated fungal polarized growth.

Effects of cell shape

In *S. pombe*, the size of the active Cdc42 domain scales with local cell surface radius of curvature over a large range and is independent of cell volume and surface [73]. In another fission yeast, *Schizosaccharomyces japonicus*, active Cdc42 also scales with changes in cell size, presumably cell surface radius of curvature [74]. These studies suggest that local cell surface curvature is, in some fashion, sensed and responded to by the cell. Cell curvature can be directly sensed, as during *S. cerevisiae* mating, Cdc42 localization is negatively affected by the positive curvature of the zone of cell fusion [75]. Computational studies also suggest that cell geometry has striking effects on reaction–

diffusion models of fungal polarization, with the active Cdc42 domain not stably localized to the tip of cells with a shmoo-like morphology, whereas it is stable at filament tips, similar to those of hyphal filaments [76]. Recent results from optogenetic perturbation of cell polarity in *C. albicans* show that the polarity site is easier to disrupt in cells with short filaments, compared with cells with longer filaments [65]. In addition, mechanical perturbation, for example, when a cell encounters a barrier, destabilizes regions of active Cdc42, suggesting that there is a dynamic feedback between growth and stable cell polarity [77]. Cell geometry can also affect spatial chemoattractant signaling, for example, pheromone is released from sites of growth during *S. pombe* mating [78]. Together, these studies point to a critical role of cell geometry on polarized growth, as local cell curvature could be recognized on larger scales by the actin network and/or on smaller scales by BAR (Bin, Amphiphysin and Rvs) containing proteins [79].

Conclusion

Research in the past several years has shed light on different mechanisms that play key roles during polarized growth in response to external stimuli in fungi. Cellular processes that establish an asymmetric state, such as directed exocytosis, site specific incorporation of lipids, and localized activation of GTPases have been extensively studied, and more recent work has focused on cellular processes that limit the location of an active species, thereby creating a boundary or a sharp gradient. These processes include a collar of endocytosis for membrane uptake, hydrolysis, or transport of lipids and GAPs, as well as GEF phosphorylation, for spatially and temporally limiting GTPase activation. We have emphasized the common themes in external signal–mediated polarized growth in fungi, yet polarization mechanisms vary within fungi and in response to different environments, depending on the time scale of the response, cell shape, and robustness of response required. In the future, it will be critical to quantitate the contributions of different positive and negative feedback loops on polarized growth in fungi with different growth rates, cell sizes, and cell shapes to identify how polarity is regulated in an ever-changing environment.

Conflict of interest statement

Nothing declared.

Acknowledgements

This work was supported by the Centre national de la recherche scientifique (CNRS), Institut national de la santé et de la recherche médicale (INSERM), Université Côte d'Azur (UCA), European Union Horizon 2020 Marie Skłodowska-Curie Research and Innovation Programme (MSCA-ITN- 2015-675407) and ANR (ANR-15-IDEX-01, ANR-11-LABX-0028-01, and ANR-16-CE13-0010-01). We apologize to authors whose work we were unable to discuss because of space constraints.

References

Papers of particular interest, published within the period of review, have been highlighted as:

* of special interest
** of outstanding interest

1. Lew RR: **Mass flow and pressure-driven hyphal extension in *Neurospora crassa***. *Microbiology* 2005, **151**:2685–2692.

2. Martinez de Maranon I, Marechal PA, Gervais P: **Passive response of *Saccharomyces cerevisiae* to osmotic shifts: cell volume variations depending on the physiological state**. *Biochem Biophys Res Commun* 1996, **227**:519–523.

3. Minc N, Boudaoud A, Chang F: **Mechanical forces of fission yeast growth**. *Curr Biol* 2009, **19**:1096–1101.

4. Robertson NA, Rizvi SRH: **Some observations on the water-relations of the hyphae of *Neurospora crassa***. *Ann Bot* 1968, **32**:279–291.

5. Schaber J, Adrover MA, Eriksson E, Pelet S, Petelenz-Kurdziel E, Klein D, Posas F, Goksor M, Peter M, Hohmann S, *et al.*: **Biophysical properties of *Saccharomyces cerevisiae* and their relationship with HOG pathway activation**. *Eur Biophys J* 2010, **39**:1547–1556.

6. Thomson DD, Wehmeier S, Byfield FJ, Janmey PA, Caballero-Lima D, Crossley A, Brand AC: **Contact-induced apical asymmetry drives the thigmotropic responses of *Candida albicans hyphae***. *Cell Microbiol* 2015, **17**:342–354.

7. Atilgan E, Magidson V, Khodjakov A, Chang F: **Morphogenesis of the fission yeast cell through cell wall expansion**. *Curr Biol* 2015, **25**:2150–2157.

8. Gonzalez-Bermudez B, Li Q, Guinea GV, Penalva MA, Plaza GR: **Probing the effect of tip pressure on fungal growth: application to *Aspergillus nidulans***. *Phys Rev E* 2017, **96**, 022402.

9. Martin SG: **Molecular mechanisms of chemotropism and cell fusion in unicellular fungi**. *J Cell Sci* 2019, **132**.

10. Araujo-Bazan L, Penalva MA, Espeso EA: **Preferential localization of the endocytic internalization machinery to hyphal tips underlies polarization of the actin cytoskeleton in *Aspergillus nidulans***. *Mol Microbiol* 2008, **67**:891–905.

11. Taheri-Talesh N, Horio T, Araujo-Bazan L, Dou X, Espeso EA, Penalva MA, Osmani SA, Oakley BR: **The tip growth apparatus of *Aspergillus nidulans***. *Mol Biol Cell* 2008, **19**:1439–1449.

12. Upadhyay S, Shaw BD: **The role of actin, fimbrin and endocytosis in growth of hyphae in *Aspergillus nidulans***. *Mol Microbiol* 2008, **68**:690–705.

13. Jose M, Tollis S, Nair D, Sibarita JB, McCusker D: **Robust polarity establishment occurs *via* an endocytosis-based cortical corralling mechanism**. *J Cell Biol* 2013, **200**:407–418.

14. Caballero-Lima D, Kaneva IN, Watton SP, Sudbery PE, Craven CJ: **The spatial distribution of the exocyst and actin cortical patches is sufficient to organize hyphal tip growth**. *Eukaryot Cell* 2013, **12**:998–1008.

15. Johansen J, Alfaro G, Beh CT: **Polarized exocytosis induces compensatory endocytosis by Sec4p-regulated cortical actin polymerization**. *PLoS Biol* 2016, **14**, e1002534.

16. * Hernandez-Gonzalez M, Bravo-Plaza I, Pinar M, de Los Rios V, Arst Jr HN, Penalva MA: **Endocytic recycling via the TGN underlies the polarized hyphal mode of life**. *PLoS Genet* 2018, **14**, e1007291.
The authors use a range of mutants to block different membrane traffic steps, together with quantitative live cell imaging, to show that endocytic cycling is critical for the polarization of a key cell wall synthetic enzyme (chitin synthase). Specifically, the sub-abical endocytic collar and trafficking to the TGN play key roles in polarization of this important chitin synthase in *A. nidulans* hyphae.

17. Ghugtyal V, Garcia-Rodas R, Seminara A, Schaub S, Bassilana M, Arkowitz RA: **Phosphatidylinositol-4-phosphate-dependent membrane traffic is critical for fungal filamentous growth**. *Proc Natl Acad Sci U S A* 2015, **112**:8644–8649.

18. * Knafler HC, Smaczynska-de II R, Walker LA, Lee KK, Gow NAR, Ayscough KR: **AP-2-Dependent endocytic recycling of the chitin synthase Chs3 regulates polarized growth in *Candida albicans***. *mBio* 2019, **10**.

This study shows that the AP-2 endocytic adaptor complex is required for the internalization of a major cell wall biosynthesis enzyme (chitin synthase). *C. albicans* mutants lacking the AP-2 mu subunit Apm4, have altered cell wall deposition and morphological defects, including the inability to polarize mannosylated proteins and ergosterol at hyphal tips, indicating that AP-2 dependent internalization and recycling are critical for polarized hyphal growth.

19. Skau CT, Courson DS, Bestul AJ, Winkelman JD, Rock RS, Sirotkin V, Kovar DR: **Actin filament bundling by fimbrin is important for endocytosis, cytokinesis, and polarization in fission yeast**. *J Biol Chem* 2011, **286**:26964–26977.

20. Riquelme M, Aguirre J, Bartnicki-Garcia S, Braus GH, Feldbrugge M, Fleig U, Hansberg W, Herrera-Estrella A, Kamper J, Kuck U, *et al.*: **Fungal morphogenesis, from the polarized growth of hyphae to complex reproduction and infection structures**. *Microbiol Mol Biol Rev* 2018, **82**.

21. Arkowitz RA, Bassilana M: **Recent advances in understanding *Candida albicans* hyphal growth**. *F1000Res* 2019, **8**.

22. Costa R, Warren DT, Ayscough KR: **Lsb5p interacts with actin regulators Sla1p and Las17p, ubiquitin and Arf3p to couple actin dynamics to membrane trafficking processes**. *Biochem J* 2005, **387**:649–658.

23. Lambert AA, Perron MP, Lavoie E, Pallotta D: **The *Saccharomyces cerevisiae* Arf3 protein is involved in actin cable and cortical patch formation**. *FEMS Yeast Res* 2007, **7**:782–795.

24. Lee SC, Schmidtke SN, Dangott LJ, Shaw BD: ***Aspergillus nidulans* ArfB plays a role in endocytosis and polarized growth**. *Eukaryot Cell* 2008, **7**:1278–1288.

25. Zhu X, Zhou T, Chen L, Zheng S, Chen S, Zhang D, Li G, Wang Z: **Arf6 controls endocytosis and polarity during asexual development of *Magnaporthe oryzae***. *FEMS Microbiol Lett* 2016:363.

26. Labbaoui H, Bogliolo S, Ghugtyal V, Solis NV, Filler SG, Arkowitz RA, Bassilana M: **Role of Arf GTPases in fungal morphogenesis and virulence**. *PLoS Pathog* 2017, **13**, e1006205.

27. Oscarsson T, Walther A, Lengeler KB, Wendland J: **An Arf-GAP promotes endocytosis and hyphal growth of *Ashbya gossypii***. *FEMS Microbiol Lett* 2017:364.

28. Chapa-y-Lazo B, Allwood EG, Smaczynska-de II R, Snape ML, Ayscough KR: **Yeast endocytic adaptor AP-2 binds the stress sensor Mid2 and functions in polarized cell responses**. *Traffic* 2014, **15**:546–557.

29. de Leon N, Hoya M, Curto MA, Moro S, Yanguas F, Doncel C, Valdivieso MH: **The AP-2 complex is required for proper temporal and spatial dynamics of endocytic patches in fission yeast**. *Mol Microbiol* 2016, **100**:409–424.

30. * Martzoukou O, Amillis S, Zervakou A, Christoforidis S, Diallinas G: **The AP-2 complex has a specialized clathrin-independent role in apical endocytosis and polar growth in fungi**. *Elife* 2017, **6**.

The authors show that in *A. nidulans* AP-2 is critical for polarity maintenance and growth. Genetic analyses indicate that this adaptor complex interacts with endocytic proteins and lipid flippases and is important for apical membrane lipid composition and cell wall synthesis.

31. Zhang J, Yun Y, Lou Y, Abubakar YS, Guo P, Wang S, Li C, Feng Y, Adnan M, Zhou J, *et al.*: **FgAP-2 complex is essential for pathogenicity and polarised growth and regulates the apical localisation of membrane lipid flippases in *Fusarium graminearum***. *Cell Microbiol* 2019, **21**, e13041.

32. Klug L, Daum G: **Yeast lipid metabolism at a glance**. *FEMS Yeast Res* 2014, **14**:369–388.

33. Solanko LM, Sullivan DP, Sere YY, Szomek M, Lunding A, Solanko KA, Pizovic A, Stanchev LD, Pomorski TG, Menon AK, *et al.*: **Ergosterol is mainly located in the cytoplasmic leaflet of the yeast plasma membrane**. *Traffic* 2018, **19**:198–214.

34. Cerbon J, Calderon V: **Changes of the compositional asymmetry of phospholipids associated to the increment in the membrane surface potential**. *Biochim Biophys Acta* 1991, **1067**:139–144.

35. Fairn GD, Hermansson M, Somerharju P, Grinstein S: **Phosphatidylserine is polarized and required for proper Cdc42 localization and for development of cell polarity**. *Nat Cell Biol* 2011, **13**:1424–1430.

36. * Haupt A, Minc N: **Gradients of phosphatidylserine contribute to plasma membrane charge localization and cell polarity in fission yeast**. *Mol Biol Cell* 2017, **28**:210–220.

This study demonstrates that phosphatidylserine is distributed in a polarized fashion in *S. pombe* budding and shmooing cells and that this lipid is critical for polarized growth. The authors suggest that this lipid may be important for plasma membrane charge distribution, which is crucial for the localization of Rho GTPases.

37. Chen YL, Montedonico AE, Kauffman S, Dunlap JR, Menn FM, Reynolds TB: **Phosphatidylserine synthase and phosphatidylserine decarboxylase are essential for cell wall integrity and virulence in *Candida albicans***. *Mol Microbiol* 2010, **75**:1112–1132.

38. Chen T, Jackson JW, Tams RN, Davis SE, Sparer TE, Reynolds TB: **Exposure of *Candida albicans* beta (1,3)-glucan is promoted by activation of the Cek1 pathway**. *PLoS Genet* 2019, **15**, e1007892.

39. Sartorel E, Unlu C, Jose M, Massoni-Laporte A, Meca J, Sibarita JB, McCusker D: **Phosphatidylserine and GTPase activation control Cdc42 nanoclustering to counter dissipative diffusion**. *Mol Biol Cell* 2018, **29**:1299–1310.

40. ** Meca J, Massoni-Laporte A, Martinez D, Sartorel E, Loquet A, Habenstein B, McCusker D: **Avidity-driven polarity establishment via multivalent lipid-GTPase module interactions**. *EMBO J* 2019, **38**.

This study uses a combination of genetics, biochemistry and live cell microscopy to show that multivalent anionic lipid interactions are crucial for polarity establishment in budding *S. cerevisiae* cells. Specifically, they demonstrate that phosphatidylserine and phosphatidylinositol phosphates are important for targeting the scaffold protein Bem1 and the Cdc42 activator Cdc24 to the cell poles.

41. ** Platre MP, Bayle V, Armengot L, Bareille J, Marques-Bueno MDM, Creff A, Maneta-Peyret L, Fiche JB, Nollmann M, Miege C, *et al.*: **Developmental control of plant Rho GTPase nano-organization by the lipid phosphatidylserine**. *Science* 2019, **364**:57–62.

This work shows that phosphatidylserine is required for stabilizing plant Rho (Rop6) nanoclustering. In addition, signaling from the plant hormone auxin induced phosphatidylserine-dependent Rho nanoclustering.

42. Adhikari H, Cullen PJ: **Role of phosphatidylinositol phosphate signaling in the regulation of the filamentous-growth mitogen-activated protein kinase pathway**. *Eukaryot Cell* 2015, **14**:427–440.

43. Guillas I, Vernay A, Vitagliano JJ, Arkowitz RA: **Phosphatidylinositol 4,5-bisphosphate is required for invasive growth in *Saccharomyces cerevisiae***. *J Cell Sci* 2013, **126**:3602–3614.

44. Mahs A, Ischebeck T, Heilig Y, Stenzel I, Hempel F, Seiler S, Heilmann I: **The essential phosphoinositide kinase MSS-4 is required for polar hyphal morphogenesis, localizing to sites of growth and cell fusion in *Neurospora crassa***. *PLoS One* 2012, **7**, e51454.

45. Vernay A, Schaub S, Guillas I, Bassilana M, Arkowitz RA: **A steep phosphoinositide bis-phosphate gradient forms during fungal filamentous growth**. *J Cell Biol* 2012, **198**:711–730.

46. Garrenton LS, Stefan CJ, McMurray MA, Emr SD, Thorner J: **Pheromone-induced anisotropy in yeast plasma membrane phosphatidylinositol-4,5-bisphosphate distribution is required for MAPK signaling**. *Proc Natl Acad Sci U S A* 2010, **107**:11805–11810.

47. Heo WD, Inoue T, Park WS, Kim ML, Park BO, Wandless TJ, Meyer T: **PI(3,4,5)P3 and PI(4,5)P_2 lipids target proteins with polybasic clusters to the plasma membrane**. *Science* 2006, **314**:1458–1461.

48. Bertin A, McMurray MA, Thai L, Garcia 3rd G, Votin V, Grob P, Allyn T, Thorner J, Nogales E: **Phosphatidylinositol-4,5-bisphosphate promotes budding yeast septin filament assembly and organization**. *J Mol Biol* 2010, **404**:711–731.

49. Orlando K, Zhang J, Zhang X, Yue P, Chiang T, Bi E, Guo W: **Regulation of Gic2 localization and function by phosphatidylinositol 4,5-bisphosphate during the establishment of cell polarity in budding yeast**. *J Biol Chem* 2008, **283**:14205–14212.

50. Takahashi S, Pryciak PM: **Identification of novel membrane-binding domains in multiple yeast Cdc42 effectors**. *Mol Biol Cell* 2007, **18**:4945–4956.

51. He B, Xi F, Zhang X, Zhang J, Guo W: **Exo70 interacts with phospholipids and mediates the targeting of the exocyst to the plasma membrane**. *EMBO J* 2007, **26**:4053–4065.

52. Bendezu FO, Vincenzetti V, Martin SG: **Fission yeast Sec3 and Exo70 are transported on actin cables and localize the exocyst complex to cell poles**. *PLoS One* 2012, **7**, e40248.

53. Zhang X, Orlando K, He B, Xi F, Zhang J, Zajac A, Guo W: **Membrane association and functional regulation of Sec3 by phospholipids and Cdc42**. *J Cell Biol* 2008, **180**:145–158.

54. Hammond GR, Fischer MJ, Anderson KE, Holdich J, Koteci A, Balla T, Irvine RF: **PI4P and PI(4,5)P_2 are essential but independent lipid determinants of membrane identity**. *Science* 2012, **337**:727–730.

55. Wild AC, Yu JW, Lemmon MA, Blumer KJ: **The p21-activated protein kinase-related kinase Cla4 is a coincidence detector of signaling by Cdc42 and phosphatidylinositol 4-phosphate**. *J Biol Chem* 2004, **279**:17101–17110.

56. Kozminski KG, Alfaro G, Dighe S, Beh CT: **Homologues of oxysterol-binding proteins affect Cdc42p- and Rho1p-mediated cell polarization in *Saccharomyces cerevisiae***. *Traffic* 2006, **7**:1224–1242.

57. Alfaro G, Johansen J, Dighe SA, Duamel G, Kozminski KG, Beh CT: **The sterol-binding protein Kes1/Osh4p is a regulator of polarized exocytosis**. *Traffic* 2011, **12**:1521–1536.

58. ** Ng AYE, Ng AQE, Zhang D: **ER-PM contacts restrict exocytic sites for polarized morphogenesis**. *Curr Biol* 2018, **28**:146–153 e145.
The restriction the location of exocytosis is important for polarized growth, however in fission yeast actomyosin-dependent delivery of exocytic vesicles is not necessary for polarized secretion. This work shows that endoplasmic reticulum-plasma membrane contact sites limit the location of exocytosis and are critical for morphogenesis in *S. pombe*.

59. Smindak RJ, Heckle LA, Chittari SS, Hand MA, Hyatt DM, Mantus GE, Sanfelippo WA, Kozminski KG: **Lipid-dependent regulation of exocytosis in *S. cerevisiae* by OSBP homolog (Osh) 4**. *J Cell Sci* 2017, **130**:3891–3906.

60. ** Quon E, Sere YY, Chauhan N, Johansen J, Sullivan DP, Dittman JS, Rice WJ, Chan RB, Di Paolo G, Beh CT, *et al.*: **Endoplasmic reticulum-plasma membrane contact sites integrate sterol and phospholipid regulation**. *PLoS Biol* 2018, **16**, e2003864.
The authors generated a *S. cerevisiae* strain that effectively lacks endoplasmic reticulum-plasma membrane contact sites and showed that this strain grows in rich media, suggesting that contact sites are not critical for polarized growth. They further demonstrated that plasma membrane PI(4)P is critical for the viability of this strain, as deletion of the OSBP *OSH4* or the PI(4)P phosphatase *SAC1* is synthetically lethal in this strain lacking endoplasmic reticulum-plasma membrane contact sites.

61. Woods B, Kuo CC, Wu CF, Zyla TR, Lew DJ: **Polarity establishment requires localized activation of Cdc42**. *J Cell Biol* 2015, **211**:19–26.

62. Woods B, Lew DJ: **Polarity establishment by Cdc42: key roles for positive feedback and differential mobility**. *Small GTPases* 2019, **10**:130–137.

63. ** Rapali P, Mitteau R, Braun C, Massoni-Laporte A, Unlu C, Bataille L, Arramon FS, Gygi SP, McCusker D: **Scaffold-mediated gating of Cdc42 signalling flux**. *Elife* 2017, **6**.
This study uses a combination of biochemistry, imaging and genetics to show how a scaffold protein (Bem1) regulates cell polarity in the budding yeast *S. cerevisiae*. The authors show that Bem1 increases Cdc24 guanine nucleotide exchange factor (GEF) activity, as well as facilitates the Cdc24 phosphorylation by the PAK Cla4, which abolishes the positive effect of Bem1 on Cdc24 GEF activity.

64. ** Witte K, Strickland D, Glotzer M: **Cell cycle entry triggers a switch between two modes of Cdc42 activation during yeast polarization**. *Elife* 2017, **6**.
The authors use optogenetics to dissect polarization in the budding yeast *S. cerevisiae* and show that the recruitment of the GEF Cdc24 or the scaffold protein Bem1 is sufficient to polarize cells. They demonstrate that site-specific recruitment of Cdc24 or Bem1 activates Cdc42, as well as recruits more polarity proteins to this specific site.

65. ** Silva PM, Puerner C, Seminara A, Bassilana M, Arkowitz RA: **Secretory vesicle clustering in fungal filamentous cells does not require directional growth**. *Cell Rep* 2019, **28**:2231–2245 e2235.
The authors used optogenetics to localize active Cdc42 all over the plasma membrane in filamentous *C. albicans* cells and show that this resets cell polarity. Optogenetic recruitment of active Cdc42 to plasma membrane disrupts exocytosis by perturbing the localization of the exocyst subunit Sec3 and results in a striking *de novo* cluster of secretory vesicles, which is highly dynamic.

66. Tong Z, Gao XD, Howell AS, Bose I, Lew DJ, Bi E: **Adjacent positioning of cellular structures enabled by a Cdc42 GTPase-activating protein-mediated zone of inhibition**. *J Cell Biol* 2007, **179**:1375–1384.

67. Revilla-Guarinos MT, Martin-Garcia R, Villar-Tajadura MA, Estravis M, Coll PM, Perez P: **Rga6 is a fission yeast Rho GAP involved in Cdc42 regulation of polarized growth**. *Mol Biol Cell* 2016, **27**:1524–1535.

68. Tatebe H, Nakano K, Maximo R, Shiozaki K: **Pom1 DYRK regulates localization of the Rga4 GAP to ensure bipolar activation of Cdc42 in fission yeast**. *Curr Biol* 2008, **18**:322–330.

69. Court H, Sudbery P: **Regulation of Cdc42 GTPase activity in the formation of hyphae in *Candida albicans***. *Mol Biol Cell* 2007, **18**:265–281.

70. * Gallo Castro D, Martin SG: **Differential GAP requirement for Cdc42-GTP polarization during proliferation and sexual reproduction**. *J Cell Biol* 2018, **217**:4215–4229.
The authors identify the Cdc42 GTPase-activating protein (GAP) Rga3 in fission yeast as important for regulating the lifetime of unstable patches of Cdc42-GTP during mating. Surprisingly, a triple mutant that lacks all Cdc42 GAPs, is still able to polarize in response to mating pheromone, suggesting that the GAP dependent inactivation of Cdc42 is not critical during external signal-mediated polarization process.

71. Kelly FD, Nurse P: **Spatial control of Cdc42 activation determines cell width in fission yeast**. *Mol Biol Cell* 2011, **22**:3801–3811.

72. * Tay YD, Leda M, Goryachev AB, Sawin KE: **Local and global Cdc42 guanine nucleotide exchange factors for fission yeast cell polarity are coordinated by microtubules and the Tea1-Tea4-Pom1 axis**. *J Cell Sci* 2018:131.
Intriguingly, the fission yeast *S. pombe* has two Cdc42 GEFs, Scd1 and Gef1. Here, the authors show that while Scd1 (a homolog of Cdc24) is localized to sites of growth, Gef1 is found throughout the cytoplasm. Gef1 activity at the cell sides is regulated by the GTPase-activating protein (GAP) Rga4, providing additional means of regulating cell polarity.

73. Bonazzi D, Haupt A, Tanimoto H, Delacour D, Salort D, Minc N: **Actin-based transport adapts polarity domain size to local cellular curvature**. *Curr Biol* 2015, **25**:2677–2683.

74. ** Gu Y, Oliferenko S: **Cellular geometry scaling ensures robust division site positioning**. *Nat Commun* 2019, **10**:268.
This work investigates the mechanisms underlying size scaling, by interfering with this process in the fission yeast *S. japonicas.* The authors show that the Cdc42 module is used in fission yeast to modulate its geometry to change cell size.

75. Smith JA, Hall AE, Rose MD: **Membrane curvature directs the localization of Cdc42p to novel foci required for cell-cell fusion**. *J Cell Biol* 2017, **216**:3971–3980.

76. Trogdon M, Drawert B, Gomez C, Banavar SP, Yi TM, Campas O, Petzold LR: **The effect of cell geometry on polarization in budding yeast**. *PLoS Comput Biol* 2018, **14**, e1006241.

77. * Haupt A, Ershov D, Minc N: **A positive feedback between growth and polarity provides directional persistency and flexibility to the process of tip growth**. *Curr Biol* 2018, **28**: 3342–3351 e3343.

This study shows that the spatial stability of active Cdc42 domains in *S. pombe* depends on the rate of growth. The authors used a number approaches to reduce growth rate, which results in unstable, wandering domains of active Cdc42, whereas increasing growth rate stabilizes this domain. This effect of growth rate may be a conserved means of responding to mechanical challenges in the fungal environment.

78. Merlini L, Khalili B, Bendezu FO, Hurwitz D, Vincenzetti V, Vavylonis D, Martin SG: **Local pheromone release from dynamic polarity sites underlies cell-cell pairing during yeast mating**. *Curr Biol* 2016, **26**:1117–1125.

79. Haupt A, Minc N: **How cells sense their own shape - mechanisms to probe cell geometry and their implications in cellular organization and function**. *J Cell Sci* 2018:131.

RESULTS

The following manuscript "Mechanical force-induced morphology changes in a human fungal pathogen," recently accepted at *BMC Biology*, was a collaboration between our group and a group of physicists. As indicated in the manuscript, co-authorship was ordered based on contributions to figures. For purposes of evaluating my contribution to this work, I would like to direct the reader to the figures that I contributed to and explain my conceptual contribution to the work. The figures that I contributed to are: Figures 1b,c,e,f; 2a-e; 3b-d; 4; 7; 8; 9; 10a-b; 11; 12; S2; S3 and S5b-d. I would also like to direct the reader to the figures contributed by the other co-authors. Nino Kukhaleishvili contributed to the physical experiments and turgor pressure calculations: Figures 2f; 5; 6 and S1. Lastly, Darren Thomson put significant amount of effort into the initial setup of this system and his work also contributed to the Figures 1d; 3a.

Conceptually, I contributed largely to the biological aspect of the experiments presented here. Invasion experiments using PDMS microchambers performed for this manuscript was initially setup by Darren Thomson; however, I invested a significant amount of time during my first year in the lab continuing to optimize these experiments. I carried out numerous microscopy experiments and performed many analyses that had significant contributions to this work.

Puerner et al. BMC Biology (2020) 18:122
https://doi.org/10.1186/s12915-020-00833-0

BMC Biology

RESEARCH ARTICLE Open Access

Mechanical force-induced morphology changes in a human fungal pathogen

Charles Puerner[1†], Nino Kukhaleishvili[1,2†], Darren Thomson[1,3†], Sebastien Schaub[1,4], Xavier Noblin[2*], Agnese Seminara[2], Martine Bassilana[1] and Robert A. Arkowitz[1*]

Abstract

Background: The initial step of a number of human or plant fungal infections requires active penetration of host tissue. For example, active penetration of intestinal epithelia by *Candida albicans* is critical for dissemination from the gut into the bloodstream. However, little is known about how this fungal pathogen copes with resistive forces upon host cell invasion.

Results: In the present study, we have used PDMS micro-fabrication to probe the ability of filamentous *C. albicans* cells to penetrate and grow invasively in substrates of different stiffness. We show that there is a threshold for penetration that corresponds to a stiffness of ~ 200 kPa and that invasive growth within a stiff substrate is characterized by dramatic filament buckling, along with a stiffness-dependent decrease in extension rate. We observed a striking alteration in cell morphology, i.e., reduced cell compartment length and increased diameter during invasive growth, that is not due to depolarization of active Cdc42, but rather occurs at a substantial distance from the site of growth as a result of mechanical compression.

Conclusions: Our data reveal that in response to this compression, active Cdc42 levels are increased at the apex, whereas active Rho1 becomes depolarized, similar to that observed in membrane protrusions. Our results show that cell growth and morphology are altered during invasive growth, suggesting stiffness dictates the host cells that *C. albicans* can penetrate.

Keywords: Cell invasion, Mechanical force, Cell polarity, Cdc42, Cell morphology

Background

Polar tip growth, in which extension is limited to the apical surface, enables walled cells such as fungi and plants to explore their environment for nutrients and mating partners, while maintaining their surface to volume ratio [1]. Campas and Mahadevan [2] have derived simple scaling laws for cell geometry and identified a single dimensionless parameter that is sufficient to describe variation in the shape of tip growing cells using turgor pressure, cell wall elastic properties, and secretion rate. However, little is known with respect to the response of tip growing cells to mechanical stress. There are five fundamental types of mechanical stress: tension, compression, shear, torsion, and bending. Human and plant fungal pathogens can penetrate host tissue, and it is likely that they encounter compressive stress upon penetration and subsequent invasive growth. In addition to tissue penetration, growth within a spatially confined environment is critical for infection and successful dissemination of such fungal pathogens.

Fungal pathogens take advantage of different strategies to interact with their environment, of which tip

* Correspondence: xavier.noblin@unice.fr; arkowitz@unice.fr
†Charles Puerner, Nino Kukhaleishvili, and Darren Thomson are co-first authors; order was determined by contribution to figures.
[2]Université Côte d'Azur, CNRS, Institute Physics of Nice (INPHYNI), Ave. J. Vallot, Nice, France
[1]Université Côte d'Azur, CNRS, INSERM, Institute of Biology Valrose (iBV), Parc Valrose, Nice, France
Full list of author information is available at the end of the article

growth is a common theme. Penetration of host tissue is critical for both human and plant fungal pathogens and requires not only the generation of sufficient force but also adhesion to the host cells to counter this force [3, 4]. Fungal pathogens have turgor pressures in the MPa range [3, 4], and for human fungal pathogens, this turgor pressure exceeds host cell resistance to penetration. Such host cells have elastic moduli that are in the 1–100 kPa range [5–7], although the critical stress for material rupture is determinant. Both the human fungal pathogens *Candida albicans* [8] and *Aspergillus fumigatus* [9] can actively penetrate host tissue, which is a critical step in the infection process [10–14]. Previous studies have revealed that *C. albicans* can invade cells via host-induced endocytosis and/or active penetration [8]. *C. albicans* invasion of the intestinal epithelia (small intestinal enterocytes) occurs almost exclusively by active penetration [8, 15, 16], whereas both endocytosis and active penetration are important for invasion of the oral epithelia [17]. However, even with oral epithelia, at the early stages of infection, active penetration is the major route for tissue invasion [17]. Hence, a better understanding of active penetration should provide insight into the initial step of tissue damage for mucosal infections. Translocation of *C. albicans* through intestinal epithelial layers is facilitated by the fungal peptide toxin candidalysin [16, 18]. Previous studies have shown that *C. albicans* hyphal tips are asymmetrically positioned during growth on a stiff surface, i.e., a "nose down" morphology, and that perpendicular growth and contact to a stiff topographical ridge (less than the hyphal radius) results in an indentation of the ridge [19].

To investigate the relationship between substrate stiffness and *C. albicans* penetration and invasive growth, we have used micro-fabrication, together with time-lapse microscopy. We show that there is a threshold for penetration that corresponds to a stiffness of ~ 200 kPa and that invasive growth within a stiff substrate is characterized by dramatic filament buckling along with a stiffness-dependent decrease in extension rate. Nonetheless, a small percentage of cells are able to invade 200 kPa PDMS, suggesting that these cells may play a key role in infection, similar to that of the persister cells in biofilms. Furthermore, we observed a striking alteration in cell morphology during invasive growth, which is not due to depolarization of active Cdc42, but rather occurs at a substantial distance from the site of growth, as a result of mechanical forces. Our data reveal that in response to mechanical forces, *C. albicans* has increased active Cdc42 at the apex while active Rho1 is depolarized, similar to what is observed in PDGF-induced fibroblast membrane protrusions [20].

Results

Monitoring *Candida albicans* filamentous growth in micro-fabricated chambers

To investigate *C. albicans* hyphal growth, we took advantage of micro-fabrication approaches using the elastomer polydimethylsiloxane (PDMS) that, in particular, have been reported as single-cell force sensors for fission yeast cells [21]. We generated PDMS arrays with approximately 10^5 microchambers, which were cylindrical in shape with a diameter of 10 μm, a depth of 5 μm, and 15 μm spacing between adjacent chambers (Fig. 1a). *C. albicans* cells in micro-fabricated PDMS chamber arrays were visualized with inverted microscopes; imaging was carried out through an upright array of 150–200-μm-thick PDMS. Figure 1b shows an XZ confocal reflectance scan through the PDMS microarray with the chambers and media at the top (highest position) and the coverslip below for support (a zoom of chambers is shown in Fig. 1c). *C. albicans* cells were mixed with fetal calf serum, added to the PDMS array, incubated for ~ 1 h, and subsequently, filamentous growth was followed over time (Fig. 1d). With low-stiffness PDMS (a high polymer to cross-linker ratio of 40:1) we observed two predominant filamentous growth modes: non-invasive growth on the PDMS surface and invasive growth within PDMS (Fig. 1e, f). By examination of the focal plane of the PDMS surface and the fungal filaments, using DIC optics, we were able to distinguish between non-invasive (surface) and invasive growth, referring to whether the filament tip is on or within the PDMS, respectively. Invasive growth was also confirmed by labeling the PDMS surface and filamentous cells (see below). Furthermore, we observed that the blastospore (round cell) portion of the filamentous cells, which grew in the microchambers, pushed back against the chamber wall upon PDMS filament penetration and the filament frequently buckled within PDMS, presumably due to the resistive force during growth within the elastomer (Figs. 1f and 2a). These results indicate that, in addition to having ideal optical properties, PDMS is compatible with *C. albicans* filamentous growth.

Growth modes depend on substrate stiffness

We followed *C. albicans* filamentous growth in PDMS of different stiffness, i.e. the extent to which an object resists deformation in response to an applied force, by varying the ratio of polymer to cross-linker. We observed two main growth modes from cells initially in chambers depending on PDMS stiffness: invasive growth, which predominated with less stiff PDMS (40:1) (Fig. 2a) and dramatic bending in the stiffer PDMS (30:1) chambers, which was predominantly subapical (Fig. 2b, top panel). In contrast to *Schizosaccharomyces pombe* [21], extensive deformation of the chambers was not

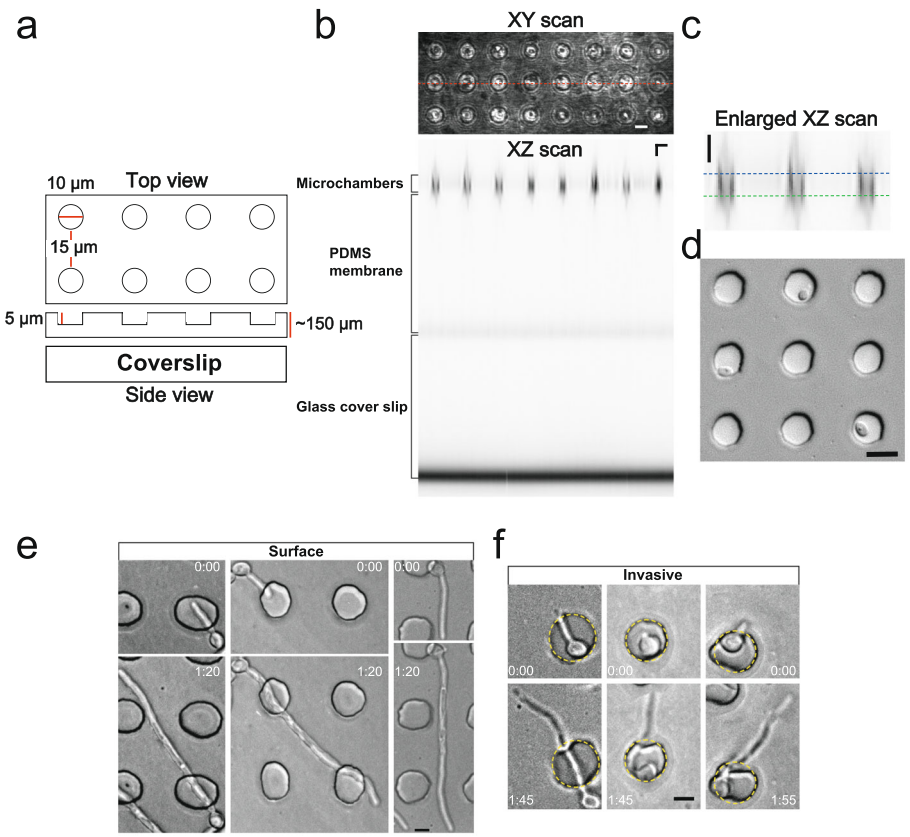

Fig. 1 Filamentous growth in and on PDMS. **a** Schematic of PDMS microchamber array. Top and side views are shown with dimensions indicated. **b** Characterization of PDMS microchamber array. XY transmission view (top) with the location of XZ confocal reflection scan (bottom) of upright PDMS mounted on a coverslip (indicated by dotted red line). Bars are 10 µm in XY and XZ. **c** Enlarged XZ scan of PDMS microchambers. XZ confocal reflection microscopy of 3 microchambers with dotted lines, indicating top and bottom. Bar is 10 µm. **d** PDMS microchambers with *C. albicans* cells entrapped. *C. albicans* cells were mixed with serum (75%) and added to PDMS microchamber arrays, and DIC image is shown. Note the cell with a germ tube (top row). Bar is 10 µm. **e** Non-invasive filamentous growth on PDMS micro-arrays. DIC images of growth on PDMS surface from 3 independent experiments on 40:1 PDMS to cross-linker, with indicated times (h:min). **f** Invasive filamentous growth within PDMS microarrays. DIC images of growth within PDMS from 2 independent experiments using 40:1 PDMS to cross-linker with times indicated. The initial PDMS chamber is outlined with a dotted yellow line to highlight deformation upon invasive filament extension

observed with *C. albicans*, which we attribute to the different sizes, geometries, and growth modes of these fungi; fission yeast has a radius of ~ 2 µm, compared to *C. albicans* hyphal filaments with a radius of ~ 1 µm [22] (and our observations), resulting in a greater than 4-fold difference in the cross-sectional area. At most, a slight chamber deformation was observed with *C. albicans*, as cells frequently popped out of the chambers comprised of stiff PDMS or penetrated this material, when less stiff. Occasionally, at intermediate PDMS stiffness, we observed filamentous cells growing on the PDMS surface that appeared to be probing the surface with a "nose down" growth (Fig. 2b, bottom panel), as similarly observed [19]. This type of growth was suggestive of the filaments attempting to penetrate into PDMS and, consistent with this, we observed these filaments buckling and/or bending subapically at each attempt, prior to the tip popping out and forward. Buckling is defined as a sudden change in the shape of a component under load, i.e. change in the shape of the filament due to the physical forces it experiences. Subapical bending is, additionally, defined as a change in the direction of growth that results in curved filaments (Fig. 2c). In buckling, it is expected that the shape changes are largely reversed upon removal of the external forces, whereas in bending, the shape changes are not a result of the mechanical forces directly. Buckling can occur with a filament initially straight or bent/curved.

We next examined whether cells, initially in chambers, which were unable to invade, underwent bending. Figure 2d shows that as the stiffness of PDMS increased (from 50:1 to 30:1 PDMS to cross-linker), there was an increase in the percentage of cells undergoing bending, concomitant with a decrease in those invading PDMS. During invasive growth, we also frequently observed buckling of the filament (Fig. 2a red arrowheads, c), i.e. a

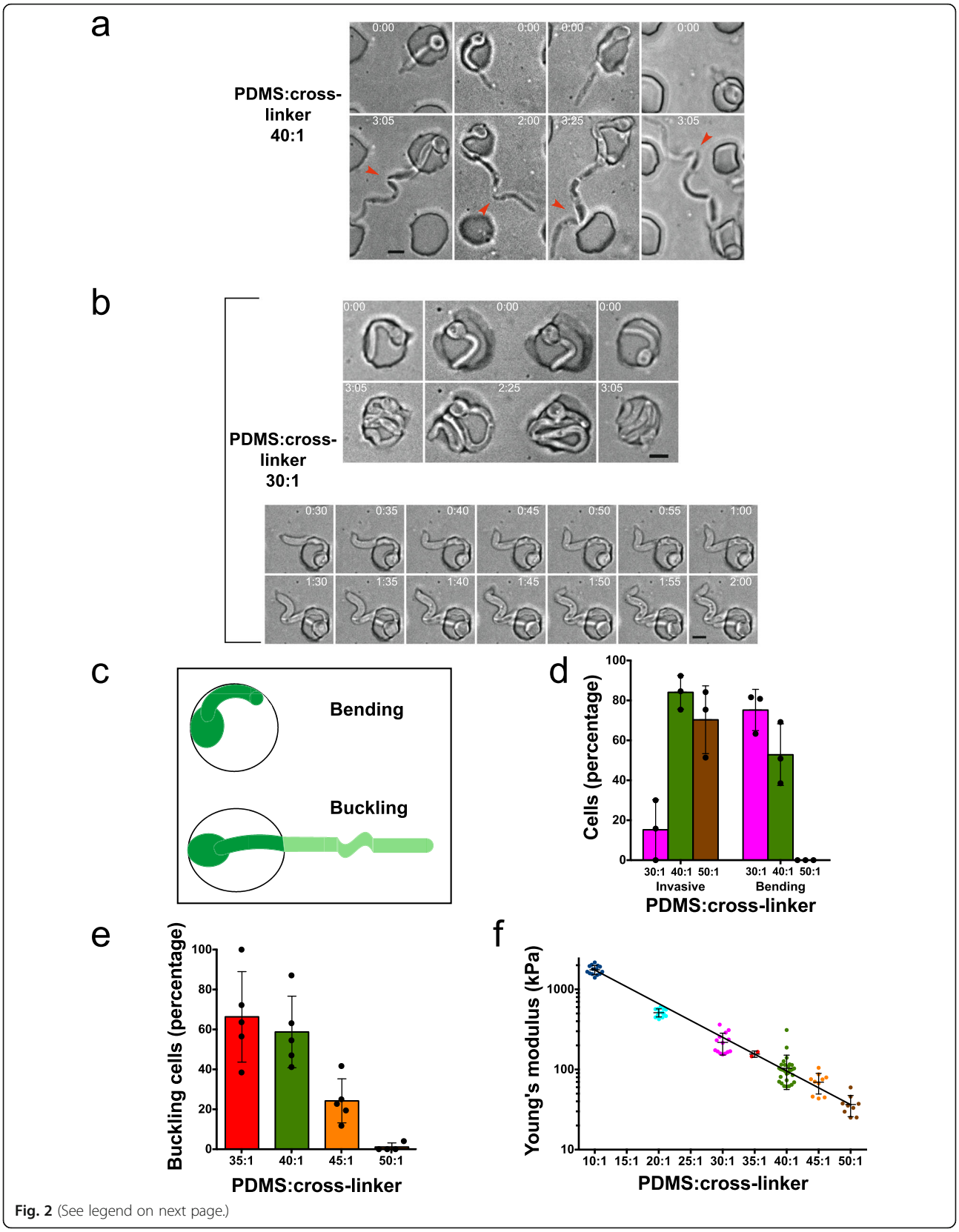

Fig. 2 (See legend on next page.)

(See figure on previous page.)
Fig. 2 Filament subapical bending or buckling during invasive growth or confinement in PDMS chamber. **a** Filament buckling during invasive growth. DIC images of representative cells growing within PDMS at indicated times; red arrowheads indicate filament buckling. **b** Filament buckling upon confinement in stiff PDMS chambers. Cells entrapped in the PDMS chamber at indicated times visualized by DIC (top panel). Time-lapse of a cell grown on PDMS, probing the surface (bottom) followed by filament buckling and release, at indicated times. **c** Schematic of bending and buckling cells. Top cell bending in the microchamber and bottom filament buckling within PDMS (lighter green indicates part within PDMS). **d** PDMS invasion and filament bending are inversely correlated. Three independent time-lapse experiments were carried out at indicated PDMS to cross-linker ratios. Filament curvature upon contact or penetration of PDMS was scored as bending (bending or buckling within PDMS was not scored). Bars indicate SD, and points indicate experimental mean ($n = 20–60$ cells per experiment and 90–140 per condition). **e** Filament buckling increases with increasing PDMS stiffness. Independent time-lapse experiments (4–5) were carried out at indicated PDMS ratio, with $n = 20–50$ invasive cells per experiment (90–125 per condition). Bars indicate SD, and points indicate experimental means. Invasive filaments were considered buckling if the angle of the filament was 90° or greater, compared to filament tip. Note that no buckling was observed in filaments growing on the PDMS surface. **f** Young's modulus of PDMS preparations. Young's modulus was determined by a viscoanalyzer for 10–30 preparations (except 35:1, only 2 preparations) at indicated PDMS to cross-linker ratios

growth-dependent curvature that typically occurred at the portion of the filament within PDMS. Figure 2e shows that such buckling was dependent on the PDMS stiffness, with over half of invasive filaments buckling in the two stiffest PDMS (40:1 and 35:1).

To determine the mechanical properties of the different PDMS preparations, we used dynamic mechanical analysis for which measurements were reproducible over a range of PDMS stiffness. Oscillating strain at a frequency of 10 Hz was applied to PDMS samples, and stress (σ)-strain (ε) curves were obtained (Additional file 1: Figure S1), from which Young's modulus was determined (initial $d\sigma/d\varepsilon$). Young's modulus is the quantitation of the stiffness, i.e. the ratio stress/strain for a uniaxial load, where stress is the force per unit area and strain is the proportional deformation (change in length divided by original length) and is dimensionless. Figure 2f shows the Young's modulus of different ratios of PDMS to cross-linker, which are in good agreement with published values [23–26]. The stiffness of lower ratio samples (10:1 and 20:1), intermediate ratios (30:1 to 40:1), and higher ratios (45:1 and 50:1) was similar to that of medical silicone implants [27], with a Young's modulus of ~ 1 MPa; stiff tissues such as the myocardium [7], with a Young's modulus of ~ 0.1–0.2 MPa; and less stiff tissues such as the epithelia [5, 6], with a Young's modulus of ~ 40–70 kPa, respectively.

Penetration into and escape from PDMS

Given that active penetration is critical during the process of *C. albicans* epithelium invasion [10–12, 14], we examined in further detail this process in PDMS. Figure 3a shows a filamentous cell that penetrates PDMS after 4 min (II; note that I, not shown, is prior to the filament contacting the chamber wall); subsequently grows invasively within PDMS (III); deforms the adjacent chamber (IV), resulting in a dramatic invagination; and exits PDMS into the adjacent well at 2:04 (V), followed by penetration into the opposing chamber at 2:08 (VI) and subsequent invasive growth (2:12; VII). The resistive force revealed by buckling of the filament, as well as deformation of the initial chamber during invasive growth (III), likely increases upon deformation and subsequent piercing into the adjacent well (IV), as the portion of the filament within PDMS buckled during this time (1:22–2:02), resulting in an S-shaped filament (Fig. 3a). The tension on the filament was released upon exiting PDMS into the adjacent well (V), as the tip of the filament appears to jump forward (2:04). The resistive force from the final step of growth (VII) also resulted in buckling of the filament (portion in the well) leading to an M shape (2:42–3:00). This escape from PDMS is analogous, in some respects, to filaments bursting out of a macrophage [28–31]. Here, the filament pushes into a circle resulting in a deformation that does not require expansion of the surface area but rather local invagination of the chamber, which is easier to detect (Fig. 3a). Indeed, such a bursting out of PDMS was observed a number of times, and Additional file 1: Figure S2 shows such examples in different PDMS stiffness (40:1, 110 kPa; 35:1, 150 kPa; and 30:1, 250 kPa).

In order to better visualize the invasive growth within PDMS during these different steps, we followed cells in which GFP was targeted to the plasma membrane [32], by confocal spinning disk microscopy acquisition over a range of z-positions. Figure 3b and c show a typical time-lapse acquisition in which the analysis of the cell outline did not reveal a substantial change in the shape of the filament tip during invasive growth and bursting into the next well (Fig. 3c, d; Additional file 1: Figures S3A and S3B). Indeed, the radius of the curvature of the cell tip was identical to that of surface-growing cells, and there were no changes upon burst out of PDMS. Buckling of the filament was evident upon invasive growth and occurred over 35–45 min, prior to the appearance of a septum (Fig. 3b (red arrowheads) and Fig. 4a, two examples). Analyses of the angle of the filament at which the septum formed ultimately, indicate that during invasive growth, cytokinesis occurs the majority of the time after the filament buckles (Fig. 4b).

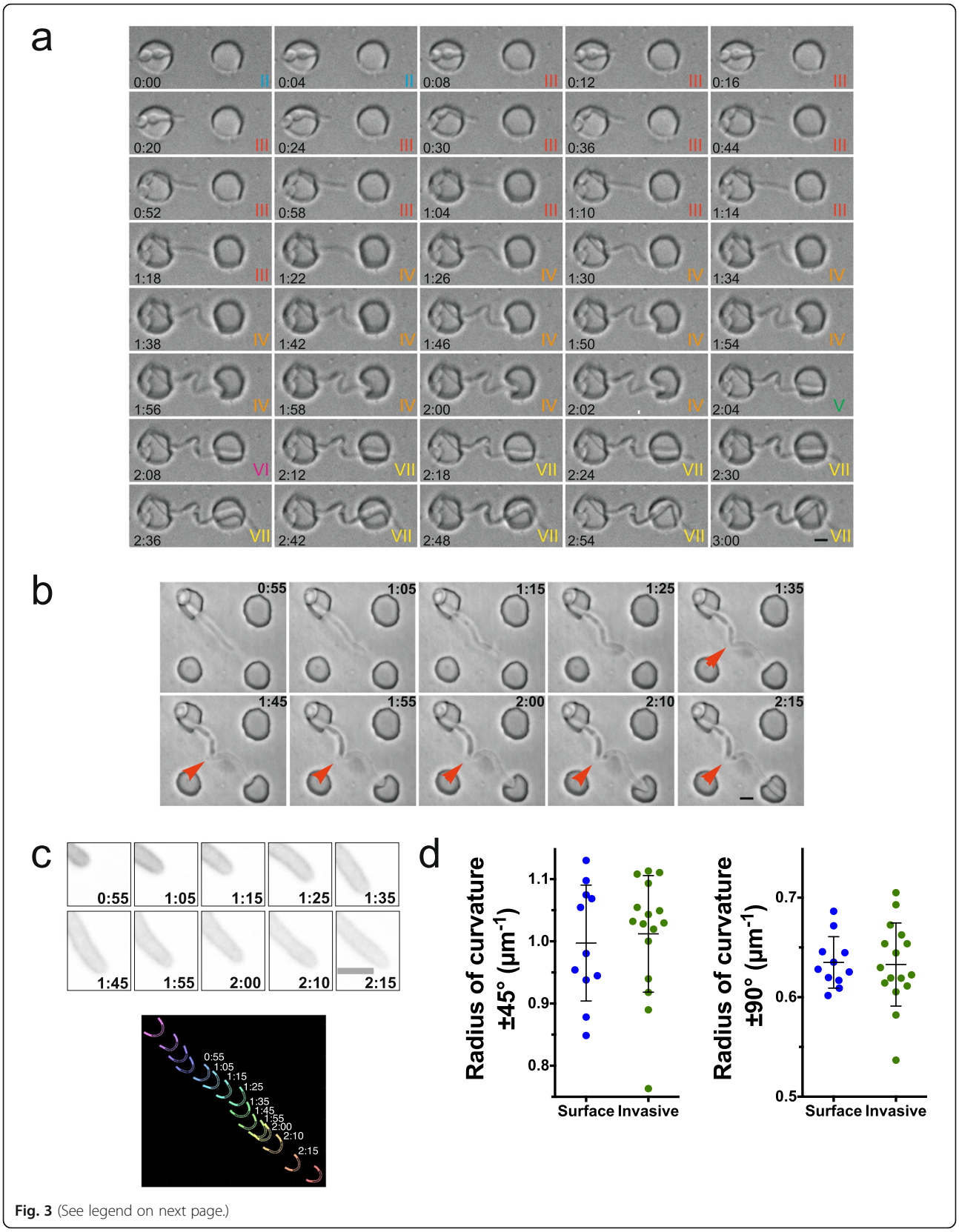

Fig. 3 (See legend on next page.)

(See figure on previous page.)
Fig. 3 The filament tip shape is not substantially altered upon invasive growth and burst out. **a** Filament buckling and release upon invasive growth and penetration. Time-lapse experiment at PDMS to cross-linker ratio of 40:1 (Young's modulus ~ 100 kPa) with DIC images acquired every 2 min. **b**, **c** Filament tip shape does not substantially change during PDMS burst out. **b** Typical time-lapse experiment at 40:1 PDMS to cross-linker ratio (Young's modulus ~ 100 kPa) with DIC images every 5 min. Red arrowheads indicate filament buckling. **c** Close up of sum projections of 13 × 0.5 μm *z*-sections GFP-Ct_{Rac1} fluorescent images from 3B (top), with tip curvature (bottom) at indicated times and ± 45° curvature indicated by open lines and ± 90° indicated by solid lines. **d** The radius of the curvature of invasive and surface growing cells is indistinguishable. The radius of the curvature is the average of 12–24 × 5 min time points (n = 11–16 cells) from 3 to 4 independent experiments for surface (PDMS ratio 40:1; Young's modulus ~ 100 kPa) or invasively growing cells (with PDMS ratio 35:1–40:1; Young's modulus 150–100 kPa). Bars indicate SD

To analyze the physical constraints during penetration, invasive growth, and tip escape from the PDMS matrix, we established a physical experimental model, which consisted of a steel probe that mimics the filament shape, continuously advancing up to and into a cylinder of PDMS of different stiffness (Fig. 5a, b). The steel probe tip approximated the shape of the filament tip (Fig. 5c) with a radius of curvature (± 45°) of 1.1 μm when normalized to the hyphal filament, compared to that of 1.0 ± 0.1 μm for the surface and invasively growing hyphal filaments. Figure 5d shows the probe prior to PDMS rupture and subsequent to exiting from the PDMS. Experiments were carried out with a range of probe displacement rates encompassing that of the filament extension rates (~ 0.3 μm/min [33]), when scaled down to the filament diameter. Figure 6a shows an example of such a force versus displacement curve. The initial phase of increasing force corresponds to the elastic compression of PDMS ($F_{\text{elast compr}}$; analogous to growth stage II, Fig. 3a), culminating in the force required to break the PDMS surface, F_{crit}. The next phase corresponds to the extension within PDMS, analogous to invasive growth, F_{invas} (analogous to growth stage III, Fig. 3a) culminating in PDMS exit (F_{exiting}; analogous to the end of growth stage IV, Fig. 3a). The final phase corresponds to when the end of the probe has emerged from the PDMS (F_{out}; analogous to growth stage V, Fig. 3a). Figure 6b shows the F_{crit} from the physical probe experiments as a function of PDMS stiffness. Filaments are able to penetrate PDMS of ratio 35:1, for which we measured F_{crit} of ~ 7 N with a 1-mm-diameter probe. Scaled to the diameter of a hyphal filament, this would correspond to a force of ~ 31 μN, indicating that hyphal filaments generate forces larger than 31 μN to penetrate PDMS. Scaling to the diameter of a hyphal filament was done assuming a constant critical stress, given the filament diameter is several orders of magnitude greater than the PDMS mesh size, and was calculated by taking the ratio of the metal probe/filament radius squared. Furthermore, our results indicate that at a stiffness of 200 kPa, for which little PDMS penetration is observed (Fig. 2d), the F_{crit} is ~ 8 N with a 1-mm-diameter probe, i.e. ~ 35 μN when scaled to a hyphal filament, which would correspond to the growth stalling force.

Resistive force affects hyphal extension and morphology

The buckling of the filaments, as well as the deformation of the PDMS wells during invasive growth, indicated that these filaments were responding to resistive force, whose magnitude we have measured in the physical model. The percentage of cells that penetrate PDMS is dependent on Young's modulus (Fig. 2d, f), and analyses of percent of PDMS invasion at two stiffness values indicate that the threshold for invasion is between 120 and 200 kPa (Fig. 7a). Hence, to investigate the effects of resistive force on filamentous growth, we determined the length of the filaments over time from cells growing on and within PDMS in this range of stiffness. Figure 7b shows that cells extend at a constant rate, which is reduced by ~ 30% within PDMS from an average of 0.28 ± 0.07 μm/min (n = 29) for surface growth to 0.19 ± 0.05 μm/min (n = 32) when filaments were growing within PDMS with a stiffness of ~ 100 kPa (Fig. 7c). This filament extension rate was further reduced to 0.15 ± 0.08 μm/min (n = 23) upon growth in PDMS with a stiffness of ~ 150 kPa (Fig. 7c). To confirm that the reductions in extension rate during invasive growth were not due to the substantial changes in the *z*-position of the growing filament apex, cells were grown in PDMS chambers that had been stained with fluorescent ConA and *z*-section images were projected onto the XZ plane (Fig. 7d). These projections show that the filaments grow slightly downward in PDMS, below the bottom of the chamber, with maximally 5 μm displacement in the *z*-axis for a 25-μm filament, resulting in at most a 2% reduction in extension rate upon projection in the XY plane. In contrast, Fig. 8a shows that the mean filament extension rate of cells grown on the surface is not dependent on the substrate's stiffness, with indistinguishable rates on PDMS with Young's modulus from 100 to 200 kPa. Furthermore, the extension rate of invasive growth normalized for that of surface growth from each experiment correlates with substrate stiffness (Fig. 8b). Extrapolation to the *y*-intercept, where the invasive extension rate, equals the surface rate indicates a substrate stiffness of ~ 20 kPa, suggesting that during filamentous growth on PDMS, the cells experience this resistive force from adhesion. Consistently, the surface extension rate was slightly reduced compared to that in

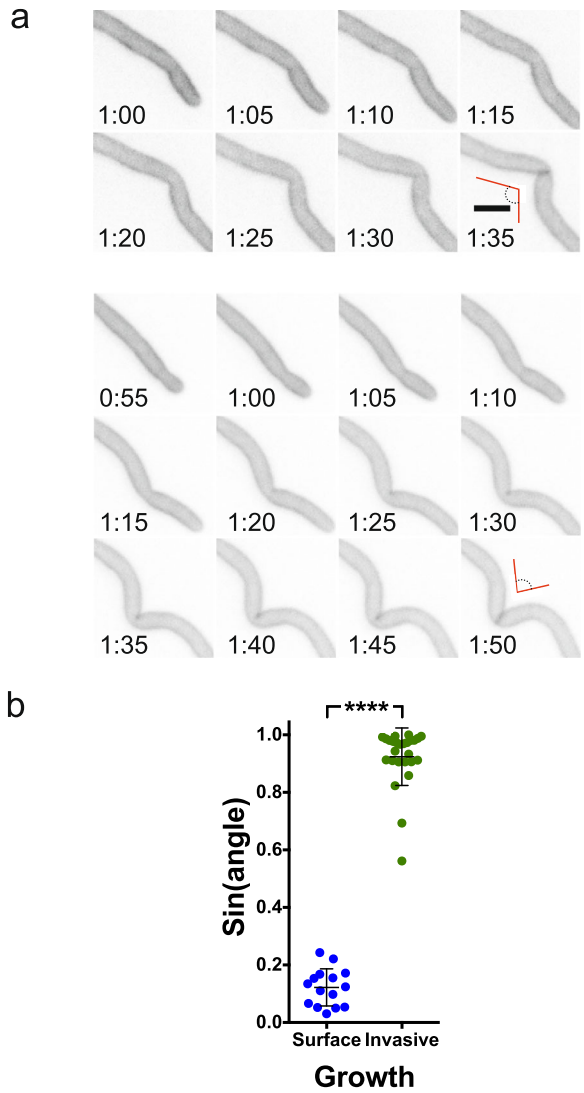

Fig. 4 Cell division occurs at the site of filament buckling during invasive growth. **a** Examples (upper and lower panels) of time-lapse images (GFP sum projections) during invasive growth in 40:1 PDMS ratio, showing cell division site at the location of filament buckling with red lines highlighting the buckling angle. **b** Cell division site occurs where the filament is buckled. Cells were grown either invasively within PDMS (40:1; Young's modulus ~ 100 kPa) or on the surface of PDMS (30:1–40:1; Young's modulus 250–100 kPa), $n = 26$ and 15, respectively. GFP sum projections were analyzed over time from 5 independent experiments and Sin of angle when the septum formed is shown. Septum formation was observed on average 47 ± 20 min after buckling was evident in invasive cells. Bars indicate SD with $p < 0.0001$

liquid media (0.26 ± 0.09 μm/min compared to 0.32 ± 0.01 μm/min; $p = 0.001$) (Fig. 8a). Of note, very few cells invaded PDMS at 200 kPa, on average ~ 5% (Fig. 7a), but, strikingly, the filament extension rate for these "escapers" was similar to that of less stiff PDMS, raising the attractive possibility that these cells may play a critical role in tissue invasion.

The difference in filament extension rate could either be due to an overall reduction in cell growth or a reduction in polarized, apical growth. To differentiate between these possibilities, we determined the length and diameter of compartments (between 2 septa) for cells growing on the surface and within PDMS (100 kPa). Figure 9a and b show that the compartment length decreased ~ 30%, from 24.6 ± 3.0 μm ($n = 100$) for surface growing cells to 16.6 ± 1.8 μm ($n = 120$) during invasive growth, and the filament diameter increased concomitantly from 2.1 ± 0.2 μm for surface growing cells to 2.5 ± 0.2 μm during invasive growth. As a result, the compartment volume remained constant (83 ± 17 μm^3 for surface growing cells compared to 80 ± 18 μm^3 for invasively growing cells), indicative of altered polarized growth. Consistently, analyses of filamentous cells grown within stiffer PDMS (150 kPa) revealed a further decrease in compartment length (14.6 ± 2.5 μm) and an increased diameter (2.8 ± 0.3 μm). This altered morphology is dependent on growth against a resistive force in PDMS as the diameter in the part of the filament outside PDMS was similar to that of surface growing cells (Fig. 10a). In addition to the comparison of cells growing on the surface and within PDMS, we examined the relatively rare occurrence of cells transitioning between these growth modes. Figure 10b and c show an example of such a transition, in which the extension rate is reduced during invasive growth in PDMS and increases exiting PDMS. Measurements of the filament diameter just before and after the filament exited PDMS revealed an increased filament diameter during invasive growth that was significantly reduced upon exiting PDMS (2.7 ± 0.2 μm compared to 2.3 ± 0.3 μm, Fig. 10d).

Reduced filament extension rate in response to a resistive force suggested that similar effects could be observed in cells undergoing non-invasive, dramatic subapical bending in chambers of stiff PDMS (Additional file 1: Figure S4A). Additional file 1: Figure S4B shows that, in such conditions, there was indeed a dramatic reduction in filament extension rate with an average (over 100–150 min) of 0.10 ± 0.01 μm/min. Surface growth rates were constant over time, whereas extension rates of cells undergoing dramatic subapical bending decreased concomitantly with the cell filling the well (Additional file 1: Figure S4C); initial rates of extension were 3-fold reduced from surface growth, and these were further reduced 3-fold after 2 h of growth. Due to the complex geometries during such a growth mode, we were unable to determine the resistive force that the filament experiences while it fills up the chamber; however, the initial extension rate is similar to that of filaments growing invasively in 150 kPa PDMS.

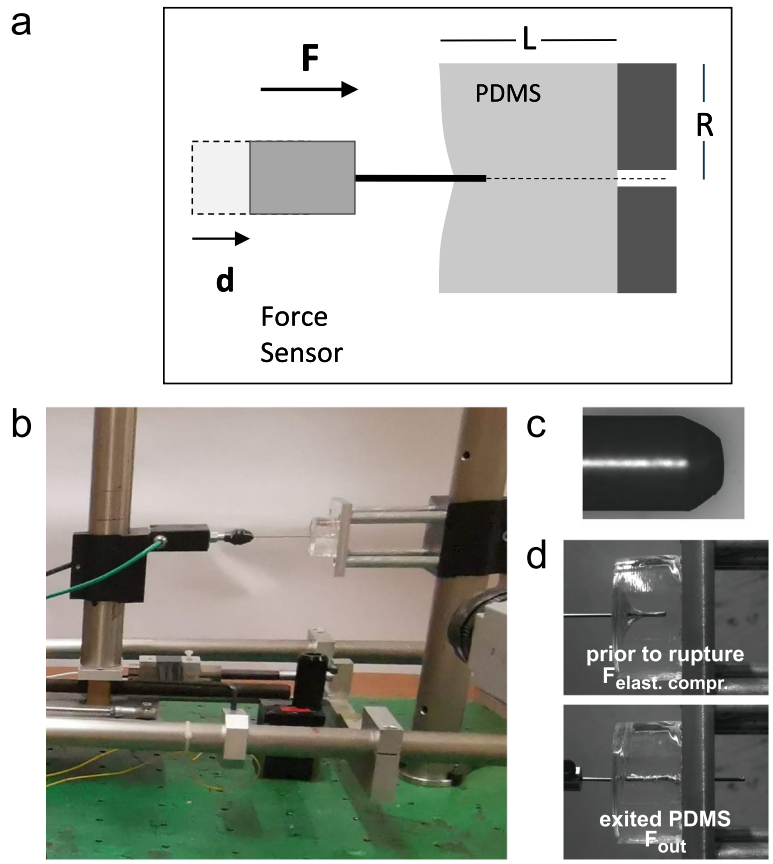

Fig. 5 Physical model of PDMS invasive growth. **a** Schematic of the physical model. The distance probe traveled is *d*; *F* is the force detected by the sensor; *L* is the PDMS length, and *R* is the PDMS radius. **b** Image of the physical model setup. Force sensor attached to 1-mm-diameter probe (left) and PDMS on the right as indicated in **a**. **c** Shape of the steel probe tip. Probe is 1 mm diameter. **d** PDMS penetration. PDMS (40:1; Young's modulus ~ 100 kPa) cylinder (1.75 cm length and radius) with 1 mm probe displacement of 1.6 μm/s. Upper image, prior to rupture of PDMS; lower image, probe exit from PDMS

Determination of the effective turgor pressure

From the comparison of extension rates within PDMS of different stiffness (Fig. 7c), we determined the effective turgor pressure in *C. albicans* hyphae, using the visco-plastic growth model [21]. This determination makes use of F_{invas} values, measured from the physical model (Fig. 6), after scaling these forces from a cylinder with a radius of 0.5 mm to that of 1.04 μm. In order to correctly extrapolate the macroscopic measurements to the microscopic scale of filamentous cells, we analyzed the physical forces at play. The mode of extension during hyphal growth and in this physical experimental model is different, as new material is incorporated into the hyphal tip, i.e. growth occurs via apical extension, whereas in the physical experimental model, the probe is pushed into the PDMS from the back. Given that only a small portion of the filamentous cell apex extends in the PDMS, we removed the contribution from friction/adhesion due to the displacement of a 1-mm-diameter probe within PDMS by subtracting the F_{out} value from the F_{invas} (Fig. 6c). These corrected F_{invas} values, i.e. F_{in}, were largely independent of probe displacement rates over a range equivalent to cell filament extension rates when scaled down (0.2–0.4 μm/min). We used the equation that was established for *S. pombe* by Minc and colleagues;

$$\frac{V_{(F)}}{V_o} = \left(1 - \frac{F_{(\text{PDMS})}}{\pi R^2 \Delta P}\right) \quad (1)$$

$V_{(F)}$ and V_o are the filament extension rates within PDMS and on the surface, respectively; $F_{(\text{PDMS})}$ is the resistive force of PDMS during filament displacement within this material (F_{in}); R is the filament radius; and ΔP is the effective turgor pressure. The $F_{(\text{PDMS})}$ was 1.5 ± 0.7 N and 0.7 ± 0.3 N at PDMS to cross-linker 35:1 (Young's modulus of 150 kPa) and 40:1 (Young's modulus of 100 kPa), respectively; scaling to the size of the hyphal filament (radius 1.04 μm for surface growth) yielded 6 ± 3 μN and 3.2 ± 1.4 μN, respectively. From these

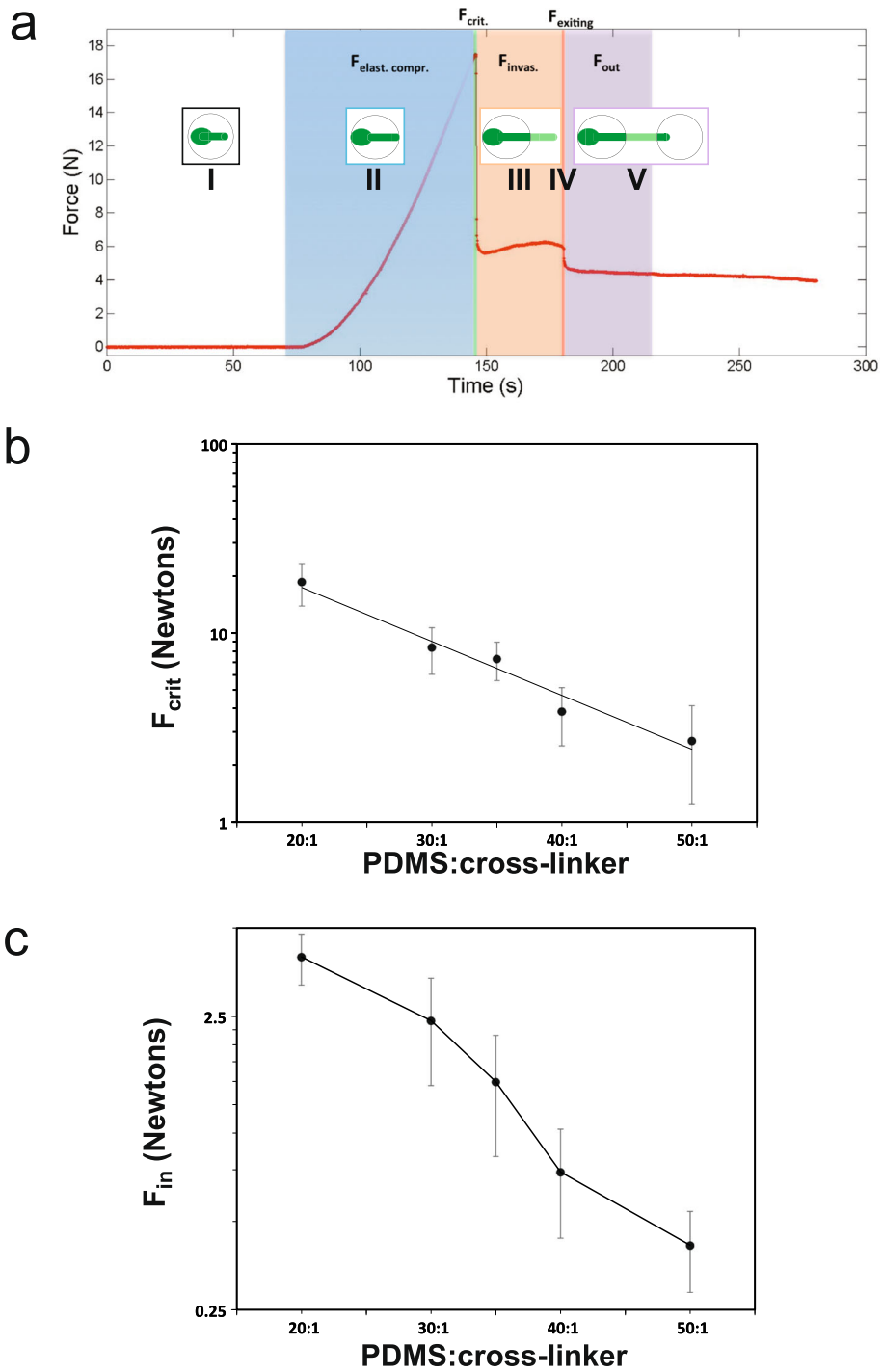

Fig. 6 Forces in physical model of PDMS invasive growth. **a** Forces encountered upon probe displacement into and out of PDMS. A 1-mm-diameter steel probe was advanced perpendicularly into the base of the cylindrical piece of cured PDMS (10:1 PDMS to cross-linker ratio, Young's modulus ~ 2 MPa). Probe displacement rate was 63 μm/s, and force was determined during different stages, as indicated, i.e., compression, penetration, and after the probe tip emerged from PDMS. Analogous stage of hyphal filament invasive growth indicated in insets along with the growth stage from time-lapse in Fig. 3a (I–V). **b**, **c** Resistive forces as a function of PDMS to cross-linker ratio. **b** F_{crit} was determined using a 1-mm-diameter steel probe, with either 3.5- or 8-cm-diameter PDMS cylinders of indicated PDMS to cross-linker ratio, with probe displacement set to 1.6–3.2 μm/s. Bars are SD for on average 10 independent determinations for each PDMS ratio. **c** F_{in} was determined by subtracting F_{out} from F_{invas} from the probe penetration experiment described in **a**. Bars are SD

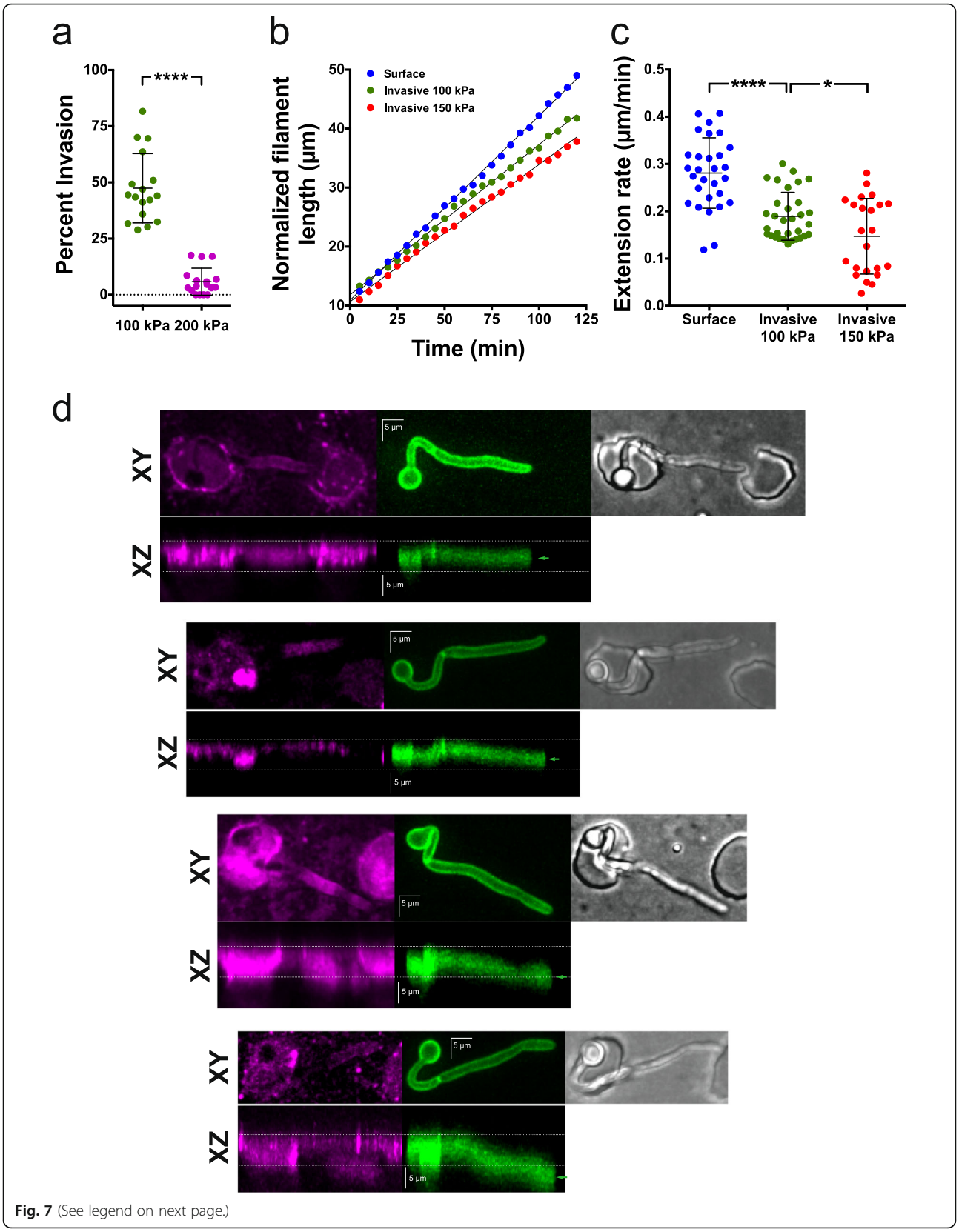

Fig. 7 (See legend on next page.)

(See figure on previous page.)
Fig. 7 Filament extension rate is decreased during invasive growth. **a** A PDMS substrate stiffness limit for filament penetration. Percentage of invading cells from time-lapse experiments (4 independent experiments for each PDMS stiffness, Young's modulus indicated, 40:1 and 30:1) was quantified ($n = 50–60$ cells per determination from a total of 900–1200 cells) using wide-field microscopy. Bars indicate SD and ****$p < 0.0001$. **b** Filament extension rate is linear during surface and invasive growth. Cells grown on or in PDMS at indicated stiffness (35:1 and 40:1) over 2 h, with images every 5 min. Filament length was determined from the sum projection GFP images and normalized to an initial length of 10–12 μm. **c** Filament extension rate is reduced upon invasive growth. The extension rate was determined from the time-lapse acquisition of cells grown within PDMS at indicated stiffness (35:1 and 40:1). Surface growth was carried out on PDMS with a stiffness 190-85 kPa (30:1–40:1). Quantification from 2 to 4 independent experiments, $n = 20–30$ cells per PDMS stiffness. Bars indicate SD with ****$p < 0.0001$ and *$p < 0.05$. **d** Invasively growing filaments do not undergo substantial changes in the *z*-position. Cells expressing plasma membrane GFP were imaged (green; middle panel) after growth in ~ 150 kPa PDMS (35:1), chambers that were labeled with Alexa-633 ConA (magenta; left panel), and 100 × 0.2 μm *z*-sections were acquired with DIC image shown (right panel). XY (upper panels) and XZ maximum projections are shown with dotted lines indicating the upper and lower limits of the microchamber and the green arrow indicating the center in the *z*-axis of the filament tip

values, we determined the effective turgor pressure, ΔP, to be 6 ± 3 MPa and 2 ± 1 MPa in these two conditions, respectively. Given that the hyphal filament diameter increases during invasion (radius 1.42 μm at Young's modulus of 150 kPa and 1.24 μm at Young's modulus of 100 kPa), the calculated ΔP are 3.1 ± 1.5 MPa and 1.5 ± 0.7 MPa, suggesting that the hyphal turgor pressure is 1–3 MPa. This value for turgor pressure is within the range reported both for planktonic and biofilm *C. albicans* cells, ~ 1.2 MPa [19] and ~ 2 MPa [34], respectively, as well as *S. pombe*, 0.85–1.5 MPa [21, 35]. Nonetheless, it must be noted that these values are effective turgor pressure. In other words, ΔP is the turgor pressure exceeding the critical stress needed to deform the cell wall [21]. Hence, a combination of local compartment turgor pressure alteration, difference in cell wall deformability, or potentially finer adjustments in tip geometry may play important roles in penetration and invasion.

Resistive force affects cell polarity

The change in morphology during invasion, resulting in shorter and wider cells, could be explained by tip growth becoming more isotropic in response to a resistive force, raising the possibility that cell polarity is adversely affected. In *S. pombe*, it was observed that reducing the growth rate chemically, genetically, or mechanically destabilized active Cdc42 polarization, a cell polarity master regulator [36]. To investigate whether cell polarity was altered in hyphal filaments growing invasively in PDMS, we examined the distribution of active Cdc42 (Cdc42•GTP), using a CRIB-GFP reporter [37]. Surprisingly, we observed a striking increase in polarized active Cdc42 at the filament tip throughout invasive growth, compared to surface growth (Fig. 11a, b). We determined, using a tailor-made MATLAB program, that this results from an increase in the concentration of Cdc42•GTP at the tip, rather than an alteration in the position of the maximum signal or spread of active Cdc42 further down the filament (Additional file 1: Figure S5A-D). These results suggest that, in response to a resistive force, there is an increase in cell polarization, perhaps reflecting a direct response to such external forces. We speculate that this higher level of active Cdc42 during invasive growth is due to the increased recruitment of the Cdc42 activator, Cdc24 [38]. We next examined active Rho1, as cell wall stress mediated by the cell surface mechanosensors Wsc1/Mid2 results in Rho1 depolarization in *S. cerevisiae* [39, 40]. Figure 11c and d show that, in contrast to the increase in tip localized active Cdc42, active Rho1 is depolarized during invasive growth. We attribute this depolarization of active Rho1 to the mechanical properties of PDMS, which are likely to impose a uniform force over the hyphal filament surface, in addition to the resistive force in response to the tip extension.

The increase in tip-localized active Cdc42 during invasive growth suggests that the increase in filament diameter does not result from growth becoming more isotropic in response to resistive force. To examine whether this morphological change results from mechanical forces, we compared cell morphology over time during growth on the surface and within PDMS. Figure 12a and b show that the relative filament diameter (D1) was not altered during surface growth (mean diameter 2.26 ± 0.15 μm initially compared to 2.44 ± 0.06 μm after 2 h growth), in contrast to the invasive growth where there was a striking increase (2.38 ± 0.22 μm initially compared to 2.98 ± 0.15 μm, $p < 0.0001$). Specifically, the diameter of the filament compartment increased even > 10 μm back from the tip (Fig. 12b). This ~ 25% increase in diameter during invasive growth could either occur upon tip growth or subsequent to tip growth. The hyphal tip diameter was constant over 2 h of invasive growth and only slightly wider than that of cells growing on the surface (2.53 ± 0.11 μm compared to 2.24 ± 0.09 μm; $p = 0.0003$) (Fig. 12c, d). In contrast, Fig. 12d shows that there was a significant difference between the mean diameter at the tip of the apical cell and that of the cell proximal to the apical cell during invasive growth (mean proximal cell diameter 2.99 ± 0.17 μm; $p < 0.0001$). Together, these results indicate that relatively small changes in the tip morphology are not sufficient to

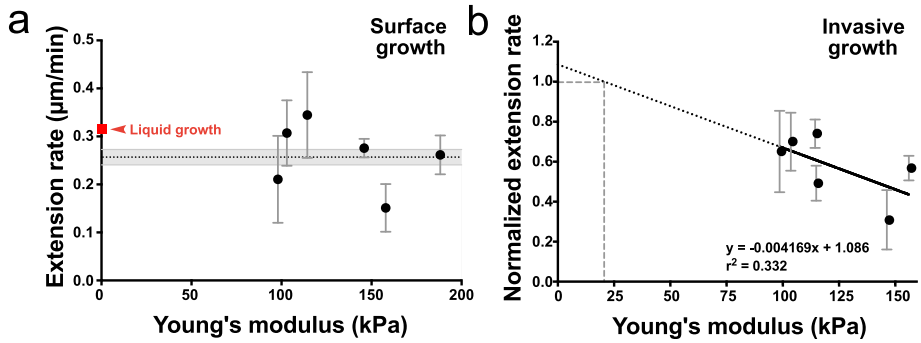

Fig. 8 Filament extension rate on the PDMS surface is slightly reduced compared to that in liquid media. **a** Filament extension rate on the PDMS surface is independent of stiffness and reduced compared to that in liquid media. The extension rate was determined as in Fig. 7c. Filament lengths of cells grown in serum-containing liquid media ($n = 75–80$ cells) were measured every 30 min with mean and SEM shown in red. Surface extension rates determined as in Fig. 7c ($n = 30$ cells; 3–9 experiments per PDMS stiffness). Bars indicate SD. The mean of all surface extension rates (dotted black line) and SEM (gray zone) are indicated. **b** Cells experience a resistive force on the PDMS surface. Invasive extension rates determined as in Fig. 7c ($n = 53$ cells; 5–10 experiments per PDMS stiffness) and normalized to surface extension rates, with bars indicating SD and dotted line the best fit. At $Y = 1$, X is ~ 20 kPa

explain the altered morphology of the filament, back from the tip, which are due to external mechanical forces.

Discussion

We used PDMS micro-fabrication to probe the relationship between substrate stiffness and growth of *C. albicans* filamentous cells. Below a stiffness threshold of ~ 200 kPa, *C. albicans* can penetrate and grow within PDMS. The chemical inertness of this polymer, as well as the observed well deformation, suggest that turgor pressure-driven active penetration is critical for this invasive growth. *C. albicans* filamentous growth within a stiff substrate is characterized by dramatic filament buckling, which correlates with the position of cell division sites, in addition to a stiffness-dependent decrease in extension rate. Growth within

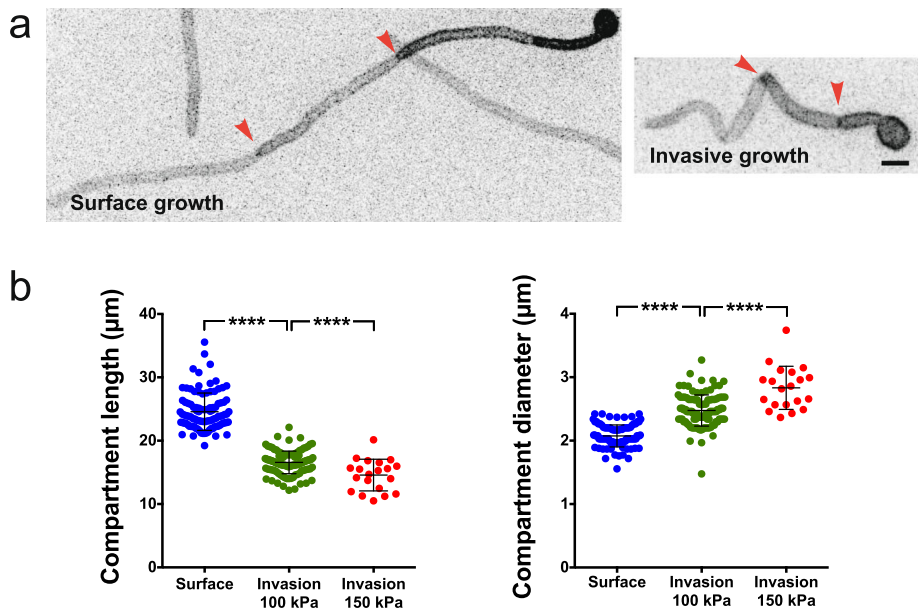

Fig. 9 Filament morphology is altered during invasive growth. **a** Sum projection images of cells expressing GFP-Ct_{Rac1} grown in the presence of FCS on or within PDMS of 115 kPa stiffness, for 3h15 or 2h15, respectively. Arrowheads indicate the septa that delimit the measured compartment. **b** Compartment length is reduced and diameter is increased when cells are grown within a substrate of increasing stiffness (40:1 and 35:1). The length between two septa (left panel) along with the filament diameter (right panel), either the 2nd or the 3rd compartment from the tip, was measured in $n = 20–115$ cells, 2–22 experiments. SD are indicated and $p < 0.0001$

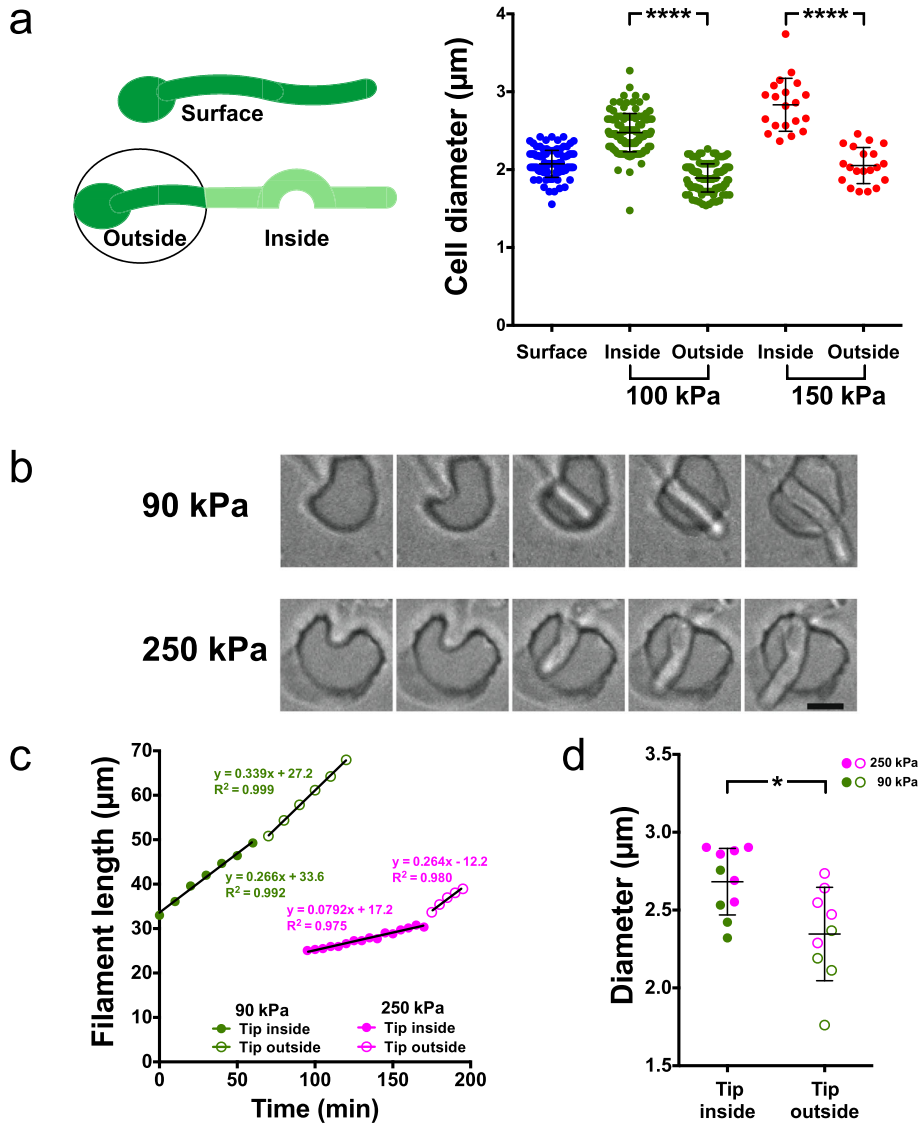

Fig. 10 Filament diameter increases during growth in PDMS and decreases upon bursting out. **a** Filament diameter inside and outside PDMS at two stiffness values. The diameter of the filament was measured as in Fig. 9a and b (surface and portion inside PDMS). The diameter of the filament adjacent to the mother cell neck in the chamber was measured (portion outside indicated in the schematic). Bars indicate SD, with $p < 0.0001$ between inside and outside for each PDMS stiffness value (40:1 and 35:1). **b** Images of filament bursting out of PDMS. Cells grown in PDMS at indicated times over 2 h, with DIC images every 5 min (~ 250 kPa; 30:1) or 10 min (90 kPa; 40:1) shown. **c** Filament extension rate increases upon exiting PDMS. Filament length was measured from the sum projection GFP images prior to (green and magenta-filled symbols) and following emerging from PDMS (green and magenta-open symbols). **d** Filament tip diameter is slightly reduced upon emerging from PDMS. The tip diameter was determined at 4–5 times before or after exiting PDMS from **b** and **c**. Bars indicate SD and $*p = 0.01$

a substrate also resulted in a striking alteration in morphology, i.e. reduced cell compartment length and increased diameter. Our results reveal that changes in morphology are not due to a depolarization of active Cdc42, but rather to the mechanical forces from the substrate.

Growth behavior as a function of substrate stiffness

Substrate stiffness determines whether *C. albicans* will grow on a surface or within it, below a threshold corresponding to a stiffness of 200 kPa. During growth within PDMS, a substantial fraction of filaments buckle, with greater than 50% buckling in a substrate with a Young's modulus of ~ 100 kPa. Cells trapped in stiff (200 kPa or greater) microchambers undergo dramatic subapical bending. While both filament buckling and subapical bending depend on filament extension, the former occurs at least 5–10 μm away from the apex whereas the latter occurs at the filament tip. In a number of cases, filaments buckled as the tip (within PDMS)

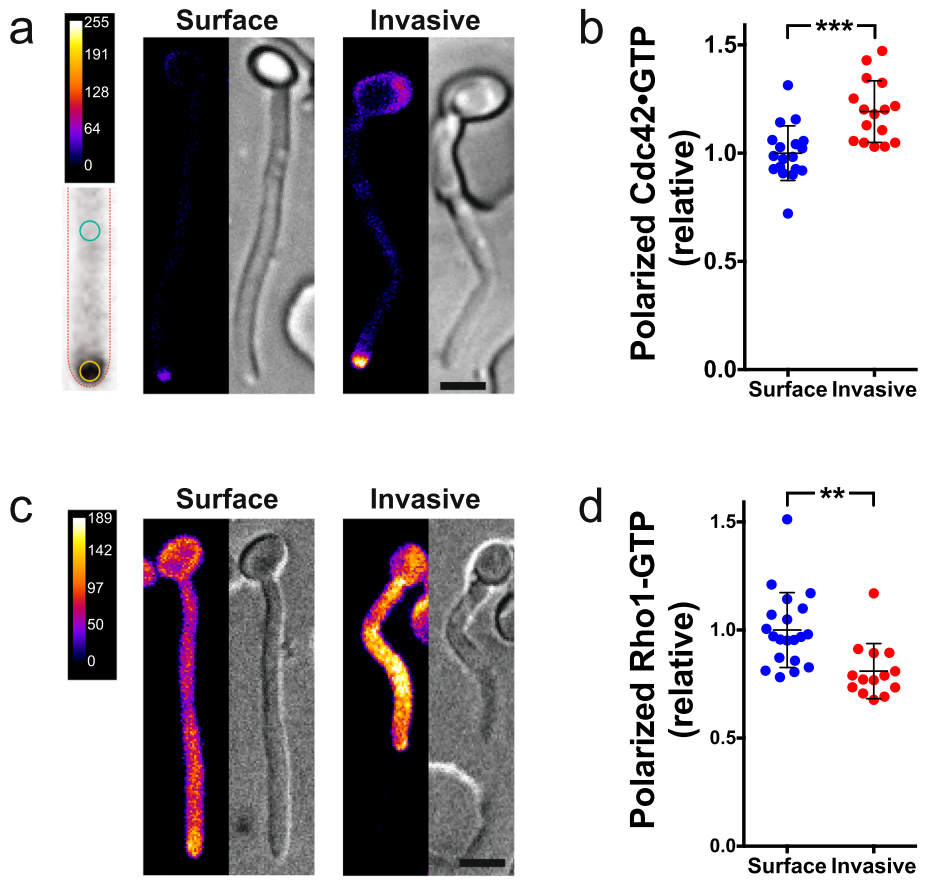

Fig. 11 Invasively growing filaments have increased levels of active Cdc42 at the tip. **a**, **b** Tip-localized Cdc42•GTP is increased during invasive growth. **a** Representative sum projection and DIC images of cells expressing CRIB-GFP on or in 35:1 PDMS (~ 150 kPa). False colored sum projection of 23 × 0.4 μm *z*-sections (LUT, top) with schematic indicating regions quantitated at the tip and 5–10 μm back from the tip (bottom). **b** Mean Cdc42•GTP at the tip and 5–10 μm subapically determined from 4 independent time-lapse experiments (images every 5 min for ~ 2 h and sum projections of 23 × 0.4 μm *z*-sections; $n = 16–18$ cells). Polarized Cdc42•GTP is the tip signal divided by the subapical signal, 5–10 μm behind the tip (3.5-fold enrichment apically for surface growing cells, normalized to 1). Bars indicate SD and $^{***}p = 0.0002$. **c**, **d** Active Rho1 is delocalized during invasive growth. **c** Representative sum projections and DIC images as in **a** of cells expressing GFP-RID after growth on or in 35:1 PDMS (~ 150 kPa). **d** Mean Rho1•GTP at the tip and at 5–10 μm subapically was determined from 3 independent time-lapse experiments, as in **b** ($n = 14–20$ cells). Polarized Rho1•GTP is the tip signal divided by the subapical signal (1.4-fold enrichment apically for surface growing cells, normalized to 1, as in **b**). Bars indicate SD and $^{**}p = 0.001$

approached a well, followed by partial release upon penetration into this well. This bursting out event is similar, in some respects, to damaging of or escaping from host cells, such as macrophages [28–31].

Despite the estimated resistive force during invasive growth of 3–10 μN at the hyphal scale, we did not observe dramatic changes in the filament tip shape. Interestingly, the location of cell division sites appeared to be affected by filament buckling, in that there was a high correlation between the division site location and the site of buckling. Septins have been shown to be enriched preferentially at locations of high curvature in *Ashbya gossypii* hyphal filaments, i.e. at branch points [41]. An attractive possibility is that the location of the cell division site at the buckle, or vice versa, may minimize physical stress or damage to the filament.

Effects of substrate stiffness on invasive growth

Filament extension rate is reduced, and cell compartment length decreases with increasing substrate stiffness; however, cell volume is largely unaffected during growth within 100 kPa PDMS, due to an increase in filament diameter. These results suggest that the overall growth rate is unaffected in this condition, raising the possibility that the cell tip growth area is altered by resistive force. Given that altering growth in *S. pombe* by chemical, genetic, or mechanical means, results in destabilization of the active Cdc42 cluster at the growth site, we investigated the distribution of this key GTPase during invasive growth. Surprisingly, the distribution of active Cdc42 was not altered during invasive growth, but rather there was an increase in the concentration of active Cdc42 at the tip. In contrast, active Rho1, which is critical for glucan synthesis, was less polarized and

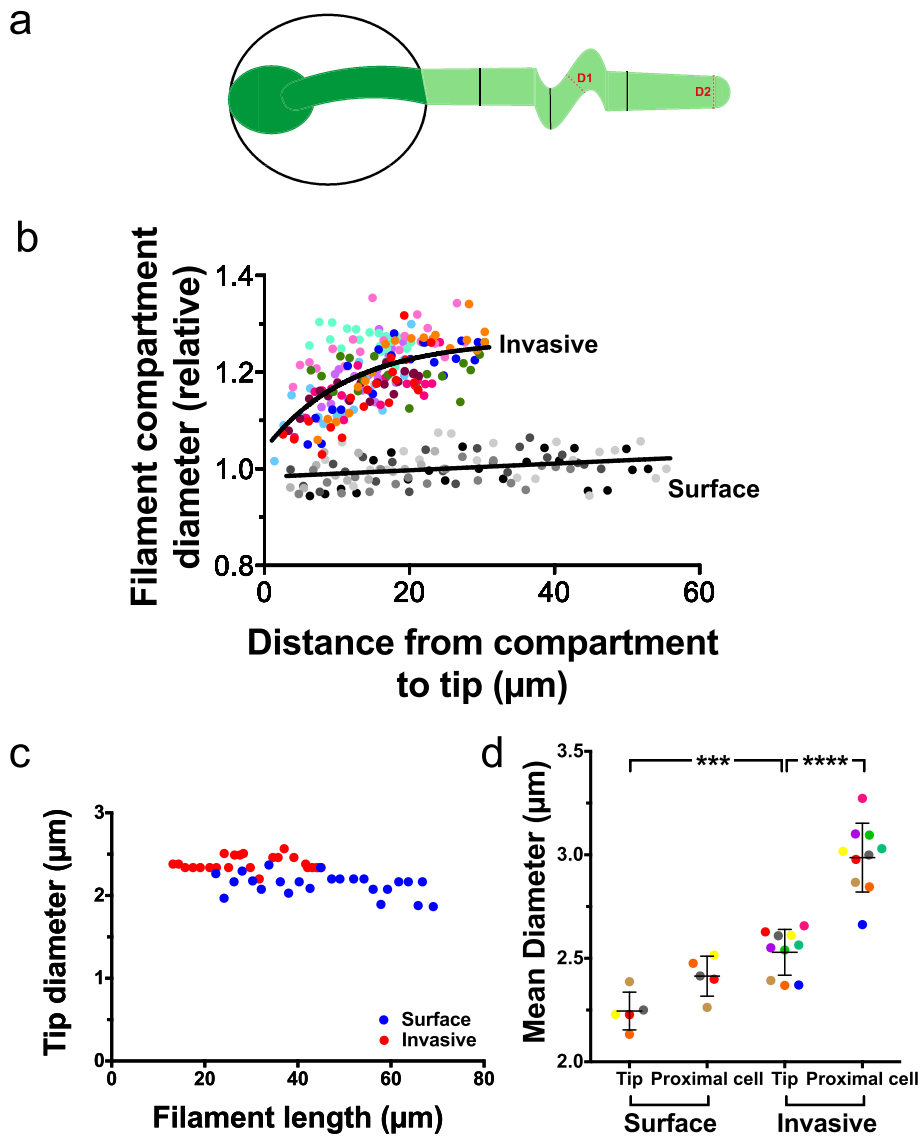

Fig. 12 Mechanical forces are critical for filament morphology changes. **a** Schematic of filament during invasive growth. Lighter green indicates a portion of the filament within PDMS; D1, compartment or proximal cell diameter; and D2, tip diameter. **b** The diameter of the cell compartment increases as it becomes further away from the filament tip during invasive growth. Cell compartment diameter (measured at 5 equidistant positions between 2 septa), initially on average 5 μm from tip, was determined from 3 independent experiments acquired as in Fig. 11b ($n = 5–10$ cells) grown on or within 35:1 PDMS (~ 150 kPa). Distance from the compartment center to the tip was determined at each time. The diameter was normalized to the diameter of the last time point for each cell and further normalized by the mean difference between the final compartment diameters of invasive cells compared to surface cells. Each color represents a cell. **c** Filament tip diameter does not vary as a function of filament length for surface and invasive growth. Tip diameter (2 μm back from the apex) measured for one cell growing on PDMS surface and one cell growing within PDMS, over a 2-h time course. **d** Tip diameter increase does not underlie proximal cell diameter increase during invasive growth. Tip and proximal cell diameters were measured from the same cells as in **a**. Proximal cell diameter was measured at the center of the cell proximal to the apical cell over the 2nd hour of the time course (filaments > 30 μm long). Bars indicate SD, with $^{****}p < 0.0001$ between the tip and the proximal cell during invasive growth and $^{***}p = 0.0003$ between the invasive and surface tips

observed throughout the filament during invasive growth. Together, these results suggest that, during invasive growth, cells sense resistive force from the PDMS and polarization increases at the tip, while remodeling their cell walls throughout the filament to counter this resistive force and/or the increase in turgor pressure. A likely possibility is that this resistive force is sensed by the mechano-sensing pathway, via a module composed of the mucin Msb2 and the cell wall protein Sho1 [42] critical for *S. cerevisiae* survival during compressive stress. In this yeast, Msb2 localizes to sites of growth and binds active Cdc42 [43], and cell wall stress has been shown to depolarize Rho1, as well as to

hyperactivate this GTPase [39, 40] via the cell surface sensors, Wsc1 and Mid2. Indeed, *S. cerevisiae* cells sense compressive stress via Mid2, which localizes uniformly at the plasma membrane [44]. We speculate that the increased compression around the hyphal filament leads to depolarized active Rho1 via Mid2, in contrast to localized active Cdc42 via Msb2.

We have used a viscoplastic model for fungal growth that was originally established to describe cell shape control in plants [45, 46] and used, more recently, to analyze cell growth in fission yeast [21]. In such models, viscoplastic deformation of the cell wall underlies growth, which is driven by high turgor pressure. Specifically, the pressure (P) has to exceed the threshold plastic yield strain (P_c) of the cell wall—the cell growth rate is proportional to the wall strain that exceeds this threshold: $V_o \propto \frac{(P - P_c)}{E_{CW}}$. Hence, we have used Eq. (1) to derive the effective turgor pressure in *C. albicans* hyphae. Here, we used the differences in growth rates on PDMS surface and within PDMS, as well as an approximation of the external force. This latter force was calculated based on the displacement within PDMS of a 1-mm-diameter steel probe, minus the contribution from friction/adhesion and scaled to the hyphal diameter, assuming scaling with respect to the cross-sectional area and the absence of dramatic changes in geometry. From this analysis, we determined the effective turgor pressure ($\Delta P = P - P_c$) to be 1.5 and 3.1 MPa, in 100 kPa and 150 kPa PDMS, respectively. Either increasing filament diameter or decreasing extension rate results in a lower ΔP. The physical experimental model, however, does not take into account the geometry of the hyphal tip, which has a different curvature than the metal probe, which could result in an overestimation of the forces in the physical model. More precise measurements of forces relevant to hyphae will require a more accurate description of the hyphal tip size and geometry. One possibility is that, upon growth in stiffer PDMS, there is an increase in turgor pressure; our results are consistent with such a scenario as ΔP increases from 1.5 to 3.1 MPa, with an increase in PDMS stiffness from 100 to 150 kPa. This increase in turgor pressure could be responsible for the increased volume of the invasive cell compartment within 150 kPa PDMS (92 μm^3 compared to 83 μm^3 for surface growing cells, $p = 0.045$). Previous studies on cell wall expansion in *S. pombe* [35] have shown that $\frac{\Delta P}{Y} = \frac{(R^*)t}{R_1}$; where Y is the cell wall Young's modulus; R^* is the expansion ratio in width ($[R_1 - R_0]/R_0$); R_1 and R_0 are the cell radius within the PDMS and on the surface, respectively; and t is the cell wall thickness (~ 0.2 μm). Assuming Y is constant at these two PDMS stiffness conditions, $\frac{\Delta P}{Y}(35{:}1)$ is 1.7-fold greater than $\frac{\Delta P}{Y}(40{:}1)$, consistent with the observed increase in turgor pressure we derived from the growth rate difference. The slightly reduced extension rate on PDMS surface compared to that in liquid, together with the extrapolation of normalized extension rate as a function of PDMS stiffness to where $\frac{V_{(F)}}{V_o} = 1$, indicates that during growth on a surface, the hyphae experience a small resistive force, equivalent to growth within less stiff PDMS (~ 20 kPa), which we attribute to adherence/friction. It is likely that depending on the cellular surface, the contribution of adherence/friction will vary.

Cell morphology is dependent of substrate stiffness

Our results indicate that effects on cell morphology are only observed in filaments within the PDMS, suggesting that resistive forces from the PDMS lead to an alteration in morphology. Strikingly, during growth in the stiffest PDMS, we observed a progressive increase in compartment diameter, even when this compartment was more than 10 μm back from the hyphal tip. This could be due to the additional modification of the cell wall in this proximal compartment, i.e. resulting in a less stiff cell wall, an increase in turgor pressure, and/or mechanical deformation of the filament. Although we cannot rule out that the cell wall in this proximal compartment is less stiff during invasive growth, we favor the latter two possibilities, as the cell compartment volume increases and ~ 60% of invasively growing hyphae buckle in this PDMS stiffness (150 kPa). The dramatic alteration in filament morphology was not solely due to a widened tip, as it only increased slightly during invasive growth, compared to the proximal compartment that increased 25% more than the tip diameter. It is likely that these morphology changes are due to the mechanical forces from growing against a resistive substrate together with an increase in turgor pressure.

A number of fungal pathogens penetrate host tissues, including medically relevant *C. albicans* [8, 10, 12] and *A. fumigatus* [9], and plant pathogens [47, 48], including *Colletotrichum* sp. [49], *Ustilago maydis* [50], *Magnaporthe* sp. [51, 52], and *Fusarium* sp. [53]. For the latter plant pathogens, high turgor pressure is generated inside a specialized cell, called an appressorium, that generates pressures in excess of 8 MPa [51]. Blocking host cell endocytosis of the human fungal pathogens *C. albicans* [8, 15–17] and *A. fumigatus* [9] with Cytochalasin D has revealed that both of these fungi can enter epithelial tissue by active penetration. Young's moduli for mammalian host cells are in the 1–100 kPa range. Hence, the effects we observe on filament extension rate and morphology are likely to be relevant during active penetration of epithelial cells, and it is attractive to speculate that turgor pressure, in particular the osmolytes critical

for generating this force, might be a target for antifungal drugs.

Conclusions

Our results suggest that the stiffness of host cells dictates which cell type *C. albicans* can penetrate. Interestingly, even with stiffer PDMS (~ 200 kPa), we observed a small percentage of cells that were able to invade the substrate, suggesting these cells have specific properties that could be an advantage during epithelium invasion.

Methods

Strains, media, and genetic methods

Standard methods were used for *C. albicans* cell culture, molecular, and genetic manipulations as described. Derivatives of the BWP17 strain were used in this study and are listed in Table S1. Strains were grown in rich media (yeast extract peptone dextrose) at 30 °C for all experiments, and induction of filamentous growth was carried out with fetal calf serum (FCS) at 37 °C. Oligonucleotides and synthesized DNA used in this study are listed in Tables S2 and S3. pDUP5-mScarlet-Ct_{Rac1} was generated by PCR amplification of CamScarlet with a unique 5′ AscI site and a 3′ CtRac1 followed by a unique MluI site (oligonucleotides CamScarletAscIp and yemChmCtRacMluI) and cloned into pDUP5-ADH1p-CibN-Ct_{Rac1}-ACT1t [33] resulting in pDUP5-ADH1p-CamScarlet-Ct_{Rac1}-ACT1t. The nucleotide sequence for RFP mScarlet [54] was codon optimized for *C. albicans* and commercially synthesized (Genscript). mScarlet was PCR amplified with unique PstI and AscI sites (oligonucleotides GA3CamScarPstIp and CamScarletmAscI) and cloned into a pFA-GFPγ-URA3 backbone [55] resulting in pFA-CamScarlet-URA3. The RID, CRIB, and Ct_{Rac1} plasmids were linearized with StuI or NgoMIV and transformed into strains.

Micro-fabrication

Microchambers were fabricated using standard soft-lithography methods [56, 57]). Chambers were 5 μm deep and 10 μm in diameter with 15 μm spacing between them. The overall thickness of microchamber preparations was approximately 150 μm. PDMS microchambers of varying stiffness were generated by varying the ratios of polymer and cross-linker (Sylgard 184; Dow Corning). Polymer-cross-linker mixtures were spin coated (Laurell Technologies corporation) on molds (5 s 100 rpm followed by 50 s 500 rpm) to achieve ~ 150 μm thickness and then cured for 1 h at 60 °C PDMS (10:1). Thick PDMS frames were then placed on top of the partially cured chambers, which were baked for an additional 2 h at 90 °C, in order to peel the thin chambers off the mold. For viscoanalyzer measurements, 20 × 20 × 5 mm PDMS pieces were similarly cured and samples subjected to an amplitude of oscillation of 5–150 μm at 10 Hz frequency using a DMA3007000 Metravib 52 (Areva) with Dynaset20 software. Young's moduli were calculated using the following formula, $E = \frac{\sigma}{\varepsilon} = \frac{F \times h}{D \times l \times e}$; with F being the force, D the deformation amplitude, H the sample height, e the sample thickness, and l the sample length. For analysis of each PDMS preparation, measurements at 5 different deformation values (5–150 μm) were carried out, and the mean of 3 of these measurements was used for Young's modulus determination. For indentation experiments, varying ratios of polymer and cross-linker were poured into two different sized cylindrical aluminum molds, 3.5 (d) × 1.75 cm (h) and 8 (d) × 2 cm (h), and cured as described above.

Physical model of penetration

Half of the PDMS cylinders were adhered to an aluminum plate with a 5-mm-diameter hole. For the other half of the PDMS cylinders, the bottom of the mold was removed such that they were fixed around their circumference. Cylindrical PDMS pieces from both conditions were indented in their center with a hemispherical 1-mm-diameter steel probe, which was highly polished. This probe tip was machined with a slight conical shape ending in a spherical cap to approximate a hyphal filament tip and had a 2-daN force sensor (Kistler), as well as a displacement sensor (Fastar Data Instruments) attached. This probe was extended using a moving deck with a motor (Cerclet) at speeds of 1.6–3.2 μm/s. Measurements were made on average 10 samples at each PDMS ratio. From force versus displacement curves, the following forces were derived: the maximum value was the F_{crit}, the mean of the first plateau following penetration F_{invas}, and the mean of the second plateau (following the exit of the PDMS) F_{out}. Forces were then averaged and scaled to the cross-sectional area of the hyphal filament. We assumed that in the physical model of penetration and in the *C. albicans* growth experiments, the PDMS behaved as a homogenous material, and hence, scaling in terms of size was carried out with a constant critical stress. This assumption is justified, as the diameter of the filament, ~ 2 μm, is 10^3-fold greater than the PDMS mesh size, which is 2–3 nm with 40:1 PDMS. Hence, scaling of the force, as stress during rupture is constant, was achieved by dividing for the ratio of the metal probe/filament radii squared.

Microscopy sample preparation

PDMS microchambers were activated by plasma treatment (Harrick Plasma Cleaner) for 14 s at 500 mTorr on low setting submerged in DH_2O until usage. Prior to usage, PDMS samples were dried with nitrogen gas, treated with poly-D-lysine (1 mg/ml) and subsequently

treated with concanavalin A (0.4 mg/ml), each incubated for 20 min followed by drying with a stream of nitrogen gas. Exponentially growing cells were mixed with FCS media (75% FCS, 0.6 × minimal media and 2% dextrose) and spotted onto the microchambers and were sealed with a coverslip. Typically, cells on PDMS microchambers were incubated for ~ 1 h at 37 °C prior to microscopy to initiate filamentation.

Microscopy and image analysis

Cells were imaged as described [33] using either spinning disk confocal microscopy or wide-field fluorescence microscopy with a UPLANAPO 1.2 NA × 60 or Plan-Neofluar 0.75 NA × 40 objectives, respectively. Images were acquired at indicated times, with 0.4 or 0.5 μm *z*-sections (13 to 24) to capture the entire filament. For growth depth experiments, 100 × 0.2 μm *z*-sections were acquired. For the analyses of extension rate, compartment morphology, tip morphology, and cell depth images were deconvolved with the Huygens Professional software version 18.04 (Scientific-Volume Imaging) with recommended settings and a signal to noise ratio of 10, and sum projections were used. Reflection images in XZ were acquired on an upright Leica DM5500 TCS SPE laser-scanning microscope (Leica Microsystems, Mannheim, Germany) equipped with a galvanometric stage, using an APO 0.3 NA × 10 objective. Reflection images were acquired in XZ reflection mode using a 488-nm laser and an 80/20 dichroic filter. Scale bars, unless otherwise indicated, are 5 μm.

Image analysis for extension rate, compartment/tip diameter, and active Rho GTPase polarization was carried out with Fiji (version 1.51) [58]. For the determination of the extension rate, the filament lengths (mother cell neck to filament tip) were determined over time using plasma membrane fluorescence signal and values are from a curve fit of minimally 1 h acquisition ($\geq$ 12 time points). For liquid extension rates, cells induced with 50% FCS at 37 °C were fixed every 30 min and average cell lengths for each time point (0–90 min) were used. Compartment lengths were measured using the edge-to-edge fluorescence signal between two formed septa. Only invasive compartments that were entirely within the PDMS were used for analyses. Active Cdc42 and Rho1 polarization was determined using a fixed size ROI to quantitate the signal intensity at the tip and in a subapical region. The ratio of the tip to subapical signal was averaged over the time-lapse, and the mean for invasive cells was normalized to the mean ratio for non-invasive cells. The percentage of cells undergoing subapical bending within a chamber and filament buckling within PDMS was assessed using DIC images. For the determination of errors from values derived from multiple measurements, classical error propagation was carried out [59]. Statistical significance was determined with Student's *t* test.

For the representation of 3D DIC images, an algorithm was applied to image *z*-stacks using a custom-developed MATLAB program called InFocus inspired from Extended Depth of Field plugin [60]. The program extracts from any 3D multi-channel acquisition, the local contrast per channel. From these maps, it determines the *Z* of highest contrast per pixel from one or a combination of channels and then extracts a smoothened plane to get a 2D multichannel image. Parameters can be adapted through the graphical user interface. For quantitation of filament tip curvature over time, we developed another MATLAB program called TipCurve with an intuitive interface dedicated for morphological analyses along the major axis of filamentous cells. For such analyses, 3D images were converted into 2D images by sum projection, and similar to the HyphalPolarity program [33], a backbone was extracted from images over time, but also the cell contour, specifically extracting the tip first, we estimate the extremity of the backbone subtracted by the tip radius. Then, we estimate the local curvature only along the tip (either − 45° to + 45° or − 90 to 90°) from the curvilinear function f(s) extracted from cell contour:

$$C(s) = \frac{1}{R(s)} = \frac{f''(s)}{(f'(s))^2}$$

The distribution of active Cdc42 and Rho1 at the filament tip was determined by TipCurve. For these analyses, images that had a polarized fluorescent signal along with a uniform cytoplasmic signal were used. The latter was used to identify the cell and extract the backbone. Then, an additive projection on the backbone was done to get kymograph curves per time point and per fluorescence channel. To estimate the distribution of intensity at the tip of Cdc42 and Rho1, we fitted the kymograph to estimate x_{max}, the distance of maximum of intensity from the tip and the decay of intensity above x_{max} as an exponential function. Both Infocus and TipCurve can be provided as executables on demand.

Supplementary information

Supplementary information accompanies this paper at https://doi.org/10.1186/s12915-020-00833-0.

Additional file 1: Figure S1. Strain versus stress dependence of PDMS. Analyses carried out using a Viscoanalyzer, with oscillation at 10 Hz of PDMS at cross-linker ratio of 40:1. **Figure S2.** Invasive growth and penetration into adjacent chamber in PDMS of different stiffness. DIC time-lapse experiments at indicated PDMS:cross-linker ratio and measured stiffness (Young's modulus). The adjacent chamber is highlighted with a dotted yellow line and deformation of this chamber lasted ~40 min with 40:1 PDMS ratio and 80-90 min for the two stiffer PDMS substrates. **Figure S3.** The shape of filament tip is not substantially altered during invasive growth in PDMS. A) Radius of curvature over time is constant in

surface and invasively growing cells. Radius of curvature with an arc of ± 90° or ± 45° at the filament tip. B) Shape of filament tip of surface growing cells over time. Cells were grown on PDMS (30:1; 250 kPa) and 31 × 5 min GFP sum projections were analyzed. Radius of curvature with ± 45° by indicated open lines and ± 90° indicated by solid lines. **Figure S4.** Cells confined within a stiff PDMS chamber have reduced filament extension rates. A) Constricted growth within a PDMS chamber. Typical time-lapse experiment using 160 kPa PDMS, with DIC images every 5 min shown. B) Filament extension rate within a stiff chamber is not linear. Filament length was determined from images every 5 min for ~ 2 h and GFP sum projections (n = 9 cells). C) Filament extension rate is substantially reduced as chamber fills up. Initial (filament length 10-20 μm) and final (filament length > 20 μm) extension rates were determined from fits to 6 × 5 min GFP sum projections. (colors represent individual cells). Bars indicate SD and **** $p < 0.0001$. **Figure S5.** Distribution of active Cdc42 is not altered during invasive growth. A) Schematic indicating fluorescence signal over the filament long axis. Quantitation of slope of Gaussian farthest from tip in red (Max Slope, in relative units), distance maximum signal to tip (x_{max} in μm), and half width half max of the Gaussian farthest from tip in red (x_{Spread}-x_{max}), i.e. the signal spread (Spread in μm). Signal is denoted by I and distance from tip by x. B) Distribution of active Cdc42 during surface and invasive filamentous growth. Experiment described in Figure 11a and 11b with the mean signal for each cell (colors represents individual cells), normalized to the mean signal for tip Cdc42•GTP in surface growing cells. Bars indicate SD. C) Distribution of active Cdc42 is not altered upon invasive growth. Relative maximum slope (left), distance from maximum signal to the tip (middle) and spread of signal (right) determined from 6-8 cells, using tailor-made Matlab program. Bars indicate SD; surface and invasive cells were not significantly different. D) Apical and subapical active Cdc42 signals are stable over time. Relative signals from apical and subapical region of sum projections, normalized to maximum invasive subapical signal.

Additional file 2: Movie S1. Invasive growth and penetration into adjacent chamber. Cells grown with indicated stiffness PDMS and followed over time either by DIC optics or fluorescence of labeled with plasma membrane GFP.

Additional file 3: Movie S2. Invasively growing filaments have increased levels of active Cdc42 at the tip. False colored sum projections of cells expressing CRIB-GFP reporter for active Cdc42.

Additional file 4: Table S1. Strains used in the study [61, 62]. **Table S2.** Oligonucleotides used in the study. **Table S3.** Synthesized DNA used in the study.

Acknowledgements
We thank J. Konopka for reagents, Y. Izmaylov, S. Bogliolo, O. Domenge, and S. Lachambre for the assistance and N. Minc for stimulating discussion.

Authors' contributions
Conceptualization: X.N., A.S., M.B., and R.A.A. Methodology: C.P., N.K., D.T., S.S., X.N., and R.A.A. Software: S.S. Validation: X.N., A.S., and R.A.A. Formal analysis: C.P., N.K., A.S., and R.A.A. Investigation: C.P., N.K., D.T., and X.N. Data curation: S.S., A.S., and R.A.A. Writing—original draft: M.B. and R.A.A. Writing—review and editing: C.P., N.K., D.T., X.N., A.S., M.B., and R.A.A. Visualization: R.A.A. Supervision: X.N., M.B., and R.A.A. Project administration: X.N., M.B., and R.A.A. Funding acquisition: X.N., A.S., M.B., and R.A.A. All authors read and approved the final manuscript.

Funding
This work was supported by the CNRS, INSERM, Université Nice-Sophia Antipolis, Université Côte d'Azur and ANR (ANR-15-IDEX-01, ANR-11-LABX-0028-01, and ANR-16-CE13-0010-01), and EU H2020 (MSCA-ITN- 2015-675407) grants and the Platforms Resources in Imaging and Scientific Microscopy facility (PRISM) and Microscopy Imaging Côte d'Azur (MICA).

Availability of data and materials
All the data on which the conclusions of the paper are based are presented in the paper and its additional files.

Ethics approval and consent to participate
Not applicable.

Consent for publication
Not applicable.

Competing interests
The authors declare that they have no competing interests.

Author details
[1]Université Côte d'Azur, CNRS, INSERM, Institute of Biology Valrose (iBV), Parc Valrose, Nice, France. [2]Université Côte d'Azur, CNRS, Institute Physics of Nice (INPHYNI), Ave. J. Vallot, Nice, France. [3]Present Address: Manchester Fungal Infection Group, School of Biological Sciences, University of Manchester, Manchester, UK. [4]Present Address: Sorbonne University, CNRS, Developmental Biology Laboratory (LBDV), Villefranche-sur-mer, France.

Received: 8 April 2020 Accepted: 22 July 2020
Published online: 11 September 2020

References
1. Campas O, Rojas E, Dumais J, Mahadevan L. Strategies for cell shape control in tip-growing cells. Am J Bot. 2012;99(9):1577–82.
2. Campas O, Mahadevan L. Shape and dynamics of tip-growing cells. Curr Biol. 2009;19(24):2102–7.
3. Lew RR. How does a hypha grow? The biophysics of pressurized growth in fungi. Nat Rev Microbiol. 2011;9(7):509–18.
4. Mendgen K, Hahn M, Deising H. Morphogenesis and mechanisms of penetration by plant pathogenic fungi. Annu Rev Phytopathol. 1996;34:367–86.
5. Akhtar R, Sherratt MJ, Cruickshank JK, Derby B. Characterizing the elastic properties of tissues. Mater Today (Kidlington). 2011;14(3):96–105.
6. Alonso JL, Goldmann WH. Feeling the forces: atomic force microscopy in cell biology. Life Sci. 2003;72(23):2553–60.
7. Mathur AB, Collinsworth AM, Reichert WM, Kraus WE, Truskey GA. Endothelial, cardiac muscle and skeletal muscle exhibit different viscous and elastic properties as determined by atomic force microscopy. J Biomech. 2001;34(12):1545–53.
8. Dalle F, Wachtler B, L'Ollivier C, Holland G, Bannert N, Wilson D, Labruere C, Bonnin A, Hube B. Cellular interactions of *Candida albicans* with human oral epithelial cells and enterocytes. Cell Microbiol. 2010;12(2):248–71.
9. Bertuzzi M, Schrettl M, Alcazar-Fuoli L, Cairns TC, Munoz A, Walker LA, Herbst S, Safari M, Cheverton AM, Chen D, et al. The pH-responsive PacC transcription factor of *Aspergillus fumigatus* governs epithelial entry and tissue invasion during pulmonary aspergillosis. PLoS Pathog. 2014;10(10):e1004413.
10. Basmaciyan L, Bon F, Paradis T, Lapaquette P, Dalle F. *Candida Albicans* interactions with the host: crossing the intestinal epithelial barrier. Tissue Barriers. 2019;7(2):1612661.
11. Richardson JP, Ho J, Naglik JR. *Candida*-epithelial interactions. J Fungi (Basel). 2018;4(1).
12. Swidergall M, Filler SG. Oropharyngeal candidiasis: fungal invasion and epithelial cell responses. PLoS Pathog. 2017;13(1):e1006056.
13. Westman J, Hube B, Fairn GD. Integrity under stress: host membrane remodelling and damage by fungal pathogens. Cell Microbiol. 2019;21(4):e13016.
14. Wilson D, Naglik JR, Hube B. The missing link between *Candida albicans* hyphal morphogenesis and host cell damage. PLoS Pathog. 2016;12(10):e1005867.
15. Goyer M, Loiselet A, Bon F, L'Ollivier C, Laue M, Holland G, Bonnin A, Dalle F. Intestinal cell tight junctions limit invasion of *Candida albicans* through active penetration and endocytosis in the early stages of the interaction of the fungus with the intestinal barrier. PLoS One. 2016;11(3):e0149159.
16. Allert S, Forster TM, Svensson CM, Richardson JP, Pawlik T, Hebecker B, Rudolphi S, Juraschitz M, Schaller M, Blagojevic M, et al. *Candida albicans*-induced epithelial damage mediates translocation through intestinal barriers. mBio. 2018;9(3):e00915–18.
17. Wachtler B, Citiulo F, Jablonowski N, Forster S, Dalle F, Schaller M, Wilson D, Hube B. *Candida albicans*-epithelial interactions: dissecting the roles of active penetration, induced endocytosis and host factors on the infection process. PLoS One. 2012;7(5):e36952.

18. Moyes DL, Wilson D, Richardson JP, Mogavero S, Tang SX, Wernecke J, Hofs S, Gratacap RL, Robbins J, Runglall M, et al. Candidalysin is a fungal peptide toxin critical for mucosal infection. Nature. 2016;532(7597):64–8.
19. Thomson DD, Wehmeier S, Byfield FJ, Janmey PA, Caballero-Lima D, Crossley A, Brand AC. Contact-induced apical asymmetry drives the thigmotropic responses of *Candida albicans* hyphae. Cell Microbiol. 2015; 17(3):342–54.
20. Martin K, Reimann A, Fritz RD, Ryu H, Jeon NL, Pertz O. Spatio-temporal co-ordination of RhoA, Rac1 and Cdc42 activation during prototypical edge protrusion and retraction dynamics. Sci Rep. 2016;6:21901.
21. Minc N, Boudaoud A, Chang F. Mechanical forces of fission yeast growth. Curr Biol. 2009;19(13):1096–101.
22. Sevilla MJ, Odds FC. Development of *Candida albicans* hyphae in different growth media-variations in growth rates, cell dimensions and timing of morphogenetic events. J Gen Microbiol. 1986;132(11):3083–8.
23. Brown XQ, Ookawa K, Wong JY. Evaluation of polydimethylsiloxane scaffolds with physiologically-relevant elastic moduli: interplay of substrate mechanics and surface chemistry effects on vascular smooth muscle cell response. Biomaterials. 2005;26(16):3123–9.
24. Demichelis A, Pavarelli S, Mortati L, Sassi G, Sassi M. Study on the AFM force spectroscopy method for elastic modulus measurement of living cells. J Phys Conf Ser. 2013;459:012050.
25. Xie J, Zhang Q, Zhu T, Zhang Y, Liu B, Xu J, Zhao H. Substrate stiffness-regulated matrix metalloproteinase output in myocardial cells and cardiac fibroblasts: implications for myocardial fibrosis. Acta Biomater. 2014;10(6):2463–72.
26. Wang Z, Volinsky A, Gallant ND. Crosslinking effect on polydimethylsiloxane elastic modulus measured by custom-built compression instrument. J Appl Polym Sci. 2014;131(22):41050.
27. Feng L, Li S, Feng S. Preparation and characterization of silicone rubber with high modulus via tension spring-type crosslinking. RSC Adv. 2017; 7:13130–7.
28. Lorenz MC, Bender JA, Fink GR. Transcriptional response of *Candida albicans* upon internalization by macrophages. Eukaryot Cell. 2004;3(5):1076–87.
29. McKenzie CG, Koser U, Lewis LE, Bain JM, Mora-Montes HM, Barker RN, Gow NA, Erwig LP. Contribution of *Candida albicans* cell wall components to recognition by and escape from murine macrophages. Infect Immun. 2010; 78(4):1650–8.
30. Rudkin FM, Bain JM, Walls C, Lewis LE, Gow NA, Erwig LP. Altered dynamics of *Candida albicans* phagocytosis by macrophages and PMNs when both phagocyte subsets are present. mBio. 2013;4(6):e00810–3.
31. Westman J, Moran G, Mogavero S, Hube B, Grinstein S. *Candida albicans* hyphal expansion causes phagosomal membrane damage and luminal alkalinization. mBio. 2018;9(5):e01226–18.
32. Vauchelles R, Stalder D, Botton T, Arkowitz RA, Bassilana M. Rac1 dynamics in the human opportunistic fungal pathogen *Candida albicans*. PLoS One. 2010;5(10):e15400.
33. Silva PM, Puerner C, Seminara A, Bassilana M, Arkowitz RA. Secretory vesicle clustering in fungal filamentous cells does not require directional growth. Cell Rep. 2019;28(8):2231–45 e2235.
34. Desai JV, Cheng S, Ying T, Nguyen MH, Clancy CJ, Lanni F, Mitchell AP. Coordination of *Candida albicans* invasion and infection functions by phosphoglycerol phosphatase Rhr2. Pathogens. 2015;4(3):573–89.
35. Atilgan E, Magidson V, Khodjakov A, Chang F. Morphogenesis of the fission yeast cell through cell wall expansion. Curr Biol. 2015;25(16):2150–7.
36. Haupt A, Ershov D, Minc N. A positive feedback between growth and polarity provides directional persistency and flexibility to the process of tip growth. Curr Biol. 2018;28(20):3342–51 e3343.
37. Corvest V, Bogliolo S, Follette P, Arkowitz RA, Bassilana M. Spatiotemporal regulation of Rho1 and Cdc42 activity during *Candida albicans* filamentous growth. Mol Microbiol. 2013;89(4):626–48.
38. Bassilana M, Hopkins J, Arkowitz RA. Regulation of the Cdc42/Cdc24 GTPase module during *Candida albicans* hyphal growth. Eukaryot Cell. 2005;4(3): 588–603.
39. Delley PA, Hall MN. Cell wall stress depolarizes cell growth via hyperactivation of *RHO1*. J Cell Biol. 1999;147(1):163–74.
40. Philip B, Levin DE. Wsc1 and Mid2 are cell surface sensors for cell wall integrity signaling that act through Rom2, a guanine nucleotide exchange factor for Rho1. Mol Cell Biol. 2001;21(1):271–80.
41. Bridges AA, Jentzsch MS, Oakes PW, Occhipinti P, Gladfelter AS. Micron-scale plasma membrane curvature is recognized by the septin cytoskeleton. J Cell Biol. 2016;213(1):23–32.
42. Delarue M, Poterewicz G, Hoxha O, Choi J, Yoo W, Kayser J, Holt L, Hallatschek O. SCWISh network is essential for survival under mechanical pressure. Proc Natl Acad Sci U S A. 2017;114(51):13465–70.
43. Cullen PJ, Sabbagh W Jr, Graham E, Irick MM, van Olden EK, Neal C, Delrow J, Bardwell L, Sprague GF Jr. A signaling mucin at the head of the Cdc42- and MAPK-dependent filamentous growth pathway in yeast. Genes Dev. 2004;18(14):1695–708.
44. Mishra R, van Drogen F, Dechant R, Oh S, Jeon NL, Lee SS, Peter M. Protein kinase C and calcineurin cooperatively mediate cell survival under compressive mechanical stress. Proc Natl Acad Sci U S A. 2017;114(51): 13471–6.
45. Boudaoud A. Growth of walled cells: from shells to vesicles. Phys Rev Lett. 2003;91(1):018104.
46. Lockhart JA. An analysis of irreversible plant cell elongation. J Theor Biol. 1965;8(2):264–75.
47. Demoor A, Silar P, Brun S. Appressorium: the breakthrough in Dikarya. J Fungi (Basel). 2019;5(3).
48. Ryder LS, Talbot NJ. Regulation of appressorium development in pathogenic fungi. Curr Opin Plant Biol. 2015;26:8–13.
49. De Silva DD, Crous PW, Ades PK, Hyde KD, Taylor PWJ. Life styles of *Colletotrichum* species and implications for plant biosecurity. Fungal Biol Rev. 2017;31(3):155–68.
50. Matei A, Doehlemann G. Cell biology of corn smut disease-Ustilago maydis as a model for biotrophic interactions. Curr Opin Microbiol. 2016;34:60–6.
51. Howard RJ, Ferrari MA, Roach DH, Money NP. Penetration of hard substrates by a fungus employing enormous turgor pressures. Proc Natl Acad Sci U S A. 1991;88(24):11281–4.
52. Tanaka E. Appressorium-mediated penetration of *Magnaporthe oryzae* and *Colletotrichum orbiculare* into surface-cross-linked agar media. FEMS Microbiol Lett. 2015;362(10):fnv066.
53. Parry DW, Pegg GF. Surface colonization, penetration and growth of three *Fusarium* species in lucerne. Trans Br Mycol Soc. 1985;85(3):495–500.
54. Bindels DS, Haarbosch L, van Weeren L, Postma M, Wiese KE, Mastop M, Aumonier S, Gotthard G, Royant A, Hink MA, et al. mScarlet: a bright monomeric red fluorescent protein for cellular imaging. Nat Methods. 2017; 14(1):53–6.
55. Zhang C, Konopka JB. A photostable green fluorescent protein variant for analysis of protein localization in *Candida albicans*. Eukaryot Cell. 2010;9(1): 224–6.
56. Minc N. Microfabricated chambers as force sensors for probing forces of fungal growth. Methods Cell Biol. 2014;120:215–26.
57. Whitesides GM, Ostuni E, Takayama S, Jiang X, Ingber DE. Soft lithography in biology and biochemistry. Annu Rev Biomed Eng. 2001;3:335–73.
58. Schindelin J, Arganda-Carreras I, Frise E, Kaynig V, Longair M, Pietzsch T, Preibisch S, Rueden C, Saalfeld S, Schmid B, et al. Fiji: an open-source platform for biological-image analysis. Nat Methods. 2012;9(7):676–82.
59. Bevington P, Robinson DK. Data reduction and error analysis for the physical sciences. New York: University of California: McGraw-Hill Education; 2003.
60. Forster B, Van De Ville D, Berent J, Sage D, Unser M. Complex wavelets for extended depth-of-field: a new method for the fusion of multichannel microscopy images. Microsc Res Tech. 2004;65(1–2):33–42.
61. Wilson RB, Davis D, Mitchell AP. Rapid hypothesis testing with *Candida albicans* through gene disruption with short homology regions. J Bacteriol. 1999;181(6):1868–74.
62. Bassilana M, Blyth J, Arkowitz RA. Cdc24, the GDP-GTP exchange factor for Cdc42, is required for invasive hyphal growth of *Candida albicans*. Eukaryot Cell. 2003;2(1):9–18.

Publisher's Note

Additional files

Supplementary Figure S1.

Strain versus stress dependence of PDMS. Analyses carried out using a Viscoanalyzer, with oscillation at 10 Hz of PDMS at cross-linker ratio of 40:1.

Supplementary Figure S2.

Invasive growth and penetration into adjacent chamber in PDMS of different stiffness. DIC time-lapse experiments at indicated PDMS:cross-linker ratio and measured stiffness (Young's modulus). The adjacent chamber is highlighted with a dotted yellow line and deformation of this chamber lasted ~40 min with 40:1 PDMS ratio and 80-90 min for the two stiffer PDMS substrates.

Supplementary Figure S3.

The shape of filament tip is not substantially altered during invasive growth in PDMS. A) Radius of curvature over time is constant in surface and invasively growing cells. Radius of curvature with an arc of ± 90° or ± 45° at the filament tip. B) Shape of filament tip of surface growing cells over time. Cells were grown on PDMS (30:1; 250 kPa) and 31 × 5 min GFP sum projections were analyzed. Radius of curvature with ± 45° by indicated open lines and ± 90° indicated by solid lines.

Supplementary Figure S4.

Cells confined within a stiff PDMS chamber have reduced filament extension rates. A) Constricted growth within a PDMS chamber. Typical time-lapse experiment using 160 kPa PDMS, with DIC images every 5 min shown. B) Filament extension rate

within a stiff chamber is not linear. Filament length was determined from images every 5 min for ~ 2 hr and GFP sum projections (n = 9 cells). C) Filament extension rate is substantially reduced as chamber fills up. Initial (filament length 10-20 μm) and final (filament length > 20μm) extension rates were determined from fits to 6 × 5 min GFP sum projections. (colors represent individual cells). Bars indicate SD and **** $p < 0.0001$.

Supplementary Figure S5.

Distribution of active Cdc42 is not altered during invasive growth. A) Schematic indicating fluorescence signal over the filament long axis. Quantitation of slope of Gaussian farthest from tip in red (Max Slope, in relative units), distance maximum signal to tip (x_{max} in μm), and half width half max of the Gaussian farthest from tip in red (x_{Spread}-x_{max}), *i.e.* the signal spread (Spread in μm). Signal is denoted by I and distance from tip by x. B) Distribution of active Cdc42 during surface and invasive filamentous growth. Experiment described in Figure 11A and 11B with the mean signal for each cell (colors represents individual cells), normalized to the mean signal for tip Cdc42-GTP in surface growing cells. Bars indicate SD. C) Distribution of active Cdc42 is not altered upon invasive growth. Relative maximum slope (left), distance from maximum signal to the tip (middle) and spread of signal (right) determined from 6-8 cells, using tailor-made Matlab program. Bars indicate SD; surface and invasive cells were not significantly different. D) Apical and subapical active Cdc42 signals are stable over time. Relative signals from apical and subapical region of sum projections, normalized to maximum invasive subapical signal.

Movie captions

Movie S1. Invasive growth and penetration into adjacent chamber. Cells grown with indicated stiffness PDMS and followed over time either by DIC optics or fluorescence of labeled with plasma membrane GFP.

Movie S2. Invasively growing filaments have increased levels of active Cdc42 at the tip. False colored sum projections of cells expressing CRIB-GFP reporter for active Cdc42.

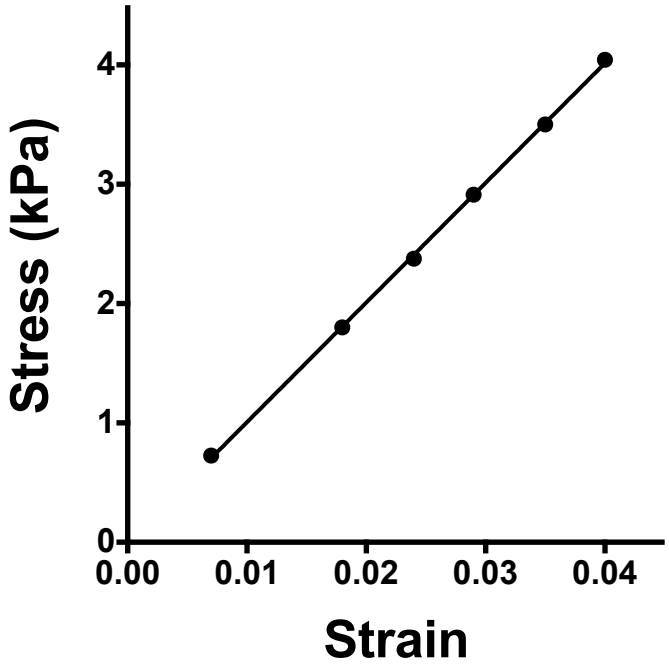

Figure S1

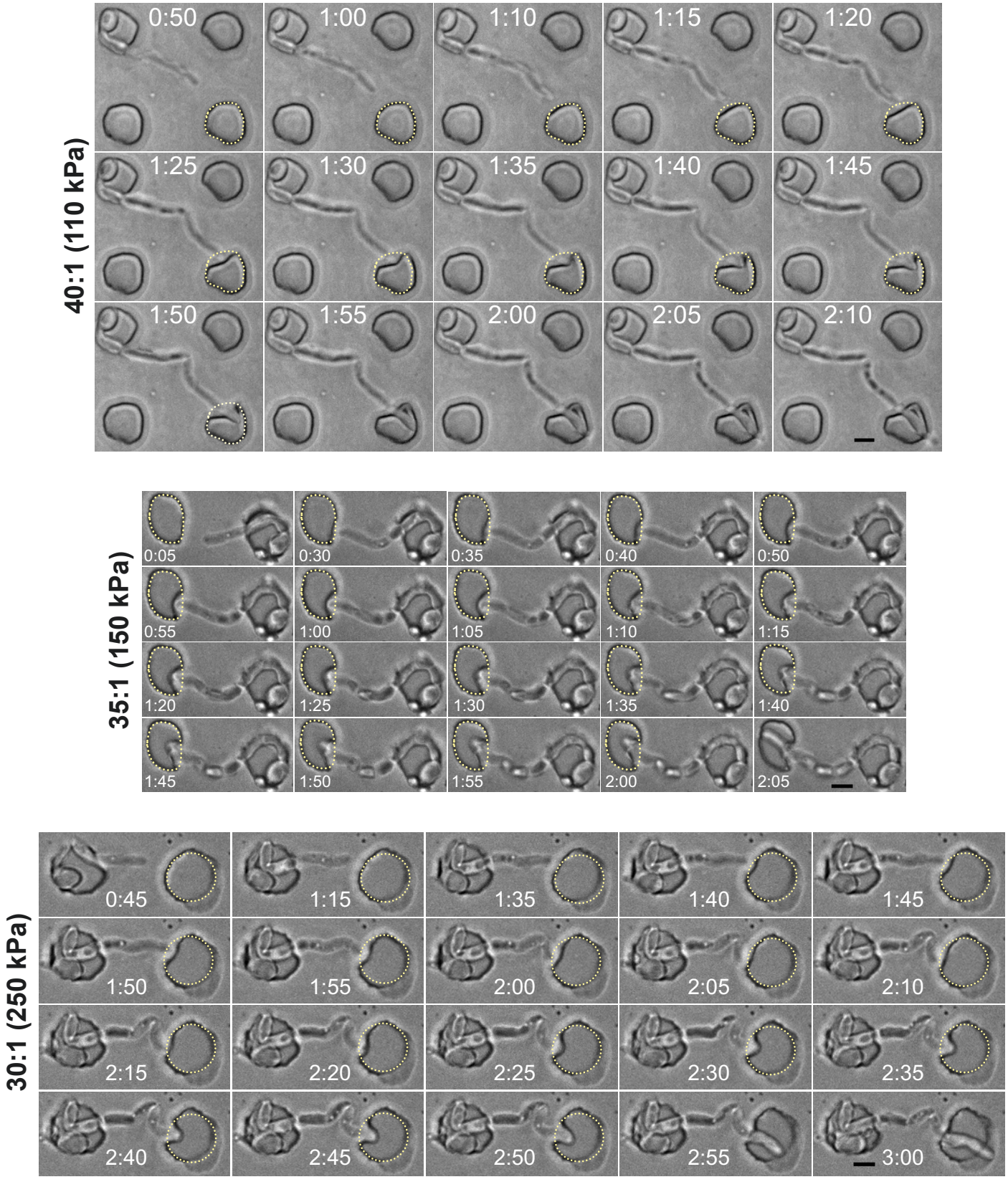
40:1 (110 kPa)
0:50
1:00
1:10
1:15
1:20
1:25
1:30
1:35
1:40
1:45
1:50
1:55
2:00
2:05
2:10
35:1 (150 kPa)
0:05
0:30
0:35
0:40
0:50
0:55
1:00
1:05
1:10
1:15
1:20
1:25
1:30
1:35
1:40
1:45
1:50
1:55
2:00
2:05
30:1 (250 kPa)
0:45
1:15
1:35
1:40
1:45
1:50
1:55
2:00
2:05
2:10
2:15
2:20
2:25
2:30
2:35
2:40
2:45
2:50
2:55
3:00

Figure S2

a

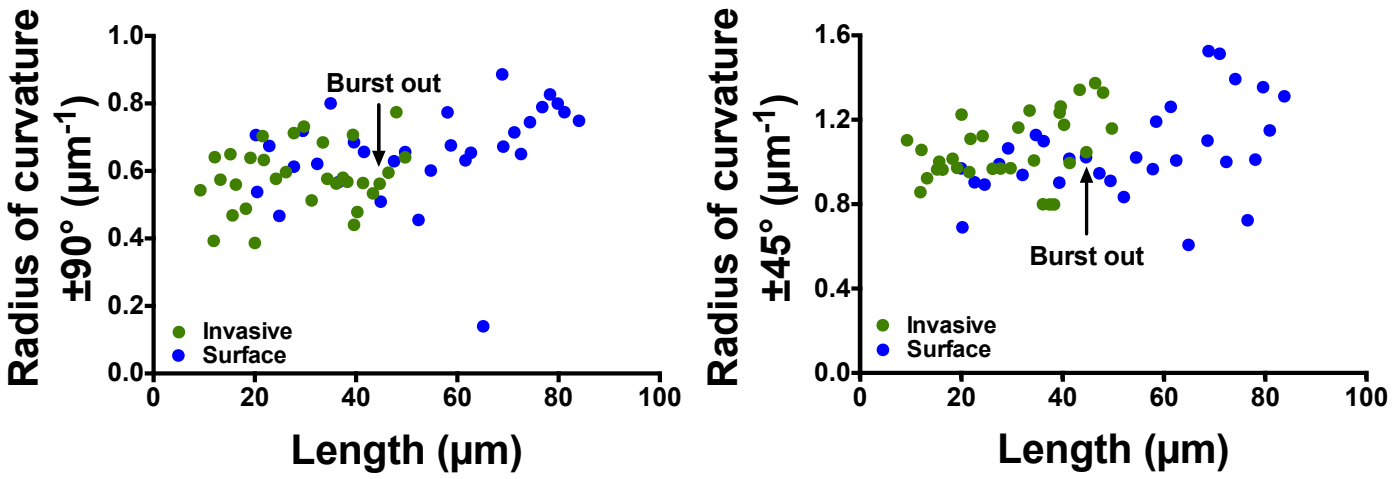
Radius of curvature
±90° (μm-1)
1.0
0.8
0.6
0.4
0.2
0.0
Burst out
Invasive
Surface
0
20
40
60
80
100
Length (μm)
Radius of curvature
±45° (μm-1)
1.6
1.2
0.8
0.4
0.0
Burst out
Invasive
Surface
0
20
40
60
80
100
Length (μm)

b

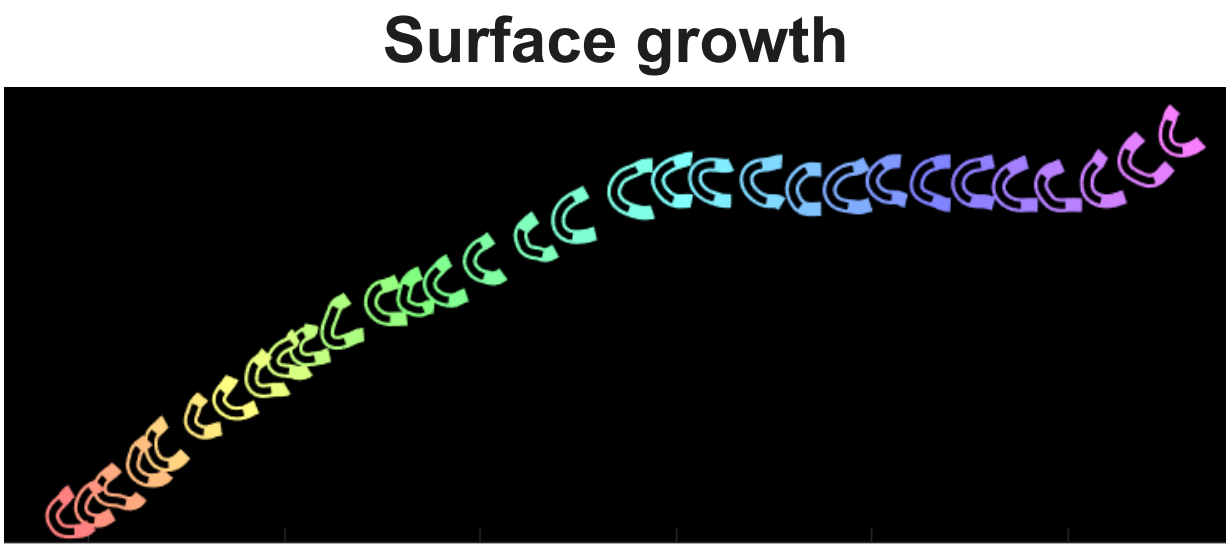
Surface growth

Figure S3

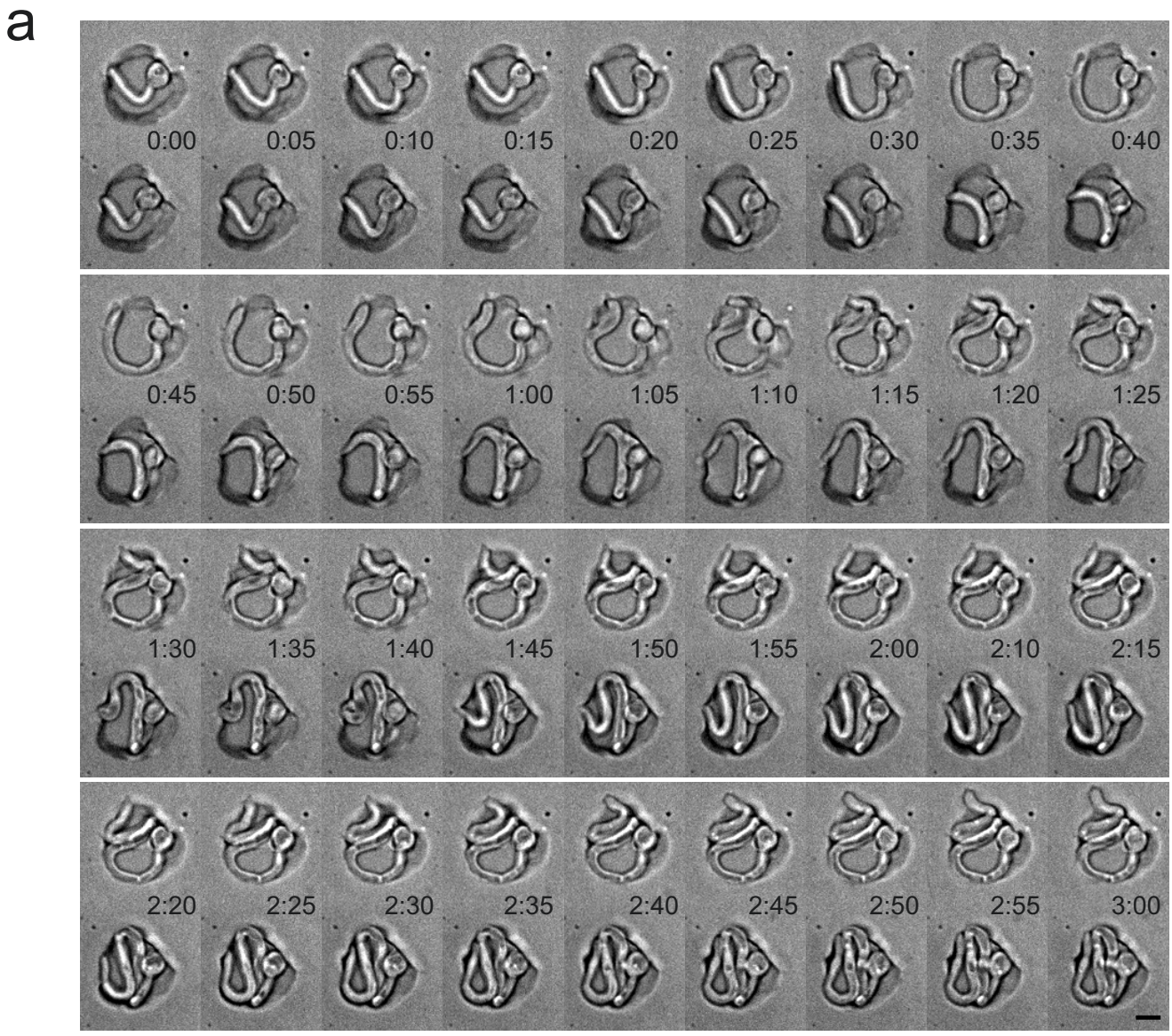
a
0:00
0:05
0:10
0:15
0:20
0:25
0:30
0:35
0:40
0:45
0:50
0:55
1:00
1:05
1:10
1:15
1:20
1:25
1:30
1:35
1:40
1:45
1:50
1:55
2:00
2:10
2:15
2:20
2:25
2:30
2:35
2:40
2:45
2:50
2:55
3:00
b
Filament length (μm)
30
25
20
15
10
0
25
50
75
100
125
Time (min)
c
Extension rate (μm/min)
0.25
0.20
0.15
0.10
0.05
0.00
****
Initial
Final
Time

Figure S4

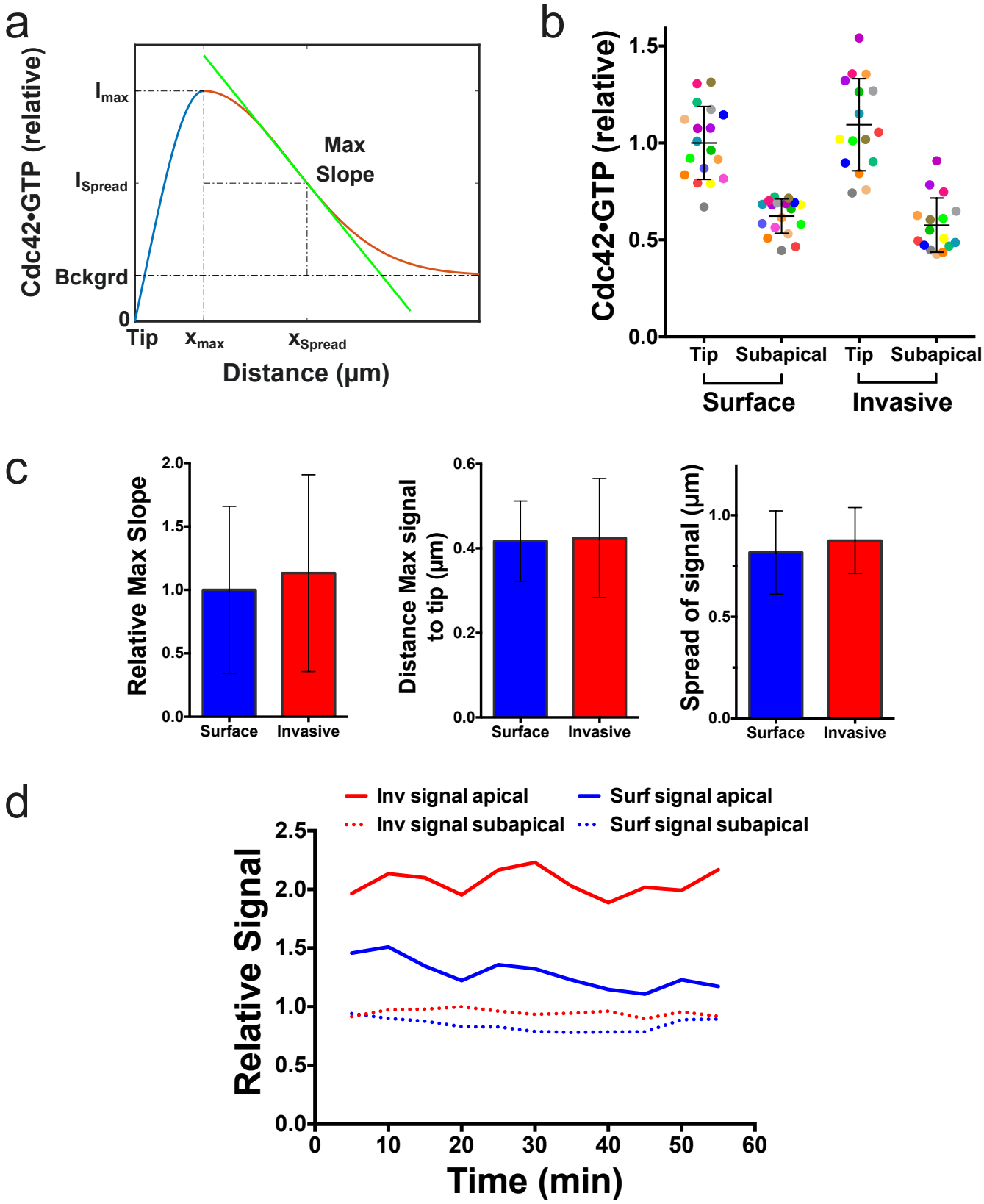
a
Cdc42•GTP (relative)
Imax
ISpread
Bckgrd
0
Tip
xmax
xSpread
Max
Slope
Distance (µm)
b
Cdc42•GTP (relative)
1.5
1.0
0.5
0.0
Tip
Subapical
Tip
Subapical
Surface
Invasive
c
Relative Max Slope
2.0
1.5
1.0
0.5
0.0
Surface
Invasive
Distance Max signal to tip (µm)
0.6
0.4
0.2
0.0
Surface
Invasive
Spread of signal (µm)
1.0
0.5
0.0
Surface
Invasive
d
Inv signal apical
Surf signal apical
Inv signal subapical
Surf signal subapical
Relative Signal
2.5
2.0
1.5
1.0
0.5
0.0
0
10
20
30
40
50
60
Time (min)

Figure S5

II – The Spitzenkörper is critical for the regulation of filament morphology and growth in the human fungal pathogen *C. albicans*

This work is in the process of being made into a manuscript to be submitted later this year. The following are the results and discussion of this work on the Spitzenkörper.

Results and Discussion

The *C. albicans* Spitzenkörper is composed entirely of secretory vesicles

The *C. albicans* Spitzenkörper was previously shown by electron microscopy to be comprised of a homogenous population of 70-nm diameter vesicles (Weiner et al., 2019); therefore, I sought to investigate if these vesicles were essentially secretory vesicles. The myosin light chain protein Mlc1 was previously established as a Spitzenkörper marker (Crampin et al., 2005), and the small Rab GTPase, Sec4, which is found on secretory vesicles (Li et al., 2007; Ortiz et al., 2002), co-localized with Mlc1 (Silva et al., 2019). Live-cell dual-camera confocal microscopy confirmed that functional mScarlet-Sec4 (mSc-Sec4) colocalized with Mlc1-GFP at the Spitzenkörper (Fig. 1A). Analyses of the shape of both the Mlc1-GFP and mSc-Sec4 signals indicated they were identical, with circularity shape factors slightly below 1 (Fig. 1B), indicating that both proteins are found at a spherical structure in the same location, *i.e.* the Spitzenkörper.

High-resolution images were then acquired using this functional mSc-Sec4 fusion as the sole Sec4 copy expressed in hyphal filaments 5-20 μm long to probe the Spitzenkörper. Images were acquired using 0.2 μm z-steps with a piezo z-step motor for rapid z-stacks acquisition. Stacks of images were analyzed in three dimensions using 5.5 standard deviations above the background to identify the Spitzenkörper by the mSc-Sec4 signal. The total intensity of the Spitzenkörper in different cells in a population showed a weak correlation with filament length (Fig. 1C). However, from the analysis of the intensity of the Spitzenkörper overtime,

obtained and averaged from time-lapse acquisitions of individual cells, it was apparent that the mSc-Sec4 intensity was constant (Fig 1D).

Using the high-resolution single time point images, signals were identified for single secretory vesicles by filtering to voxel counts of 2 to 8 voxels. This range of voxels corresponds to the area that a vesicle the size of ~70 nm would occupy. Given light resolution limits, an object this size results in an XY axis length of 200 nm. Additionally, this range corresponds to the cluster of bright objects with the S/N criteria. From this, an average mSc-Sec4 labeled secretory vesicle signal value of 3134 ± 434 (n = 38 cells with 81 ± 52 vesicles per cell) was obtained (Fig. 1E and S1).

Using the average secretory vesicle signal intensity compared to the Spitzenkörper signal intensity (mean Spitzenkörper intensity is 350380 ± 154620) (Fig. 1E), I determined the number of secretory vesicles in the Spitzenkörper to be an average 110 ± 50 vesicles (Fig. 2A). This is similar to the number of vesicles observed by electron microscopy of 58 ± 19 vesicles (Weiner et al., 2019) and indicates that the *C. albicans* Spitzenkörper is composed entirely of Sec4 labeled secretory vesicles. The average Spitzenkörper volume of 0.67 ± 0.31 μm^3 (Fig. 2B) corresponds to a radius of slightly over 0.5 μm, and average surface area of 7.58 ± 3.85 μm^2 (Fig. 2C). The shape of the Spitzenkörper in three dimensions is relatively similar within a population of cells (Fig. 2D). It is not possible to compare this 3D shape factor with the 2D shape factor from Figure 1B. The volume of the Spitzenkörper is only weakly correlated with the length of the filament (Fig. 2E). As expected, Spitzenkörper volume is strongly correlated with the number of secretory vesicles (Fig. 2F) and the linear relationship between these two, suggesting a roughly constant packing of secretory vesicles over a 4-fold range of Spitzenkörper vesicle population numbers.

To further elucidate the function of the Spitzenkörper, I attempted to perturb this structure *via* three different approaches: alter its composition, *i.e.* deletion mutants, the mis-localization of a Spitzenkörper component, and the alteration of Spitzenkörper stability.

In the absence of Mlc1 cells can still filament but are defective in substrate invasion

In an attempt to alter the Spitzenkörper composition, I generated a homozygous *mlc1* null mutant. The *mlc1*Δ/Δ mutant was viable and capable of forming filamentous cells in liquid media FCS inducing conditions (Fig 3A), albeit the filaments exhibited morphological defects (see below). This mutant had a substantially increased colony growth rate of 0.7 mm/day compared to the wild-type of 0.2 mm/day (Fig. S2). Budding *mlc1*Δ/Δ cells were often enlarged and grew as chains, suggestive of a cell separation defect. Cell size measurements showed a significant increase of budding cells (area of cells projected in two dimensions) (Fig. S3A). Shape measurements, acquired by fitting an ellipse to the shape of budding cells, revealed a 16% increase in aspect ratio and a decrease in the circular shape factor (Fig. S3B, C), revealing that there is an overall elongation of budding cells in this mutant. The qualitative morphological defects observed in *mlc1*Δ/Δ strains were restored by re-addition of the *MLC1* gene, indicating that they were due to the absence of Mlc1 activity. The heterozygote mutant (*mlc1*+/Δ) had no observable defect and, hence, was used hereafter as a control.

We previously established an invasive growth assay using polydimethylsiloxane (PDMS) microchambers in which we could vary the substrate PDMS stiffness. Here, I used growth chambers that were fabricated with a ratio of polymer to reticulating agent of 35:1, which corresponds with a Young's modulus (stiffness) of ~ 150 kPa. The *mlc1*Δ/Δ mutant exhibited little invasion (13%; comparable to the percentage of invasive filaments, or 'escapers', in stiff PDMS (Puerner et al., 2020)) compared to that of the wild-type and the complemented strain (mean invasion of 35% and 30%, respectively) (Fig. 3C). Additionally, the *mlc1*Δ/Δ mutant was completely defective for invasive growth on FCS plates after a 7-day

incubation period, whereas the complemented strain was similar to the wild-type. Thus, in the absence of Mlc1, cells were still able to undergo the yeast to filamentous growth transition in liquid media, yet were completely defective for substrate invasion. This suggests that the Spitzenkörper may play a role in the invasive ability of *C. albicans*. Since active penetration is important during the infection of the host, it will be important to further investigate how Mlc1 specifically functions in substrate invasion.

I also examined the sensitivity of this *mlc1*Δ/Δ mutant to a variety of cell wall perturbants and antifungal drugs at different concentrations (Fig. 4). The sensitivity to the antifungal drugs caspofungin, micafungin and fluconazole was investigated (Fig. 4A). The *mlc1*Δ/Δ mutant was highly sensitive to all three drugs at all concentrations tested, with the exception of minor growth at the lowest concentrations of caspofungin. This *mlc1*Δ/Δ mutant was also sensitive to the cell wall perturbants congo red and calcofluor white (Fig 4B), with decreased sensitivity at lower concentrations of both perturbants. I tested two independently generated mutants along with the respective complemented strains. In both cases the complemented strains restored growth in the presence of these antifungal drugs and cell wall perturbants to that of the wild-type. Together, these results show that Mlc1 plays a significant role in the ability of *C. albicans* to undergo invasive growth, grow in the presence of antifungal drugs, and the integrity of the cell wall of *C. albicans*, suggesting that Mlc1 or the Spitzenkörper, or both, may be a good target for enhancement of antifungal treatment and reduce the ability of *C. albicans* to actively penetrate host tissue.

Cells lacking *MLC1* are multinucleated

I next investigated how the absence of Mlc1 affects cell division by investigating the septin Cdc10 and the nucleolus marker Nop1 (Fig. 5A and 5F). I observed an increased filament length after 3 hr growth (Fig. 5C). I determined the number of Cdc10-GFP septin rings that appeared during this 3 hr period and observed a slight decrease in the number of rings per

filament (Fig. 5D), due predominantly to longer filaments. The average cell compartment length measured between 2 septin rings (Fig. 5B) is unaltered in the *mlc1*Δ/Δ mutant (Fig. 5E). I next investigated the number of nuclei in these cells using the nucleolus marker Nop1 (Fig. 5F). I quantified the number of Nop1 nucleoli in hyphae after 3 hr for the *mlc1*Δ/Δ mutant and the wild-type. There was an increase in the number of nuclei as visualized by the Nop1 signals (Fig. 5G), equivalent to an average of 2 nuclei per compartment (ranging from 1 - 4 nuclei per compartment). I also confirmed that each Nop1 signal is associated with 1 nucleus, by staining fixed cells with the DNA dye DAPI; therefore, the increase in nucleoli per cell compartment and filament reflects an increase in the number of nuclei per compartment and filament. These results suggest that the *mlc1* mutant may uncouple nuclear division from cell division.

A Spitzenkörper still forms in the absence of *MLC1*

Despite the absence of the Spitzenkörper component, Mlc1 cells still appeared to form a Spitzenkörper vesicle cluster in the filament apex, which was visualized by mSc-Sec4 (Fig 6A). Similarly, the Rab11 homolog Ypt31 was also at this location (Fig. S4). Given that a Spitzenkörper was observable, and filaments formed without substantial constrictions, it can be concluded that the *mlc1* mutant forms true hyphae.

As the Spitzenkörper was visible, I next determined if altering the composition of the Spitzenkörper had an effect on its shape or size. I used the same high-resolution imaging as described above to acquire images of *mlc1* mutant filaments with mSc-Sec4 labeling. Here, the data was analyzed in two dimensions from sum z-projections, as described in Figure 1B, to extract the overall shape, size and intensity (presumably reflecting the number of secretory vesicles) of this structure.

The mSc-Sec4 labeled Spitzenkörper was identified by signal intensity 8 standard deviations above the mean. Analysis of this structure revealed that in *mlc1*Δ/Δ cells there was nearly a two-fold increase in the intensity of the Spitzenkörper compared to the control strains

(Fig. 6B). The area and shape of the Spitzenkörper was, however, similar to that of the control strains (Fig. 6C,D). The ratio of total signal to area suggests that *mlc1*Δ/Δ cells may have a higher packing of secretory vesicles in the Spitzenkörper or increased Sec4 per vesicle (Fig 6E). There appeared to be a correlation between Spitzenkörper intensity and area for the *mlc1* mutant (Fig. 6F) similar to that in Figure 1E (note Fig. 6F uses a two-dimensional projected area while Fig. 1E uses a three-dimensional volume). Additionally, no correlation was observed between the Spitzenkörper intensity with the filament diameter (Fig. 6G). Furthermore, preliminary results reveal the *mlc1*Δ/Δ mutant has a decreased endocytic collar mean intensity, as observed by the actin binding protein Abp1 (Fig. S5). Together, these analyses indicate that in the absence of Mlc1 a Spitzenkörper forms with increased levels of the Rab GTPase Sec4.

Using the values of secretory vesicle intensities from Figure 1E, I estimated the number of secretory vesicles from mSc-Sec4 intensities in these strains, assuming a constant amount of Sec4 per vesicle. I determined a conversion factor using the combined average intensity of the Spitzenkörpers in the control strains (both *mlc1*+/Δ and *mlc1*Δ/Δ+*MLC1*) compared to the average intensity of the Spitzenkörpers in Figure 1E, which was 2.4. I then estimated the number of secretory vesicles in the *mlc1*Δ/Δ mutant, which has an average of 200 ± 140 vesicles, or roughly twice the number compared to wild-type control strains. This will need to be confirmed by electron microscopy.

The *mlc1*Δ/Δ mutant is larger and grows faster

Qualitatively *mlc1*Δ/Δ hyphal filaments appeared larger when compared to the wild-type (Fig. 3A). Hence, I quantified the diameter and length of these filamentous cells using time-lapse imaging. The mean filament diameter for *MLC1*+/Δ was 2.3 ± 0.1 (Fig. S6A), while *mlc1*Δ/Δ mutant had a significantly increased diameter that was restored upon re-addition of *MLC1* (Fig 7A). The mean diameter of *MLC*+/Δ and complemented strains was comparable to

that of the wild-type (Puerner *et al.*, 2020). Interestingly, I also observed a significant increase in the variability of filament diameters in the *mlc1*Δ/Δ mutant.

Length over time measurements were used to determine filament extension rates (Fig. 6B). The null mutant, the heterozygote, and the recovery strain all had constant extension rates; therefore, the slope of the filament length versus time plots was used. The mean extension rate for *MLC1*+/Δ was 0.37 ± 0.06 μm/min, similar to that previously reported (BMC Biol) (Fig. S6B), which was used to normalize the values (Fig 7B). No difference was observed in the mean filament extension rates for these three mutants; however, as observed with filament diameter, the extension rates of the *mlc1*Δ/Δ cells had a significant increase in variation.

Using these length and diameter measurements, the volume was calculated at each time point. From this, I determined a rate of volume increase from a linear fit of volume calculation over time, which is also the cell growth rate. The growth rates were significantly increased in *mlc1*Δ/Δ (Fig. 7C). Additionally, the *mlc1*Δ/Δ mutant growth rate was much more variable from cell to cell, as expected from the cell diameter and extension rates. It is important to note that the growth rate at the single cell level was constant since the length versus time plots were all linear and the filament diameter over time was essentially constant (Fig. S7), indicating that this was variation between cells in a population.

By sorting rates of filament extension and volume increase by filament diameters, and color coding the data with a color gradient, it was evident that filaments with increased diameters exhibited in general higher extension and volume increase rates (Fig. 7A-C), suggesting a positive correlation with diameter. Indeed, plotting the extension rate as a function of diameter revealed a significant positive correlation in the *mlc1*Δ/Δ (Fig. 7D). As expected, the heterozygote and recovery strain were indistinguishable from one another in Fig. 7C but interestingly fell on the linear fit of the *mlc1*Δ/Δ data (Fig 7E).

The diameter and extension rate were also analyzed for a mutant lacking the Spitzenkörper localized formin Bni1. The *bni1*Δ/Δ mutant had a similar increased diameter as the *mlc1*Δ/Δ mutant; however, the mean extension rate was significantly less than both *mlc1*Δ/Δ and the wild-type (Fig. S8A-C). The extension rate and diameter for *bni1*Δ/Δ were also correlated, and a best fit line had a similar slope to that of *mlc1*Δ/Δ, yet the y-intercept was reduced (Fig. S8F-G). These data suggest that there is a link between filament diameter, *i.e.* region of insertion of new membrane material, and extension rate, *i.e.* number of secretory vesicles fusing with the plasma membrane.

These morphological changes suggest that the composition of the Spitzenkörper, specifically the presence of Mlc1, is critical for cell shape regulation. An attractive possibility is that the region in which vesicles fuse with the plasma membrane is dependent on this secretory vesicle cluster–the Spitzenkörper. Specifically, if the Spitzenkörper is altered, the region in which new material is inserted in the plasma membrane may broaden together with a concomitant increase in vesicle flux, which could also result in increased morphological variation. One could imagine that in the absence of Mlc1, directed vesicle traffic from the Spitzenkörper to the adjacent plasma membrane might be altered, with secretory vesicles arriving at the cell cortex by a diffusive mechanism. However, I would expect if this were the case, variable growth rates and diameters at the single cell level might be evident.

It is striking that there is little variation in these growth parameters at the individual cell level. During the hyphal transition, a filament diameter appears to be set and maintained throughout the extension process. This suggests that Mlc1 plays a role in setting up the area and location of vesicles and vesicle fusion, which dictates subsequent filament diameter that varies from cell to cell. In the absence of Mlc1, this process would be less regulated and, hence, stochastic variation between cells might be more evident.

As mlc1Δ/Δ mutant cells were also larger during budding growth, and there was more size variability, we tested the hypothesis that the filament diameter is related to the initial cell size by examining if there was a correlation between the area of the blastospore and the filament diameter. The area of each blastospore was measured and compared to its filament diameter. Figure 7F shows there is a good correlation between the area and filament diameter measurements for each cell, indicating that Mlc1 affects the polarity site (presumably the region of new membrane insertion) in both budding and filamentous C. albicans cells.

Perturbation of the Spitzenkörper using synthetic physical interactions

The distribution and stability of Mlc1 was altered by fusion with a GFP nanobody (GNB) to the endogenous Mlc1 together with the far-red fluorescent protein miRFP670 (miR) for visualization. This GFP nanobody is a nanobody protein that is endogenously expressed as a tag and has a strong affinity for the GFP auto fluorescent protein (Rothbauer et al., 2006). From this *MLC1*-miR-GNB strain, I generated two GFP tagged strains, one expressing GFP-Sec4 (SPK-stabilized) and the other expressing plasma membrane targeted GFP (PM-targeted), *i.e.* GFP-Ct_{Rac1} that localizes uniformly to the plasma membrane (Vauchelles et al., 2010). In both cases, cells were viable and formed hyphae in FCS inducing conditions (Fig. 8A). In the PM-targeted strain, GFP-Ct_{Rac1} was observed at the plasma membrane with a substantial accumulation that colocalized with Mlc1-miR-GNB at the filament tip, which appeared to be more spread out (Fig 8A left). In the SPK-stabilized strain, both GFP-Sec4 and Mlc1-miR-GNB localized to the Spitzenkörper, as would be expected; however, the intensity of GFP-Sec4, as well as Mlc1-miR-GNB, at the apex appeared to be increased (Fig. 8A center). Qualitative observations of the Spitzenkörper in these GNB strains compared to the wild-type revealed differences in its morphology. Schematics showing the GNB interactions and resulting Spitzenkörper disruptions are shown in figure 8B.

To investigate if the Spitzenkörper in the strain expressing both GFP-Sec4 and Mlc1-miR-GNB (SPK-stabilized) was more stabilized, I carried out fluorescence recovery after photobleaching (FRAP) experiments. Photobleaching was carried out on the Spitzenkörper in live hyphae. The curves for fluorescence recovery revealed that the $t_{½}$ for recovery was similar (6.7 ± 2.3 compared to 6.9 ± 3.6 sec) between the strains; however, there was a reduction in the level of signal recovery (Fig. 8C), *i.e.* the immobile fraction - the pool that does not undergo exchange. These analyses revealed that forced binding of Mlc1 and Sec4 resulted in a substantial increase in the immobile fraction from 0.36 ± 0.11 to 0.59 ± 0.11 (Fig. 8E). To rule out that this was due a difference in the amount of cellular GFP-Sec4 that was photobleached, I examined the fraction of the total cell signal that was bleached. Figure 8E shows that the fraction of fluorescence that was bleached was similar in the two strains. This result confirms that there is a significant decrease in the Sec4 mobility in the SPK-stabilized strain. FRAP experiments carried out with the *mlc1* deletion mutant and control strains did not reveal a significant difference in the immobile fraction or the recovery rates ($t_{1/2}$), indicating that even in the absence of Mlc1, Sec4 dynamics at the Spitzenkörper are similar (Fig. S9).

Spitzenkorper morphology and composition is altered upon mis-localization and stabilization

I also analyzed the intensity, shape and area of the Spitzenkörper in these altered Spitzenkörper strains using Sec4 intensity. The analysis was carried out as described above, and the Spitzenkörper was identified by 25 standard deviations above the mean for GFP-Sec4 and 8 Standard deviations for mSc-Sec4. The SPK-stabilized strain had a significant increase in Sec4 Spitzenkörper intensity, while the PM-targeted strain was similar to the wild-type control (Fig 9A). This is consistent with an increase in the immobile fraction in this strain from the FRAP experiments (Fig. 8D). In contrast, the size of the Sec4 Spitzenkörper of the PM-targeted strain was significantly increased, whereas the SPK-stabilized strain was comparable

to the wild-type control strain (Fig 9B), consistent with a more spread out cluster of vesicles. Analysis of the two-dimensional shape revealed that the SPK-stabilized strain had a Spitzenkörper shape similar to the wild-type, while the PM-targeted strain exhibited a slight, yet significant, decrease in the 2D shape factor, *i.e.* was less circular (Fig. 9C), consistent with a more spread out vesicle cluster. The SPK-stabilized strain had a significant increase in the signal to area ratio (Fig. 9D), consistent with the notion of the tighter packing of vesicles in strain (or higher levels of Sec4 on secretory vesicles). Together, these results indicate altering the distribution and stability of the Spitzenkörper alters its morphology and composition. Given that the SPK-stabilized strain has a nearly two-fold increase in intensity, it is likely that the number of secretory vesicles in the Spitzenkörper of this strain would increase by nearly two-fold as well, similar to the *mlc1* deletion mutant. Electron microscopy visualization and quantification of vesicles would be needed to confirm this.

Perturbation of the Spitzenkörper alters filament morphology and growth

The morphology of the PM-targeted and SPK-stabilized cells was analyzed similarly to the *mlc1* mutant strains described above. Both the PM-targeted and SPK-stabilized strains had a significant increase in filament diameter, with the former having the greatest increase. The average diameter for the wild-type strain was 2.2 ± 0.2 μm (Fig. S10A) and was used to normalize the diameters of these altered Spitzenkörper strains (Fig. 10A). Filament extension rates were normalized to that of the wild-type (0.35 ± 0.07 μm/min, Fig. S10B), and a significant increase in extension rate was also observed with the PM-targeted strain (Fig. 10B).

As expected, rate of volume increase was significantly increased for both altered Spitzenkörper strains, with the PM-targeted strain having the largest increase (Fig. 10C). As can be seen in the color-coded gradient by filament diameter, cells with largest diameters appear to extend the fastest, similar to what was observed with the *mlc1*Δ/Δ mutant. Indeed, there was a strong correlation between the filament and the extension rates of these altered

Spitzenkörper strains (Fig. 10D), providing further evidence of the link between morphology and extension. The linear fits for these two altered Spitzenkörper strains, *i.e.* PM-targeted strain and SPK-stabilized, were within error of the values for the wild-type (Fig. 10E). Interestingly, variation in filament extension rates in the *mlc1*Δ/Δ mutant and PM-targeted and SPK-stabilized strains were comparable, however the variation in filament diameter is lower in the latter two strains compared to the deletion mutant. This could be due to the fact that these altered Spitzenkörper strains still have a wild-type copy of *MLC1*.

With respect to the PM-targeted strain, we speculate that the increase in filament diameter is due to the targeting of the secretory vesicles to the apical PM, which may spread out the Spitzenkörper vesicle cluster, resulting in vesicle fusion over a wider region than in a wild-type filament. Taken all together, my results show that the Spitzenkörper plays a central role in regulating the growth and morphology of the *C. albicans* hyphae. Perturbing the Spitzenkörper by three different approaches results in an increase in the variation of Spitzenkörper morphology as well as cellular morphologies and growth rates across cells.

Figure 1

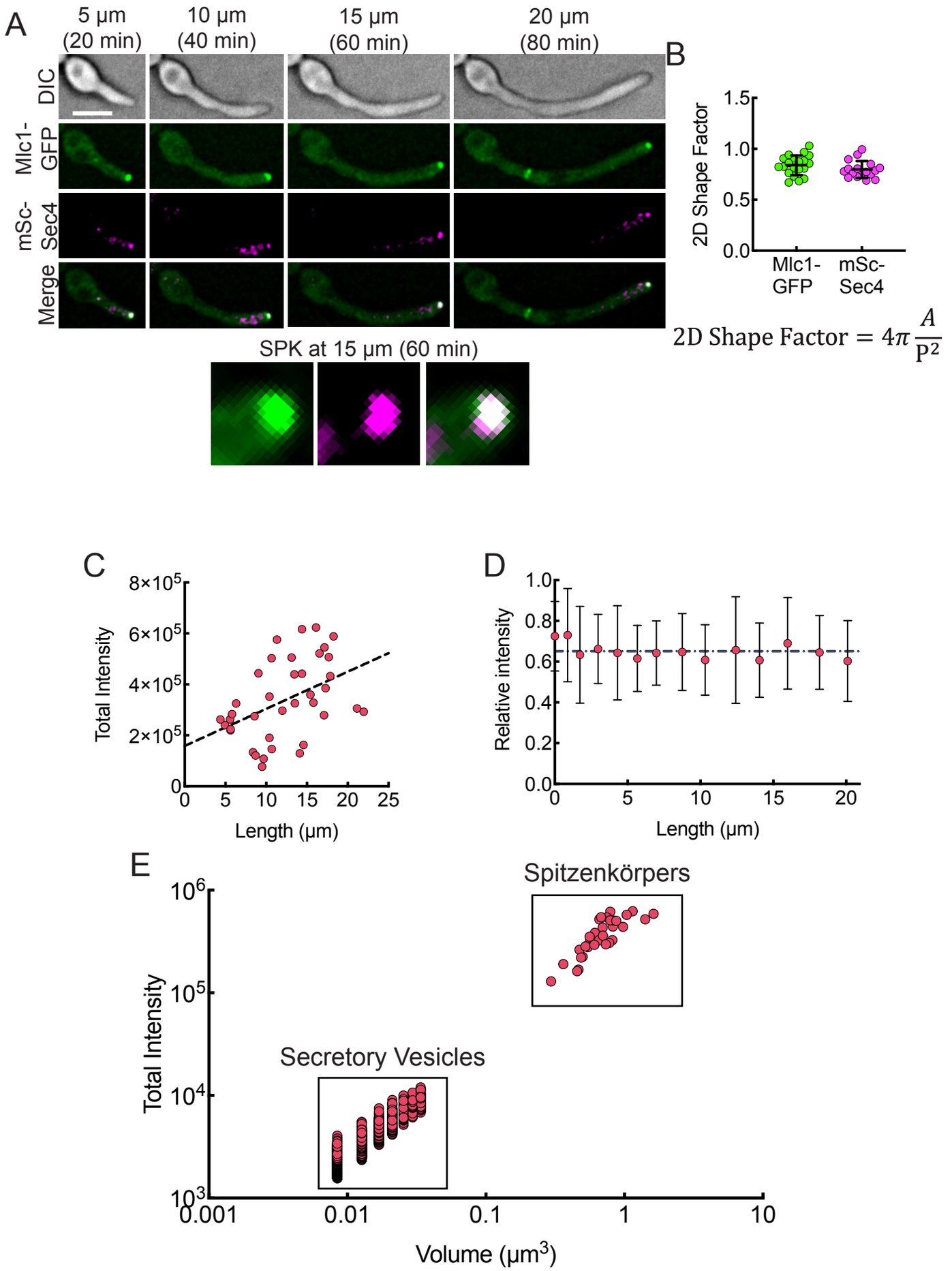
A
5 µm (20 min)
10 µm (40 min)
15 µm (60 min)
20 µm (80 min)
DIC
Mlc1-GFP
mSc-Sec4
Merge
SPK at 15 µm (60 min)
B
2D Shape Factor
1.5
1.0
0.5
0.0
Mlc1-GFP
mSc-Sec4
2D Shape Factor = 4π A/P²
C
Total Intensity
8×10⁵
6×10⁵
4×10⁵
2×10⁵
0
0 5 10 15 20 25
Length (µm)
D
Relative intensity
1.0
0.8
0.6
0.4
0.2
0.0
0 5 10 15 20
Length (µm)
E
Total Intensity
10⁶
10⁵
10⁴
10³
0.001 0.01 0.1 1 10
Volume (µm³)
Spitzenkörpers
Secretory Vesicles

Figure 1: **The Spitzenkörper (Spitzenkörper) is stable over time with a constant shape and size.** A) Mlc1 and Sec4 colocalize to the Spitzenkörper over time. Images shown are at approximate filament lengths with times indicated from germ tube emergence. Below are 35x enlarged region of the Spitzenkörper for 15 μm cell to highlight shape. Cells were imaged using live-cell dual-camera microscopy. Images were taken every 5 min for 110 min using z-sections of 13 x 0.5 μm. Scale bar is 5 μm. B) The shape of the Spitzenkörper by Mlc1-GFP and mSc-Sec4 is equivalent. The Spitzenkörper structure was identified by signal intensity using standard deviations above the mean (3 SDs for mSc-Sec4 and 13 SDs for Mlc1-GFP). The shape of sum projections of 13 x 0.5 μm z-sections was analyzed using the 2D circularity shape factor equation with the perimeter and area of the Spitzenkörper determined for both signals. Each point represents a time point from the cell to the left. C) Spitzenkörper intensity is loosely correlated with filament length. Spitzenkörpers from filaments imaged at single time points were identified by standard deviations above the mean (n = 38). Acquisitions were carried out with 26 x 0.2 μm z-sections and images were analyzed in 3D for total intensity associated with this structure. The r^2 was 0.20 with a slightly significant correlation p = 0.0053. D) The Sec4 labeled Spitzenkörper intensity is constant over time. Spitzenkörper signal intensity was measured from sum projections (13 x 0.5 μm z-sections) over a 110 min time-course using mSc-Sec4. The intensity over time for each cell, in each time course, was normalized to 1, and points represent the mean of 13 cells and bars are standard deviation. Dashed line represents the average relative intensity over the entire time course. E) Individual secretory vesicles can be detected. Secretory vesicle and Spitzenkörper signals were identified by standard deviations of 5.5 above the mean. A mean of 81 ± 52 secretory vesicles were identified per cell (n = 38). Criteria for secretory vesicles and Spitzenkörpers was based on the smallest (2-8 voxels) and the largest objects (more than 80 voxels), respectively. Log scale of Y-axis is to show both the secretory vesicles and Spitzenkörpers.

Figure 2

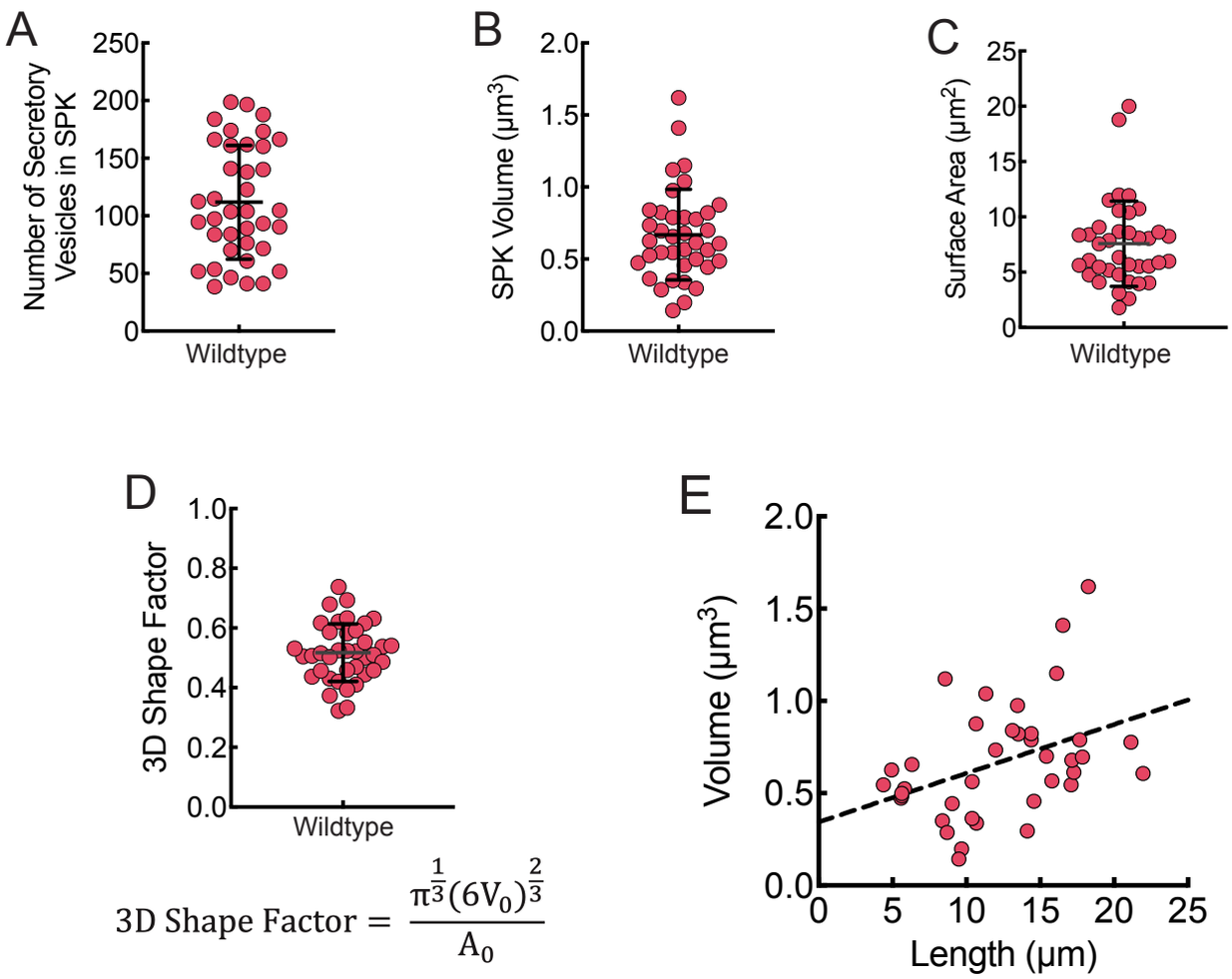
A
Number of Secretory Vesicles in SPK
250
200
150
100
50
0
Wildtype
B
SPK Volume (μm3)
2.0
1.5
1.0
0.5
0.0
Wildtype
C
Surface Area (μm2)
25
20
15
10
5
0
Wildtype
D
3D Shape Factor
1.0
0.8
0.6
0.4
0.2
0.0
Wildtype
3D Shape Factor = π^(1/3)(6V0)^(2/3) / A0
E
Volume (μm3)
2.0
1.5
1.0
0.5
0.0
0 5 10 15 20 25
Length (μm)
F
Volume of SPK (μm3)
2.0
1.5
1.0
0.5
0.0
0 50 100 150 200 250
Number of Secretory Vesicles

Figure 2: **The Spitzenkörper is comprised entirely of secretory vesicles, the number of which varies from cell to cell**. A) The Spitzenkörper is comprised of an average of 100 secretory vesicles. The intensity values of Spitzenkörpers and secretory vesicles were identified from 3D image stacks (26 x 0.2 μm z-sections) of filaments expressing mSc-Sec4 as the sole copy of Sec4. Filaments analyzed had a mean length of 12.3 ± 4.8 μm. Intensities were identified using 5.5 standard deviations above the mean. The mean signals for secretory vesicles were background subtracted (signal outside the cell) resulting in a mean corrected intensity of 3134 ± 434 for secretory vesicles. This mean background subtracted signal intensity of single vesicles (Fig. 1E) was used to calculate the number of secretory vesicles in each Spitzenkörper, cells from Fig. 1C. The mean number of secretory vesicles is 112 ± 49 with a mean volume (B) of 0.67 ± 0.31 μm^3 and a mean surface area (C) of 7.58 ± 3.85 μm^2. D) The Spitzenkörper has an elliptical shape in 3D. The average 3D shape factor of identified Spitzenkörpers was 0.52 ± 0.1 (a perfect sphere has a 3D shape factor of 1) with more elongated objects deviating from this value. E) Spitzenkörper volume is loosely correlated with filament length. Lengths measured from sum projections of the mSc-Sec4 channel. Correlation has a r^2 of 0.16 with a $p = 0.0135$. F) An increased number of secretory vesicles in the Spitzenkörper correlates with an increased volume. The correlation has an r^2 of 0.53 with a significant $p < 0.0001$.

Figure 3

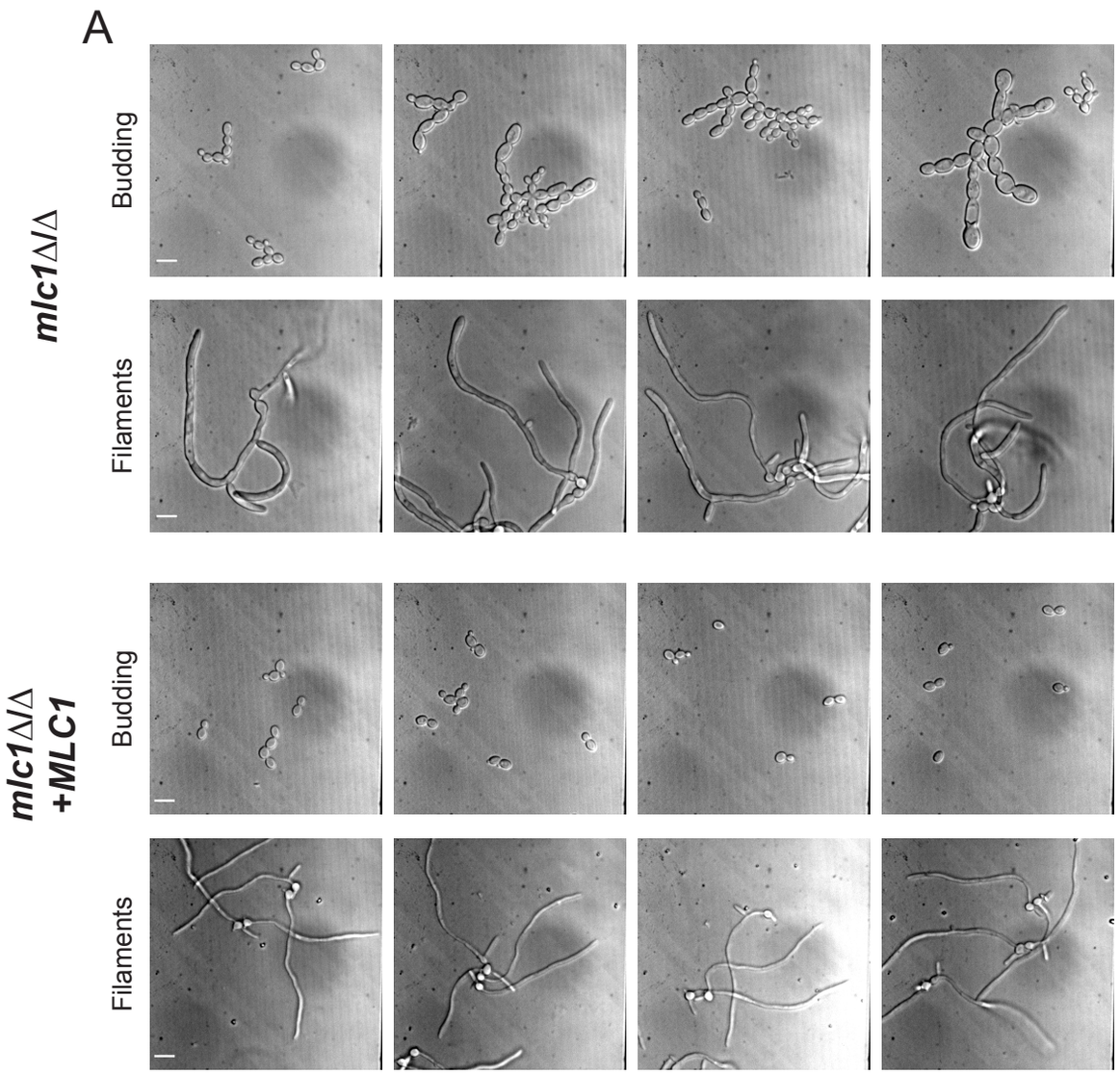
A
mlc1Δ/Δ
Budding
Filaments
mlc1Δ/Δ
+MLC1
Budding
Filaments

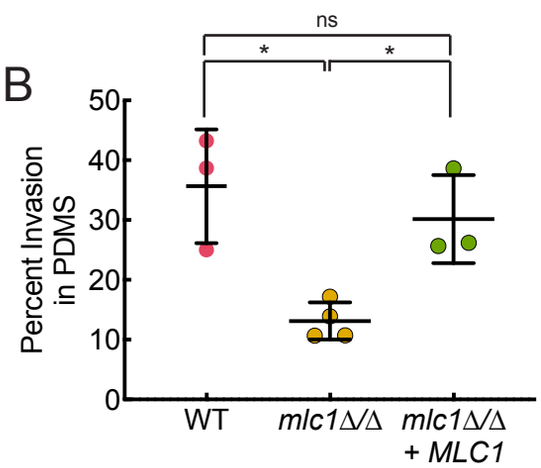
B
ns
*
*
Percent Invasion in PDMS
50
40
30
20
10
0
WT
mlc1Δ/Δ
mlc1Δ/Δ
+ MLC1

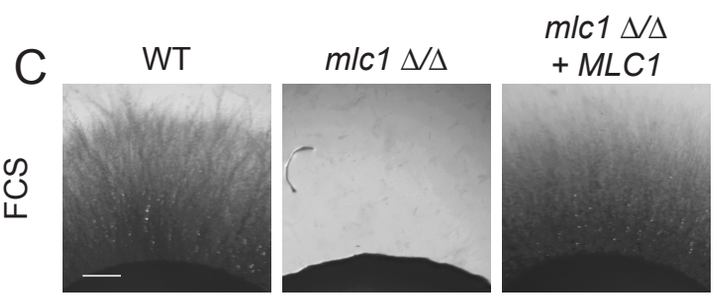
C
WT
mlc1 Δ/Δ
mlc1 Δ/Δ
+ MLC1
FCS

Figure 3: **An *mlc1* deletion mutant is viable, can form filaments in liquid media, but is defective for invasive growth**. A) Representative DIC images of *mlc1*Δ/Δ and *mlc1*Δ/Δ + *MLC1*. Scale bar is 10 μm. B) Percent invasion in 35:1 PDMS microchambers (Youngs modulus of ~ 150 kPa). Each point is the mean of an experiment, n = 30-100 cells per experiment. Standard deviations are shown and *$p<0.05$ and ns $p>0.05$. C) Invasive growth in rich serum media containing agar. Indicated strains were spotted on YEPD+FCS agar plates and incubated at 30°C for 7 days. Scale bar is 0.5 mm.

Figure 4

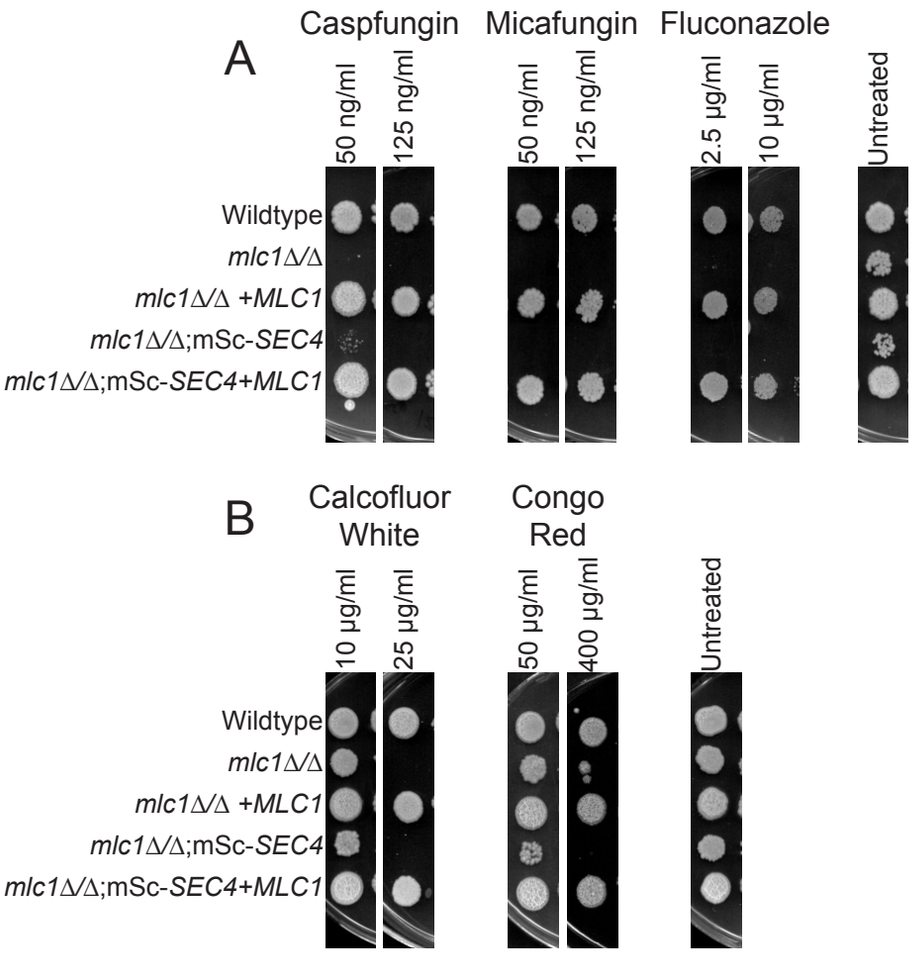
A
Caspfungin
Micafungin
Fluconazole
50 ng/ml
125 ng/ml
50 ng/ml
125 ng/ml
2.5 µg/ml
10 µg/ml
Untreated
Wildtype
mlc1Δ/Δ
mlc1Δ/Δ +MLC1
mlc1Δ/Δ;mSc-SEC4
mlc1Δ/Δ;mSc-SEC4+MLC1
B
Calcofluor White
Congo Red
10 µg/ml
25 µg/ml
50 µg/ml
400 µg/ml
Untreated
Wildtype
mlc1Δ/Δ
mlc1Δ/Δ +MLC1
mlc1Δ/Δ;mSc-SEC4
mlc1Δ/Δ;mSc-SEC4+MLC1

Figure 4: **The *mlc*1 deletion mutant is sensitive to antifungal drugs and cell wall perturbants**. The *mlc*1Δ/Δ mutant was tested for sensitivity to antifungal drugs (A) and cell wall perturbants (B) at indicated concentrations. Shown are the 1:10 dilutions of 0.1 OD_{600}. Images were acquired after an incubation period of 4 days.

Figure 5

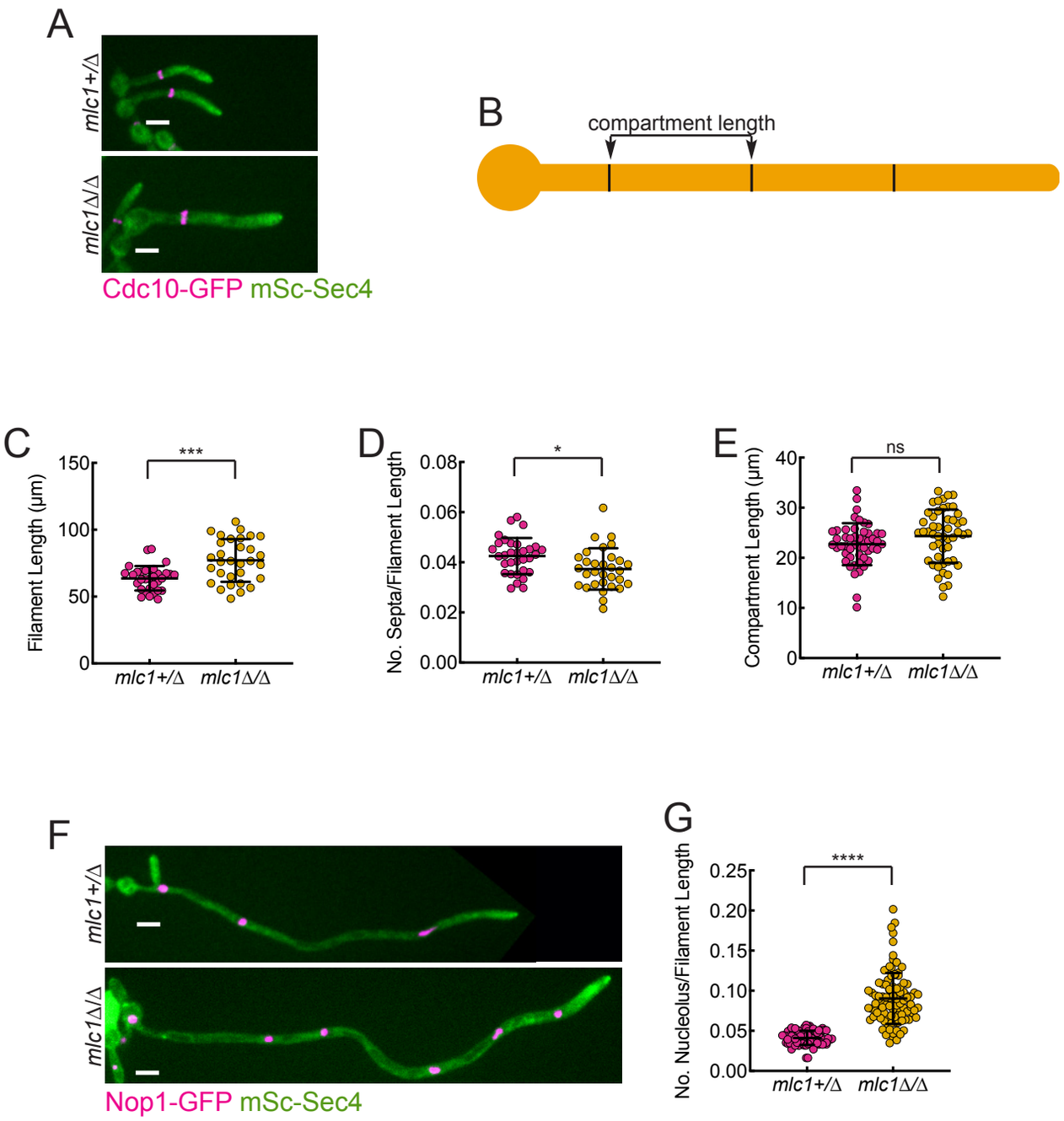
A
mlc1+/Δ
mlc1Δ/Δ
Cdc10-GFP mScSec4
B
compartment length
C
Filament Length (μm)
150
100
50
0
***
mlc1+/Δ
mlc1Δ/Δ
D
No. Septa/Filament Length
0.08
0.06
0.04
0.02
0.00
*
mlc1+/Δ
mlc1Δ/Δ
E
Compartment Length (μm)
40
30
20
10
0
ns
mlc1+/Δ
mlc1Δ/Δ
F
mlc1+/Δ
mlc1Δ/Δ
Nop1-GFP mScSec4
G
No. Nucleolus/Filament Length
0.25
0.20
0.15
0.10
0.05
0.00
****
mlc1+/Δ
mlc1Δ/Δ

Figure 5: **The *mlc1* deletion mutant has an increased number of nuclei per filament.** A) Representative images of *mlc1*+/Δ and *mlc1*Δ/Δ expressing mSc-Sec4 and Cdc10-GFP. Cells were induced on FCS+agarose pads. Images were taken every 10 min for 180 min using 26 x 0.4 µm z-stacks and sum projection is shown and bar is x µm. B) Schematic of filament cell compartments. C) The *mlc1*Δ/Δ mutant filaments are longer than the wild-type. Filament lengths were measured at the end of 180 min time-lapses D) The *mlc1*Δ/Δ mutant has a decreased number of septa per filament. The total number of septin rings which formed during the 180 min time-lapse was determined and divided by final filament length. E) Lengths of filament cell compartments are similar between *mlc1*Δ/Δ and wild-type. Compartment lengths were measured throughout the time-lapse, when two septin rings were simultaneously visible. F) Representative sum projection of *mlc1*+/Δ and *mlc1*Δ/Δ expressing mSc-Sec4 and Nop1-GFP. Cells were induced and imaged as in A) and bar is x µm. G) The *mlc1*Δ/Δ mutant has an increased number of nuclei per filament. Cell lengths were measured using mSc-Sec4 signal, and the number of Nop1-GFP nucleoli was determined and divided by the respective filament length. Each Nop1-GFP signal (nucleoleus) coincides with one nucleus, confirmed by co-labeling with DAPI. Standard deviations are indicated and ***$p < 0.001$, ****$p < 0.0001$, ns $p > 0.05$.

Figure 6

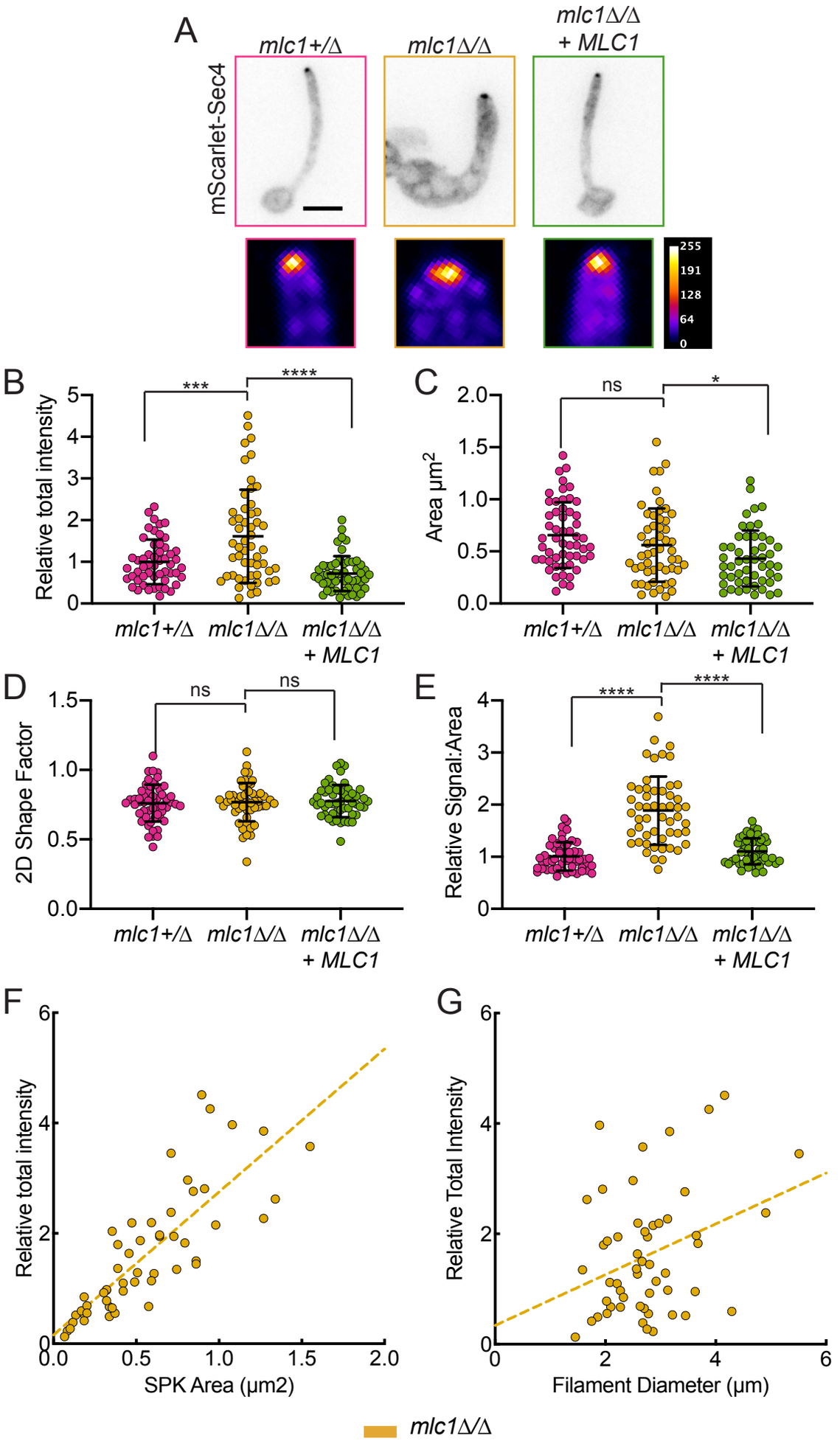
A
mlc1+/Δ
mlc1Δ/Δ
mlc1Δ/Δ + MLC1
mScarlet-Sec4
255
191
128
64
0
B
Relative total intensity
***
****
C
Area µm2
ns
*
D
2D Shape Factor
ns
ns
E
Relative Signal:Area
****
****
mlc1+/Δ
mlc1Δ/Δ
mlc1Δ/Δ + MLC1
F
Relative total intensity
SPK Area (µm2)
G
Relative Total Intensity
Filament Diameter (µm)
mlc1Δ/Δ

Figure 6: **The *mlc1* deletion mutant has a Sec4 labeled Spitzenkörper that is unaltered in shape and size but has an increased intensity.** A) A cluster of Sec4 vesicles are observed in the *mlc1* deletion mutant. Representative images and 20x enlargement of filament tip in the indicated strains. Images are sum projections and LUTs (greyscale and false colored) were the same for all images and bar is 5 μm. B) An increase in Sec4 signal at the Spitzenkörper is observed in the absence of Mlc1. Normalized total intensity for Sec4 vesicle clusters in the indicated strains. Vesicle clusters were identified by 8 standard deviations above the mean and intensity values were normalized to the mean of the *mlc1*+/Δ strain. C) The size of the Sec4 Spitzenkörper vesicle cluster does not depend on Mlc1. Two-dimensional areas of the Sec4 Spitzenkörper vesicle clusters were determined from sum projections (31 x 0.2 μm z-sections). D) The shape of the Sec4 Spitzenkörper vesicle cluster does not depend on Mlc1. The Spitzenkörper vesicle cluster circularity shape factor was determined as in Fig. 1B. E) In the absence of Mlc1 there is an increase in Sec4 signal concentration at the filament tip. Normalized ratio of total Sec4 Spitzenkörper signal to the area of vesicle cluster at filament tip. Values were normalized to the mean of the *mlc1*+/Δ strain. F) The Sec4 signal correlates with the size of the Spitzenkörper in the *mlc1* mutant. The goodness of fit r^2 was 0.66 with a significant correlation $p < 0.0001$. G) The Sec4 vesicle signal at the Spitzenkörper does not correlate with filament diameter. The goodness of fit r^2 was 0.11 with a $p = 0.015$.

Figure 7

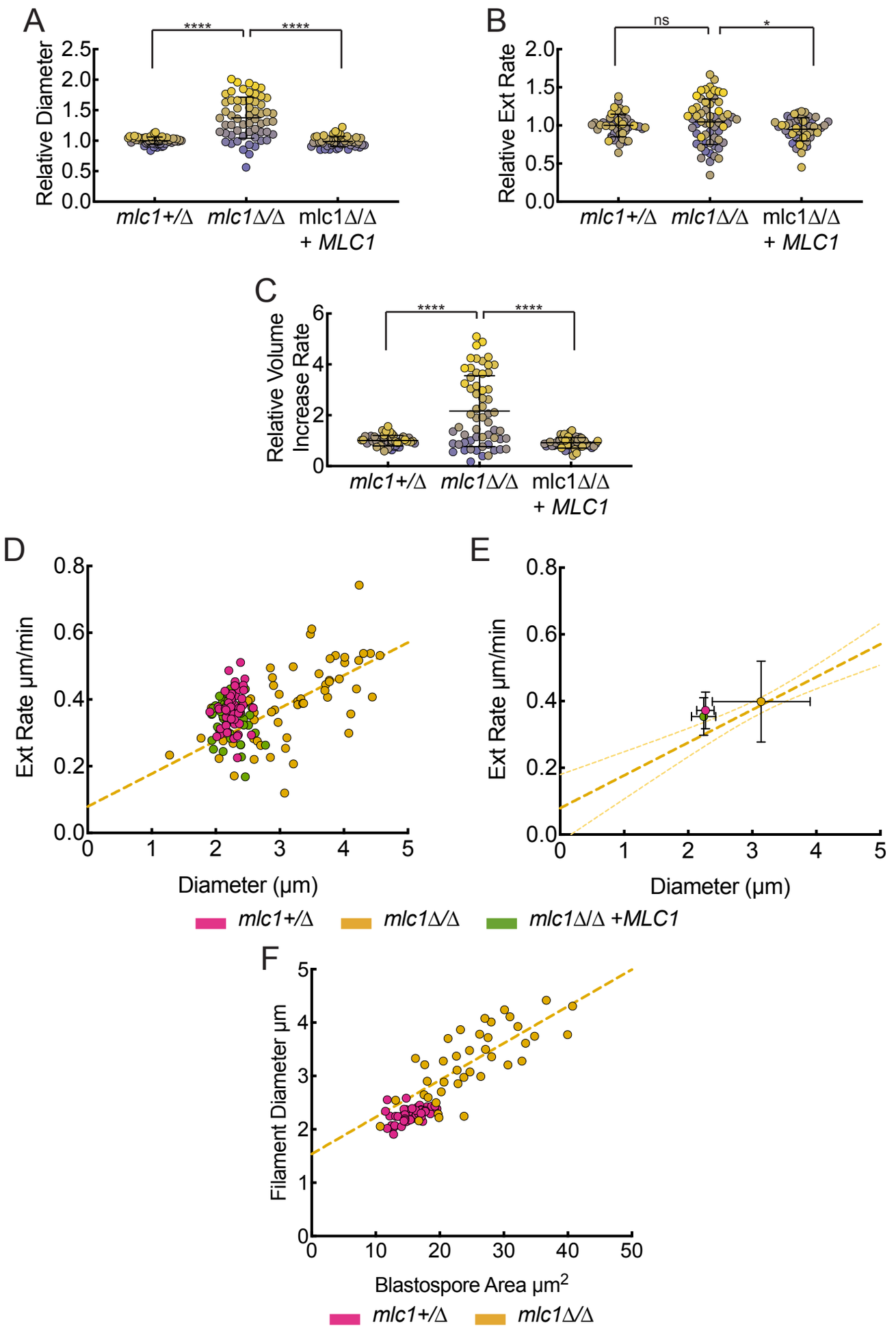
A
Relative Diameter
2.5
2.0
1.5
1.0
0.5
0.0
****
****
mlc1+/Δ
mlc1Δ/Δ
mlc1Δ/Δ + MLC1
B
Relative Ext Rate
2.0
1.5
1.0
0.5
0.0
ns
*
mlc1+/Δ
mlc1Δ/Δ
mlc1Δ/Δ + MLC1
C
Relative Volume Increase Rate
6
4
2
0
****
****
mlc1+/Δ
mlc1Δ/Δ
mlc1Δ/Δ + MLC1
D
Ext Rate µm/min
0.8
0.6
0.4
0.2
0.0
0
1
2
3
4
5
Diameter (µm)
E
Ext Rate µm/min
0.8
0.6
0.4
0.2
0.0
0
1
2
3
4
5
Diameter (µm)
mlc1+/Δ
mlc1Δ/Δ
mlc1Δ/Δ +MLC1
F
Filament Diameter µm
5
4
3
2
1
0
0
10
20
30
40
50
Blastospore Area µm2
mlc1+/Δ
mlc1Δ/Δ

Figure 7: **Mlc1 is critical for regulating filament diameter and extension rate.** A) The filament diameter of *mlc1* mutant is increased. Each point is the relative mean diameter of one cell filament measured every 5-10 min over 120 min. Values were normalized to the *mlc1*+/Δ mean diameter of 2.3 ± 0.1 μm. The data shown in 7A-D was sorted by filament diameter and color-coded with a color gradient (gradients seen in 7A). Each cell has the same color gradation value associated with it for the graphs in A-C to highlight the growth as a function of filament diameter. B) The extension rate of *mlc1* mutant is similar to that of the wild-type. Extension rates were determined from time-lapse experiments of filaments growing on agarose+FCS pads. Each point represents one cell and is the slope of a linear line fit ($r^2 > 0.9$) to a length versus time curve over at least 60 min. Values were normalized to the *mlc1*+/Δ mean extension rate of 0.37 ± 0.06 μm/min. C) *mlc1* mutant filaments exhibit dramatic increases in volume. Volumes were calculated at each time point using the formula for volume of a cylinder $V = \pi r^2 h$ where *r* is the radius and *h* is the length of the filament. The relative volume increase rate is shown with each point representing the normalized slope volume increase over time. Slopes were normalized to the mean of *mlc1*+/Δ of 1.78 ± 0.36 μm^3/min. Standard deviations are indicated and ****p<0.0001, *p<0.05, ns p>0.05. D) *mlc1* mutant extension rate increase correlates with increase in filament diameter. The line fit correlation is for the *mlc1*Δ/Δ and has r^2 of 0.40 and a $p < 0.0001$. E) Same as D but with mean values shown. The best fit line for *mlc1*Δ/Δ is shown with 95% confidence limits. F) The area of the blastospore correlates with filament diameter. An ellipse was fit to the blastospore and its area was measured. The fit, r^2 for *mlc1*Δ/Δ the $r^2 = 0.56$ with $p < 0.0001$.

Figure 8

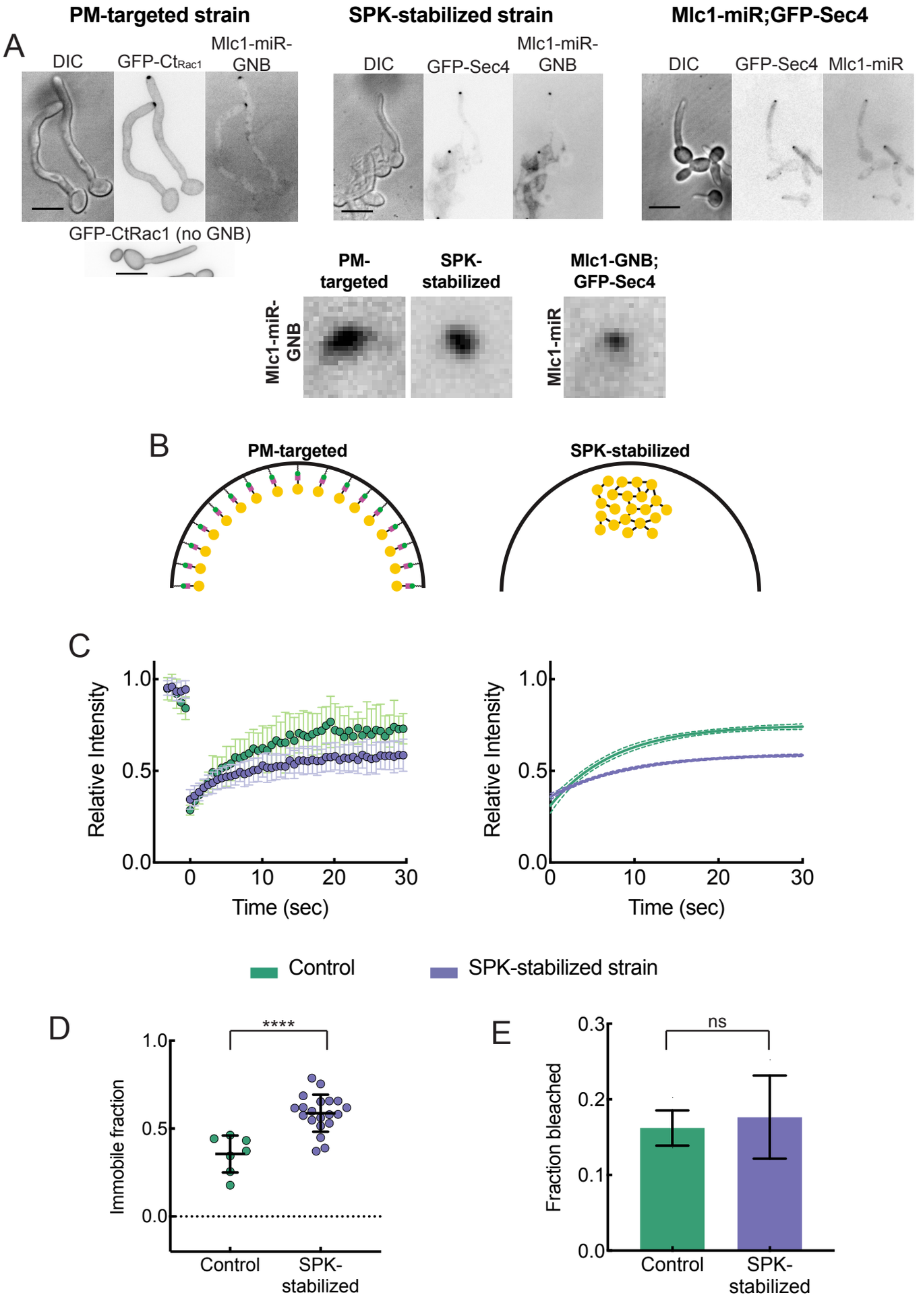
PM-targeted strain
SPK-stabilized strain
Mlc1-miR;GFP-Sec4
A
DIC
GFP-CtRac1
Mlc1-miR-GNB
DIC
GFP-Sec4
Mlc1-miR-GNB
DIC
GFP-Sec4
Mlc1-miR
GFP-CtRac1 (no GNB)
PM-targeted
SPK-stabilized
Mlc1-GNB; GFP-Sec4
Mlc1-miR-GNB
Mlc1-miR
B
PM-targeted
SPK-stabilized
C
Relative Intensity
1.0
0.5
0.0
0
10
20
30
Time (sec)
Relative Intensity
1.0
0.5
0.0
0
10
20
30
Time (sec)
Control
SPK-stabilized strain
D
****
Immobile fraction
1.0
0.5
0.0
Control
SPK-stabilized
E
ns
Fraction bleached
0.3
0.2
0.1
0.0
Control
SPK-stabilized

Figure 8: **Manipulation of the Spitzenkörper distribution and stability using GFP nanobodies.** A) Forced interactions between Mlc1 and the plasma membrane (PM-targeted) or Sec4 (SPK-stabilized) alters Spitzenkörper. Representative images of indicated strains are shown with a 25x enlargement of the Spitzenkörper region is shown. Images are sum projections of 38 x 0.4 µm z-stacks. Scale bar is 10 µm. B) Schematics of GNB interactions for Spitzenkörper disruption. Left: Yellow circle are vesicle, black lines are miR, magenta half-circles are GNB, green circle are GFP, and black zig-zag lines are Ct_{Rac1} tag. Right: yellow circle are vesicles and black line represents miR-GNB-GFP complex. C) Fluorescence recovery after photobleaching of Sec4 upon forced interaction with Mlc1 (SPK-stabilized). Mean FRAP recovery curve (n = 8-20) with standard deviation indicated (left) and one phase exponential association with 95% confidence interval indicated (right). D) Forced interaction between Sec4 and Mlc1 increases the Sec4 immobile fraction at the Spitzenkörper. FRAP Immobile fraction is, $1-((I_{final} - I_{postbleach})/(I_{prebleach} - I_{postbleach}))$, values with standard deviation are shown. E) Similar amounts of cell Sec4 signal were bleached in the two strains. Fraction of total cell signal bleached during FRAP experiments. Control strain is with GFP-Sec4 in a wild-type background. Standard deviations are shown with ****$p<0.0001$ and ns $p>0.005$.

Figure 9

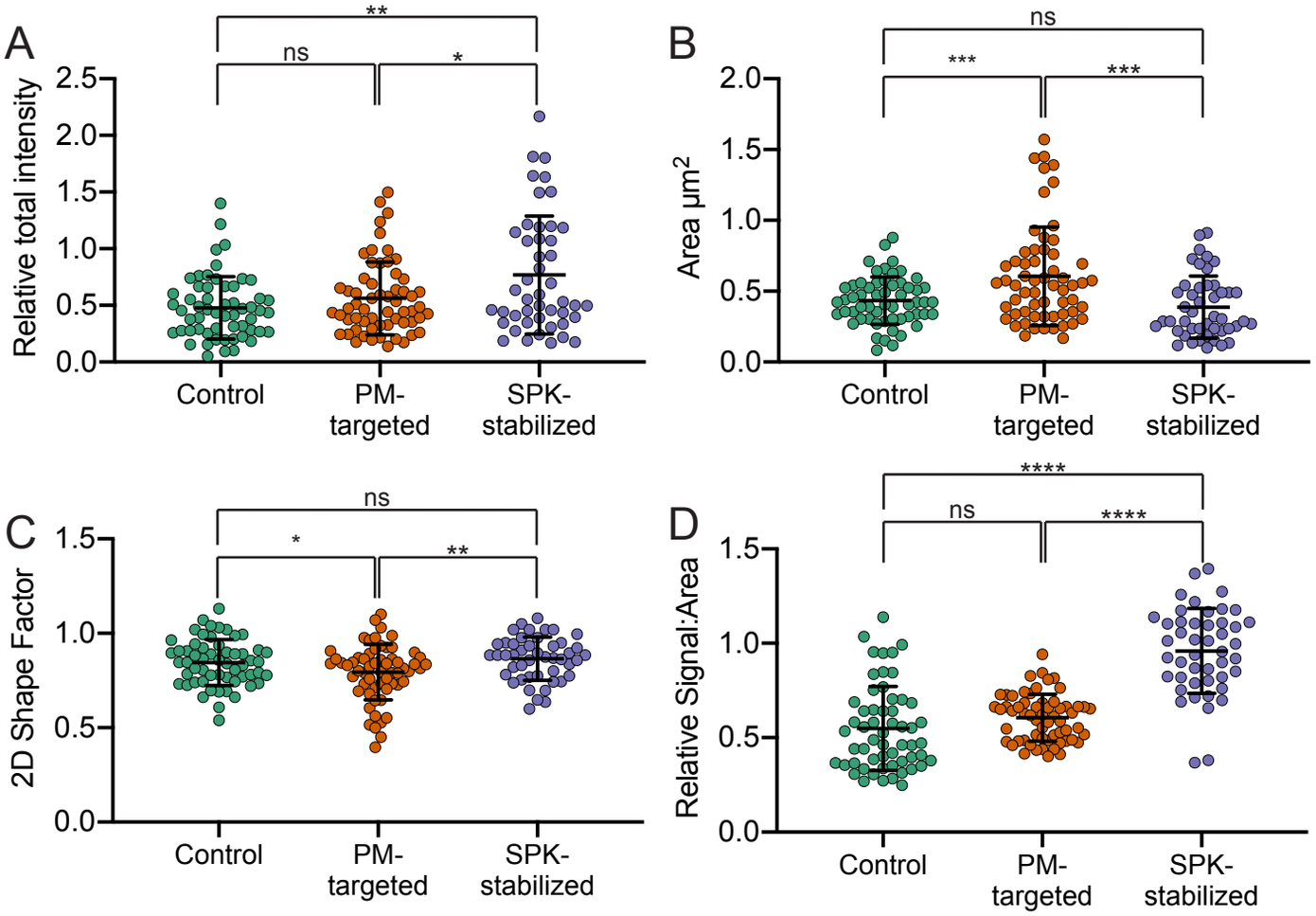
A
Relative total intensity
2.5
2.0
1.5
1.0
0.5
0.0
**
ns
*
Control
PM-targeted
SPK-stabilized
B
Area µm2
2.0
1.5
1.0
0.5
0.0
ns
***
***
Control
PM-targeted
SPK-stabilized
C
2D Shape Factor
1.5
1.0
0.5
0.0
ns
*
**
Control
PM-targeted
SPK-stabilized
D
Relative Signal:Area
1.5
1.0
0.5
0.0
****
ns
****
Control
PM-targeted
SPK-stabilized

Figure 9: **Stabilizing the Spitzenkörper *via* forced interaction between Mlc1 and Sec4 results in increased Sec4 at this structure**. A) An increase in Sec4 signal at the Spitzenkörper is observed in the SPK-stabilized strain. Normalized total intensity for Sec4 Spitzenkörper vesicle cluster in indicated strains. Spitzenkörpers were identified by standard deviations above the mean (13 for GFP-Sec4 and 8 for mScarlet-Sec4 in the PM-targeted strain). Intensity values were normalized to the mean of the control strain. B) The Spitzenkörper size is increased upon PM-targeting. Areas of the Sec4 Spitzenkörper vesicle clusters were determined from sum projections (31 x 0.2 µm z-sections). C) The Sec4 Spitzenkörper shape is less circular upon PM-targeting. The Spitzenkörper vesicle cluster circularity shape factor was determined as in Fig. 1B. D) Stabilizing the Mlc1 and Sec4 interaction results in an increase in Sec4 signal concentration at the filament tip. Normalized ratio of total Sec4 signal to area of vesicle cluster at filament tip. Values were normalized to that of the mean of the control strain. Control strain is with GFP-Sec4 in a wild-type background. Standard deviations are shown with ****$p<0.0001$, ***$p<0.001$, **$p<0.01$, *$p<0.05$, ns $p>0.05$.

Figure 10

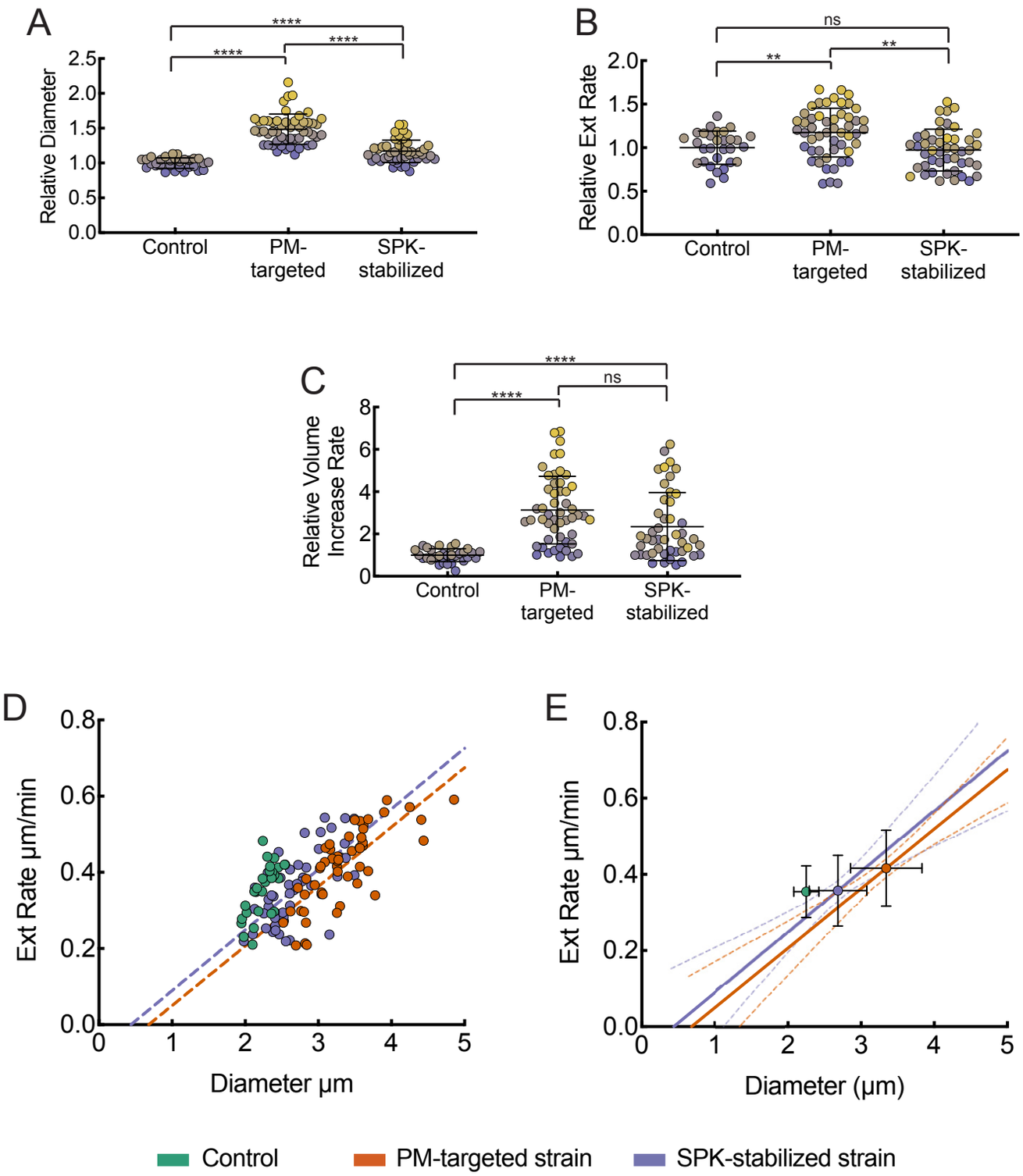
A
Relative Diameter
2.5
2.0
1.5
1.0
0.5
0.0
****
****
****
Control
PM-targeted
SPK-stabilized
B
Relative Ext Rate
2.0
1.5
1.0
0.5
0.0
ns
**
**
Control
PM-targeted
SPK-stabilized
C
Relative Volume Increase Rate
8
6
4
2
0
****
****
ns
Control
PM-targeted
SPK-stabilized
D
Ext Rate µm/min
0.8
0.6
0.4
0.2
0.0
0
1
2
3
4
5
Diameter µm
E
Ext Rate µm/min
0.8
0.6
0.4
0.2
0.0
0
1
2
3
4
5
Diameter (µm)
Control
PM-targeted strain
SPK-stabilized strain

Figure 10: **Perturbation of Spitzenkörper distribution or dynamics dramatically increases filament growth rate.** A) Altering Spitzenkörper distribution or stability results in increased filament diameter. Diameters were quantitated and represented as described in Fig. 7A and normalized to the mean for the control strains (2.2 ± 0.2 μm). B) Cells with an altered Spitzenkörper distribution have an increased filament extension rate. Extension rates of indicated strains were measured as described in 7B and normalized to the mean the control strains (0.35 ± 0.07 μm/min). C) Perturbation of Spitzenkörper distribution or stability results in a striking filament volume increase. The relative volume increase rate is shown, with each point representing the normalized slope of rate of volume increase as in 7C. Slopes were normalized to the mean of the control strain (1.67 ± 0.52 μm^3/min). Standard deviations are shown with **** $p<0.0001$, ** $p<0.01$, ns $p>0.05$. D) Increase in the extension rate in Spitzenkörper mutants correlates with an increase in filament diameter. A $r^2 = 0.59$ for the fit for Spitzenkörper distribution mutant and 0.46 for the Spitzenkörper stability mutant. Both mutants had $p < 0.0001$. E) Same as G but with mean values shown. The best fit line for *mlc1* distribution/stability mutants are show with 95% confidence lines. Control strain is with GFP-Sec4 in a wild-type background.

Figure S1

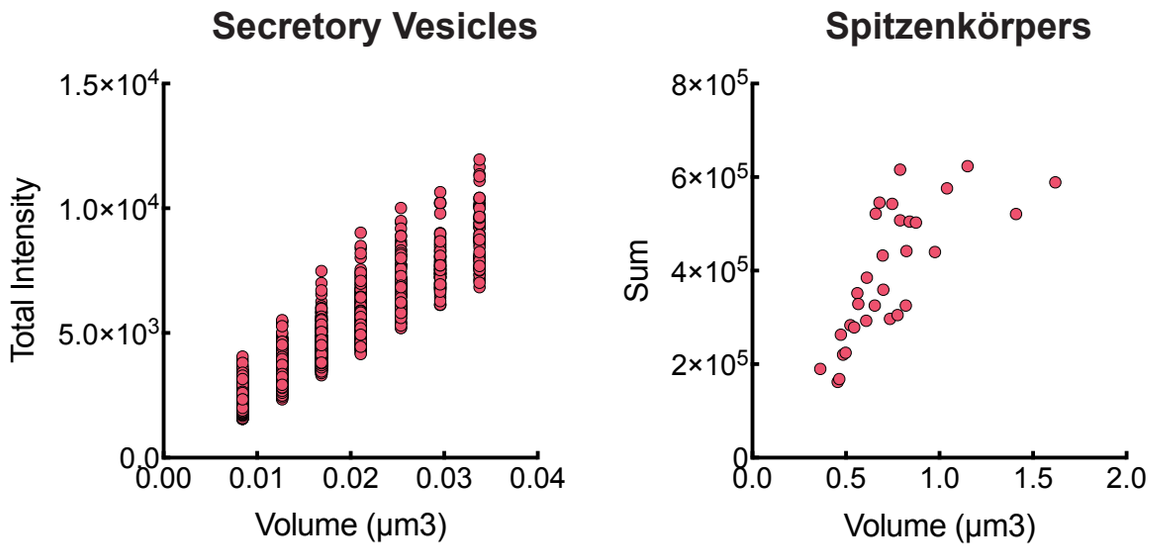
Secretory Vesicles
Total Intensity
1.5×10^4
1.0×10^4
5.0×10^3
0.0
0.00
0.01
0.02
0.03
0.04
Volume (µm3)
Spitzenkörpers
Sum
8×10^5
6×10^5
4×10^5
2×10^5
0
0.0
0.5
1.0
1.5
2.0
Volume (µm3)

Figure S1: **Distribution of secretory vesicle and Spitzenkörper intensities.** Separated graphs from Figure 1E. Intensities of identified secretory vesicles (left) and Spitzenkörpers intensities. Signals from objects of 2-8 voxels were assumed to be secretory vesicles.

Figure S2

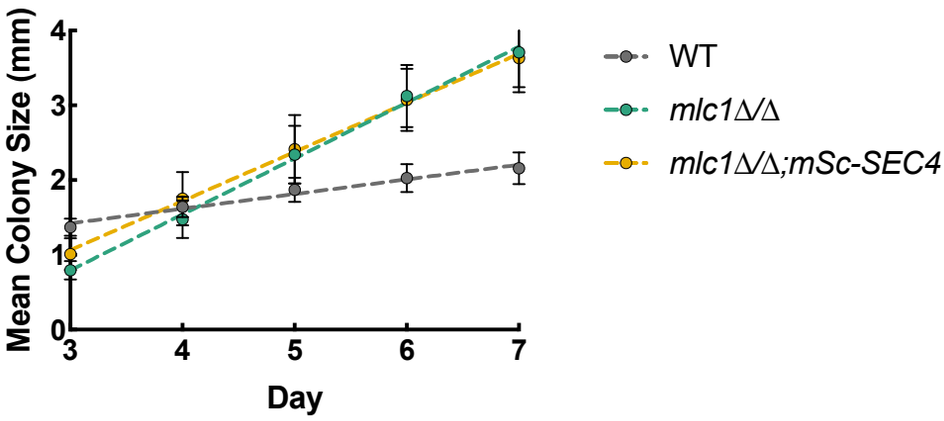
Mean Colony Size (mm)
0
1
2
3
4
3
4
5
6
7
Day
WT
mlc1Δ/Δ
mlc1Δ/Δ;mSc-SEC4

Figure S2: **The *mlc1*Δ/Δ mutant has an increased colony growth rate.** Exponentially growing cultures (0.1 OD_{600}) were diluted 1:15000 and 0.2 ml was spread on YEPD plates. Plates were incubated for 7 days. Colony diameters were measured over the indicated days for two independent *mlc1*Δ/Δ mutants. Points represent averages with standard deviations shown and linear best fit are dashed lines.

Figure S3

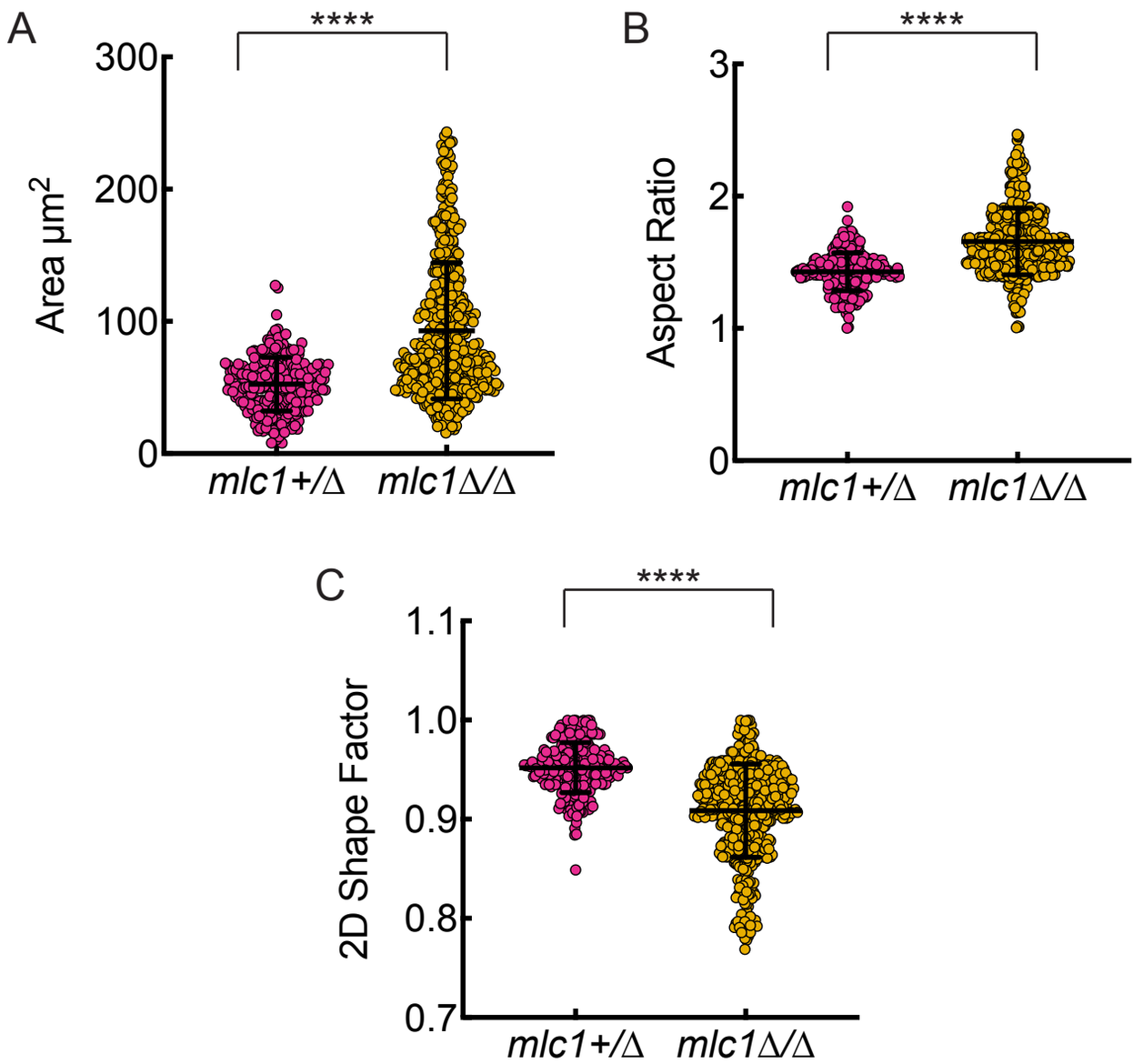
A
****
300
200
100
0
Area µm2
mlc1+/Δ
mlc1Δ/Δ
B
****
3
2
1
0
Aspect Ratio
mlc1+/Δ
mlc1Δ/Δ
C
****
1.1
1.0
0.9
0.8
0.7
2D Shape Factor
mlc1+/Δ
mlc1Δ/Δ

Figure S3: ***mlc1*Δ/Δ budding cells have an altered morphology.** A) The *mlc1*Δ/Δ mutant budding cells are larger than the wild-type. Images were acquired in DIC and in fluorescence (mSc-Sec4) using 16 x 0.4 µm z-stacks. An ellipsoid was fit to each cell from a sum projected of the fluorescence signal (n = X). Area was calculated using the long and short axis of the ellipse. B) *mlc1*Δ/Δ mutant budding cells are more elongated than the wild-type. The aspect ratio (long/short axis) is shown for the *mlc1*Δ/Δ mutant and wild-type cells. C) *mlc1*Δ/Δ mutant budding cells are less circular than the wild-type. The 2D circular shape factor is shown. Standard deviations are indicated with **** $p<0.0001$.

Figure S4

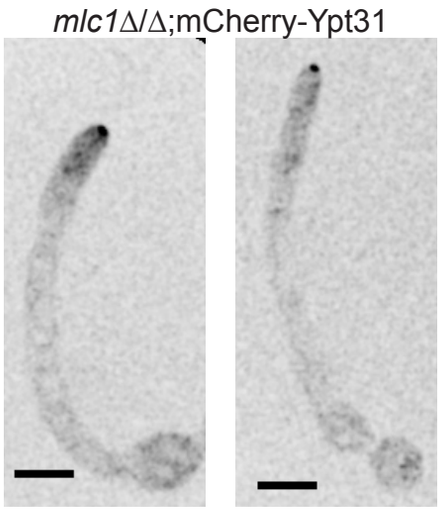

Figure S4: **Ypt3l localizes to the Spitzenkörper in the *mlc1*Δ/Δ mutant.** Images are from a time-lapse acquisition of *mlc1*Δ/Δ expressing mCherry-Ypt31. Both images at 70 min. Z-stacks of 26 x 0.4 µm images were deconvolved and then sum projected for representation.

Figure S5

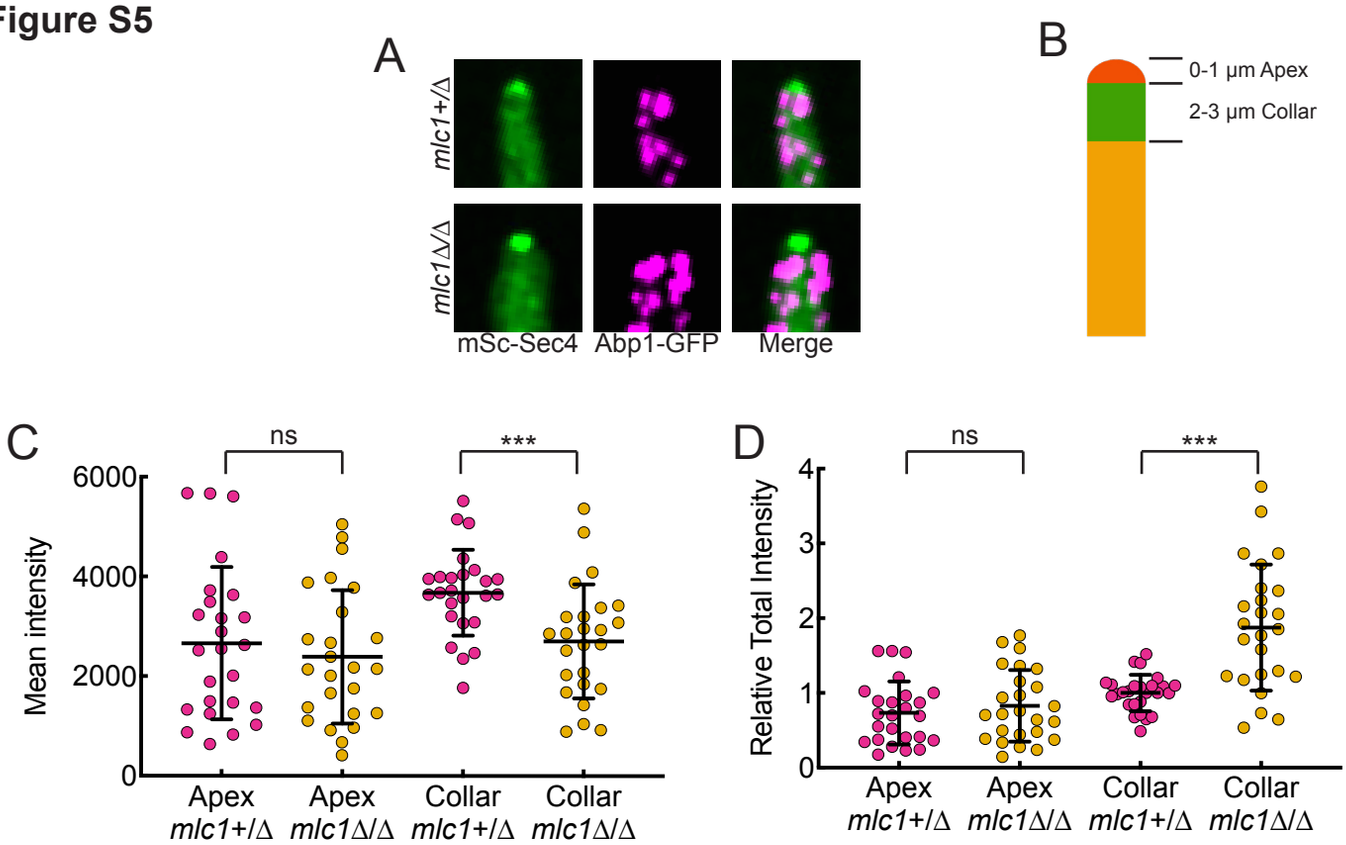
A
mlc1+/Δ
mlc1Δ/Δ
mSc-Sec4
Abp1-GFP
Merge
B
0-1 μm Apex
2-3 μm Collar
C
Mean intensity
6000
4000
2000
0
ns
***
Apex mlc1+/Δ
Apex mlc1Δ/Δ
Collar mlc1+/Δ
Collar mlc1Δ/Δ
D
Relative Total Intensity
4
3
2
1
0
ns
***
Apex mlc1+/Δ
Apex mlc1Δ/Δ
Collar mlc1+/Δ
Collar mlc1Δ/Δ

Figure S5: **There is a decrease in endocytosis collar intensity in the absence of Mlc1.** A) Representative images of Apb1-GFP and mSc-Sec4 in wild-type and *mlc1*Δ/Δ mutant. Images were acquired with 26 x 0.4 µm z-stacks and deconvolved. Sum projections are shown. B) Representation of the location where the apex and the collar were measured. C) *mlc1*Δ/Δ has a decrease in endocytosis collar mean intensity. Mean intensities were measured for the apex (0-1µm from tip) and the collar (1-3 µm from the tip) for both strains. D) Wider *mlc1*Δ/Δ cells results in increased total collar intensity. The total intensity of the collar was measured at the apex and collar. Standard deviations are shown and *** $p<0.001$ and ns $p>0.05$.

Figure S6

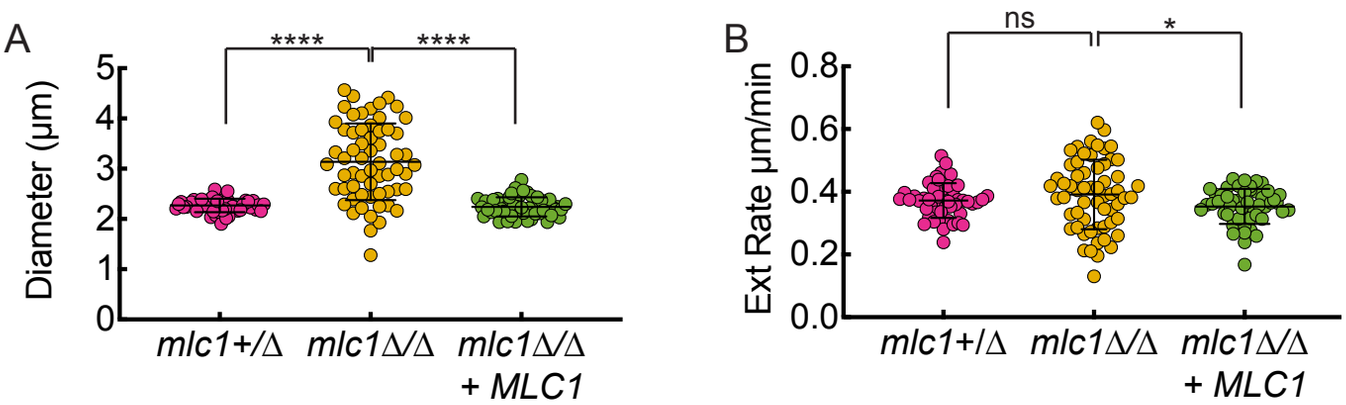
A
Diameter (µm)
****
****
mlc1+/Δ
mlc1Δ/Δ
mlc1Δ/Δ + MLC1
B
Ext Rate µm/min
ns
*
mlc1+/Δ
mlc1Δ/Δ
mlc1Δ/Δ + MLC1

Figure S6: **Morphology measurements of the *mlc1* mutants.** Same as Figure 7 except data is not normalized with A) being the diameter and B) is extension rates. Standard deviations are shown and **** $p<0.0001$, *$p<0.05$ and ns $p>0.05$.

Figure S7

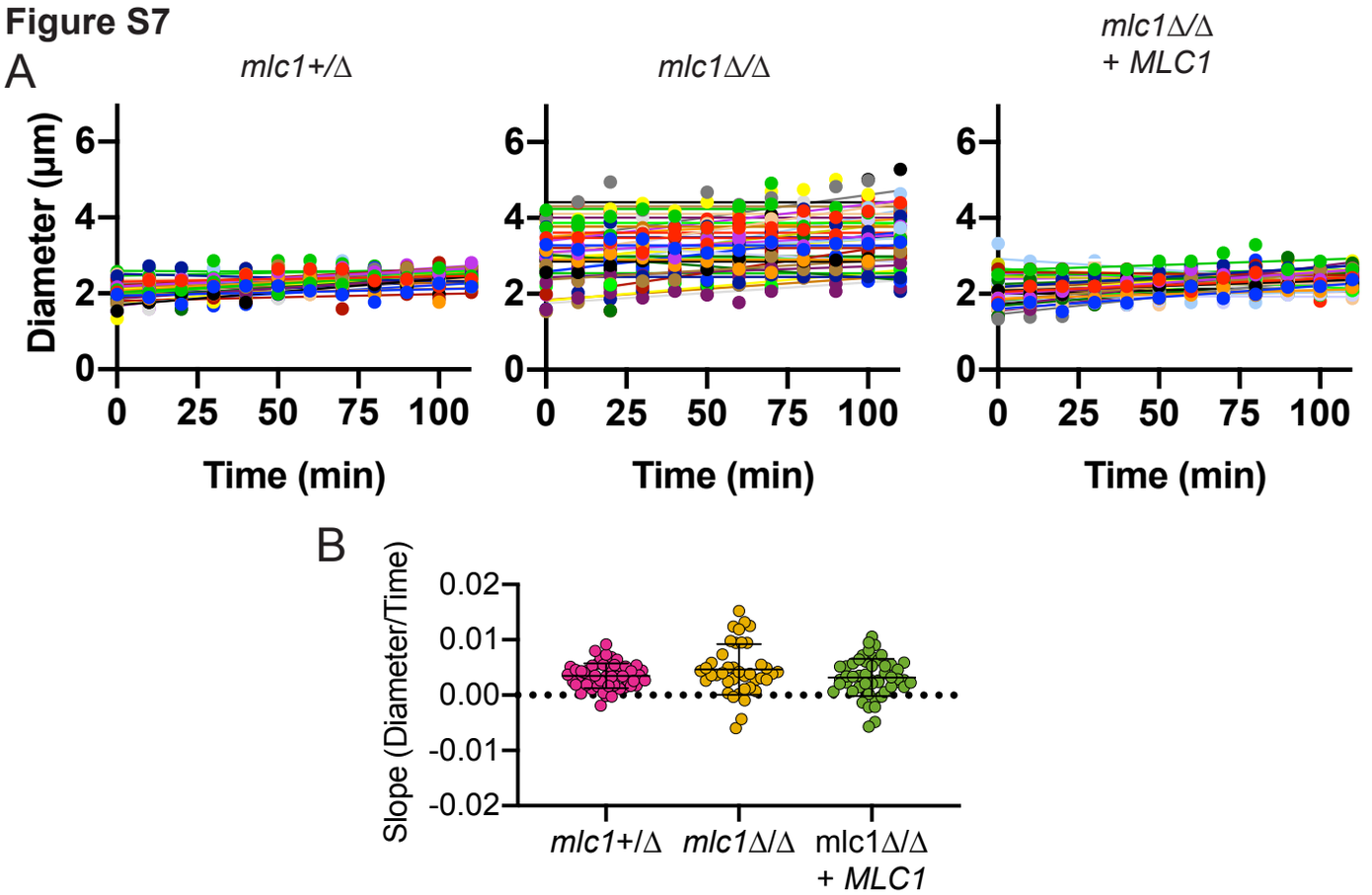
A
mlc1+/Δ
mlc1Δ/Δ
mlc1Δ/Δ
+ MLC1
Diameter (μm)
Time (min)
B
Slope (Diameter/Time)
mlc1+/Δ
mlc1Δ/Δ
mlc1Δ/Δ
+ MLC1

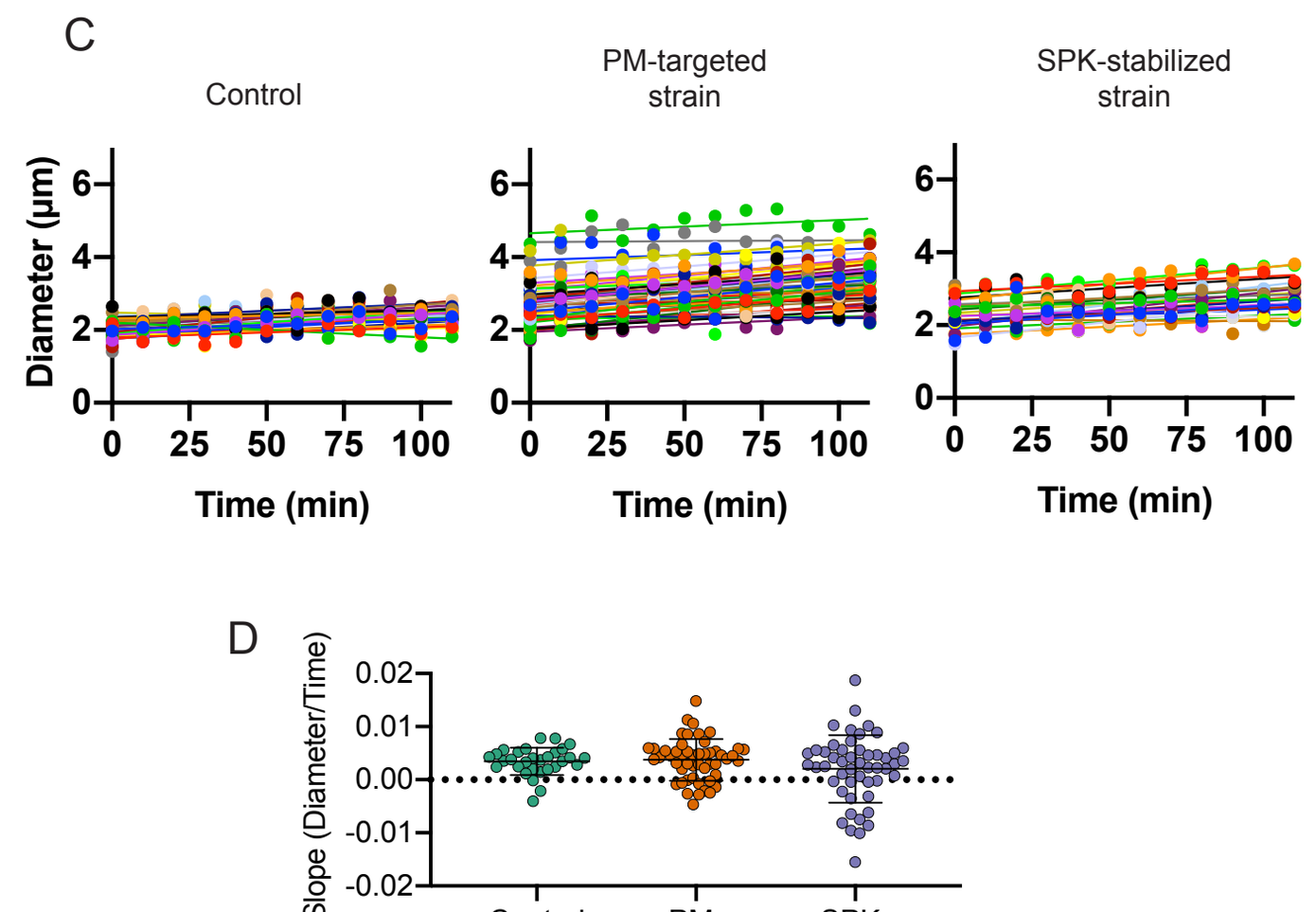
C
Control
PM-targeted
strain
SPK-stabilized
strain
Diameter (μm)
Time (min)
D
Slope (Diameter/Time)
Control
PM-
targeted
SPK-
stabilized

Figure S7: **Filament diameters are constant over time.** A) The *MLC1* mutants have a constant filament diameter. Diameter measurements from Fig. 7A were plotted over time for all cells analyzed (I = 50-60 per strain). B) Linear fits have a very minor slope. Lines were fit to the diameter plots and the slope for each cell is shown. C) The altered Spitzenkörper mutant strains have a constant filament diameter. Diameter measurements from Fig. 9A were plotted over time for all cells analyzed (n = 50 per strain). D) Linear fits of the altered Spitzenkörper mutant strain diameters have a very minor slope. Lines were fit to the diameter plots and the slope for each cell is shown.

Figure S8

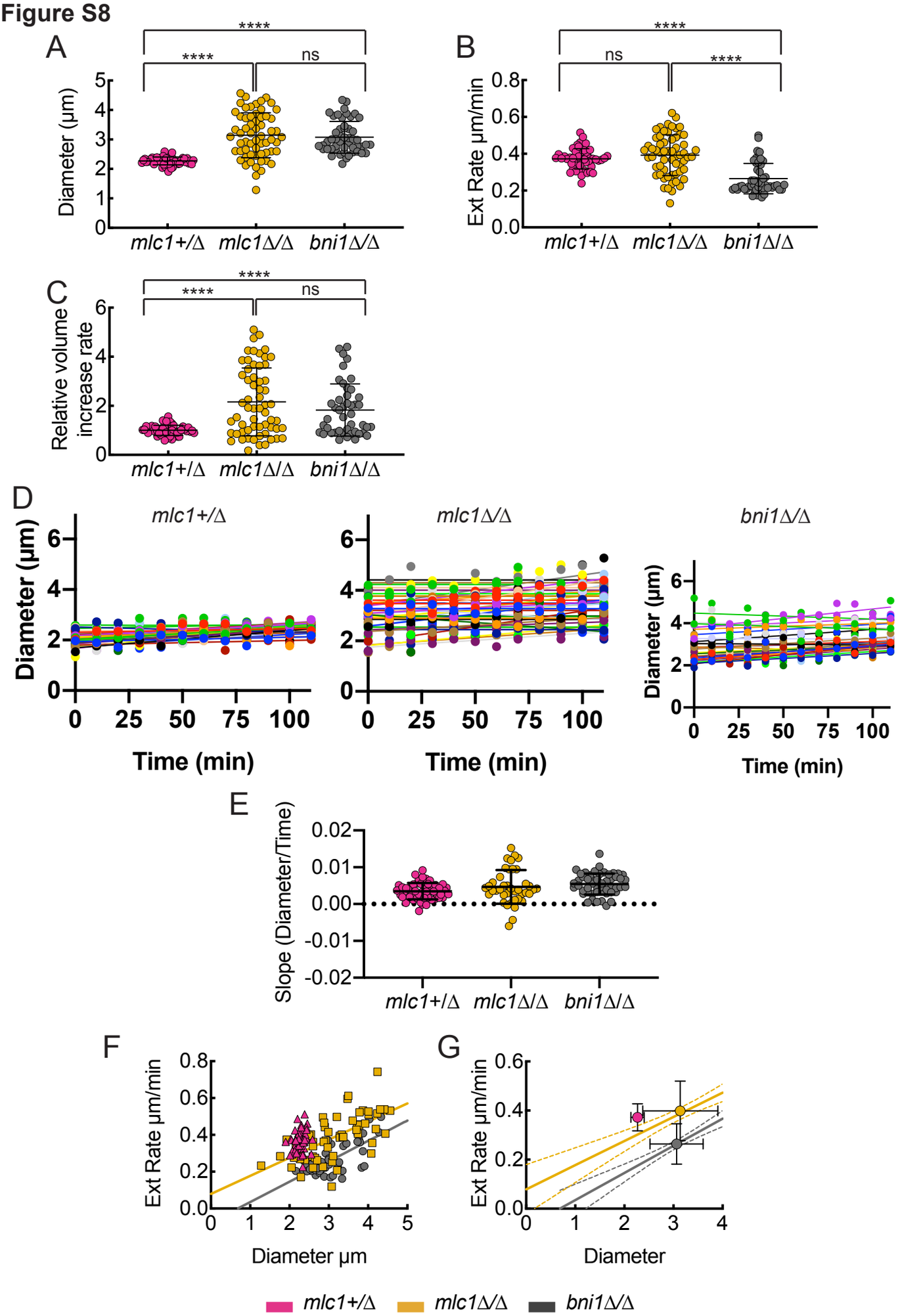
A
Diameter (µm)
****
****
ns
mlc1+/Δ
mlc1Δ/Δ
bni1Δ/Δ
B
Ext Rate µm/min
****
ns
****
C
Relative volume increase rate
****
****
ns
D
mlc1+/Δ
mlc1Δ/Δ
bni1Δ/Δ
Diameter (µm)
Time (min)
E
Slope (Diameter/Time)
F
Ext Rate µm/min
Diameter µm
G
Ext Rate µm/min
Diameter
mlc1+/Δ
mlc1Δ/Δ
bni1Δ/Δ

Figure S8: **The formin Bni1 is important for of filament morphology and extension rate.** A) The *bni1*Δ/Δ mutant has an increased filament diameter. Each point is the relative mean diameter of one cell filament measured every 10 min over 120 min. B) The extension rate of the *bni1*Δ/Δ mutant is reduced compared to the wild-type and the *mlc1*Δ/Δ mutant. Extension rates were determined from time-lapse experiments of filaments on agarose+FCS pads. Each point represents a cell and is the slope of a linear fit (r^2 values > 0.9) to a length versus time plot over > 60 min. C) *bni1*Δ/Δ mutant have an increased growth rate. Volumes were calculated at each time point using the formula for volume of a cylinder $V=\pi r^2 h$ where *r* is the filament radius and *h* is its length. The relative rate of volume increase is shown with each point representing the normalized slope of rate of volume increase over time *i.e.* growth rate. Slopes were normalized to the mean of *mlc1*+/Δ strain,1.78 ± 0.36 μm^3/min. Standard deviations are shown with **** p<0.0001, ns p>0.05. D) *bni1*Δ/Δ mutants have a constant filament diameter over time. Diameter measurements from Fig. 7A were plotted over time for all cells analyzed (*n* = 50-60 per strain). E) *bni1*Δ/Δ mutants filament diameter have a very small change over time. Lines were fit to the diameters over times, and the slope for each cell is shown. F) *bni1*Δ/Δ mutant extension rate increase correlates with increase in filament diameter. The line fit correlation for *bni1*Δ/Δ has a r^2 of 0.52 and *mlc1*Δ/Δ has a r^2 of 0.40 both with p-values < 0.0001. G) Same as D but mean values shown. The best line fits for *bni1*Δ/Δ and *mlc1*Δ/Δ are shown with 95% confidence limits.

Figure S9

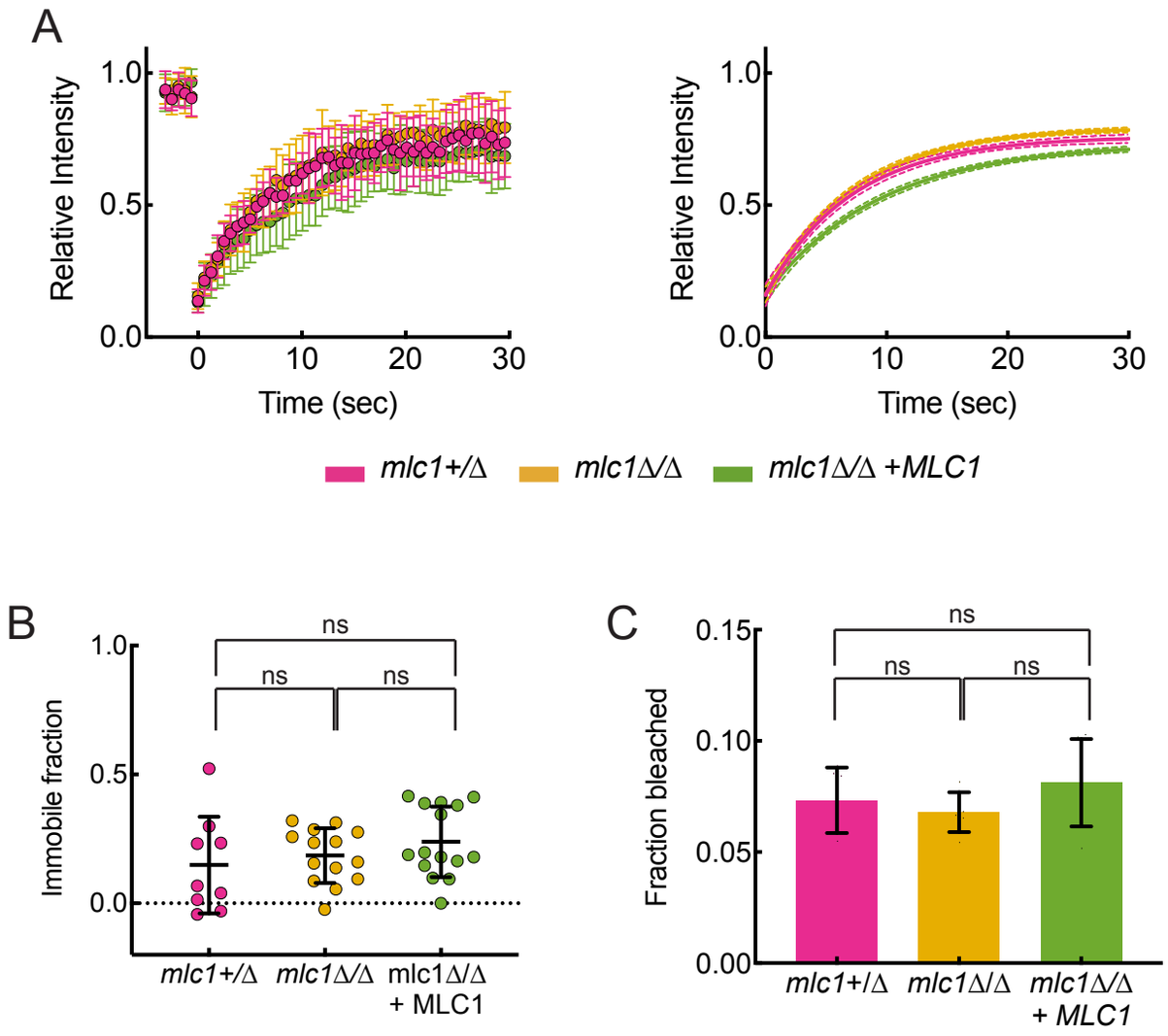
A
Relative Intensity
1.0
0.5
0.0
0
10
20
30
Time (sec)
Relative Intensity
1.0
0.5
0.0
0
10
20
30
Time (sec)
mlc1+/Δ
mlc1Δ/Δ
mlc1Δ/Δ +MLC1
B
Immobile fraction
1.0
0.5
0.0
ns
ns
ns
mlc1+/Δ
mlc1Δ/Δ
mlc1Δ/Δ
+ MLC1
C
Fraction bleached
0.15
0.10
0.05
0.00
ns
ns
ns
mlc1+/Δ
mlc1Δ/Δ
mlc1Δ/Δ
+ MLC1

Figure S9: **Mlc1 is not critical for Sec4 Spitzenkörper stability.** A) Fluorescence recovery after photobleaching (FRAP) of mSc-Sec4 in *mlc1* mutant strains. Mean FRAP recovery (n = 9-15) with standard deviation indicated (left) and one phase exponential association with 95% confidence interval indicated (right). B) The immobile fraction is unaffected in the *mlc1*Δ/Δ mutant. FRAP immobile fraction is, $1-((I_{final} - I_{postbleach})/(I_{prebleach} - I_{postbleach}))$, values with standard deviation are shown. E) Similar amounts of Sec4 signal were photobleached in the two strains. Fraction of total cell signal that was bleached in FRAP experiments. Standard deviations are shown with ns $p>0.05$.

Figure S10

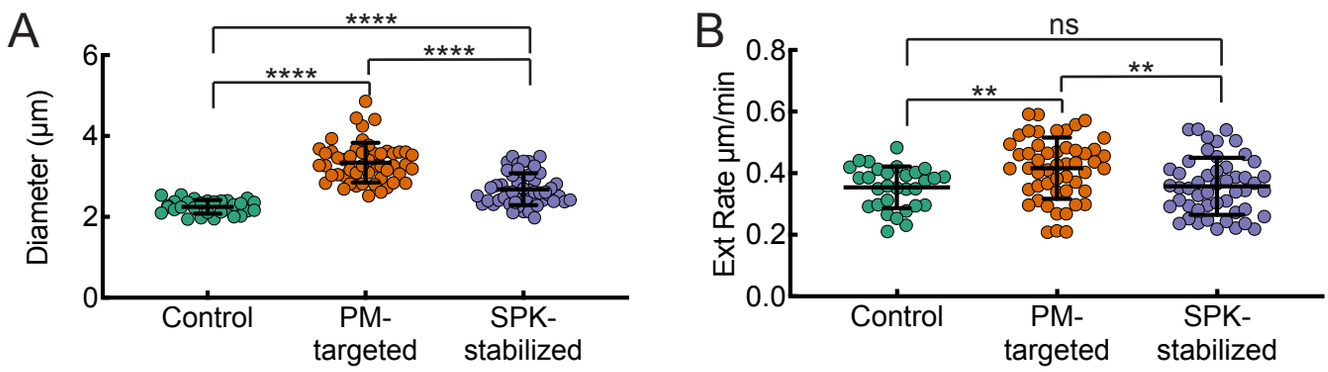
A
Diameter (µm)
0
2
4
6
****
****
****
Control
PM-targeted
SPK-stabilized
B
Ext Rate µm/min
0.0
0.2
0.4
0.6
0.8
ns
**
**
Control
PM-targeted
SPK-stabilized

Figure S10: **Morphology in measurements of the GNB strains.** Same as Figure 9 except data is not normalized with A) being the diameter and B) is extension rates. Standard deviations are shown and **** $p<0.0001$, **$p<0.01$ and ns $p>0.05$.

III – Secretory vesicle clustering in fungal filamentous cells does not require directional growth

Patrícia M. Silva, **Charles Puerner**, Agnese Seminara, Martine Bassilana, and Robert A. Arkowitz

Silva et al., 2019, Cell Reports 28, 2231–2245

In this section I will briefly highlight my contributions as a second author for the article by Silva et al., 2019, that was published in *Cell Reports*. This article uses an optogenetic approach to disrupt polarized growth by recruiting active Cdc42 all over the membrane and quantifying the effects. This was largely the work of Patrícia Silva, a PhD student in the Arkowitz laboratory. As a second author, I made contributions through developing the use of longer wavelength fluorescent proteins and tagging constructs, which were necessary due to the sensitivity of the optogenetic system to wavelengths in the blue end of the visible light spectrum. I developed the use of the red fluorescent protein, mScarlet (Bindels et al., 2016), which is significantly more bright and stable than the previous option mCherry. From this I developed a triple tandem version (3xmScarlet) with unique coding sequences to prevent recombination and improved signal. I also developed the use of the near-infrared monomeric fluorescent protein miRFP670 (Shcherbakova et al., 2016). This allowed for imaging in two spectrally distinct fluorescent channels that were compatible with the optogenetic system. I developed the fully functional mScarlet-Sec4 construct because a previous construct used GFP and the *URA3* marker (Li et al., 2007), which were both already in use for the optogenetic system. Overall my contributions through developing the use of two spectrally distinct fluorescent proteins compatible with this system was important for the success of this work, particularly allowing for the ability to observe two protein localizations simultaneously as can be seen in Figures 4 and 5 of this article.

Article

Cell Reports

Secretory Vesicle Clustering in Fungal Filamentous Cells Does Not Require Directional Growth

Graphical Abstract

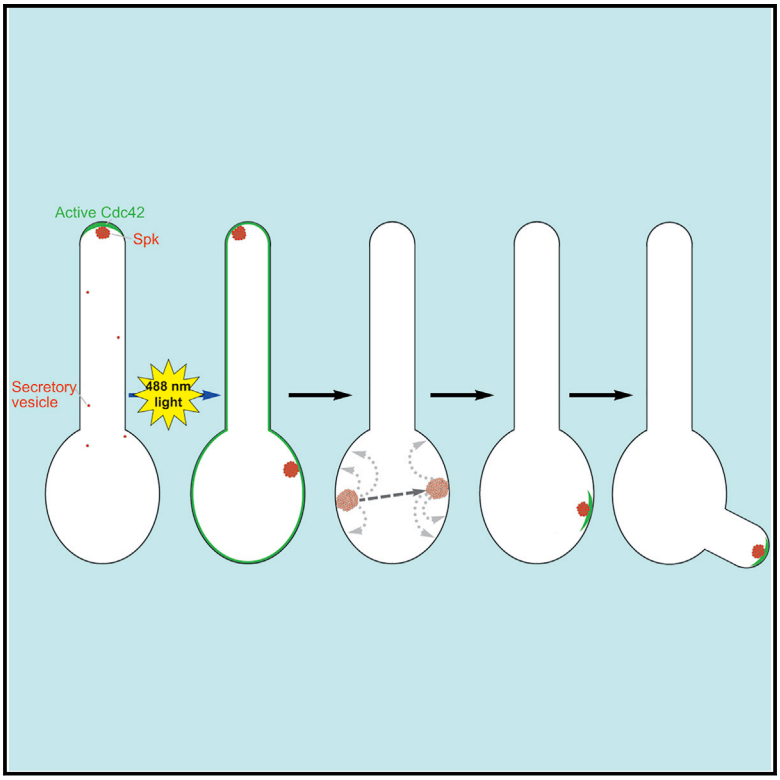

Authors

Patrícia M. Silva, Charles Puerner, Agnese Seminara, Martine Bassilana, Robert A. Arkowitz

Correspondence

arkowitz@unice.fr

In Brief

Silva et al. use light-dependent plasma membrane recruitment of active Cdc42 to reset polarity in asymmetric filamentous fungal cells. This transient increase in plasma membrane active Cdc42 disrupted membrane traffic and resulted in the formation of a striking *de novo* secretory vesicle cluster, in the absence of directional growth.

Highlights

- Photo-recruitment of active Cdc42 over the plasma membrane resets growth
- Transient increase of active Cdc42 at the plasma membrane disrupts membrane traffic
- Increase in plasma membrane active Cdc42 results in *de novo* secretory vesicle cluster
- Secretory vesicle clustering can occur in the absence of directional growth

Silva et al., 2019, Cell Reports *28*, 2231–2245
August 20, 2019
https://doi.org/10.1016/j.celrep.2019.07.062

CellPress

Cell Reports
Article

Secretory Vesicle Clustering in Fungal Filamentous Cells Does Not Require Directional Growth

Patrícia M. Silva,[1] Charles Puerner,[1] Agnese Seminara,[2] Martine Bassilana,[1] and Robert A. Arkowitz[1,3,*]
[1]Université Côte d'Azur, CNRS, INSERM, Institute of Biology Valrose (iBV), Parc Valrose, Nice, France
[2]Université Côte d'Azur, CNRS, Institute Physics of Nice (INPHYNI), Ave. J. Vallot, Nice, France
[3]Lead Contact
*Correspondence: arkowitz@unice.fr
https://doi.org/10.1016/j.celrep.2019.07.062

SUMMARY

During symmetry breaking, the highly conserved Rho GTPase Cdc42 becomes stabilized at a defined site via an amplification process. However, little is known about how a new polarity site is established in an already asymmetric cell—a critical process in a changing environment. The human fungal pathogen *Candida albicans* switches from budding to filamentous growth in response to external cues, a transition controlled by Cdc42. Here, we have used optogenetic manipulation of cell polarity to reset growth in asymmetric filamentous *C. albicans* cells. We show that increasing the level of active Cdc42 on the plasma membrane results in disruption of the exocyst subunit Sec3 localization and a striking *de novo* clustering of secretory vesicles. This new cluster of secretory vesicles is highly dynamic, moving by hops and jumps, until a new growth site is established. Our results reveal that secretory vesicle clustering can occur in the absence of directional growth.

INTRODUCTION

Highly polarized growth in a range of elongated cell types, including fungal hyphae (Riquelme, 2013; Riquelme and Sánchez-León, 2014; Virag and Harris, 2006), plant pollen tubes (Bibeau et al., 2018; Bou Daher and Geitmann, 2011; Bove et al., 2008), and neurons (Denker et al., 2011; Milovanovic and De Camilli, 2017; Mukherjee et al., 2010) requires a specific cellular organization to overcome long distances. In these elongated cells, clusters of vesicles are typically observed just behind the growing cell tip and thought to provide a reservoir of material necessary for rapid cellular extension or synaptic activity. In *Saccharomyces cerevisiae,* such a cluster of vesicles also appears to be present in elongated pseudohyphal cells (Kim and Rose, 2015) and shmoos (Chapa-Y-Lazo et al., 2011), yet has not been observed in budding cells. In filamentous fungi, including *Neurospora crassa* and *Ashbya gossypii*, a number of studies have revealed that this structure, referred to as the Spitzenkörper (Spk), depends on and maintains growth (Brunswik, 1924; Girbardt, 1957, 1969; Grove and Bracker, 1970; López-Franco and Bracker, 1996; Reynaga-Peña et al., 1997; Riquelme, 2013; Riquelme and Sánchez-León, 2014; Virag and Harris, 2006). In *Candida albicans*, disruption of the actin cytoskeleton (Crampin et al., 2005; Jones and Sudbery, 2010), as well as mutants that perturb secretion, i.e., *sec3* and *sso2*, disrupt the Spk (Bernardo et al., 2014; Li et al., 2007). Together these results strongly suggest that this cluster of vesicles is a build-up resulting from limiting fusion with the plasma membrane and is intimately associated with cell growth.

Cell polarity is a fundamental process that is not fixed but rather is dynamic, allowing cells to readjust to their environment in response to a range of temporal and spatial cues. In both model yeasts *S. cerevisiae* and *Schizosaccharomyces pombe*, the active form of the highly conserved Rho GTPase Cdc42 accumulates at a unique, presumptive growth site in symmetrical, unpolarized cells (Bendezú and Martin, 2011; Bendezú et al., 2015; Butty et al., 2002; Das et al., 2009; Gallo Castro and Martin, 2018; Gulli et al., 2000; Howell et al., 2012; Jaquenoud and Peter, 2000; Kelly and Nurse, 2011; Ozbudak et al., 2005; Smith et al., 2013). This patch or cap of activated Cdc42 ultimately results in polarized growth by promoting the activation and/or recruitment of a range of effector proteins, which have critical roles in cytoskeleton organization and membrane traffic (Chiou et al., 2017). Polarization in the absence of established landmarks is thought to be the result of feedback mechanisms that amplify small differences in active Cdc42 levels via reaction-diffusion mechanisms, actin-dependent transport, membrane extraction, and differential lateral diffusion (Freisinger et al., 2013; Goryachev and Leda, 2017; Kuo et al., 2014; Martin, 2015; Witte et al., 2017; Woods and Lew, 2019; Wu et al., 2015; Wu and Lew, 2013). Recently, optogenetic recruitment of either the Bem1 scaffold protein or the Cdc42 unique guanine nucleotide exchange factor (GEF), Cdc24, was shown to be sufficient to bias the position of the polarization site in budding yeast (Witte et al., 2017).

Cdc42 is also critical for filamentous growth in a range of fungi, including pathogenic species. This GTPase has been shown to control directional growth in *N. crassa* germ tubes (Lichius et al., 2014), and deletion mutants have severe morphological

Cell Reports *28*, 2231–2245, August 20, 2019

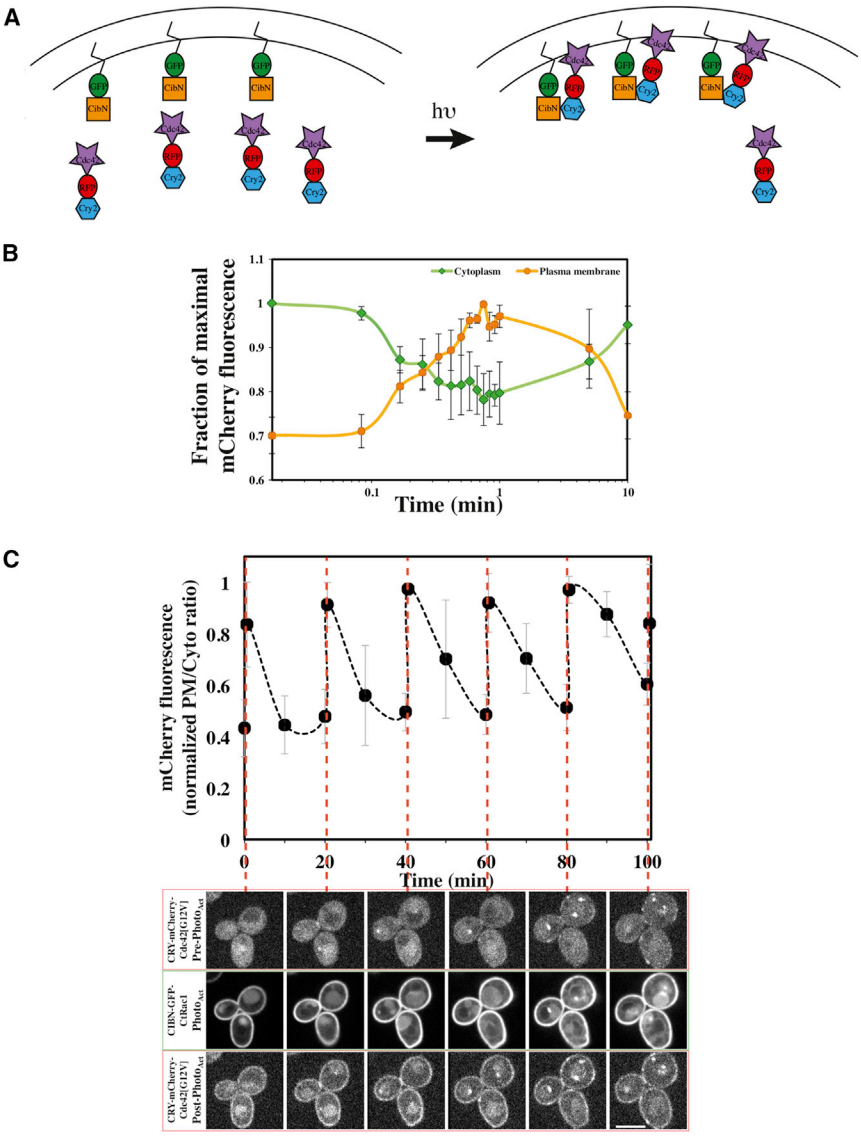

Figure 1. Rapid Recruitment of Active Cdc42 to the Plasma Membrane

(A) Schematic of optogenetic system for recruitment of active Cdc42 to the plasma membrane in *C. albicans*.

(B) Recruitment of Cdc42•GTP to the plasma membrane occurs concomitant with depletion from the cytoplasm. A strain expressing CibN-GFP-Ct_{Rac1} and Cry2-mCh-Cdc42[G12V]$_{cyto}$ was incubated on agar pads at 30°C, and the entire field of view was exposed to a 300-ms, 488-nm, 2.5-mW pulse immediately after the initial time point. The mean signals from a region of interest (ROI) of the cytoplasm or plasma membrane were quantified (n = 3) and maximum signals were normalized to 1; the average and standard deviation are shown.

(C) Cdc42•GTP can be recruited to the plasma membrane multiple times. Strain was incubated on agar pads as in Figure 1B and similarly exposed to 488 nm light every 20 min; image acquisition order was 561 nm (top row), 488 nm (middle row) and 561 nm (bottom) excitation. Signals were quantified as in Figure 1B and the mean plasma membrane to cytoplasm ratio calculated, with the maximum normalized to 1; the average and standard deviation are shown. Scale bar, 5 μm.

defects (Araujo-Palomares et al., 2011). In *Aspergillus nidulans*, mutants lacking *CDC42* exhibited defects in hyphal polarity, although the organization of the microtubule and actin cytoskeleton and the apical vesicle cluster known as the Spk were not affected (Virag et al., 2007). In the human fungal pathogen *C. albicans*, Cdc42 is required for filamentous growth, with mutants that have reduced levels of this GTPase unable to form hyphae and specific Cdc42 point mutants exhibiting defects in the yeast to hyphal transition (Bassilana et al., 2003; Ushinsky et al., 2002; VandenBerg et al., 2004). A dramatic redistribution of active Cdc42 has been observed at the incipient germ tube in *C. albicans*, with a 10-fold increase in local concentration (Corvest et al., 2013). In *C. albicans* germ tubes, the Ras-like GTPase Rsr1 is important for the tight localization of active Cdc42 at the apex (Pulver et al., 2013). Expression of a constitutively active GTP-bound form of Cdc42 is lethal in *C. albicans* (Ushinsky et al., 2002), and conditional expression of this activated mutant in hyphal cells resulted in cell swelling and reduced or altered polarity (Brand et al., 2014; Court and Sudbery, 2007).

To investigate how a new polarized growth site occurs in an asymmetric cell, we have used optogenetic tools to recruit the key GTPase Cdc42 to the cortex in *C. albicans* filamentous cells. Here, we show that photo-recruitment of active Cdc42 all over the plasma membrane resets growth and results in a striking *de novo* cluster of secretory vesicles, which is highly dynamic, moving by hops and jumps, until a new growth site is subsequently established. Our results reveal that clustering of secretory vesicles can occur in the absence of directional growth.

RESULTS

Photo-Recruitment of Active Cdc42 Disrupts Polarized Growth

To investigate cell polarization in asymmetric cells, we established optogenetic tools, based on *Arabidopsis thaliana* cryptochromes (Kennedy et al., 2010), to recruit the key regulator of polarity Cdc42 all over the cortex in *C. albicans* cells. Specifically, we co-expressed membrane-tethered CibN (CibN-GFP-Ct_{Rac1}) with Cry2-mCh fused to a constitutively active Cdc42 mutant lacking its C-terminal membrane-targeting prenylation sequence (Cry2-mCh-Cdc42[G12V]$_{cyto}$) (Figure 1A). Cells co-expressing both fusions grew normally in the dark and the mutated

version of Cdc42 was quantitatively recruited to the plasma membrane (Figure 1B). A single pulse of 488-nm light (over the entire field of view), identical to the levels and times used for a GFP image, was sufficient to recruit active Cdc42 to the plasma membrane, with maximal recruitment observed after ~1 min, concomitant with depletion from the cytosol. Within 10 min of maximal plasma membrane recruitment, there was a decrease in plasma membrane signal (to pre-photoactivation levels) and a concomitant increase in cytoplasmic signal. Figure 1C shows that this fusion protein, which could be repeatedly recruited, was observed over the entire plasma membrane.

We next examined whether photo-recruitment of active Cdc42 perturbs cell growth. Recruitment of active Cdc42 dramatically perturbed budding growth, compared to control cells (Figure 2A). Measurements of the bud and mother cell size indicated that recruitment of active Cdc42 largely blocks polarized growth (Figure 2B)—the bud volume increased by on average only 2.6-fold following four photoactivation pulses, compared to 33-fold in the absence of Cdc42 recruitment. Nonetheless, we did observe non-polar growth, as unbudded and budded cells increased in overall size (compare cell sizes in Figure 1C at 0 and 100 min and Figure 2A at 0 and 80 min), indicating that plasma membrane recruitment of constitutively active Cdc42 specifically blocks polarized growth.

In cells that had begun to filament upon induction with serum, light-dependent recruitment of active Cdc42 blocked filament extension. Subsequently, new filamentous growth emerged more than 20 min after the last photoactivation pulse when the Cry2 fusion was no longer detectable at the cortex (Figures 1C and S1A). There was no correlation between the location of plasma-membrane-recruited active Cdc42 (over the entire plasma membrane with occasional clusters) and the new growth site (Figure S1B). As indicated above, photoactivation consisted of a 488-nm pulse identical to that used for a GFP image, which we have previously shown has no effect on filamentous growth (Ghugtyal et al., 2015; Labbaoui et al., 2017). Furthermore, addition of a mutation (Thr at position 35 in the effector loop changed to Ala) shown to disrupt active Cdc42 binding to its effectors (Davis et al., 1998; Gladfelter et al., 2001; Ottilie et al., 1995; Peter et al., 1996; Zheng et al., 1994) and plasma membrane recruitment of the resulting fusion (Cdc42[G12V,T35A]$_{cyto}$) did not alter filamentous growth (Figure S1C), with extension rates (0.3 μm/min; n = 9) identical to that of wild-type cells. These results indicate that the 488-nm pulses had no deleterious effect on filamentous growth and suggest that the perturbation we observe is due to an association of active Cdc42 with its effector. We also examined whether light-dependent recruitment of wild-type Cdc42 (which could be activated by endogenous GEF) altered filamentous growth and approximately 40% of cells (n = 100) displayed altered morphology following photoactivation. Given that upon recruitment of constitutively active Cdc42[G12V]$_{cyto}$ all of the filamentous cells exhibited altered morphology, this activated mutant was used for all subsequent studies.

New Growth Occurs in the Mother Cell or along the Filament

Since growth resumed subsequent to optogenetic recruitment in filamentous cells, we examined where this growth occurs. Strikingly, we observed that new filamentous growth could emerge from either the mother cell or the filament. In the latter case, growth occurred along the filament or resumed at the tip (Figure 2C). New growth, whether in the mother cell or the filament, had an identical extension rate to that of initial growth (Figure 2D), corroborating its physiological relevance. The majority of cells, ~75%, resumed growth at the tip, whereas ~20% of the cells initiated growth in the mother cell and ~5% initiated growth in the filament. Cells with shorter germ tubes (2–6 μm long) were more likely to initiate new growth in the mother cell, whereas cells with longer filaments (8–12 μm long) were more likely to initiate growth in the filament (Figure 2E). Following photo-recruitment, new growth, irrespective of its location, initiated on average 20 min after the last pulse, indicating that it occurred subsequent to the plasma membrane dissociation of Cry2-mCh- Cdc42[G12V]$_{cyto}$. We next examined the location of new growth along the filament as a function of filament length at the time of photoactivation. New growth could occur anywhere along the filament with a preference farther away from the tip with increasing initial filament lengths (Figure 2F). We also examined the angle between the new filament and initial filament when growth occurred in the mother cell. Figure 2G shows that growth occurred predominantly in the distal half of the mother cell (between ± 60° and 180° from the initial filament). Together, these data indicate *de novo* growth site formation and suggest that growth in longer filaments is more refractory to disruption.

Recruitment of Cdc42·GTP Disrupts Endogenous Active Cdc42 Localization

The timing of new filamentous growth relative to light-dependent active Cdc42 recruitment suggested that new growth occurs subsequent to the dissociation of Cry2-mCh-Cdc42[G12V]$_{cyto}$ from the membrane. To determine whether active Cdc42 recruitment either directly induces polarized growth or instead resets cell polarity, we followed the distribution of a reporter for active Cdc42 derived from the *S. cerevisiae* Cdc42 effector protein Gic2 (Cdc42- and Rac-interactive binding [CRIB]-mCh) (Corvest et al., 2013). In filamentous cells, a cluster of active Cdc42 observed at the filament apex prior to photoactivation (Figure 3A; Video S1) was no longer detectable following Cry2-GFP-Cdc42 [G12V]$_{cyto}$ recruitment. Quantitation of the ratio of growth site (tip) plasma membrane to cytoplasmic CRIB-mCh signal revealed an average reduction of ~2-fold following the second or third photoactivation (Figure 3B). Just prior to new growth, ~30 min after the last photoactivation pulse (28 ± 6 min; n = 15 cells), a cluster of active Cdc42 was again observed. Together, these results indicate that recruitment of Cdc42•GTP disrupts the initial cluster of active Cdc42, which subsequently forms a cluster at a distinct location.

Endocytic Sites Disperse Subsequent to Cdc42·GTP Recruitment

As our results suggested that photo-recruitment of active Cdc42 resets cell polarity, we examined whether the sites of endocytosis and exocytosis remained localized. In growing hyphal filaments, endocytic sites localize as a collar 1–3 μm from the filament tip (Caballero-Lima et al., 2013; Ghugtyal et al., 2015;

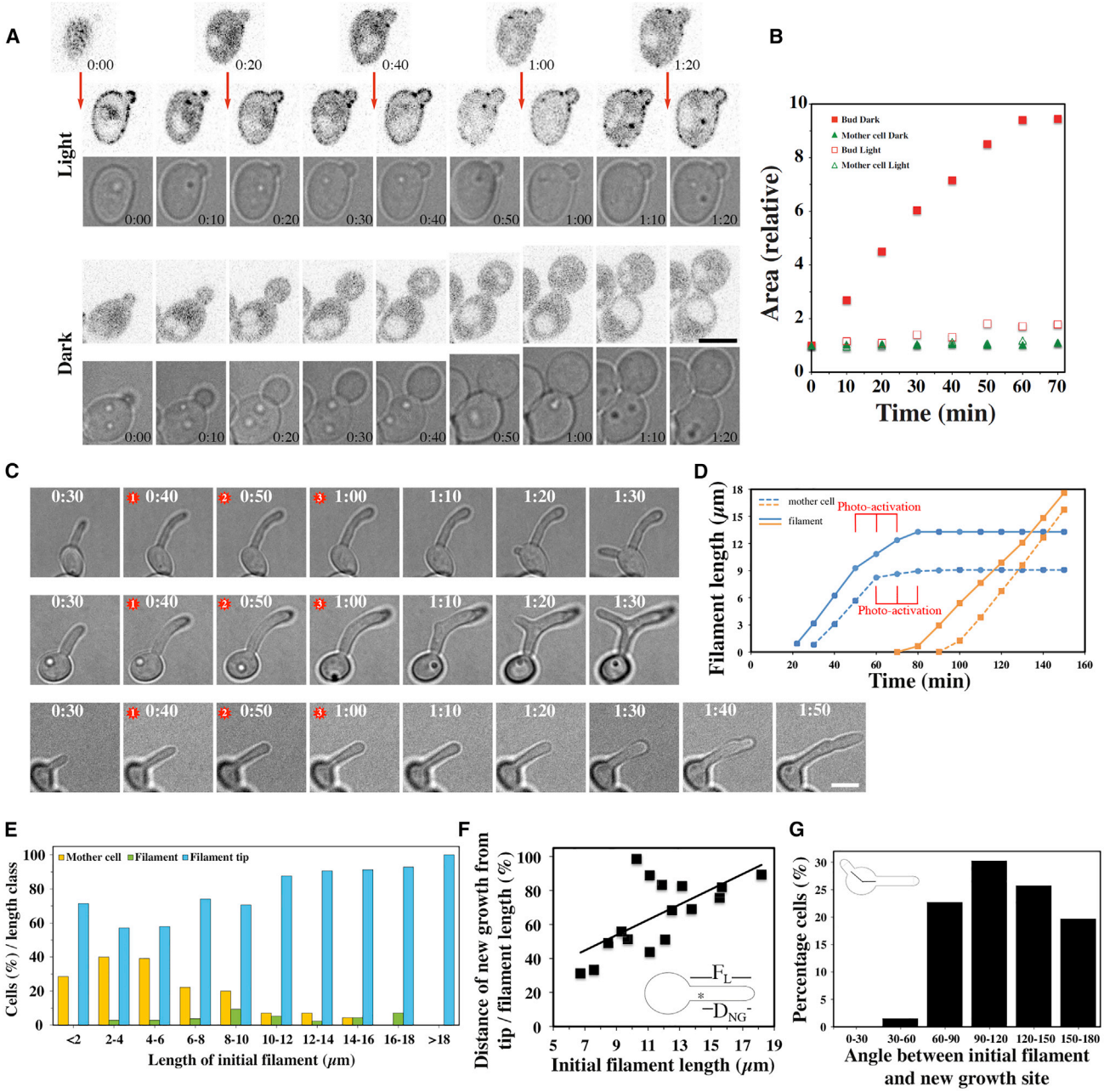

Figure 2. Plasma Membrane Recruitment of Cdc42·GTP Disrupts Polarized Growth

(A) Polarized budding growth is blocked following Cdc42•GTP recruitment. Strain was incubated as in Figure 1B and either exposed (Light) or not (Dark) to 488-nm light, as in Figure 1C. mCh (upper panel) and differential interference contrast (DIC) images (lower panel) for each time course are shown.

(B) Quantification of bud and mother cell area following photo-recruitment of Cdc42•GTP. Average relative area in cells (n = 5) with photoactivation at 0, 20, 40, and 60 min.

(C) Following recruitment of Cdc42•GTP in filamentous cell, new growth can occur in the mother cell or along the filament. Strain as in Figure 1B was incubated on agar pads containing serum at 37°C and exposed to 3 pulses of 488-nm light (red stars). In the absence of 488-nm light, filamentous cells grew normally.

(D) New growth occurs at same rate as the initial filament. Length of new filament emerging either from filament (solid lines) or mother cell (dashed lines) is shown.

(E) New growth location depends on initial filament length. Percentage of cells in each filament length class in which new growth emerged from mother cell (yellow), filament (green), or resumed at tip (blue). Strain and conditions as in Figure 2C. Quantification of 425 cells (from 11 experiments) followed by time-lapse microscopy (n = 15–80/length class).

(F) New growth in filament occurs preferentially farther from the tip for cells with longer initial filaments. Strain and conditions as in Figure 2C. Location of growth in filament divided by initial filament length is shown (n = 16; 8 experiments followed by time-lapse microscopy).

(G) New growth in the mother cell occurs medially to initial filament. Strain and conditions as in Figure 2C. Angle of the new germ tube relative to the initial filament was quantified (n = 66 cells; 9 time-lapse experiments). Scale bar, 5 μm.

Zeng et al., 2012) and secretory vesicles localize to the tip, in a cluster referred to as a Spk (Riquelme, 2013; Riquelme and Sánchez-León, 2014). We visualized sites of endocytosis using actin-binding protein 1 (Abp1), which localizes to this endocytic collar. Following recruitment of active Cdc42 to the plasma membrane, the tip cluster of the Abp1-mCh dispersed, and ~10 min after the last photoactivation pulse, there was an increase in Abp1-mCh signal in the mother cell, which clustered at the incipient germ tube ~30 min later (Figures 3C and 3D; Video S2). These results suggest that endocytosis at the filament tip is disrupted by photo-recruitment of active Cdc42 over the plasma membrane.

Cdc42·GTP Recruitment Results in a *De Novo* Secretory Vesicle Cluster

To visualize secretory vesicles, we examined a number of proteins that associate with these vesicles and have been localized to the Spk. These include the myosin light chain, Mlc1, the Rab GTPases, Sec4 and Ypt31, and the Sec4 GEF, Sec2, which associate on secretory vesicles in *S. cerevisiae* (Ortiz et al., 2002; Wagner et al., 2002), as well as localize to the Spk at the filament tip (Bishop et al., 2010; Crampin et al., 2005; Jones and Sudbery, 2010; Li et al., 2007; Ortiz et al., 2002; Pantazopoulou et al., 2014; Sánchez-León et al., 2015). Strikingly, immediately following plasma membrane recruitment of Cdc42·GTP, a second cluster of Mlc1-mCh was observed, typically in the cell body or base of the filament (Figures 3E and S2; Video S3, compare with Video S4). Note that while one additional cluster of Mlc1 was observed subsequent to photoactivation, occasionally we observed 2 or more clusters. The initial cluster of Mlc1-mCh persisted for some time after the appearance of the second Mlc1 cluster, moved down the filament over time, and eventually appeared to coalesce with the second Mlc1 cluster. This coalesced Mlc1 cluster, which was always localized to the cell cortex, was highly dynamic before settling down to the site of the incipient germ tube (Figures 3F and S2). In all cells examined, the final location of the secretory vesicle cluster at the cell cortex was precisely where the new filament emerged, suggesting that this vesicle cluster is physiologically relevant. While we focused on cells in which plasma membrane recruitment of Cdc42·GTP ultimately resulted in filamentous growth at new location (Figures 3E, 3F, and S2; Video S3), we also examined cells in which, after a pause, tip growth resumed. Figure S3A shows a second cluster of Mlc1-mCh, observed frequently in the cell body, which behaved similarly as that in Figures 3E, 3F, and S2. However, in these cells, this second cluster of Mlc1-mCh did not settle at new location from which a new filament would emerge. When we compared cells with the same initial filaments length, it appeared that more photoactivation pulses were required to disrupt the initial Spk when new growth resumed at the tip (Figures 3E and S2 compared to Figure S3A), suggesting that when the growth site was more robust, new growth resumed at the tip.

Hence, we examined whether there was a correlation between the ability to disrupt the Spk and filament length upon photoactivation. Fewer photoactivation pulses were required to disrupt the initial Spk in cells with shorter filaments than in cells with longer filaments (Figure 3G). These results suggest that the growth site in shorter filaments is less robust compared to that of longer filaments. In the absence of photoactivation, the cluster of Mlc1 was restricted to the tip and moved as the filament extended at a rate of ~0.3 μm/min (Video S4). Following photoactivation, there was a dramatic increase in the instantaneous velocity of the Mlc1 cluster, with peaks of up to 10-fold higher, i.e., 3–4 μm/min (Figure S4A), inconsistent with association and dissociation. The shape of the Mlc1 cluster, which appeared as a sphere (projected onto the XY plane) in the absence of photoactivation, elongated along the axis of movement following photoactivation, further consistent with its displacement (Figure S4B). While photo-recruitment of active Cdc42 blocked polarized growth, tip swelling was observed (Figure 2C), suggesting a switch to isotropic growth. Unstable, dynamic polarity clusters, in particular active Cdc42 visualized by the CRIB domain, have been observed in *S. pombe* upon slowing or stopping cell growth (Bendezú and Martin, 2013; Bonazzi et al., 2014, 2015; Haupt et al., 2018; Mutavchiev et al., 2016), hence we examined whether such dynamic behavior of the Mlc1 cluster was observed upon decreasing growth rate using an *arl1* mutant that has a decreased filament extension rate, as well as frequently abandoning tip growth (Labbaoui et al., 2017). In these mutant cells, the Spk was unaffected by the reduced growth rate, and upon abandoning growth at the filament tip, a new vesicle cluster only became visible at the incipient germ tube site either concomitant with or subsequent to the loss of the initial cluster (Figure S3B). Together these results indicate that recruitment of active Cdc42 over the plasma membrane results in a *de novo* cluster of Mlc1, which is highly dynamic and not a consequence of reduced growth rate.

In *C. albicans* hyphae, while Mlc1 is observed at the Spk with little to no signal elsewhere in the cell (Crampin et al., 2005; Jones and Sudbery, 2010), Sec4 is found both at this apical location and associated with individual secretory vesicles (Ghugtyal et al., 2015; Jones and Sudbery, 2010; Li et al., 2007; Wakade et al., 2017). Using mScarlet (mSc) fused to Sec4, we followed the distribution of secretory vesicles after photoactivation. Figure 4A (Video S5 compared to Video S4 without photoactivation) shows Sec4 at the tip of an emerging germ tube and, within 1 min of photo-recruitment of active Cdc42, a new cluster of Sec4 forms in the mother cell. This new cluster was highly dynamic (Figure S4C), similar to the dynamics of the Mlc1 cluster, and in a strain expressing both mSc-Sec4 and Mlc1-miRFP, these two proteins co-localized throughout the time course (Figure S4D; Video S6). To provide additional evidence that this new cluster of Mlc1 and Sec4 was composed of secretory vesicles, we examined two additional secretory vesicle components, the Sec4 GEF, Sec2, and the Rab11 homolog, Ypt31; the former is found at the Spk in *C. albicans* (Bishop et al., 2010), and the latter localized to secretory vesicles in *S. cerevisiae*, *N. crassa*, and *A. nidulans* and the Spk in *N. crassa*, *A. nidulans*, and *C. albicans* (Ortiz et al., 2002; Pantazopoulou et al., 2014; Sánchez-León et al., 2015; Wakade, 2017). Immediately following plasma membrane photo-recruitment of active Cdc42, we observed that Sec2 and Ypt31 co-localized with Mlc1 at the new cluster (Figures 4B, 4C, S5A, and S5B), despite the relatively low signals of Sec2-mSc and Ypt31-mCh. To determine whether this new cluster of secretory vesicles also contained markers for other membrane compartments, we used

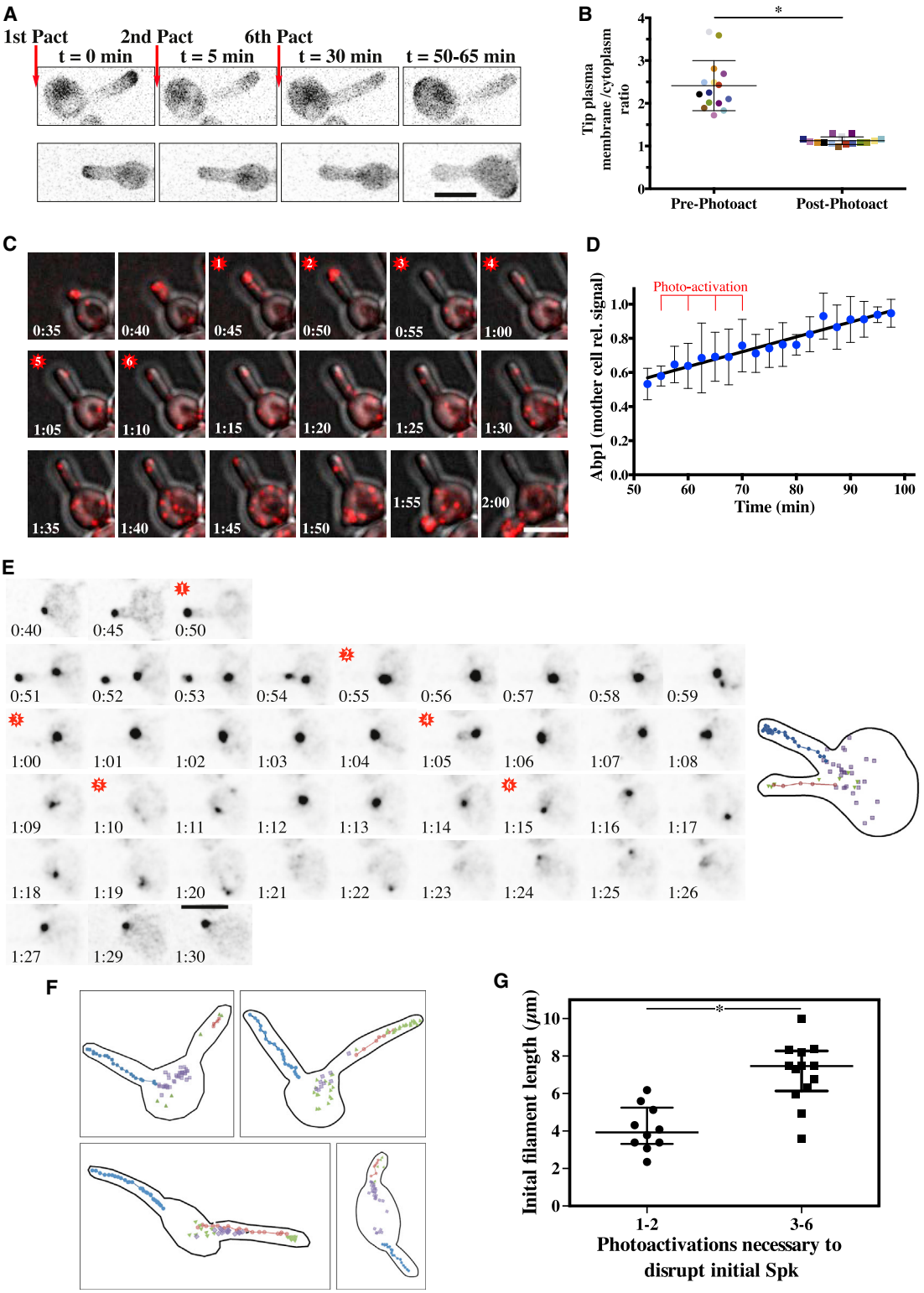

Figure 3. Photo-Recruitment of Cdc42·GTP Disrupts Endogenous Cdc42 Activation and Endocytosis Sites at Filament Tip

(A) Following photoactivation, active Cdc42 at the filament tip is no longer detectable. A strain expressing CibN-Ct_{Rac1}, Cry2-GFP-Cdc42[G12V]$_{cyto}$, and CRIB-mCh was incubated as in Figure 2C and exposed to 6 pulses of 488-nm light every 5 min. DIC and maximum projection mCh images are shown from

(legend continued on next page)

strains expressing Mlc1-miRFP and either the endoplasmic reticulum (ER) marker phosphatidylinositol-4-phosphate phosphatase, Sac1 (Foti et al., 2001; Weiner et al., 2019), or the late Golgi maker Arf GEF, Sec7 (Ghugtyal et al., 2015). Figures 4D and S5C show that the ER is distinct from the new cluster labeled with Mlc1, which is best visualized in a three-dimensional reconstruction (Video S7), indicating there is a gap between the ER membranes and the Mlc1 cluster. In *C. albicans* hyphae, the Golgi cisternae are somewhat enriched at the apex (Ghugtyal et al., 2015; Rida et al., 2006), and consistently, prior to plasma membrane photo-recruitment of active Cdc42, Sec7-mSc labeled Golgi cisternae also clustered behind the Spk (Figures 4E and S5D). Recruitment of active Cdc42 resulted in dispersal of the Golgi cisternae, which appeared to transiently align between the two vesicle clusters without any detectable overlap (Figures 4E and S5D). Together, these data indicate that photo-recruitment of active Cdc42 results in a *de novo* secretory vesicle cluster, which is distinct from ER and Golgi membrane compartments.

We noted that the new cluster of vesicles, visualized with mSc-Sec4, appeared larger than the initial cluster (Figure 4A; Video S5). Quantitation of its maximal cross-sectional area revealed a 4.7-fold increase (n = 14; compared to the initial cluster), and the average signal of this new cluster increased ~4-fold, following photoactivation, concomitant with a decrease in the cytoplasmic signal (Figure S4E). Furthermore, the ratio of Sec4 to Mlc1 signal in a strain co-expressing mSc-Sec4 and Mlc1-miRFP increased 3- to 4-fold, resulting in a shift in the cluster of vesicles from magenta (Mlc1) to green (Sec4) upon photoactivation and then back to magenta ~10 min after the last photoactivation pulse (Figures S4D, S4F, and S4G; Video S6). Sec4 recruitment was observed at both the initial Spk and the new dynamic vesicle cluster (Figure S4H). Unfortunately, the relatively low signals of Ypt31-mCh and Sec2-mSc prevented such extensive analyses, yet immediately following photoactivation, we observed at the new vesicle cluster a similar increase of Ypt31 (2- to 3-fold, n = 13, compared to Mlc1-miRFP levels) and in two-thirds of the cells quantified (n = 12) a transient increase of Sec2 (~2-fold compared to Mlc1-miRFP levels). Together, these data suggest that photo-recruitment of active Cdc42 results in a *de novo* secretory vesicle cluster, with a concomitant increase level of Sec4 and Ypt31.

Cdc42·GTP Recruitment Disrupts Sec3 Localization and Reduces Turnover of Secretory Vesicles

As the new cluster of secretory vesicles was substantially larger than the initial Spk and hyphal filaments did not appear to extend (polarized tip growth) following photo-recruitment of active Cdc42, we speculated that there was a defect in polarized secretion. Since the exocyst subunit Sec3, which localizes to the cortical tip of the hyphae in *C. albicans* (Ghugtyal et al., 2015; Jones and Sudbery, 2010; Li et al., 2007), is critical for targeting and/or tethering secretory vesicles (Luo et al., 2014) and binds active Cdc42 (Zhang et al., 2001) in *S. cerevisiae*, we examined whether it remains at the filament tip subsequent to photo-recruitment of active Cdc42. Figures 5A and 5B show that upon photo-recruitment of active Cdc42, Sec3-mSc signal is no longer detectable at the apex, which we expect would lead to a reduction in polarized vesicle fusion with the plasma membrane. Therefore, one expects that the turnover of secretory vesicles in this new cluster should be reduced, compared to that of the initial Spk. The dynamics of secretory vesicle turnover was determined using fluorescence recovery after photobleaching (FRAP) (Figure 6A). The FRAP $t_{1/2}$ of the initial Spk, 8.1 ± 2.7 s (n = 10), was in good agreement with the value determined previously (7.3 s) (Jones and Sudbery, 2010), while the new cluster of secretory vesicles was significantly less dynamic with a FRAP $t_{1/2}$ of 22.0 ± 9.0 s (n = 11) (Figure 6B), consistent with a reduction in vesicle fusion with plasma membrane.

The Actin Cytoskeleton Is Associated with the New Vesicle Cluster

The delivery of secretory vesicles to the Spk requires actin cables, which emanate from this structure; indeed, depolymerization of F-actin disrupts the Spk (Crampin et al., 2005). To determine whether actin cables were intact following active Cdc42 photo-recruitment, actin was visualized in fixed cells expressing Mlc1-miRFP after the appearance of two clusters (Figure 7A). Figure 7A (Light) shows an apparent decrease in the actin cables around the initial Spk following photoactivation, while the new cluster appears to have actin cables emanating from it, frequently oriented toward the back of the mother cell. This raises the attractive possibility that movement of this new cluster might be actin driven, much like actin-dependent propulsion of endosomes, pinosomes, and phagosomes

2 time-lapses. Photo-recruitment did not result in an increase in the CRIB-mCh reporter on the plasma membrane, suggesting that the Cry2 fusion does not efficiently bind the reporter, perhaps due to the Cry2-GFP moiety.

(B) The level of active Cdc42 at the growth site decreases following photoactivation. The ratio of tip to cytoplasmic signal was determined at the 1st and either 2nd or 3rd photoactivation as in Figure 3A (n = 15 cells; 5 experiments); colors indicate same cell. The average and SD are shown, and the difference was statistically significant using an unpaired t test, $p < 0.0001$.

(C) Endocytosis sites become dispersed upon photo-recruitment of Cdc42•GTP. A strain expressing CibN-Ct_{Rac1}, Cry2-GFP-Cdc42[G12V]$_{cyto}$, and Abp1-mCh was incubated as in Figure 3A (red stars, photo-activations). DIC and maximum projection mCh images are shown from a representative time-lapse.

(D) Abp1 in the mother cell increases following photoactivation. Quantification of Abp1-mCh signal in the mother cell (n = 7; 3 experiments) over time is shown, with the signal at time of new germ tube emergence set to 1. The average and SD are shown.

(E) Cluster of secretory vesicles becomes highly dynamic following recruitment of active Cdc42. A strain expressing CibN-Ct_{Rac1}, Cry2-GFP-Cdc42[G12V]$_{cyto}$ and Mlc1-mCh was incubated as in Figure 3A. DIC and sum projection mCh images are shown from a representative time-lapse (images every 2.5 min prior to photoactivation and 1 min, thereafter, left panel). Right panel shows location of Mlc1 cluster in the final cell shape with location in initial extending germ tube (red), existence of two clusters (green), dynamic cluster in mother cell (purple), and cluster in final extending germ tube (blue).

(F) Mlc1 cluster is highly dynamic following recruitment of active Cdc42. Location of Mlc1 cluster in 4 cells as in Figure 3E.

(G) Mlc1 cluster is more easily disrupted in shorter filaments. Strain as in Figure 3E was analyzed as above and the number of photoactivation pulses necessary to disrupt initial Mlc1 cluster was determined as a function of filament length (n = 25; 9 experiments), followed by time-lapse microscopy. The average and SD are shown, and the difference between cells with shorter and longer filaments was statistically significant using an unpaired t test, $p < 0.0001$. Scale bar, 5 μm.

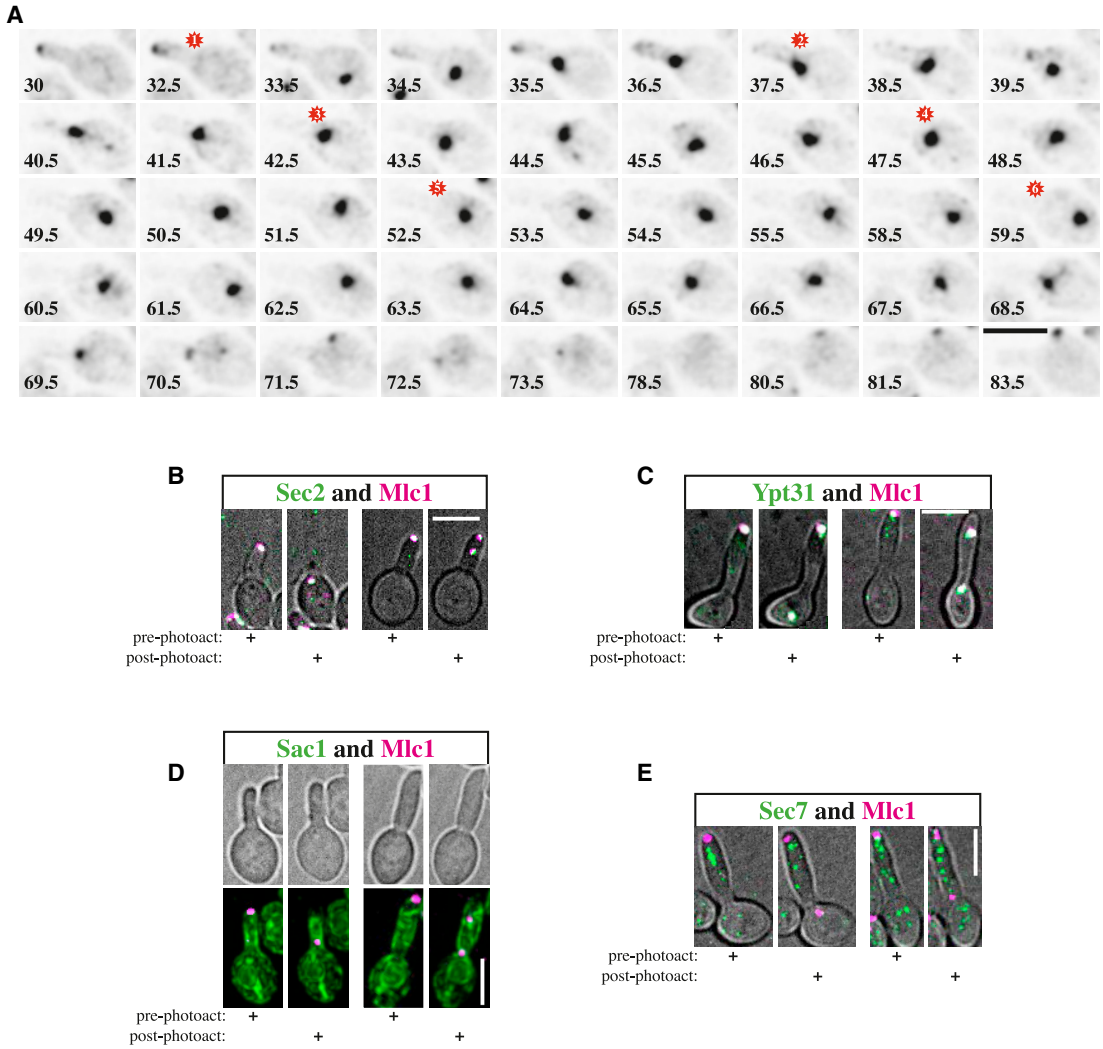

Figure 4. Recruitment of Cdc42·GTP Induces *De Novo* Secretory Vesicle Clustering

(A) Sec4 dynamics following photo-recruitment of active Cdc42. Strain expressing CibN-Ct_{Rac1}, Cry2-GFP-Cdc42[G12V]$_{cyto}$, and mSc-Sec4 was incubated and analyzed as in Figure 3E, and a representative time-lapse is shown.

(B) Sec2 is localized to the new vesicle cluster. A strain expressing CibN-Ct_{Rac1}, Cry2-GFP-Cdc42[G12V]$_{cyto}$, Sec2-3x-mSc, and Mlc1-miRFP was incubated as in Figure 3E, and maximum projections of RFP (green) and miRFP (magenta) images merged with DIC images from a representative time-lapse are shown. Pre-photoactivation denotes < 1 s after 488-nm light exposure and post-photoactivation 2.5 min later.

(C) Ypt31 is localized to the new vesicle cluster. A strain expressing CibN-Ct_{Rac1}, Cry2-GFP-Cdc42[G12V]$_{cyto}$, mCh-Ypt31, and Mlc1-miRFP was incubated and analyzed as described in Figure 4B.

(D) The new vesicle cluster does not overlap with the endoplasmic reticulum. A strain expressing CibN-Ct_{Rac1}, Cry2-GFP-Cdc42[G12V]$_{cyto}$, Sac1-mSc, and Mlc1-miRFP was incubated and analyzed as described in Figure 4B, except pre-photoactivation indicates 1 min prior exposure to 488-nm light and post-photoactivation 5 min later.

(E) The new vesicle cluster is distinct from the late Golgi. A strain expressing CibN-Ct_{Rac1}, Cry2-GFP-Cdc42[G12V]$_{cyto}$, Sec7-3x-mSc, and Mlc1-miRFP was incubated and analyzed as described in Figure 4B. Scale bar, 5 μm.

(Merrifield et al., 1999; Southwick et al., 2003; Taunton et al., 2000).

Modeling Secretory Vesicle Cluster Dynamics

To determine whether this cluster of vesicles moves in a random or directed fashion, we analyzed its movement on the cortex (approximating the mother cell as a sphere) from 10 cells following photoactivation (Figure 7B). First, we derived the colatitude of the cluster with respect to the initial position (θ in Figure S6A), and the square angular displacement (colatitude θ^2) does not depend on time, inconsistent with a pure diffusion process (Figure S6B compared to Figure S6C; Figure S6D). Figure 7C (compared to Figure S7A) confirms that the dynamics of the vesicle cluster is not simply diffusive but rather that movement is strikingly confined to a small region; from the north pole this would be roughly up to the 30th parallel north. These

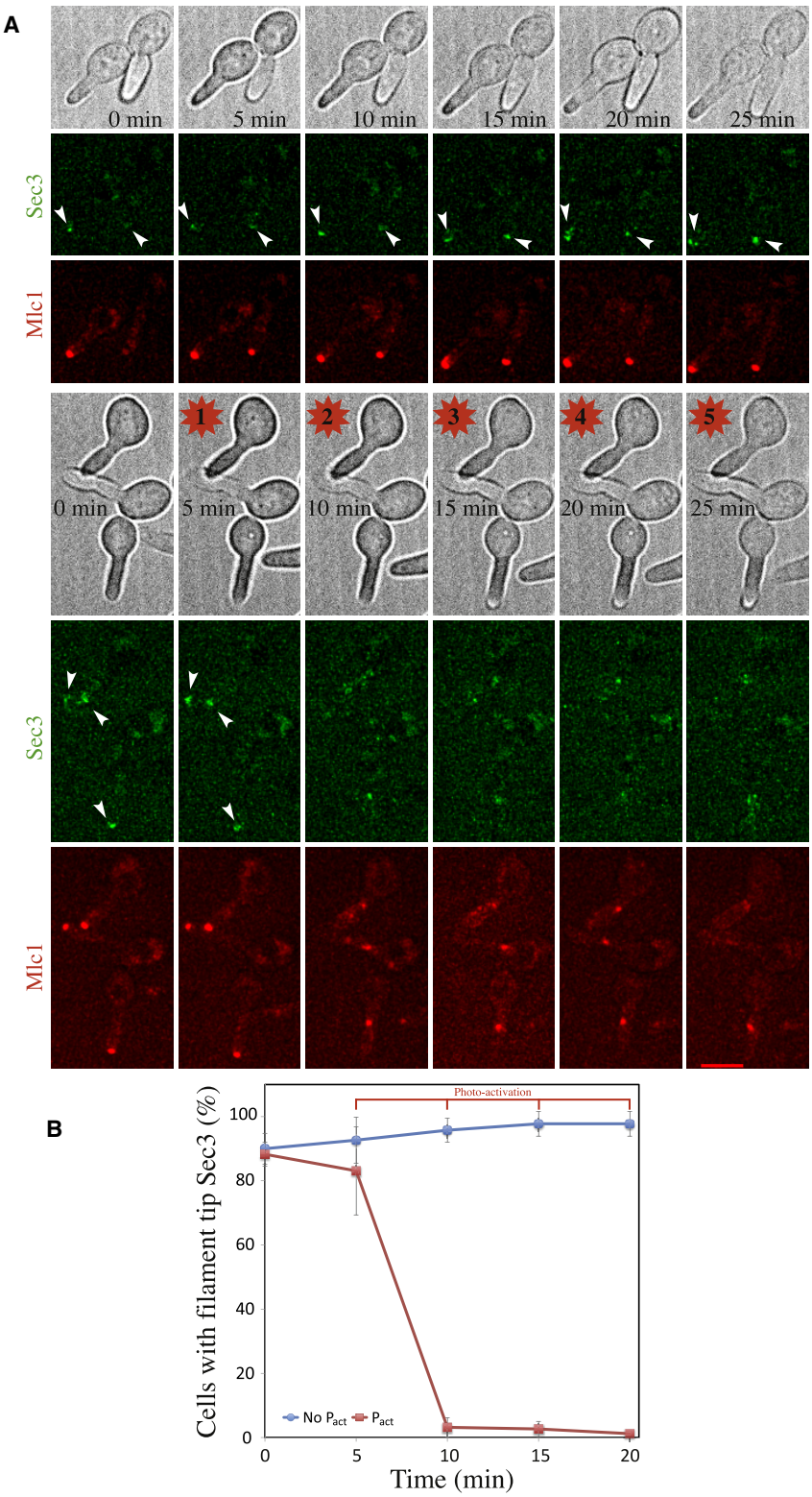

Figure 5. Optogenetic Recruitment of Cdc42·GTP Disrupts Sec3 Filament Tip Localization

(A) Following recruitment of Cdc42·GTP, Sec3 is no longer observed at filament tip. A strain expressing CibN-Ct_{Rac1}, Cry2-GFP-Cdc42[G12V]$_{cyto}$, Sec3-3x-mSc, and Mlc1-miRFP was incubated as in Figure 3E, and maximum projections of RFP (green) and miRFP (red) images are shown from a representative time-lapse (arrowheads indicate Sec3 at tip cortex).

(B) Quantitation of the percentage of cells with Sec3 localized to the hyphal apex upon optogenetic recruitment of Cdc42·GTP. The percentage of cells in which both Sec3-mSc and Mlc1-miRFP were visible at filament tip was quantitated from time-lapses as described above. Cells were exposed or not to 488-nm light (n = 15–30 cells per experiment; 3 experiments) with the mean and standard deviation shown. Scale bar, 5 μm.

conclusions are robust, even for analyses of the early (t < 10 min) or late (t > 15 min) times, corroborating that this effect is not due to a transient in time (compare Figures S7B and S7C). The cluster often moves in a series of short hops, but it occasionally undergoes large jumps (Figure 7C, inset). These long-range displacements, akin to flipping of the poles, were observed in the majority of cells and are also likely to be movement, as intermediate steps were occasionally detected (Figure 7B). We hypothesize that two non-mutually exclusive mechanisms could underlie such vesicle cluster dynamics: (1) actin cytoskeleton confines or drives movement and (2) interactions with the cortex, e.g., a protein anchor or specific lipid environment limits movement (Figure 7D). Disruption of such confining or limiting processes could result in long-range displacements across the cell.

DISCUSSION

We used optogenetic manipulation of cell polarity to reset growth in asymmetric filamentous *C. albicans* cells. A transient increase of the overall level of Cdc42·GTP on the plasma membrane disrupted the cluster of endogenous active Cdc42, the key exocyst subunit Sec3 at the filament tip, and the collar of endocytosis sites proximal to the filament apex. In contrast, a striking *de novo* cluster of secretory vesicles formed, distinct from the ER and Golgi, which had a number of hallmarks of the Spk. Furthermore, it was highly dynamic, moving in an active fashion by hops and jumps, until a new growth site was subsequently established.

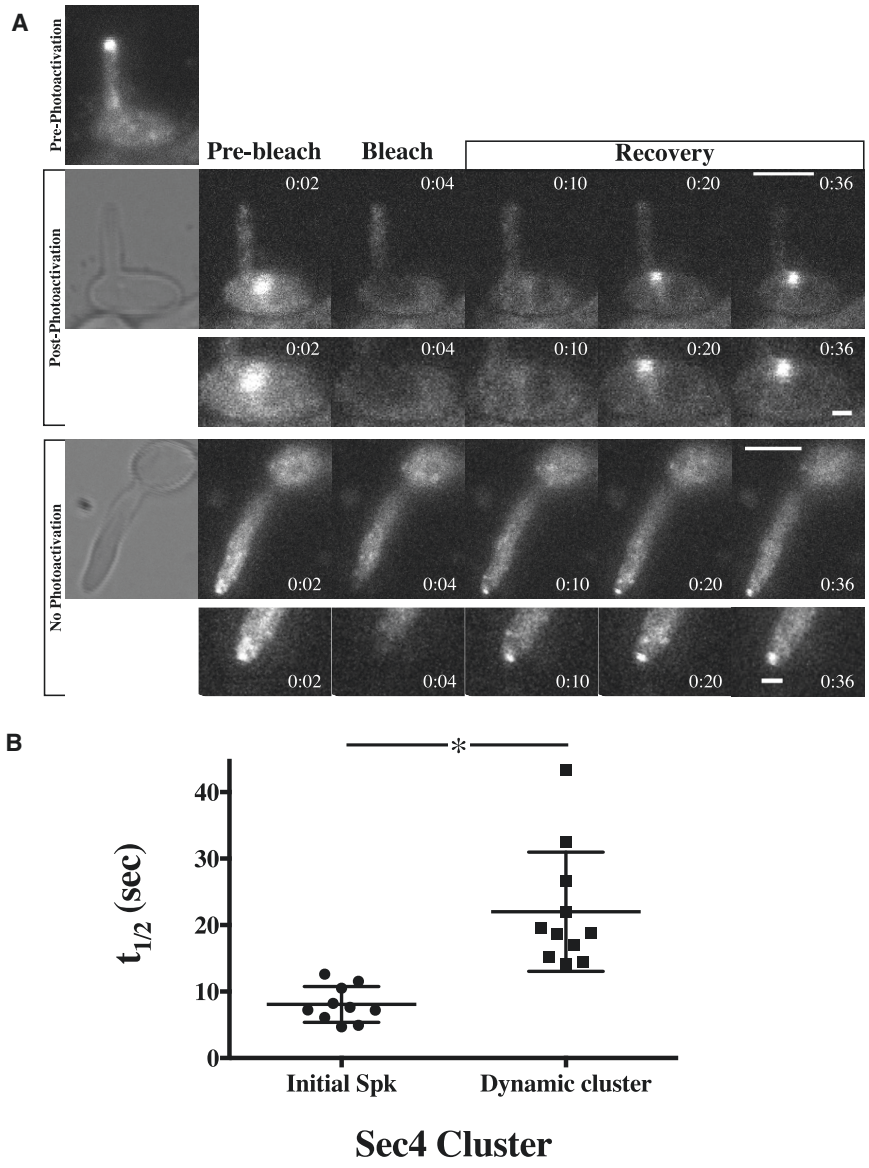

Figure 6. Sec4 Exchanges More Slowly in the New Secretory Vesicle Cluster Than in the Initial Spitzenkörper

(A) Fluorescent recovery after photobleaching of Sec4 prior to or following photo-recruitment of active Cdc42. A strain expressing CibN-Ct_{Rac1}, Cry2-GFP-Cdc42 $[G12V]_{cyto}$, and mSc-Sec4 was incubated as in Figure 4A, RFP images were acquired at indicated times (in seconds), and a representative FRAP experiment is shown. Photobleaching was at 4 s, and a zoom of the region analyzed is shown below. Scale bar, 5 μm and 1 μm in zoom of region.

(B) The half-time for recovery of Sec4 fluorescence is significantly slower in the new cluster. The $t_{1/2}$ for fluorescence recovery was determined for 10–11 cells, with the average and SD shown, and the difference was statistically significant using an unpaired t test, p = 0.0001.

How does this growth reset compare to filament branching? During hyphal growth, branching is critical for increasing biomass and effectively accessing nutrients and occurs laterally, i.e., along the filament, and at the apex (Harris, 2019). During apical branching in *N. crassa*, the extension of the initial apex was substantially reduced and the Spk no longer detectable, whereas they were largely unaffected during lateral branching (Reynaga-Peña et al., 1997; Riquelme and Bartnicki-Garcia, 2004). Also, during apical branching in this fungus, as well as in *Aspergillus niger* and a range of other fungi, a new Spk, visualized by phase contrast imaging, appeared to form *de novo* via a coalescing of vesicles, where a new branch will form (Bartnicki-Garcia et al., 1995; López-Franco and Bracker, 1996; López-Franco et al., 1995; Reynaga-Peña et al., 1997; Riquelme and Bartnicki-Garcia, 2004). Transient retraction of the *N. crassa* Spk from the hyphal apex, coinciding with a reduction in filament extension and an alteration in morphology, has been visualized by following cell wall biosynthetic enzymes, the scaffold protein Spa2, and the membrane dye FM4-64; after retraction, the Spk did not return to the initial apical position, but rather

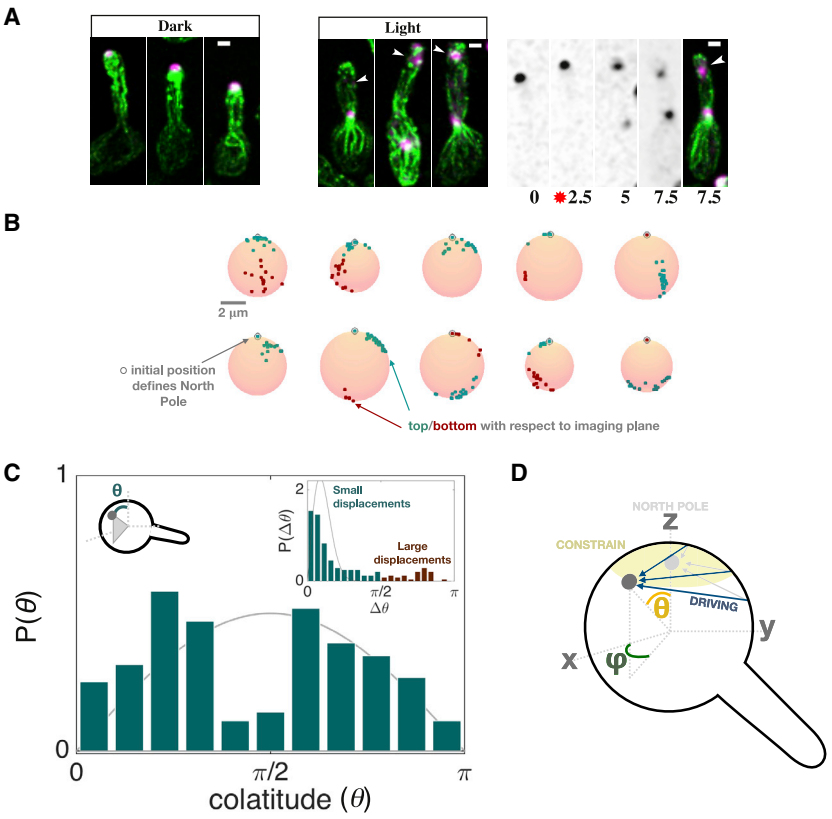

Figure 7. The Actin Cytoskeleton Is Associated with the New Vesicle Cluster, Whose Movement Is Constrained to a Small Region

(A) Actin cables emanate from newly formed cluster of secretory vesicles. A strain expressing CibN-Ct_{Rac1}, Cry2-GFP-Cdc42[G12V]$_{cyto}$, and Mlc1-miRFP was incubated and exposed to 488-nm light (Light) or not (Dark). After photoactivation (5 min), cells were fixed and the actin cytoskeleton visualized. In the right panel, cells were imaged every 2.5 min prior to fixing (7.5 min). Maximum projections of fixed cells with F-actin (green) and Mlc1 (magenta) shown. Scale bar, 1 μm.

(B) Positions of the experimentally determined vesicle clusters on mother cell cortex. The mother cell shape was approximated as a sphere and the x-y coordinates of the cluster were projected on the surface. The north pole coincides with the first cluster position in 10 cells expressing Mlc1-mCh, with spots indicating the top (green) and bottom (red) hemisphere relative to the central focal plane, respectively.

(C) Probability distribution of the cluster's colatitude for all cells at all times confirms that motion of the cluster is strikingly different from a purely diffusive process (line is theoretical prediction for diffusion at long times, no integral in time), $p = 3 \times 10^{-7}$; Kolmogorov-Smirnov test. Bimodality indicates that the cluster mostly populates a region proximal to the initial point, in addition to a distal region. The probability distribution of angular displacement in a single time step (inset) demonstrates that the cluster occasionally undergoes large jumps in a single step (dark red, frequency 18%), while most of the time it proceeds in smaller hops (green, frequency 82%). The line is the best fit of the theoretical prediction for pure diffusion to the data, inconsistent with the data ($p = 5 \times 10^{-13}$; Kolmogorov-Smirnov test). From this fit to the theoretical prediction, we obtained $\tau = 0.07$ ($t = 1$ min acquisition time and $R = 2.7$ μm is the average mother cell radius), hence this τ value corresponds to $D = 0.26$ μm^2/min.

(D) Schematic of the constrained movement of vesicle cluster. The three coordinates that define cluster location are the angles θ and φ and radius r. The region of restricted vesicle movement is highlighted in yellow, with initial cluster location indicated in light gray and subsequent location in dark gray. Light gray (initial) and dark blue (subsequent) arrows indicate the contribution of forces driving movement, e.g., actin cable polymerization.

an additional Spk appeared to form at the apex (Araujo-Palomares et al., 2009; Sánchez-León et al., 2011; Verdín et al., 2009). Although we did not observe new growth emerge within several microns of the hyphal apex, the extension of the initial tip was dramatically reduced upon photo-recruitment of active Cdc42 in *C. albicans*, suggesting that this process is similar, in some respects, to apical branching in filamentous fungi. However, it should be noted that extension rates are 10- to 100-fold slower in *C. albicans* compared to these fungi, whose growth also depends on microtubule cytoskeleton, and that the Spk composition is different (Weiner et al., 2019).

What is the relationship between growth and the *de novo* vesicle cluster? In *S. cerevisiae* and *S. pombe*, recent studies in symmetrical cells, such as spores or sexually differentiated cells exposed to low mating pheromone concentrations, have revealed situations in which polarity clusters can switch from stable behavior at a growth site to unstable wandering around the cell cortex or vice versa (Bendezú and Martin, 2013; Bonazzi et al., 2015; Bonazzi et al., 2014; Dyer et al., 2013; Haupt et al., 2018; Mutavchiev et al., 2016). These unstable polarity clusters were associated with a slowing or stopping of cell growth. Examination of a *C. albicans* mutant decreased in filament extension and altered in restricting growth to a single site (Labbaoui et al., 2017) also exhibited an unstable, wandering cluster of active Cdc42, yet in this mutant we observed only one cluster of secretory vesicles at a time, without dynamic behavior, visible at the new incipient germ tube site when the initial Spk was essentially undetectable (Figure S3B). In the recent study of Haupt et al. (2018), *S. pombe* growth inhibition by osmotic shock and physical confinement resulted in perturbation of the actin distribution. Blocking growth in *C. albicans* hyphae by actin depolymerization or in a *sec3* exocyst mutant disrupted the Spk vesicle cluster (Crampin et al., 2005; Jones and Sudbery, 2010; Li et al., 2007; Weiner et al., 2019). In contrast, in the present study, photo-recruitment of active Cdc42 did not alter actin patches and cables during the initial 5 min (Figures 3C and 7A), in which a new cluster of vesicles was already observed (Figures 3E and 4A). Hence, the cluster of secretory vesicles observed in this study appears to be distinct from the polarity cluster visualized with the CRIB reporter in the *S. pombe* study (Haupt et al., 2018), in which secretory vesicle components including a type V myosin, a cargo glucan synthase, and a v-SNARE were also less polarized at the cell tips upon blocking growth. Altogether, the distribution and dynamics of the vesicle cluster that forms

upon photo-recruitment of active Cdc42 does not appear to be solely due to blocking growth and transient destabilization of polarity. However, we consider it likely that feedback between the polarity site and the vesicle cluster via actin-cable-dependent transport, as reported in *S. pombe* (Bonazzi et al., 2015), is also implicated in the dynamics of this cluster in *C. albicans*.

What mechanisms underlie vesicle cluster dynamics? The cluster of vesicles formed immediately after photo-recruitment of active Cdc42 appears to have similarities to the initial Spk. First, this new cluster had actin cables emanating from it like the Spk, except that the cables cluster essentially on the distal side of the Spk. Second, four different proteins that localize to the Spk—a myosin light chain, two Rab GTPases, and a Rab GEF—were also found at this new vesicle cluster. In contrast, the new cluster of vesicles was not restricted to the filament apex, was highly dynamic, and the turnover of secretory vesicles was reduced compared to the Spk. Further knowledge of the Spk composition will be important for more in-depth comparison of these two structures. Our data indicate that the new cluster of vesicles undergoes active, directed movement. We envision two related driving forces for the movement of the new cluster of vesicles: (1) actin polymerization driven propulsion, similar to that observed with different organelles (Merrifield et al., 1999; Southwick et al., 2003; Taunton et al., 2000), and (2) actin-dependent myosin motors. In both of these scenarios, an intact actin cytoskeleton would be crucial, as it is for Spk integrity (Crampin et al., 2005; Jones and Sudbery, 2010; Weiner et al., 2019). Specifically, actin cables are critical in both cases, either to generate force upon elongation, when anchored at the cell cortex, or to function as tracks along which vesicle-associated motors move. We favor the former possibility, as it is hard to envision sufficient coordination of a large number of vesicle-associated motors—net displacement would be dramatically reduced as a function of number of motors. It will be necessary to correlate the displacement of the vesicle cluster with a precise number of actin cables and their length and curvature in order to distinguish between these possibilities.

In *N. crassa* and *A. gossypii*, the presence of a Spk correlated with hyphal extension rate, suggesting that this structure is a buildup of vesicles due to limiting fusion with the plasma membrane at the apical growth site (Araujo-Palomares et al., 2007; Köhli et al., 2008). Our results indicate that even in the absence of apical filament extension, a cluster of vesicles formed that appeared similar to the Spk, suggesting that clustering of secretory vesicles does not require directional growth. Our FRAP results suggest that exchange of secretory vesicles into and out of this new cluster was somewhat slower than that of the Spk. We propose that photo-recruitment of active Cdc42 resets growth by disrupting a site-specific link to the initial cluster of vesicles, which is likely to be the exocyst subunit Sec3; concomitantly, a vesicle cluster is generated elsewhere in the cell. This highly dynamic new cluster moves in a confined area with occasional large displacements, and modeling indicates that this behavior is likely to be a constrained or driven active process. In this scenario, re-establishment of a cap of endogenous active Cdc42 at a new location would anchor the cluster of secretory vesicles, facilitating subsequent fusion with the plasma membrane. Our results reveal that secretory vesicle clustering can occur in the absence of directional growth in an asymmetric cell, suggesting that such vesicle clusters found in fungi, plants, and neurons could precede stabilization of a growth site.

STAR★METHODS

Detailed methods are provided in the online version of this paper and include the following:

- KEY RESOURCES TABLE
- LEAD CONTACT AND MATERIALS AVAILABILITY
- EXPERIMENTAL MODEL AND SUBJECT DETAILS
  - Strains
- METHOD DETAILS
  - Strain and plasmid construction
  - Microscopy
  - Modeling
- QUANTIFICATION AND STATISTICAL ANALYSIS
- DATA AND CODE AVAILABILITY

SUPPLEMENTAL INFORMATION

Supplemental Information can be found online at https://doi.org/10.1016/j.celrep.2019.07.062.

ACKNOWLEDGMENTS

We thank J. Konopka and Y. Wang for reagents; S. Bogliolo, H. Labbaoui, M. Mondin, S. Schaub, and S. Lachambre for assistance; R. Wakade for the pEXPARG-YPT31p-mCh-Ypt31 construct; and F. Besse and P. Follette for comments on the manuscript. This work was supported by the CNRS, INSERM, UCA, and ANR (UCA JEDI, ANR-15-IDEX-01; SIGNALIFE, ANR-11-LABX-0028-01; FORFUNIGO, ANR-16-CE13-0010-01; DYNCELLPOL, ANR-19-CE13), CNRS PICS 2FORECAST, FRM (to P.M.S.), and EU FP7 as well as H2020 grants (PITN-GA-2013-607963 and MSCA-ITN- 2015-675407) and the Platform of Resources in Imaging and Scientific Microscopy (PRISM) facility.

AUTHOR CONTRIBUTIONS

Conceptualization, R.A.A. and M.B.; Methodology, P.M.S., C.P., A.S., and R.A.A.; Software, A.S.; Formal Analysis, A.S.; Investigation, P.M.S. and R.A.A.; Writing – Original Draft, R.A.A.; Writing – Review & Editing, M.B. and R.A.A.; Project Administration, R.A.A.; Funding Acquisition, M.B. and R.A.A.; Supervision, M.B. and R.A.A.; Visualization, R.A.A. and A.S.

DECLARATION OF INTERESTS

The authors declare no competing interests.

Received: December 30, 2018
Revised: April 22, 2019
Accepted: July 18, 2019
Published: August 20, 2019

REFERENCES

Araujo-Palomares, C.L., Castro-Longoria, E., and Riquelme, M. (2007). Ontogeny of the Spitzenkörper in germlings of *Neurospora crassa*. Fungal Genet. Biol. *44*, 492–503.

Araujo-Palomares, C.L., Riquelme, M., and Castro-Longoria, E. (2009). The polarisome component SPA-2 localizes at the apex of *Neurospora crassa* and partially colocalizes with the Spitzenkörper. Fungal Genet. Biol. *46*, 551–563.

Araujo-Palomares, C.L., Richthammer, C., Seiler, S., and Castro-Longoria, E. (2011). Functional characterization and cellular dynamics of the CDC-42 - RAC - CDC-24 module in *Neurospora crassa*. PLoS ONE *6*, e27148.

Bartnicki-Garcia, S., Bartnicki, D.D., Gierz, G., López-Franco, R., and Bracker, C.E. (1995). Evidence that Spitzenkörper behavior determines the shape of a fungal hypha: a test of the hyphoid model. Exp. Mycol. *19*, 153–159.

Bassilana, M., Blyth, J., and Arkowitz, R.A. (2003). Cdc24, the GDP-GTP exchange factor for Cdc42, is required for invasive hyphal growth of *Candida albicans*. Eukaryot. Cell *2*, 9–18.

Bassilana, M., Hopkins, J., and Arkowitz, R.A. (2005). Regulation of the Cdc42/Cdc24 GTPase module during *Candida albicans* hyphal growth. Eukaryot. Cell *4*, 588–603.

Bendezú, F.O., and Martin, S.G. (2011). Actin cables and the exocyst form two independent morphogenesis pathways in the fission yeast. Mol. Biol. Cell *22*, 44–53.

Bendezú, F.O., and Martin, S.G. (2013). Cdc42 explores the cell periphery for mate selection in fission yeast. Curr. Biol. *23*, 42–47.

Bendezú, F.O., Vincenzetti, V., Vavylonis, D., Wyss, R., Vogel, H., and Martin, S.G. (2015). Spontaneous Cdc42 polarization independent of GDI-mediated extraction and actin-based trafficking. PLoS Biol. *13*, e1002097.

Bernardo, S.M., Rane, H.S., Chavez-Dozal, A., and Lee, S.A. (2014). Secretion and filamentation are mediated by the *Candida albicans* t-SNAREs Sso2p and Sec9p. FEMS Yeast Res. *14*, 762–775.

Bibeau, J.P., Kingsley, J.L., Furt, F., Tüzel, E., and Vidali, L. (2018). F-Actin Mediated Focusing of Vesicles at the Cell Tip Is Essential for Polarized Growth. Plant Physiol. *176*, 352–363.

Bishop, A., Lane, R., Beniston, R., Chapa-y-Lazo, B., Smythe, C., and Sudbery, P. (2010). Hyphal growth in *Candida albicans* requires the phosphorylation of Sec2 by the Cdc28-Ccn1/Hgc1 kinase. EMBO J. *29*, 2930–2942.

Bonazzi, D., Julien, J.D., Romao, M., Seddiki, R., Piel, M., Boudaoud, A., and Minc, N. (2014). Symmetry breaking in spore germination relies on an interplay between polar cap stability and spore wall mechanics. Dev. Cell *28*, 534–546.

Bonazzi, D., Haupt, A., Tanimoto, H., Delacour, D., Salort, D., and Minc, N. (2015). Actin-Based Transport Adapts Polarity Domain Size to Local Cellular Curvature. Curr. Biol. *25*, 2677–2683.

Bou Daher, F., and Geitmann, A. (2011). Actin is involved in pollen tube tropism through redefining the spatial targeting of secretory vesicles. Traffic *12*, 1537–1551.

Bove, J., Vaillancourt, B., Kroeger, J., Hepler, P.K., Wiseman, P.W., and Geitmann, A. (2008). Magnitude and direction of vesicle dynamics in growing pollen tubes using spatiotemporal image correlation spectroscopy and fluorescence recovery after photobleaching. Plant Physiol. *147*, 1646–1658.

Brand, A.C., Morrison, E., Milne, S., Gonia, S., Gale, C.A., and Gow, N.A. (2014). Cdc42 GTPase dynamics control directional growth responses. Proc. Natl. Acad. Sci. USA *111*, 811–816.

Brunswik, H. (1924). Botanische Abhandlung (Jenna, Germany: Gustav Fischer).

Butty, A.C., Perrinjaquet, N., Petit, A., Jaquenoud, M., Segall, J.E., Hofmann, K., Zwahlen, C., and Peter, M. (2002). A positive feedback loop stabilizes the guanine-nucleotide exchange factor Cdc24 at sites of polarization. EMBO J. *21*, 1565–1576.

Caballero-Lima, D., Kaneva, I.N., Watton, S.P., Sudbery, P.E., and Craven, C.J. (2013). The spatial distribution of the exocyst and actin cortical patches is sufficient to organize hyphal tip growth. Eukaryot. Cell *12*, 998–1008.

Castro-Villarreal, P., Villada-Balbuena, A., Méndez-Alcaraz, J.M., Castañeda-Priego, R., and Estrada-Jiménez, S. (2014). A Brownian dynamics algorithm for colloids in curved manifolds. J. Chem. Phys. *140*, 214115.

Chapa-Y-Lazo, B., Lee, S., Regan, H., and Sudbery, P. (2011). The mating projections of *Saccharomyces cerevisiae* and *Candida albicans* show key characteristics of hyphal growth. Fungal Biol. *115*, 547–556.

Chiou, J.G., Balasubramanian, M.K., and Lew, D.J. (2017). Cell Polarity in Yeast. Annu. Rev. Cell Dev. Biol. *33*, 77–101.

Corvest, V., Bogliolo, S., Follette, P., Arkowitz, R.A., and Bassilana, M. (2013). Spatiotemporal regulation of Rho1 and Cdc42 activity during *Candida albicans* filamentous growth. Mol. Microbiol. *89*, 626–648.

Court, H., and Sudbery, P. (2007). Regulation of Cdc42 GTPase activity in the formation of hyphae in *Candida albicans*. Mol. Biol. Cell *18*, 265–281.

Crampin, H., Finley, K., Gerami-Nejad, M., Court, H., Gale, C., Berman, J., and Sudbery, P. (2005). *Candida albicans* hyphae have a Spitzenkörper that is distinct from the polarisome found in yeast and pseudohyphae. J. Cell Sci. *118*, 2935–2947.

Das, M., Wiley, D.J., Chen, X., Shah, K., and Verde, F. (2009). The conserved NDR kinase Orb6 controls polarized cell growth by spatial regulation of the small GTPase Cdc42. Curr. Biol. *19*, 1314–1319.

Davis, C.R., Richman, T.J., Deliduka, S.B., Blaisdell, J.O., Collins, C.C., and Johnson, D.I. (1998). Analysis of the mechanisms of action of the *Saccharomyces cerevisiae* dominant lethal cdc42G12V and dominant negative cdc42D118A mutations. J. Biol. Chem. *273*, 849–858.

Denker, A., Kröhnert, K., Bückers, J., Neher, E., and Rizzoli, S.O. (2011). The reserve pool of synaptic vesicles acts as a buffer for proteins involved in synaptic vesicle recycling. Proc. Natl. Acad. Sci. USA *108*, 17183–17188.

Dyer, J.M., Savage, N.S., Jin, M., Zyla, T.R., Elston, T.C., and Lew, D.J. (2013). Tracking shallow chemical gradients by actin-driven wandering of the polarization site. Curr. Biol. *23*, 32–41.

Ermak, D.L., and McCammon, J.A. (1978). Brownian dynamics with hydrodynamic interactions. J. Chem. Phys. *69*, 1352.

Foti, M., Audhya, A., and Emr, S.D. (2001). Sac1 lipid phosphatase and Stt4 phosphatidylinositol 4-kinase regulate a pool of phosphatidylinositol 4-phosphate that functions in the control of the actin cytoskeleton and vacuole morphology. Mol. Biol. Cell *12*, 2396–2411.

Freisinger, T., Klünder, B., Johnson, J., Müller, N., Pichler, G., Beck, G., Costanzo, M., Boone, C., Cerione, R.A., Frey, E., and Wedlich-Söldner, R. (2013). Establishment of a robust single axis of cell polarity by coupling multiple positive feedback loops. Nat. Commun. *4*, 1807.

Gallo Castro, D., and Martin, S.G. (2018). Differential GAP requirement for Cdc42-GTP polarization during proliferation and sexual reproduction. J. Cell Biol. *217*, 4215–4229.

Gerami-Nejad, M., Zacchi, L.F., McClellan, M., Matter, K., and Berman, J. (2013). Shuttle vectors for facile gap repair cloning and integration into a neutral locus in *Candida albicans*. Microbiology *159*, 565–579.

Ghosh, A., Samuel, J., and Sinha, S.A. (2012). A "Gaussian" for diffusion on the sphere. Europhys. Lett. *98*, 30003.

Ghugtyal, V., Garcia-Rodas, R., Seminara, A., Schaub, S., Bassilana, M., and Arkowitz, R.A. (2015). Phosphatidylinositol-4-phosphate-dependent membrane traffic is critical for fungal filamentous growth. Proc. Natl. Acad. Sci. USA *112*, 8644–8649.

Giese, W., Eigel, M., Westerheide, S., Engwer, C., and Klipp, E. (2015). Influence of cell shape, inhomogeneities and diffusion barriers in cell polarization models. Phys. Biol. *12*, 066014.

Girbardt, M. (1957). Der Spitzenkörper von *Polystictus versicolor* (L.). Planta *50*, 47–59.

Girbardt, M. (1969). Die Ultrastruktur der Apikalregion von Pilzhyphen. Protoplasma *67*, 413–441.

Gladfelter, A.S., Moskow, J.J., Zyla, T.R., and Lew, D.J. (2001). Isolation and characterization of effector-loop mutants of CDC42 in yeast. Mol. Biol. Cell *12*, 1239–1255.

Goryachev, A.B., and Leda, M. (2017). Cell Polarity: Spot-On Cdc42 Polarization Achieved on Demand. Curr. Biol. *27*, R810–R812.

Grove, S.N., and Bracker, C.E. (1970). Protoplasmic organization of hyphal tips among fungi: vesicles and Spitzenkörper. J. Bacteriol. *104*, 989–1009.

Gulli, M.P., Jaquenoud, M., Shimada, Y., Niederhäuser, G., Wiget, P., and Peter, M. (2000). Phosphorylation of the Cdc42 exchange factor Cdc24 by the PAK-like kinase Cla4 may regulate polarized growth in yeast. Mol. Cell *6*, 1155–1167.

Harris, S.D. (2019). Hyphal branching in filamentous fungi. Dev. Biol. *451*, 35–39.

Haupt, A., Ershov, D., and Minc, N. (2018). A Positive Feedback between Growth and Polarity Provides Directional Persistency and Flexibility to the Process of Tip Growth. Curr. Biol. *28*, 3342–3351e3.

Hope, H., Bogliolo, S., Arkowitz, R.A., and Bassilana, M. (2008). Activation of Rac1 by the guanine nucleotide exchange factor Dck1 is required for invasive filamentous growth in the pathogen *Candida albicans*. Mol. Biol. Cell *19*, 3638–3651.

Howell, A.S., Jin, M., Wu, C.F., Zyla, T.R., Elston, T.C., and Lew, D.J. (2012). Negative feedback enhances robustness in the yeast polarity establishment circuit. Cell *149*, 322–333.

Jaquenoud, M., and Peter, M. (2000). Gic2p may link activated Cdc42p to components involved in actin polarization, including Bni1p and Bud6p (Aip3p). Mol. Cell. Biol. *20*, 6244–6258.

Jones, L.A., and Sudbery, P.E. (2010). Spitzenkorper, exocyst, and polarisome components in *Candida albicans* hyphae show different patterns of localization and have distinct dynamic properties. Eukaryot. Cell *9*, 1455–1465.

Kelly, F.D., and Nurse, P. (2011). Spatial control of Cdc42 activation determines cell width in fission yeast. Mol. Biol. Cell *22*, 3801–3811.

Kennedy, M.J., Hughes, R.M., Peteya, L.A., Schwartz, J.W., Ehlers, M.D., and Tucker, C.L. (2010). Rapid blue-light-mediated induction of protein interactions in living cells. Nat. Methods *7*, 973–975.

Keppler-Ross, S., Noffz, C., and Dean, N. (2008). A new purple fluorescent color marker for genetic studies in *Saccharomyces cerevisiae* and *Candida albicans*. Genetics *179*, 705–710.

Kim, J., and Rose, M.D. (2015). Stable Pseudohyphal Growth in Budding Yeast Induced by Synergism between Septin Defects and Altered MAP-kinase Signaling. PLoS Genet. *11*, e1005684.

Köhli, M., Galati, V., Boudier, K., Roberson, R.W., and Philippsen, P. (2008). Growth-speed-correlated localization of exocyst and polarisome components in growth zones of *Ashbya gossypii* hyphal tips. J. Cell Sci. *121*, 3878–3889.

Kuo, C.C., Savage, N.S., Chen, H., Wu, C.F., Zyla, T.R., and Lew, D.J. (2014). Inhibitory GEF phosphorylation provides negative feedback in the yeast polarity circuit. Curr. Biol. *24*, 753–759.

Labbaoui, H., Bogliolo, S., Ghugtyal, V., Solis, N.V., Filler, S.G., Arkowitz, R.A., and Bassilana, M. (2017). Role of Arf GTPases in fungal morphogenesis and virulence. PLoS Pathog. *13*, e1006205.

Li, C.R., Lee, R.T., Wang, Y.M., Zheng, X.D., and Wang, Y. (2007). Candida albicans hyphal morphogenesis occurs in Sec3p-independent and Sec3p-dependent phases separated by septin ring formation. J. Cell Sci. *120*, 1898–1907.

Lichius, A., Goryachev, A.B., Fricker, M.D., Obara, B., Castro-Longoria, E., and Read, N.D. (2014). *CDC-42* and *RAC-1* regulate opposite chemotropisms in *Neurospora crassa*. J. Cell Sci. *127*, 1953–1965.

Löpez-Franco, R., and Bracker, C.E. (1996). Diversity and dynamics of the Spitzenkörper in growing hyphal tips of higher fungi. Protoplasma *195*, 90–111.

López-Franco, R., Howard, R.J., and Bracker, C.E. (1995). Satellite Spitzenkörper in growing hyphal tip. Protoplasma *188*, 85–103.

Luo, G., Zhang, J., and Guo, W. (2014). The role of Sec3p in secretory vesicle targeting and exocyst complex assembly. Mol. Biol. Cell *25*, 3813–3822.

Martin, S.G. (2015). Spontaneous cell polarization: Feedback control of Cdc42 GTPase breaks cellular symmetry. BioEssays *37*, 1193–1201.

Merrifield, C.J., Moss, S.E., Ballestrem, C., Imhof, B.A., Giese, G., Wunderlich, I., and Almers, W. (1999). Endocytic vesicles move at the tips of actin tails in cultured mast cells. Nat. Cell Biol. *1*, 72–74.

Milovanovic, D., and De Camilli, P. (2017). Synaptic Vesicle Clusters at Synapses: A Distinct Liquid Phase? Neuron *93*, 995–1002.

Mukherjee, K., Yang, X., Gerber, S.H., Kwon, H.B., Ho, A., Castillo, P.E., Liu, X., and Südhof, T.C. (2010). Piccolo and bassoon maintain synaptic vesicle clustering without directly participating in vesicle exocytosis. Proc. Natl. Acad. Sci. USA *107*, 6504–6509.

Mutavchiev, D.R., Leda, M., and Sawin, K.E. (2016). Remodeling of the Fission Yeast Cdc42 Cell-Polarity Module via the Sty1 p38 Stress-Activated Protein Kinase Pathway. Curr. Biol. *26*, 2921–2928.

Ortiz, D., Medkova, M., Walch-Solimena, C., and Novick, P. (2002). Ypt32 recruits the Sec4p guanine nucleotide exchange factor, Sec2p, to secretory vesicles; evidence for a Rab cascade in yeast. J. Cell Biol. *157*, 1005–1015.

Ottilie, S., Miller, P.J., Johnson, D.I., Creasy, C.L., Sells, M.A., Bagrodia, S., Forsburg, S.L., and Chernoff, J. (1995). Fission yeast *pak1+* encodes a protein kinase that interacts with Cdc42p and is involved in the control of cell polarity and mating. EMBO J. *14*, 5908–5919.

Ozbudak, E.M., Becskei, A., and van Oudenaarden, A. (2005). A system of counteracting feedback loops regulates Cdc42p activity during spontaneous cell polarization. Dev. Cell *9*, 565–571.

Pantazopoulou, A., Pinar, M., Xiang, X., and Peñalva, M.A. (2014). Maturation of late Golgi cisternae into RabE(RAB11) exocytic post-Golgi carriers visualized *in vivo*. Mol. Biol. Cell *25*, 2428–2443.

Peter, M., Neiman, A.M., Park, H.O., van Lohuizen, M., and Herskowitz, I. (1996). Functional analysis of the interaction between the small GTP binding protein Cdc42 and the Ste20 protein kinase in yeast. EMBO J. *15*, 7046–7059.

Pulver, R., Heisel, T., Gonia, S., Robins, R., Norton, J., Haynes, P., and Gale, C.A. (2013). Rsr1 focuses Cdc42 activity at hyphal tips and promotes maintenance of hyphal development in *Candida albicans*. Eukaryot. Cell *12*, 482–495.

Reijnst, P., Walther, A., and Wendland, J. (2011). Dual-colour fluorescence microscopy using yEmCherry-/GFP-tagging of eisosome components Pil1 and Lsp1 in *Candida albicans*. Yeast *28*, 331–338.

Reynaga-Peña, C.G., Gierz, G., and Bartnicki-Garcia, S. (1997). Analysis of the role of the Spitzenkörper in fungal morphogenesis by computer simulation of apical branching in *Aspergillus niger*. Proc. Natl. Acad. Sci. USA *94*, 9096–9101.

Rida, P.C., Nishikawa, A., Won, G.Y., and Dean, N. (2006). Yeast-to-hyphal transition triggers formin-dependent Golgi localization to the growing tip in *Candida albicans*. Mol. Biol. Cell *17*, 4364–4378.

Riquelme, M. (2013). Tip growth in filamentous fungi: a road trip to the apex. Annu. Rev. Microbiol. *67*, 587–609.

Riquelme, M., and Bartnicki-Garcia, S. (2004). Key differences between lateral and apical branching in hyphae of *Neurospora crassa*. Fungal Genet. Biol. *41*, 842–851.

Riquelme, M., and Sánchez-León, E. (2014). The Spitzenkörper: a choreographer of fungal growth and morphogenesis. Curr. Opin. Microbiol. *20*, 27–33.

Sánchez-León, E., Verdín, J., Freitag, M., Roberson, R.W., Bartnicki-Garcia, S., and Riquelme, M. (2011). Traffic of chitin synthase 1 (CHS-1) to the Spitzenkörper and developing septa in hyphae of *Neurospora crassa*: actin dependence and evidence of distinct microvesicle populations. Eukaryot. Cell *10*, 683–695.

Sánchez-León, E., Bowman, B., Seidel, C., Fischer, R., Novick, P., and Riquelme, M. (2015). The Rab GTPase YPT-1 associates with Golgi cisternae and Spitzenkörper microvesicles in *Neurospora crassa*. Mol. Microbiol. *95*, 472–490.

Smith, S.E., Rubinstein, B., Mendes Pinto, I., Slaughter, B.D., Unruh, J.R., and Li, R. (2013). Independence of symmetry breaking on Bem1-mediated autocatalytic activation of Cdc42. J. Cell Biol. *202*, 1091–1106.

Southwick, F.S., Li, W., Zhang, F., Zeile, W.L., and Purich, D.L. (2003). Actin-based endosome and phagosome rocketing in macrophages: activation by the secretagogue antagonists lanthanum and zinc. Cell Motil. Cytoskeleton *54*, 41–55.

Taunton, J., Rowning, B.A., Coughlin, M.L., Wu, M., Moon, R.T., Mitchison, T.J., and Larabell, C.A. (2000). Actin-dependent propulsion of endosomes and lysosomes by recruitment of N-WASP. J. Cell Biol. *148*, 519–530.

Umbach, D., and Jones, K.N. (2003). A Few Methods for Fitting Circles to Data. IEEE Trans. Instrum. Meas. *52*, 1881–1885.

Ushinsky, S.C., Harcus, D., Ash, J., Dignard, D., Marcil, A., Morchhauser, J., Thomas, D.Y., Whiteway, M., and Leberer, E. (2002). CDC42 is required for polarized growth in human pathogen *Candida albicans*. Eukaryot. Cell *1*, 95–104.

VandenBerg, A.L., Ibrahim, A.S., Edwards, J.E., Jr., Toenjes, K.A., and Johnson, D.I. (2004). Cdc42p GTPase regulates the budded-to-hyphal-form transition and expression of hypha-specific transcripts in *Candida albicans*. Eukaryot. Cell *3*, 724–734.

Vauchelles, R., Stalder, D., Botton, T., Arkowitz, R.A., and Bassilana, M. (2010). Rac1 dynamics in the human opportunistic fungal pathogen *Candida albicans*. PLoS ONE *5*, e15400.

Verdín, J., Bartnicki-Garcia, S., and Riquelme, M. (2009). Functional stratification of the Spitzenkörper of *Neurospora crassa*. Mol. Microbiol. *74*, 1044–1053.

Vernay, A., Schaub, S., Guillas, I., Bassilana, M., and Arkowitz, R.A. (2012). A steep phosphoinositide bis-phosphate gradient forms during fungal filamentous growth. J. Cell Biol. *198*, 711–730.

Virag, A., and Harris, S.D. (2006). The Spitzenkörper: a molecular perspective. Mycol. Res. *110*, 4–13.

Virag, A., Lee, M.P., Si, H., and Harris, S.D. (2007). Regulation of hyphal morphogenesis by *cdc42* and *rac1* homologues in *Aspergillus nidulans*. Mol. Microbiol. *66*, 1579–1596.

Wagner, W., Bielli, P., Wacha, S., and Ragnini-Wilson, A. (2002). Mlc1p promotes septum closure during cytokinesis via the IQ motifs of the vesicle motor Myo2p. EMBO J. *21*, 6397–6408.

Wakade, R. (2017). Role of the Rab GTPase, Ypt6, in the human fungal pathogen *Candida albicans*, PhD thesis.

Wakade, R., Labbaoui, H., Stalder, D., Arkowitz, R.A., and Bassilana, M. (2017). Overexpression of *YPT6* restores invasive filamentous growth and secretory vesicle clustering in a *Candida albicans* arl1 mutant. Small GTPases, 1–7.

Weiner, A., Orange, F., Lacas-Gervais, S., Rechav, K., Ghugtyal, V., Bassilana, M., and Arkowitz, R.A. (2019). On-site secretory vesicle delivery drives filamentous growth in the fungal pathogen *Candida albicans*. Cell. Microbiol. *21*, e12963.

Wilson, R.B., Davis, D., and Mitchell, A.P. (1999). Rapid hypothesis testing with *Candida albicans* through gene disruption with short homology regions. J. Bacteriol. *181*, 1868–1874.

Witte, K., Strickland, D., and Glotzer, M. (2017). Cell cycle entry triggers a switch between two modes of Cdc42 activation during yeast polarization. eLife *6*, e26722.

Woods, B., and Lew, D.J. (2019). Polarity establishment by Cdc42: Key roles for positive feedback and differential mobility. Small GTPases *10*, 130–137.

Wu, C.F., and Lew, D.J. (2013). Beyond symmetry-breaking: competition and negative feedback in GTPase regulation. Trends Cell Biol. *23*, 476–483.

Wu, C.F., Chiou, J.G., Minakova, M., Woods, B., Tsygankov, D., Zyla, T.R., Savage, N.S., Elston, T.C., and Lew, D.J. (2015). Role of competition between polarity sites in establishing a unique front. eLife *4*, e11611.

Zeng, G., Wang, Y.M., and Wang, Y. (2012). Cdc28-Cln3 phosphorylation of Sla1 regulates actin patch dynamics in different modes of fungal growth. Mol. Biol. Cell *23*, 3485–3497.

Zhang, C., and Konopka, J.B. (2010). A photostable green fluorescent protein variant for analysis of protein localization in *Candida albicans*. Eukaryot. Cell *9*, 224–226.

Zhang, X., Bi, E., Novick, P., Du, L., Kozminski, K.G., Lipschutz, J.H., and Guo, W. (2001). Cdc42 interacts with the exocyst and regulates polarized secretion. J. Biol. Chem. *276*, 46745–46750.

Zheng, Y., Bagrodia, S., and Cerione, R.A. (1994). Activation of phosphoinositide 3-kinase activity by Cdc42Hs binding to p85. J. Biol. Chem. *269*, 18727–18730.

STAR★METHODS

KEY RESOURCES TABLE

REAGENT or RESOURCE	SOURCE	IDENTIFIER
Chemicals, Peptides, and Recombinant Proteins		
Concanavalin A	Merck Millipore	Cat# 234567-1GM
Fetal bovine serum	Dutscher	Cat# P30-8500-500ml
Paraformaldehyde	Electorn Microscopy Sciences	Cat# RT 15710-16%
Alexa Fluor-568 phalloidin	ThermoFisher	Cat# A12380-300U
Experimental Models: Organisms/Strains		
C. albicans		N/A
ura3Δ::imm434/ura3Δ::imm434 his1Δ::hisG/his1Δ::hisG arg4Δ::hisG/arg4Δ::hisG	Wilson et al., 1999	BWP17
Same as BWP17 with *arl1Δ::HIS1/arl1Δ::URA3*	Labbaoui et al., 2017	PY2533
Same as BWP17 but with *RP10::ARG4-ACT1p-CibN-GFPγ-CtRac1-ADH1t*	This study	PY2935
Same as 2533 but with *MLC1/MLC1::MLC1-GFP-HIS1*	This study	PY3280
Same as PY2935 but with *NEUT5L::NAT1-TEF1p-Cry-mCh-Cdc42 [G12V,C188S]-TEF1t*	This study	PY3451
Same as BWP17 but with *NEUT5L::NAT1-TEF1p-Cry-GFPγ-Cdc42 [G12V,C188S]-TEF1t*	This study	PY3643
Same as PY3643 but with *NEUT5L::URA3-ADH1p-CibN-CtRac1-ACT1t*	This study	PY4059
Same as PY4059 but with *RP10::ARG4-ACT1p-CRIB-mCh-ADH1t*	This study	PY4172
Same as PY4059 but with *ABP1/ABP1::ABP1-mCh-HIS1*	This study	PY4175
Same as PY4059 but with *MLC1/MLC1::MLC1-mCh-HIS1*	This study	PY4268
Same as PY3643 but with *NEUT5L::URA3-ADH1p-CibN-CtRac1-ACT1t*	This study	PY4510
Same as PY4510 but with *RP10::ARG4-SEC4p-mSc-Sec4-ADH1t*	This study	PY4534
Same as PY4510 but with *ADH1/ADH1p::miRFP670-HIS1*	This study	PY4559
Same as PY4534 but with *MLC1/MLC1::MLC1-miRFP670-HIS1*	This study	PY4623
Same as PY4510 but with *MLC1/MLC1::MLC1-miRFP670-HIS1*	This study	PY4642
Same as PY4642 but with *RP10::ARG4-ADH1p-Sac1-mSc-ADH1t*	This study	PY4849
Same as PY4642 but with *RP10::ARG4-YPT31p-mCh-Ypt31-ADH1t*	This study	PY4949
Same as PY4642 but with *SEC7/SEC7::SEC7-3x-mSc-ARG4*	This study	PY4957
Same as PY4642 but with *SEC2/SEC2::SEC2-3x-mSc-ARG4*	This study	PY4963
Same as PY4642 but with *SEC3/SEC3::SEC3-3x-mSc-ARG4*	This study	PY4964
Same as BWP17 but with *NEUT5L::NAT1-TEF1p-Cry-GFPγ-Cdc42 [G12V,T35A,C188S]-TEF1t*	This study	PY5010
Same as PY5010 but with *NEUT5L::URA3-ADH1p-CibN-CtRac1-ACT1t*	This study	PY5058
Oligonucleotides		
cttctagtatacgcgtcttataatatagtacatttttttagctctcttaatttttctttttCTTGTACAAT TCATCCATACCATGGGTAATACC	This study	yeGFPCtRac1m
ttactagtttaattaagggcgcgccAATTGTTTTTGTATTTGTTGTTGTTGTTG	This study	CaAdh1pmAscIPacISpeI
ttactagtggcctgcaggGAGTGAAATTCTGGAAATCTGG	This study	CaAct1tpSpeISbfI
cttaattaaTTATAATATAGTACATTTTTTAGCTCTCTTAATTTTTCTTT TCTTtgatgaaccaccagctgaaccagctgaaccagctgaatcaaattcAATAT AATCAGTTTTTTCC	This study	CaCIBNlinkCtRac1mPacI
ttactagtttaattaagggcgcgccGATTGATTATGACTATAATG	This study	CaTEF1pmAscPacSpe
ttactagtggcctgcaggGCTAGTTGAATATTATGTAAGATCTG	This study	CaTEF1tpSpeISbfI
TTTAATTAAtgatgaaccaccagctgaaccagctgaaccagctgaatcaaattcAGCA GCACCAATCATAATTTGAGC	This study	CaCRYm-link-PacI

(*Continued on next page*)

Continued

REAGENT or RESOURCE	SOURCE	IDENTIFIER
ccagctgattatgttcctGcAgtttttgataattatgctgtaaccgt	This study	CaCdc42T35ApPstI
acggttacagcataattatcaaaaacTgCaggaacataatcagctgg	This study	CaCdc42T35AmPstI
Recombinant DNA		
CGTACGGACCGATGAATGGTGCTATTGGTGGTGATTTATTGTTAAA TTTTCCAGATATGTCAGTTTTAGAAAGACAAAGAGCACATTTGAAA TATTTAAATCCAACTTTTGATTCACCATTGGCTGGTTTTTTTGCTGA TTCATCAATGATTACTGGTGGTGAAATGGATTCATATTTGTCAACTG CTGGTTTAAATTTGCCAATGATGTATGGTGAAACTACTGTTGAAGG TGATTCAAGATTATCAATTTCACCAGAAACTACTTTGGGTACTGGT AATTTTAAAGCTGCTAAATTTGATACTGAAACTAAAGATTGTAATGA AGCTGCTAAAAAAATGACTATGAATAGAGATGATTTAGTTGAAGAA GGTGAAGAAGAAAAATCAAAAATTACTGAACAAAATAATGGTTCA ACTAAATCAATTAAAAAAATGAAACATAAAGCTAAAAAAGAAGA AAATAATTTTTCAAATGATTCATCAAAAGTTACTAAAGAATTGGA AAAAACTGATTATATTGGGAGCTCCGC	Genscript	CaCIBNRsrIISacI
CGCGGCGCGCCCATGAAAATGGATAAAAAAACTATTGTTTGGT TTAGAAGAGATTTAAGAATTGAAGATAATCCAGCTTTGGCTGC TGCTGCTCATGAAGGTTCAGTTTTTCCAGTTTTTATTTGGTGTC CAGAAGAAGAAGGTCAATTTTATCCAGGTAGAGCTTCAAGAT GGTGGATGAAACAATCATTAGCTCATTTGTCACAATCATTAAA AGCTTTGGGTTCAGATTTAACTTTGATTAAAACTCATAATACT ATTTCAGCTATTTTAGATTGTATTAGAGTTACTGGTGCTACTAA AGTTGTTTTTAATCATTTGTATGATCCAGTTTCATTAGTTAGA GATCATACTGTTAAAGAAAAATTGGTTGAAAGAGGTATTTC AGTTCAATCATATAATGGTGATTTATTGTATGAACCATGGGA AATTTATTGTGAAAAAGGTAAACCATTTACTTCATTTAATTCA TATTGGAAAAAATGTTTAGATATGTCAATTGAATCAGTTATGT TGCCACCACCATGGAGATTAATGCCAATTACTGCTGCTGCTG AAGCTATTTGGGCTTGTTCAATTGAAGAATTGGGTTTAGAAAA TGAAGCTGAAAAACCATCAAATGCTTTGTTAACTAGAGCTTGG TCACCAGGTTGGTCAAATGCTGATAAATTGTTAAATGAATTT ATTGAAAAACAATTGATTGATTATGCTAAAAATTCAAAAAAA GTTGTTGGTAATTCAACTTCATTATTGTCACCATATTTACATTT TGGTGAAATTTCAGTTAGACATGTTTTTCAATGTGCTAGAATG AAACAAATTATTTGGGCTAGAGATAAAAATTCAGAAGGTGAA GAATCAGCTGATTTGTTTTTAAGAGGTATTGGTTTGAGAGAAT ATTCAAGATATATTTGTTTTAATTTTCCATTTACTCATGAACAA TCATTATTGTCACATTTAAGATTTTTTCCATGGGATGCTGATGT TGATAAATTTAAAGCTTGGAGACAAGGTAGAACTGGTTATCCA TTGGTTGATGCTGGTATGAGAGAATTATGGGCTACTGGTTGGAT GCATAATAGAATTAGAGTTATTGTTTCATCATTTGCTGTTAAAT TTTTATTGTTACCATGGAAATGGGGTATGAAATATTTTTGGGA TACTTTGTTAGATGCTGATTTGGAATGTGATATTTTAGGTTGG CAATATATTTCAGGTTCAATTCCAGATGGTCATGAATTGGATA GATTAGATAATCCAGCTTTGCAAGGTGCTAAATATGATCCAG AAGGTGAATATATTAGACAATGGTTACCAGAATTGGCTAGATTA CCAACTGAATGGATTCATCATCCATGGGATGCTCCATTGACTGTT TTAAAAGCTTCAGGTGTTGAATTGGGTACTAATTATGCTAAACCAA TTGTTGATATTGATACTGCTAGAGAATTATTGGCTAAAGCTATTT CAAGAACTAGAGAAGCTCAAATTATGATTGGTGCTGCTTTAATTAAAGC	Genscript	CaCRYPHRAscIPacI
pFA-yemCh-HIS1 plasmid	Reijnst et al., 2011	N/A
pUC57 plasmid	Genscript	N/A
pDUP5 plasmid	Gerami-Nejad et al., 2013	N/A
pDUP3 plasmid	Gerami-Nejad et al., 2013	N/A
pEXPARG-ACT1p-CRIB-GFP-ADH1t	Corvest et al., 2013	N/A
pEXPARG-ACT1p-CRIB-mCh-ADH1t	This study	N/A
pEXPARG-ACT1p-CibN-GFP-ADH1t	This study	N/A

(*Continued on next page*)

Continued

REAGENT or RESOURCE	SOURCE	IDENTIFIER
pEXPARG-ACT1p-CibN-GFPγ-CtRac1-ADH1t	This study	N/A
pDUP5-ADH1p-(AscI-PacI-SpeI-SbfI)-ACT1t	This study	N/A
pDUP5-ADH1p-CibN-CtRac1-ACT1t	This study	N/A
pDUP3-TEF1-(AscI-PacI-SpeI-SbfI)-TEF1t	This study	N/A
pDUP3-TEF1-Cry2-(PacI-SpeI-SbfI)-TEF1t	This study	N/A
pDUP3-TEF1-Cry2-mCh-(SpeI-SbfI)-TEF1t	This study	N/A
pDUP3-TEF1-Cry2-mCh-Cdc42-TEF1t	This study	N/A
pDUP3-TEF1-Cry2-mCh-Cdc42[C188S]-TEF1t	This study	N/A
pDUP3-TEF1p-Cry2-mCh-Cdc42[G12V,C188S]-TEF1t	This study	N/A
pDUP3-TEF1p-Cry2-GFPγ-Cdc42[G12V,C188S]-TEF1t	This study	N/A
pDUP3-TEF1p-Cry2-GFPγ-Cdc42[G12V,T35A,C188S]-TEF1t	This study	N/A
pEXPARG-ADH1p-Sac1-GFP	Weiner et al., 2019	N/A
pEXPARG-ADH1p-Sac1-mSc	This study	N/A
Software and Algorithms		
ImageJ version 1.51 software	National Institutes of Health	ImageJ
Huygens Professional software version 18.04	Scientific-Volume Imaging	Huygens Professional
Volocity Software version 6.3	PerkinElmer	Volocity
MATLAB version 2017 software	MathWorks	MathWorks
GraphPad Prism 6 software	GraphPad	Prism
MetaMorph version 7.8.8.0 software	Molecular Devices	MetaMorph

LEAD CONTACT AND MATERIALS AVAILABILITY

Further information and requests for resources and reagents should be directed to and will be fulfilled by the Lead Contact, Robert A. Arkowitz (arkowitz@unice.fr).

EXPERIMENTAL MODEL AND SUBJECT DETAILS

Strains

C. albicans strain BWP17 was used, which is isogenic to SC5314 (Wilson et al., 1999). Derivatives of the BWP17 strain used in this study are listed in the Key Resources Table. Strains were grown in the dark in rich media (yeast extract peptone dextrose) at 30°C for all experiments and were incubated with an equal volume of fetal calf serum (FCS) at 37°C for induction of filamentous growth.

METHOD DETAILS

Strain and plasmid construction

Standard methods were used for *C. albicans* cell culture, molecular, and genetic manipulations as described (Hope et al., 2008). To generate optogenetic strains, the sequences encoding Cry2Phr and CibN (Kennedy et al., 2010) were codon optimized, synthesized and cloned into pUC57 (Genscript). CibN was cloned into pEXPARG-ACT1p-CRIB-GFP-ADH1t (Corvest et al., 2013) replacing CRIB using unique RsrII and SacI sites. GFPγ (Zhang and Konopka, 2010) was then amplified with a unique 5′ SacI site and 3′ primer encoding the Rac1 C-terminal plasma membrane targeting domain (KKRKIKRAKKCTIL) (Vauchelles et al., 2010) followed by a stop codon and MluI site. This GFPγ-CtRac1 was subsequently cloned into pEXPARG-ACT1p-CibN-GFP-ADH1t to replace GFP resulting in pEXPARG-ACT1p-CibN-GFPγ-CtRac1-ADH1t. An *ADH1* promoter and *ACT1* terminator were cloned into pDUP5 (Gerami-Nejad et al., 2013) using unique XmaI and NotI sites resulting in pDUP5-ADH1p-(AscI-PacI-SpeI-SbfI)-ACT1t. CibN was amplified with a unique 5′ AscI site and a 3′ 15 aa linker encoding EFDSAGSAGSAGGSS, followed by Rac1 C-terminal plasma membrane targeting domain and a PacI site and this was cloned into pDUP5-ADH1p-(AscI-PacI-SpeI-SbfI)-ACT1t resulting in pDUP5-ADH1p-CibN-CtRac1-ACT1t. The *TEF1* promoter and terminator were cloned into pDUP3 (Gerami-Nejad et al., 2013) using unique XmaI and NotI sites resulting in pDUP3-TEF1-(AscI-PacI-SpeI-SbfI)-TEF1t. Cry2 was cloned using unique AscI and PacI sites into pDUP3-TEF1-(AscI-PacI-SpeI-SbfI)-TEF1t resulting in pDUP3-TEF1-Cry2-(PacI-SpeI-SbfI)-TEF1t. The gene encoding yemCherry (Keppler-Ross et al., 2008) was then amplified with unique PacI and SpeI sites and cloned into pDUP3-TEF1-Cry2-(PacI-SpeI-SbfI)-TEF1t, resulting in pDUP3-TEF1-Cry2-mCh-(SpeI-SbfI)-TEF1t. Cdc42 or Cdc42[C188S] was

then cloned into the SpeI and SbfI sites resulting in pDUP3-TEF1-Cry2-mCh-Cdc42-TEF1t or pDUP3-TEF1-Cry2-mCh-Cdc42[C188S]-TEF1t. A mutation encoding the G12V alteration was generated by site directed mutagenesis resulting in pDUP3-TEF1p-Cry2-mCh-Cdc42[G12V,C188S]-TEF1t. Cry2 was amplified with 5′ AscI site and a linker encoding EFDSAGSAGSAGGSS followed by a PacI site. GFPγ was subsequently cloned into unique PacI and SpeI and finally Cdc42[G12V,C188S] was cloned into unique SpeI and SbfI sites resulting in pDUP3-TEF1p-Cry2-GFPγ-Cdc42[G12V,C188S]-TEF1t. For generation of Cdc42[G12V,T35A], a mutation encoding the T35A alteration was generated by site directed mutagenesis resulting in pDUP3-TEF1p-Cry2-GFPγ-Cdc42[G12V,T35A,C188S]-TEF1t. The CibN and Cry plasmids were linearized by either NgoMI or StuI and transformed into strains, which were subsequently grown in absence of light. The Abp1-mCh, Mlc1-mCh, Mlc1-miRFP670, Sec2-3x-mSc, Sec7-3x-mSc and Sec3-3x-mSc strains were generated by homologous recombination, using pFA-yemCh-HIS1 (Reijnst et al., 2011), pFA-miRFP670-HIS1, pFA-mSc-ARG4 and pFA-3x-mSc-ARG4 (to be described elsewhere). pEXPARG-SEC4p-mSc-Sec4 was constructed using 1311 bp *SEC4* promoter with unique NotI and RsrII sites, followed by codon optimized mSc (mSc; to be described elsewhere) with RsrII and AscI sites and *SEC4* ORF flanked by AscI and MluI sites. pEXPARG-YPT31p-mCh-Ypt31 was constructed in a similar fashion as pEXPARG-SEC4p-mSc-Sec4 (to be described elsewhere). The pEXPARG-ACT1p-CRIB-mCh plasmid was constructed by replacing GFP in pEXPARG-ACT1p-CRIB-GFP (Corvest et al., 2013) with yemCherry (Keppler-Ross et al., 2008). The pEXPARG-ADH1p-Sac1-mSc plasmid was constructed by replacing GFP in pEXPARG-ADH1p-Sac1-GFP (Weiner et al., 2019) with mSc. CRIB, Sec4, Ypt31 and Sac1 plasmids were linearized with StuI and transformed into optogenetic strains.

Microscopy

Cells were imaged as described using spinning-disk confocal microscopy (Bassilana et al., 2005; Ghugtyal et al., 2015) except that MetaMorph version 7.8.8.0 software (Molecular Devices) controlled the system and for experiments examining the actin cytoskeleton, Sec2, Sec3, Ypt31, Sac1 and Sec7, a PLANAPO TIRF 1.45 NA 100 × objective was used. A long pass LP540 filter was used in the transmission light path to prevent premature photoactivation. Exponentially growing cells (grown in the dark) were spotted on YEPD agar pads at 30°C or mixed with an equal volume of FCS and spotted on 25% (vol/vol) YEPD agar–75% (vol/vol) FCS pads at 37°C (Bassilana et al., 2005). Typically cells on FCS/agar pads were incubated for 30 – 40 min at 37°C prior to microscopy or, in order to have cells with short filaments, incubation was for 10-30 min. Photoactivation was accomplished by a 300 msec 488 nm (10% of a 25 mW diode-pumped solid-state laser) pulse, either 3 pulses 10 min apart or 6 pulses 5 min apart. For the analyses of filament extension rate with the Cdc42[G12V,T35A]$_{cyto}$ fusion, equal amounts of optogenetic strains expressing Cry2-GFP-Cdc42[G12V]$_{cyto}$ (also expressing cytoplasmic miRFP to identify it) or Cry2-GFP-Cdc42[G12V,T35A]$_{cyto}$ were mixed and imaged simultaneously. For imaging of fusions with weaker signals including Sec2, Sec3, Ypt31, Sac1 and Sec7, following incubation with FCS, cells were imaged on slides for 20-30 min. Images were acquired at indicated times, with 0.5 μm z sections (9 to 15) to capture the entire cell, except for Sec3-3x-mSc where 4 × 0.5 μm z sections were acquired every 5 min and Sac1-mSc where 33 × 0.2 μm z sections were acquired. For live cell imaging followed by actin visualization, cells were grown in a Concanavalin A treated (0.1 mg/mL) glass bottom microwell dish (MatTek Corporation). Following photoactivation, cells were fixed with 4% paraformaldehyde for 10 min, subsequently washed with PBS, and actin was labeled with Alexa Fluor-568 Phalloidin as described (Vernay et al., 2012). Fixed cells were imaged with 0.2 μm z sections (18 to 26). All images were deconvolved with Huygens Professional software version 18.04 (Scientific-Volume Imaging) with recommended settings and a signal to noise ratio of 5 to 10. Maximum or sum projections are shown and the latter was used for all quantitations. Image analysis was carried out with ImageJ (version 1.51) and Volocity Software version 6.3 (PerkinElmer). Objects were identified as previously described, using the SD mode in Volocity (Ghugtyal et al., 2015), where the selection is based on SDs above the mean intensity. Scale bar is 5 μm in all images except for actin images and zoom in of the region analyzed in FRAP images, where it is 1 μm. The data that support the findings of this study are available from the corresponding author upon request.

Fluorescence recovery after photo-bleaching (FRAP) analysis was performed on a Zeiss LSM880 inverted confocal microscope using a Plan-Apo 1.4 NA 63 × objective. Images were captured every 2 s at 0.1% maximum laser intensity. Bleaching was performed at 80% laser intensity using 10 × 0.5-1 msec photo-bleaching scans on circular area of 1-2 μm^2. Bleach areas were somewhat larger than the cluster of vesicles to account for the rapid movement of the new cluster. Photoactivation was accomplished with a 100W Hg excitation source and a 450 – 490 nm band pass filter using 2 × 1 s pulses of 25% intensity. The average signal intensity of an area somewhat smaller than the bleach ROI was determined (which was dynamic in the case of the new cluster) and was normalized to photobleaching during image acquisition, which was fit to a one phase decay regression: $Y = (Y_0 - \text{Plateau})(e^{-kx}) + \text{Plateau}$, of the average intensity elsewhere in the cell (using GraphPad Prism 6 software). Regression analysis to determine the FRAP $t_{1/2}$ was done using a one-phase exponential association function in GraphPad Prism 6 software as follows: $Y = Y_{max}(1-e^{-kx})$, where k is the rate constant and $t_{1/2}$ is $0.69/k$. Given the different sizes of the initial Spk and the dynamic vesicle cluster, it was not possible to determine the mobile fraction. In addition, as the signals were quite low, it was occasionally necessary to saturate the detector prior to bleaching.

Modeling

Data Analysis

Modeling was carried out using MATLAB version 2017 (MathWorks). To analyze movement of the vesicle clusters following photoactivation we first inferred their z-coordinate by projecting their x-y coordinate on the cortex of the mother cell, using z section information to assign the cluster to the top or bottom hemi-sphere. To this end, we approximated the shape of the mother cell as a sphere.

To determine the sphere that best approximates the mother cell, we started from a two dimensional projection of the cell shape; discarding the filament and keeping the mother cell. We then used the Average of Intersections Method (Ghosh et al., 2012) to determine the optimal circle that best approximates the projected shape of the mother cell. Briefly, we grouped the ensemble of points on the mother cell cortex into triplets and traced all circles passing through the triplets. We obtained the center of the optimal circle by averaging over all the centers and the radius was defined as the average distance between the center and all the points. To minimize instabilities, we choose triplets of points as far away from each other as possible. Mother cells are spherical to a good approximation: the distance of the points on the mother cell cortex to the optimum circle range from 0.9% to 3.4% of the radius. The colatitude θ (Figure 7D) is defined relative to the North pole, which is the initial position of the vesicle cluster is aligned to. Note that there is little variation in the statistics when the position of the cluster at any other time point, is aligned to the North pole, corroborating that the dynamics is not dependent on the initial conditions and effectively does not depend on time.

Simulations of diffusion

We obtained replicas of the experimental dataset for purely diffusive dynamics using the algorithm developed by Ermak and McCammon (1978), with an additional term to keep the process on the surface of the sphere (Castro-Villarreal et al., 2014). To this end, we let the cluster start at the initial location of the real cluster on the cell cortex. We then defined a small time step, over which the cluster takes a step in a random direction and we applied a force that keeps it on the spherical representation of the mother cell. We use

$\mathbf{x}_i(t + dt) = \mathbf{x}_i(t) + D\,\mathbf{f}_j(t)\,dt + \delta\mathbf{x}_i$ where D is the diffusivity, $\delta\mathbf{x}_i$ are random variables with multivariate statistics $\langle \delta\mathbf{x}_i \delta\mathbf{x}_j \rangle = 2Dt$; $\mathbf{f}_i$ is the term keeping the cluster on the sphere, $\mathbf{f}_i = -k(r_i - R)\mathbf{n}_i$, R is the radius of the sphere, k quantifies the strength of the force, r_i is the distance of the cluster from the center and $\mathbf{n}_i$ is the unit vector normal to the surface of the sphere. We used D = 1.4 μm^2/min, which is within the range of variation of typical diffusivities in cells (Giese et al., 2015) and k = 1000 μm^{-2}, dt = 0.5 × 10^{-5} min. We recorded the position of the walkers every 2 × 10^5 time steps, corresponding to 1 min (which is the time between subsequent experimental acquisitions).

The theoretical prediction for diffusion on a sphere can be written in the form of a series of Legendre polynomials and reduced to the simple form

$P(\theta,\tau) \sim 1/\tau\theta \exp(-\theta^2/(2\tau))$ at small τ (Umbach and Jones, 2003), where $\tau = 2Dt/R^2$, θ is the colatitude, D is diffusivity and R is the radius of the sphere. Predictions for diffusion at short and long times (Figures S7A–S7C) are obtained as integrals of the full distribution over the desired time interval (Figures S7B and S7C; t < 10 min, t > 15 min).

Sample sizes

For Figures S7B and S7C, the data have been divided into early (first 10 min after initial photo-activation) and late (times later than 15 minutes after initial photoactivation). These time windows have been chosen empirically to ensure that the two classes contain a comparable number of data points.

QUANTIFICATION AND STATISTICAL ANALYSIS

Image quantification was carried out with ImageJ (version 1.51) and Volocity Software version 6.3 (PerkinElmer). The number of experiments and cells analyzed and means with standard deviation are indicated in Figure Legends (Figure S4E, standard error of the mean is shown). Data were compared by unpaired t test using GraphPad Prism (v. 6) software or Kolmogorov–Smirnov test, with all *p* values indicated in Figure Legends.

DATA AND CODE AVAILABILITY

The raw data and code that support the findings of this study are available from the corresponding author upon request.

Cell Reports, Volume *28*

Supplemental Information

Secretory Vesicle Clustering in Fungal Filamentous Cells Does Not Require Directional Growth

Patrícia M. Silva, Charles Puerner, Agnese Seminara, Martine Bassilana, and Robert A. Arkowitz

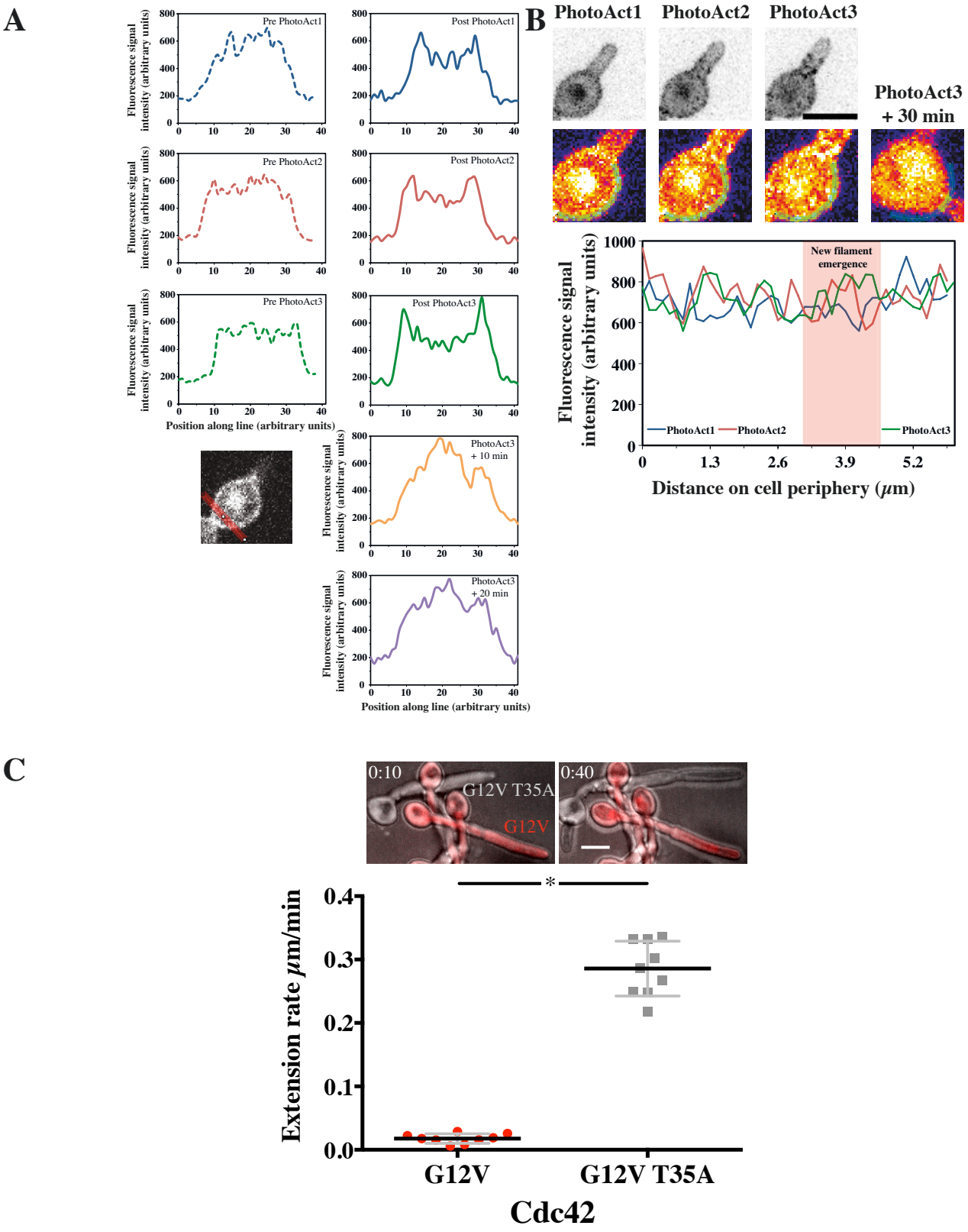

Supplementary Figure S1. *Related to Figure 1*

New growth upon uniform plasma membrane recruitment of active Cdc42 is impaired by effector binding mutation. A) New growth and location of photo-recruited Cdc42•GTP do not correlate. Cdc42•GTP is rapidly recruited to the plasma membrane. Strain as in Fig. 1B was incubated on agar pads containing serum at 37°C, and subjected to 3 pulses of 488 nm light with 10 min intervals. Line scan (red line) shows mCh signal through the cell as indicated in bottom left hand image. B) New germ tube emergence occurs subsequent to Cdc42•GTP photo-recruitment. Images showing mCh signal (top) immediately after the 3 photo-activation pulses. Line scan (green line) of mCh signal along the plasma membrane (indicated by green line in false color image) with location of new growth, which occurred 30 min after last photo-activation pulse, indicated. C) Plasma membrane recruitment of active Cdc42 with an effector binding mutation does not perturb filamentous growth. Strains expressing CibN-Ct_{Rac1} and Cry2-GFP-Cdc42[G12V T35A]$_{cyto}$ or Cry2-GFP-Cdc42[G12V]$_{cyto}$ with cytoplasmic miRFP (for identification) were mixed and incubated as in Fig. 3A with images every 10 min (488 nm light pulses at 0:10 – 1:00). Images at indicated time points (top) with Cdc42[G12V] expressing cells in red. Filament extension rate was determined from 8 time points, including the first 6 with 488 nm irradiation and two additional times (bottom), $n = 9$. The difference is statistically significant, $p < 0.0001$.

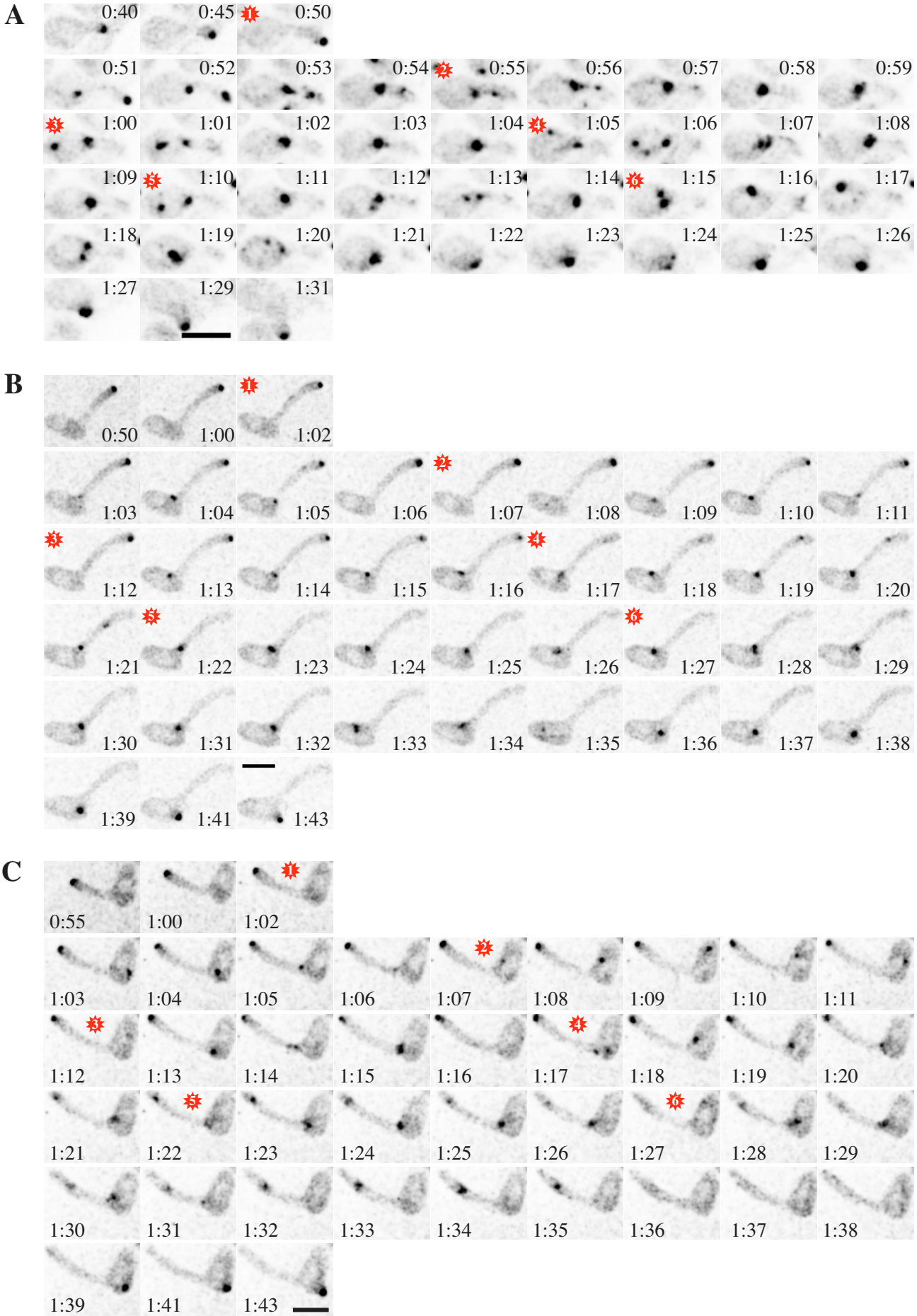

Supplementary Figure S2. *Related to Figure 3*
Mlc1 cluster dynamics following photo-recruitment of Cdc42•GTP. Location of Mlc1 cluster following photo-activation from 3 different time-lapses is shown (A-C). Strain as in Fig. 3E with red stars indicating photo-activation. At each time (every 2.5 min prior to photo-activation and every 1 min thereafter) DIC and mCh images were acquired and sum projections are shown from representative time-lapses.

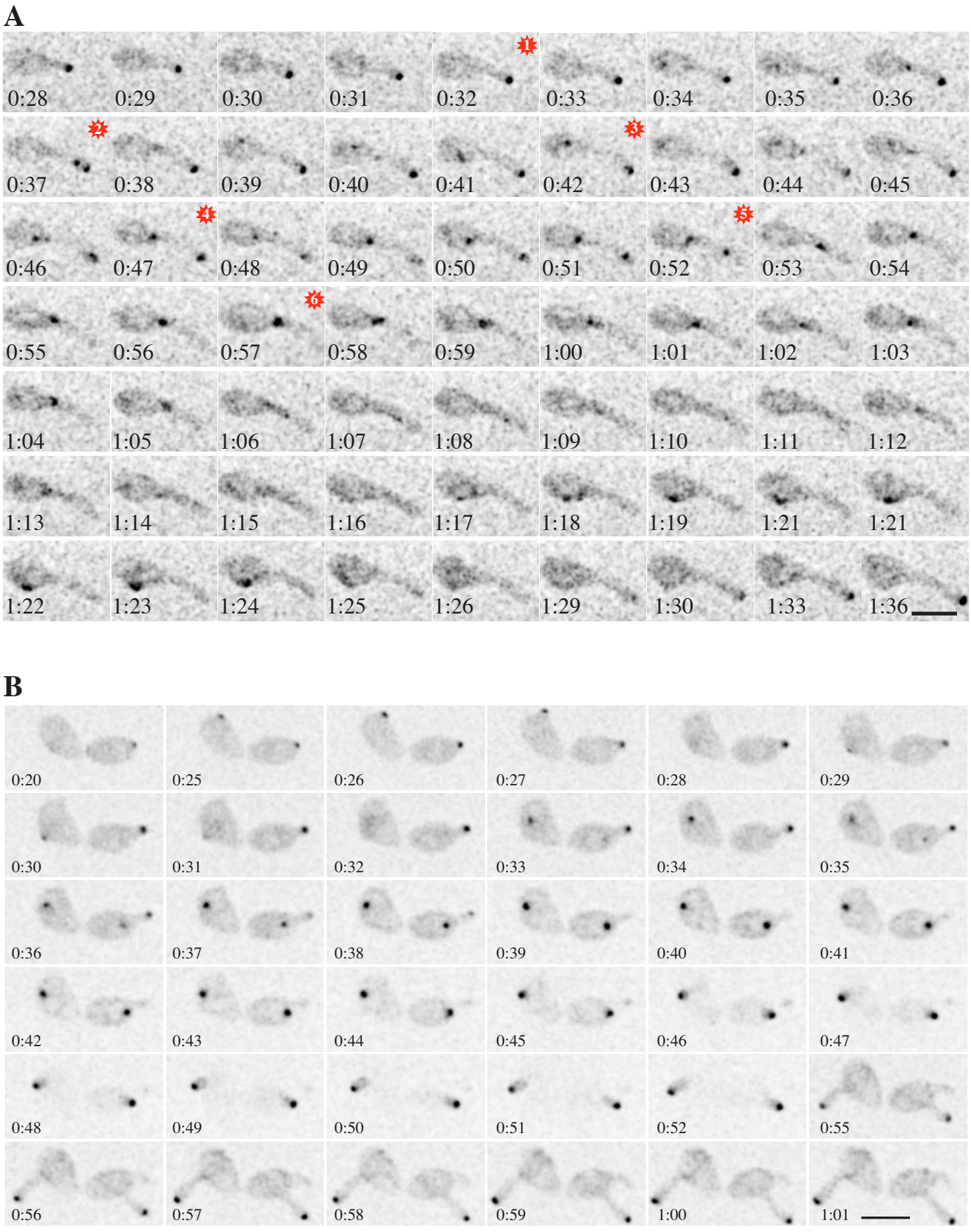

Supplementary Figure S3. *Related to Figure 3*
Mlc1 cluster dynamics when tip growth resumes following recruitment of Cdc42•GTP and in a mutant with decreased growth rate. A) Mlc1 cluster dynamics in cells in which tip growth resumes following recruitment of Cdc42•GTP. Strain as in Fig. 3E with red stars indicating photo-activation. At each time (every 1 min) mCh images were acquired and sum projections are shown from a representative time-lapse. B) Dynamic behavior of Mlc1 cluster is not a consequence of reduced filament extension rate. An *arl1* deletion mutant expressing Mlc1-GFP was examined by time-lapse microscopy and images every min from a representative experiment are shown.

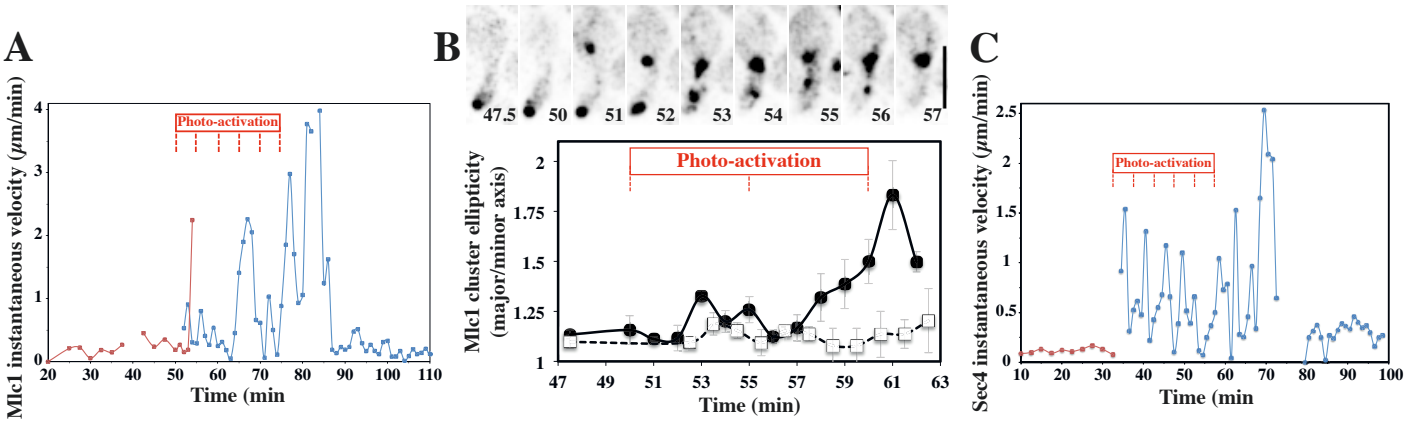
A
Mlc1 instantaneous velocity (μm/min)
Photo-activation
Time (min
B
47.5
50
51
52
53
54
55
56
57
Mlc1 cluster ellipticity (major/minor axis)
Photo-activation
Time (min)
C
Sec4 instantaneous velocity (μm/min)
Photo-activation
Time (min

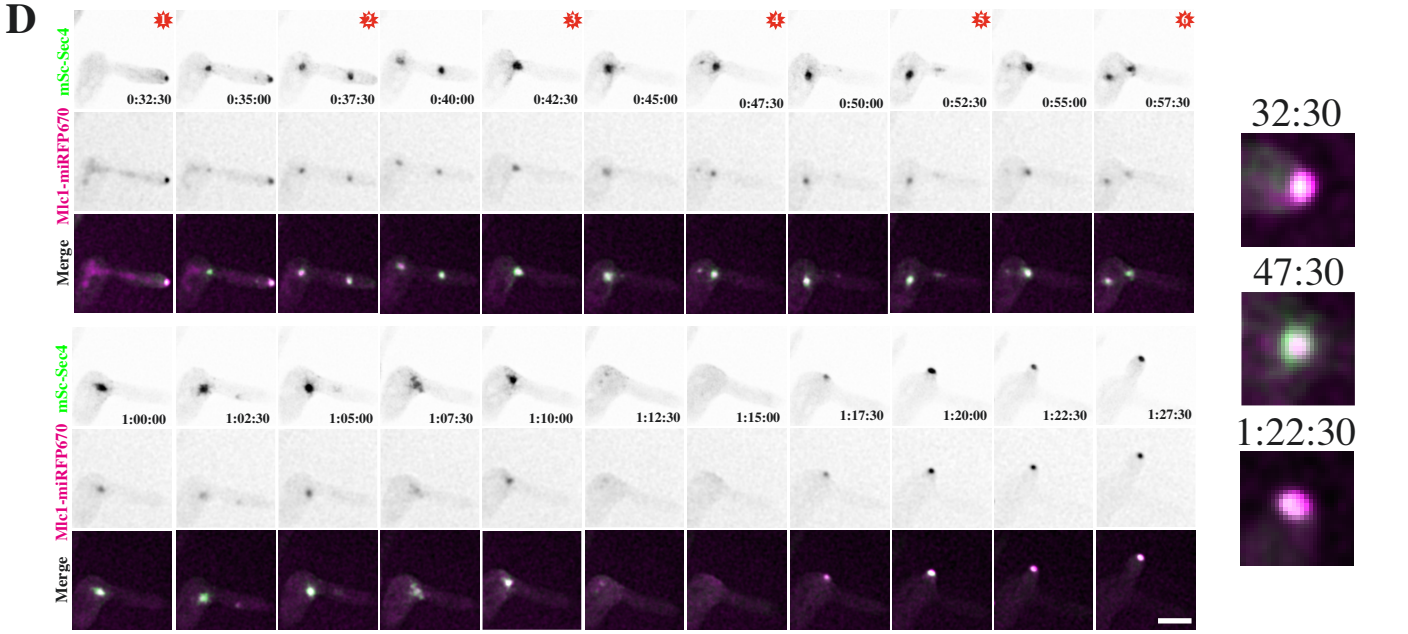
D
mSc-Sec4
Mlc1-miRFP670
Merge
0:32:30
0:35:00
0:37:30
0:40:00
0:42:30
0:45:00
0:47:30
0:50:00
0:52:30
0:55:00
0:57:30
1:00:00
1:02:30
1:05:00
1:07:30
1:10:00
1:12:30
1:15:00
1:17:30
1:20:00
1:22:30
1:27:30
32:30
47:30
1:22:30

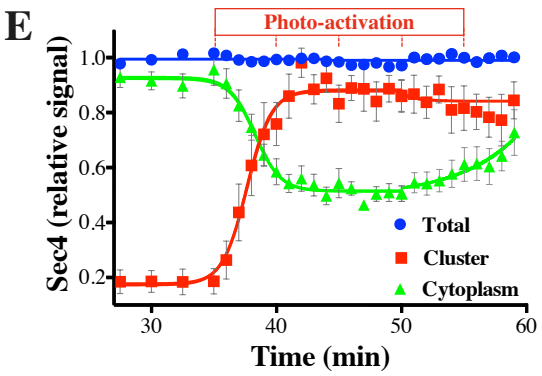
E
Photo-activation
Sec4 (relative signal)
Total
Cluster
Cytoplasm
Time (min)

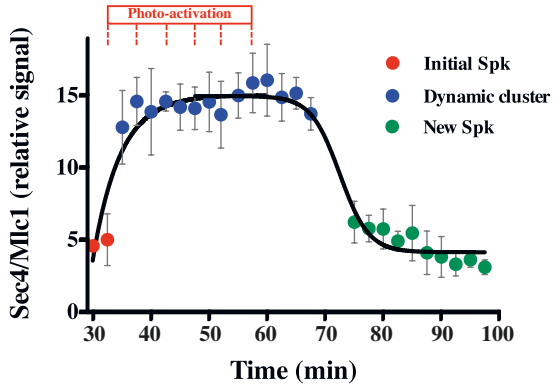
F
Photo-activation
Sec4/Mlc1 (relative signal)
Initial Spk
Dynamic cluster
New Spk
Time (min)

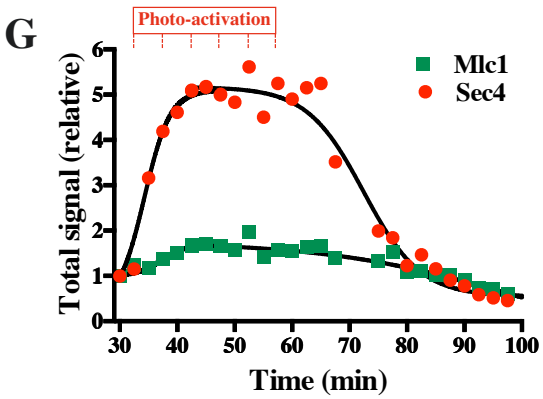
G
Photo-activation
Total signal (relative)
Mlc1
Sec4
Time (min)

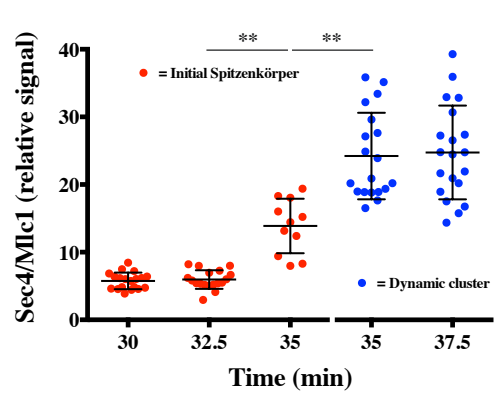
H
**
**
= Initial Spitzenkörper
= Dynamic cluster
Sec4/Mlc1 (relative signal)
Time (min)

Supplementary Figure S4. *Related to Figures 3 and 4*

The *de novo* cluster of secretory vesicles has a dramatic increase in Sec4 and is highly dynamic. A) Substantial increase in the instantaneous velocity of Mlc1 cluster. The instantaneous velocity of the Mlc1 cluster from a representative time-lapse is shown with initial Spk (red) and new dynamic cluster (blue) indicated. B) The Mlc1 cluster elongates along the axis of movement. The ratio of major over minor axis of the Mlc1 cluster at the initial Spk was determined from 4 cells (solid lines and symbol) exposed to 488 nm light and 3 cells kept in the dark (dashed lines and open symbols), with mean and standard deviation indicated. C) The Sec4 vesicle cluster is highly dynamic. The instantaneous velocity of the Sec4 cluster from a representative time-lapse is shown with initial Spk (red) and new dynamic cluster (blue) indicated. D) The increase in Sec4 level does not correlate with an increase in Mlc1 level at the new cluster. A strain expressing CibN-Ct_{Rac1}, Cry2-GFP-Cdc42$[G12V]_{cyto}$, mSc-Sec4 and Mlc1-miRFP was incubated as in Fig. 4A and exposed to 6 pulses of 488 nm light (every 5 min) as indicated by red stars. At indicated times DIC, RFP (green) and miRFP (magenta) images were acquired and sum projections are shown from a representative time-lapse. Inset (images at 32.5, 47.5 and 82.5 min) shows an enlargement of secretory vesicle cluster. E) Increase in Sec4 level at the cluster occurs concomitant with a decrease in cytoplasmic signal. RFP signal was quantified from 8 cells expressing mSc-Sec4, as in Fig. 4A. Intensities were corrected for photo-bleaching by fitting the total signal from each cell to an exponential and correcting cytoplasmic and Spk signals over time. Cytoplasmic signal is the average from 3 different areas within the cell. The Spk signal represents the total of the initial and new cluster, where relevant. The maximum values from each compartment in each experiment were set to 1 and the mean is shown with SEM indicated. F) Dramatic increase in the ratio of Sec4:Mlc1 upon recruitment of Cdc42•GTP. Quantification of RFP and miRFP signals at the cluster of secretory vesicles from 6 cells followed by time-lapse microscopy as in Fig. S4D. Mean ratios and standard deviation are shown. G) Total Sec4 and Mlc1 at the Spk following photo-activation. Values are the averages from 6 cells followed by time-lapse microscopy as in Fig. S4D and the signal at time 0 was set to 1. H) Sec4 is recruited to both the initial Spk and a new dynamic cluster subsequent to Cdc42•GTP photo-recruitment. The ratio of mSc-Sec4 signal to Mlc1-miRFP signal at the initial Spk (red) and new dynamic cluster (blue) from a total of 20 cells followed by time-lapse microscopy is shown. Cells were exposed to 488 nm light at 32.5 min. The differences between indicated conditions were statistically significant, $p < 0.0001$.

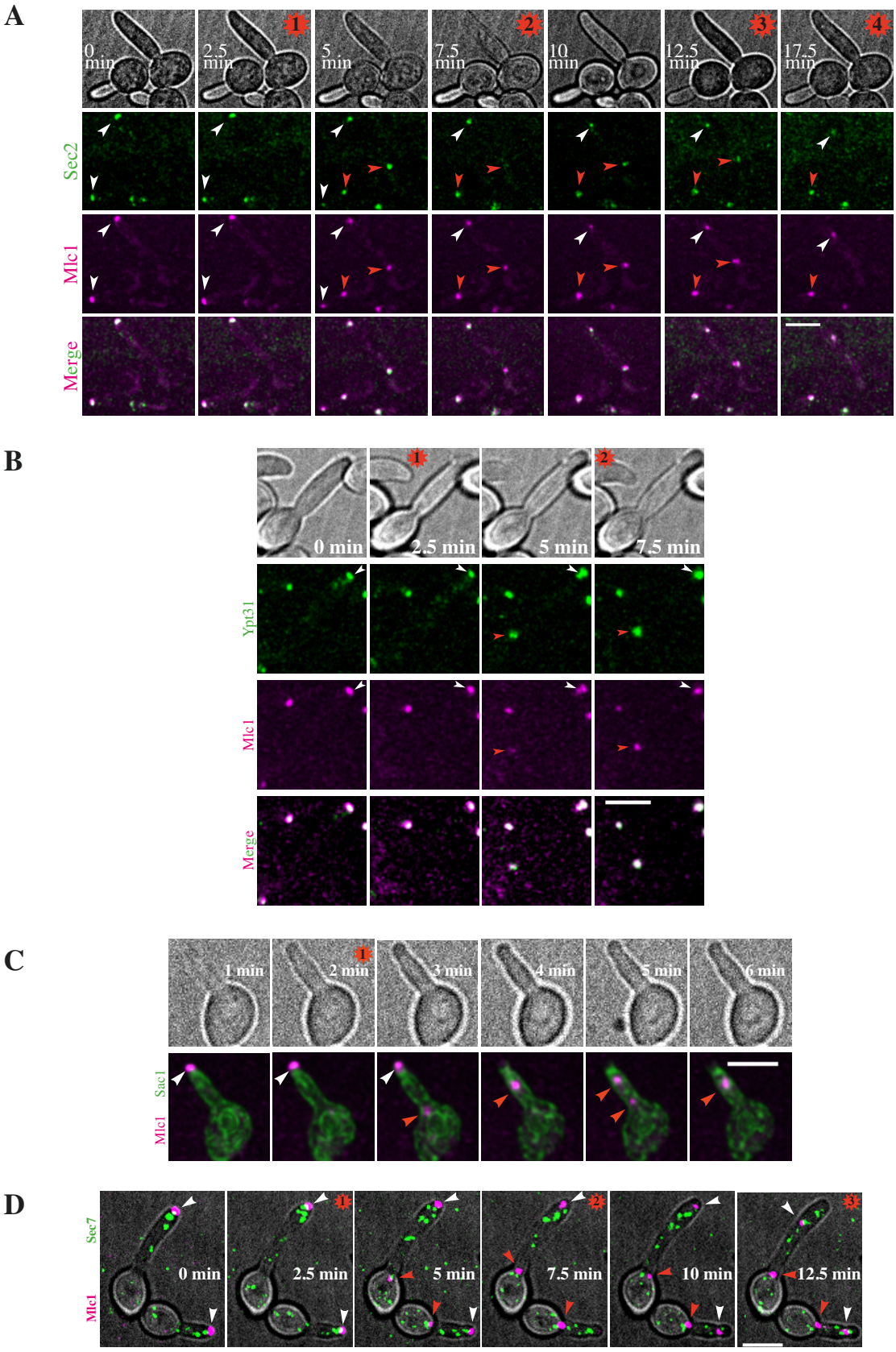

Supplementary Figure S5. *Related to Figure 4*
The Sec4 Rab GEF, Sec2, and the Rab GTPase Ypt31 are localized to new vesicle cluster, which is distinct from the ER and late Golgi. A) Sec2 is localized to the new vesicle cluster. Strain as in Fig. 4B incubated similarly; DIC and maximum projections of RFP (green) and miRFP (magenta) and merged images from a representative time-lapse are shown. Photo-activation pulses are indicated by red stars and arrowheads indicate the Spk (white) and new cluster (red). B) Ypt31 is localized to the new vesicle cluster. Strain as in Fig. 4C incubated similarly; DIC and maximum projections of RFP (green) and miRFP (magenta) and merged images from a representative time-lapse are shown. D) The new vesicle cluster does not overlap with the endoplasmic reticulum. Strain as in Fig. 4D incubated similarly; DIC and maximum projections of RFP (green) and miRFP (magenta) and merged images from a representative time-lapse are shown. E) The new vesicle cluster is distinct from the late Golgi. Strain as in Fig. 4E incubated similarly; DIC and maximum projections of RFP (green) and miRFP (magenta) and merged images from a representative time-lapse are shown.

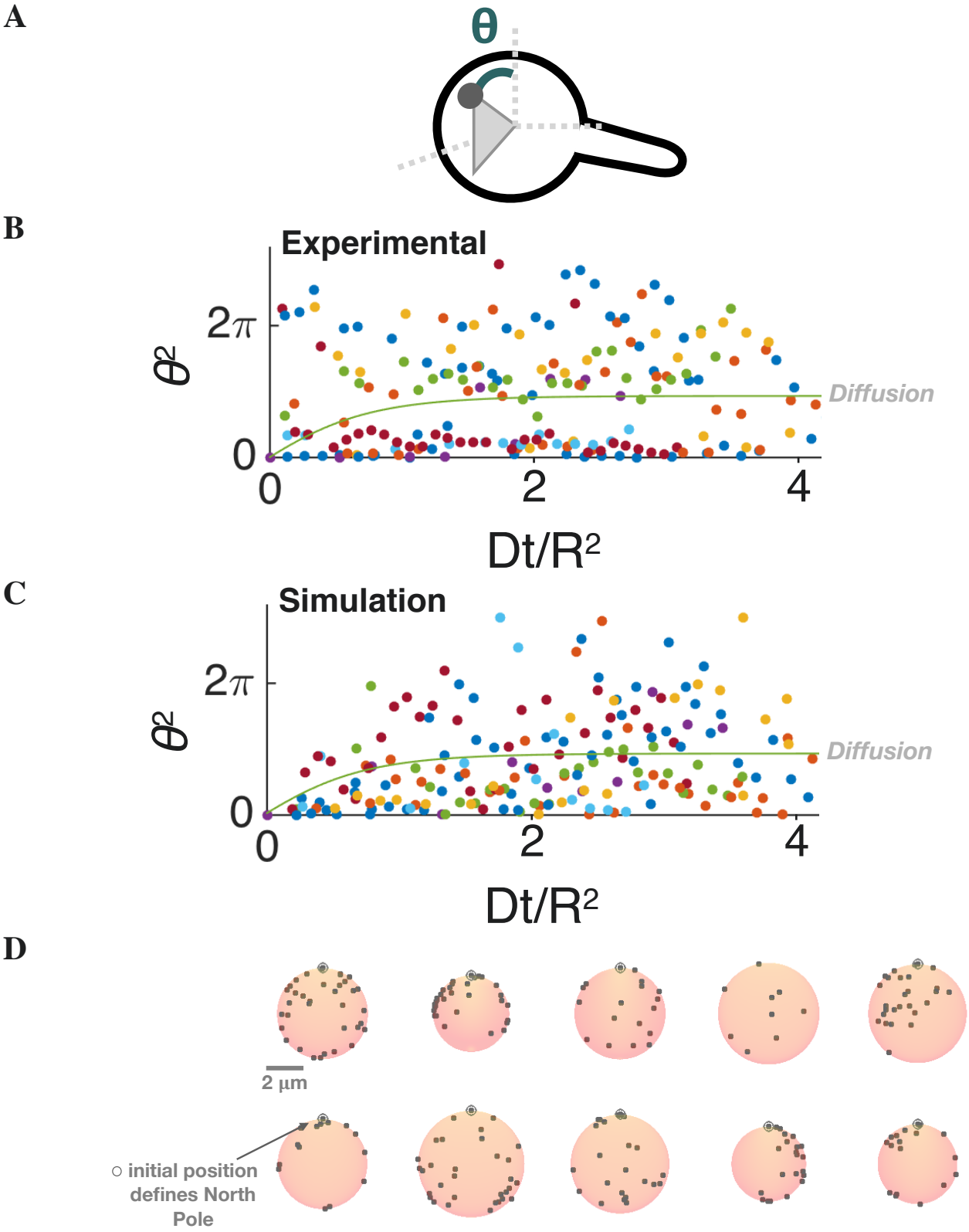

Supplementary Figure S6. *Related to Figure 7*
Vesicle cluster dynamics are inconsistent with a diffusive process. A) Schematic of colatitude (θ) representation in a filamentous cell. B) Square colatitude (θ^2) of the vesicle cluster as a function of time, each color represents data for one cell; 10 cells were used for this analysis, where the cluster remained in the mother cell (Fig. 7B). The first position of the cluster is aligned to the mother cell North pole such that $\theta^2_{t0} = 0$. Time is non-dimensionalized with R^2/D, where D = 1.4 μm²/min is within the range of variation of typical diffusivities in cells (Giese et al., 2015) and R^2 is the square radius of the mother cell. The theoretical prediction for the average colatitude as a function of the non-dimensional time Dt/R^2 for a purely diffusive motion on the spherical cortex (solid line with D = 1.4 μm²/min used for simulations) is inconsistent with motion of the cluster (fit does not converge), which shows no time dependence. Similar results were observed with θ. C) Numerical simulation of pure diffusion of vesicle cluster dynamics with identical number of cells and time points. Square colatitude (θ^2) of the simulated random vesicle cluster depends on time, consistent with the prediction for pure diffusion. Fitting the moving average to the theory provides an estimate for the diffusivity of 1 ± 0.7 μm²/min, consistent with the value used to generate these data, $r^2 = 0.62$ (upper panel). D) An identical number of cells and time points as in Fig. S6B was used and top down view of the positions of vesicle cluster (as in Fig. 7B) from pure diffusion simulation (lower panel).

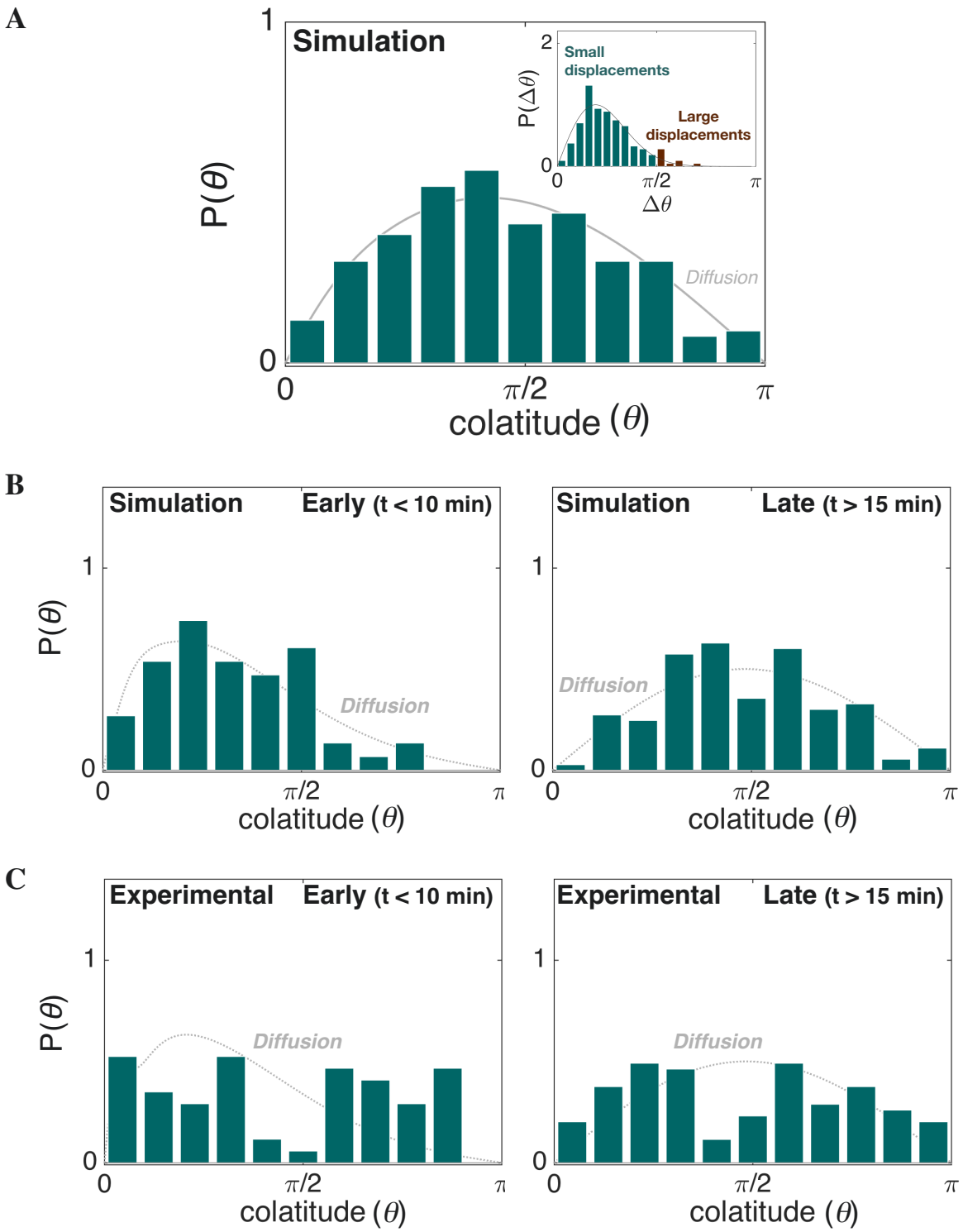

Supplementary Figure S7. *Related to Figure 7*
A) Probability distribution of the cluster's colatitude computed for simulated diffusion of all cells at all times converges to the theoretical prediction for pure diffusion (solid line, $p = 0.24$; Kolmogorov-Smirnov test). Deviations result from the finite sample size. Inset shows the probability distribution of angular displacement measured at adjacent points (1 min apart) is consistent with the prediction for pure diffusion after 1 min, solid line ($r^2 = 0.93$ and $p = 0.09$; Kolmogorov-Smirnov test). The theoretical prediction for diffusion was calculated using the diffusivity in the simulations (D = 1.5 μm^2/min), t = 1 min acquisition time and R = 2.7 μm as the average mother cell radius. Note that there are little to no large displacements. B) Purely diffusive behavior is dependent on time. The statistics computed over the first 10 min (left panel) and times greater than 15 min (right panel) are consistent with the theoretical predictions indicated by dashed grey line, with deviations due to finite sample size ($p = 0.11$ and $p = 0.14$; Kolmogorov-Smirnov test). Early and late distributions are statistically distinguishable ($p = 6 \times 10^{-4}$; Kolmogorov-Smirnov test). C) Bimodal distribution of vesicle cluster colatitude is independent of time. The statistics computed over the first 10 min (left panel) and times greater than 15 min (right panel) for experimental data are not consistent with a purely diffusive process ($p = 1.7 \times 10^{-5}$ and $p = 2.6 \times 10^{-4}$; Kolmogorov-Smirnov test). Analysis of the experimental trajectories of the vesicle clusters of the 10 cells (Fig. 7B and 7C). The prediction for a purely diffusive process is indicated by dashed grey line and the data differ only slightly from the probability distribution shown in Figure 7C. The two distributions are statistically indistinguishable ($p = 0.297$; Kolmogorov-Smirnov test).

IV – A biosensor reveals the spatiotemporal dynamics of phosphorylated Gβ in yeast cells decoding pheromone gradients

Rashida Abdul-Ganiyu[1], Leon A. Venegas[1], Xin Wang[1], **Charles Puerner[2]**, Robert A. Arkowitz[2], Brian K. Kay[1], and David E. Stone[1]

Affiliations:

[1]Department of Biological Sciences, University of Illinois at Chicago, Chicago, IL 60607, USA.

[2]Université Côte D'Azur, CNRS, INSERM, Institute of Biology Valrose (iBV), Parc, Valrose, Nice, France.

In this section I will explain my contribution to the collaborative work with the Stone lab at the University of Chicago "A biosensor reveals the spatiotemporal dynamics of phosphorylated Gb in yeast cells decoding pheromone gradients," by Abdul-Ganiyu et al. This work was submitted to the *Journal of Cell Biology*. The purpose of this work was to investigate the dynamics of the phosphorylated form of Gβ during pheromone perception and mating events in the budding yeast *Saccharomyces cerevisiae* by using a novel biosensor reporter for phosphorylated Gβ. My contribution to this work was through my extensive experience with weak signals for microscopy. I undertook several live-cell imaging experiments and deconvolution image treatment to improve the image quality of the very low-level signal observed with this biosensor. My contribution lead to the creation of Figure 6A, facilitated the quantitation in 6B-C as seen below. This article is currently being redrafted and will be re-submitted.

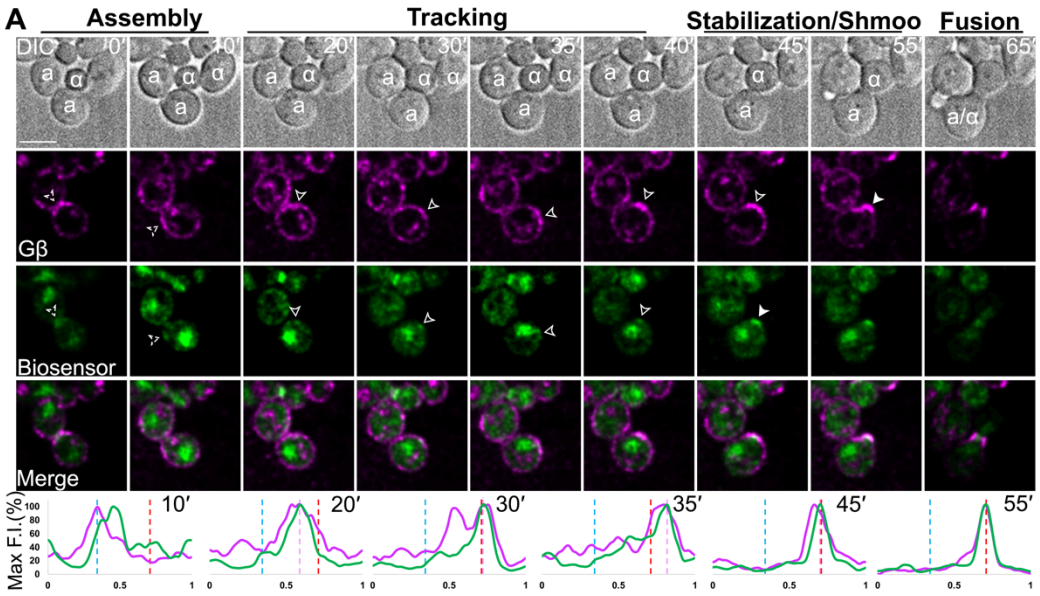
A
Assembly
Tracking
Stabilization/Shmoo
Fusion
DIC
Gβ
Biosensor
Merge
Max F.I. (%)
10′
20′
30′
35′
45′
55′
65′
a/α

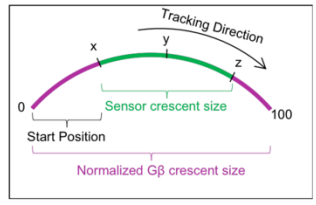
B
Tracking Direction
x
y
z
0
100
Sensor crescent size
Start Position
Normalized Gβ crescent size

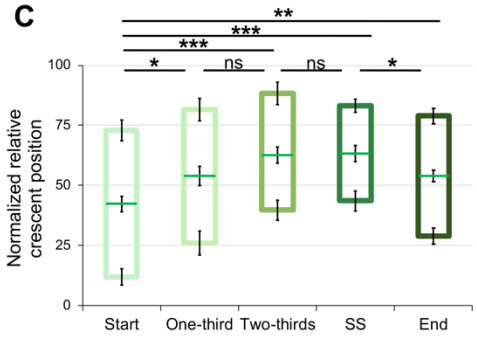
C
**
***
***
*
ns
ns
*
Normalized relative crescent position
100
75
50
25
0
Start
One-third
Two-thirds
SS
End

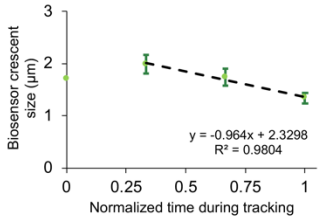
D
Biosensor crescent size (μm)
3
2
1
0
y = -0.964x + 2.3298
R² = 0.9804
0
0.25
0.5
0.75
1
Normalized time during tracking

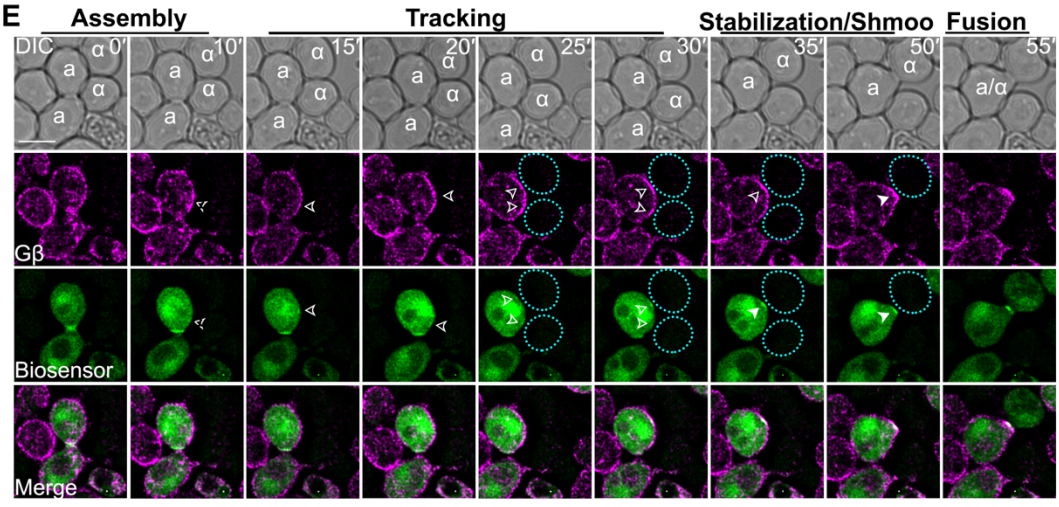
E
Assembly
Tracking
Stabilization/Shmoo
Fusion
DIC
Gβ
Biosensor
Merge
0′
10′
15′
20′
25′
30′
35′
50′
55′
a/α

Figure 6. Relative distribution of gradient-tracking Gβγ and the biosensor in WT cells. *MAT***a** cells co-expressing RFP-Gβ and the biosensor were mixed with *MAT*α cells in equal proportions and imaged at 5-minute intervals. The mating partners are labelled **a** and α in the DIC images. Fluorescent images show the localization of Gβ (magenta) and the biosensor (green) during assembly, tracking, stabilization, and fusion. The dashed, closed, and filled arrowheads indicate the peaks of the default, tracking and stabilized signals, respectively. The dotted blue outlines represent *MAT*α cells that appear to be competing to mate with the indicated *MAT***a** cells. (A) Representative time-lapse images of a *MAT***a** cell orienting toward a single partner. The plots show the relative distribution of Gβ (magenta) and the biosensor (green) on the PM at the indicated time points (10-point rolling average). The dashed blue, pink, and red lines mark the DS, tracking, and CS peak, respectively. The images are representative of 30 matings examined. Scale bars, 5μm (B) Schematic diagram of how the size and position of the biosensor crescent relative to the total Gβ crescent was measured during gradient sensing. With the size of each Gβ crescent (magenta arc) normalized to 100, the size and midpoint (y) of its corresponding biosensor crescent (green arc) are given by z-x and (z-x)/2 + y, respectively. (C) Box plots showing the mean size and position of the biosensor crescents relative to the total Gβ crescents during gradient sensing. The boxes show the mean downgradient ends, midpoints (horizontal line), and upgradient ends of biosensor crescents ± SEM superimposed on the Gβ crescents, which have been normalized to 100 at each time point. Start, the last time point before tracking begins; 1/3 and 2/3, fraction of complete distance tracked; SS, biosensor stabilization at the CS; End, Gβ stabilization at the CS. n = 20 from three independent experiments. Mean crescent midpoints ± SEM; Start = 42.3 ± 3.3; One-third = 53.9 ± 4.0; Two-thirds = 62.6 ± 3.3; SS = 63.4 ± 3.4; End = 54.0 ± 2.4; *$p < 0.05$; **$p < 0.005$; ***$p < 0.0005$; ns, not significant.

(D) Biosensor crescent size during tracking in cells co-expressing RFP-Gβ and the GFP-biosensor. Mean crescent size ± SEM; n = 20. (E) Representative time-lapse images of *MAT***a** cells orienting toward two potential partners of equal size. Scale bars, 5μm

Discussion

I – Mechanical force induced morphological changes

A significant amount of work has been done on the ability of *C. albicans* to undergo active penetration into host tissue and substrates of different stiffnesses (Allert et al., 2018; Desai et al., 2015; Goyer et al., 2016; Moyes et al., 2015). However, these studies investigated invasion by endpoints assays or snap shots of the invasion process. We aimed to study the process of invasion in real-time in a controlled environment, which has allowed for a quantitative analysis of the effects of the physical forces on this fungus. This work has led to four main conclusions regarding filamentous growth against the mechanical resistive forces, that are encountered during substrate invasion: 1) there is a substrate stiffness threshold of ~200 kPa under which *C. albicans* hyphae are able to invade; 2) invasive growth leads to altered cell morphology that depends on substrate stiffness; 3) during invasive growth there is an increase in polarized active Cdc42 and a decrease in active Rho1 polarization; 4) the observed morphological changes are a result of growth against resistive forces, *i.e.* mechanical compression and not an alteration of the growth site. Ablating cell compartments on either side of a buckling compartment of an invasive filament relieved the turgor pressure on either side. Quantification of the change in buckling angle showed a significant relaxation of the buckling angle giving further evidence that these invasive cells are under constant mechanical force during invasion (Appendix Figure 1).

Additionally, by using these quantitative data of growth during substrate invasion with substrates of known stiffnesses, we were able to determine the effective turgor pressure of *C. albicans* to be 1-3 MPa, which is within the range previously calculated using a similar indentation based method and from biofilm cells (Desai et al., 2015; Thomson et al., 2015). During invasion in 100 kPa PDMS, we calculated a turgor pressure of 1.5 MPa, which is

close value to the 1.2 MPa value calculated by Thomson *et al*. 2015, and slightly less than the 2 MPa value calculated for biofilm cells, which is to be expected since biofilm cell have a higher glycerol concentration (Desai et al., 2015, 2013; Thomson et al., 2015). Interestingly, we calculated the turgor pressure during invasive growth at a higher stiffness (150 kPa) to be 3 MPa. It appears that turgor pressure can be regulated to counter growth in a stiffer substrate. Linked to this we observed instances where there were small numbers of cells that were able to penetrate very stiff substrates; we termed these cells escapers. It is possible that the turgor pressure of these escaper cells was higher and hence they were able to penetrate more efficiently.

We initially investigated invasive growth in a wild-type strain, however, given that the *mlc1* mutant is able to invade PDMS substrate to some extent, it would be interesting to further investigate the invasion mutant over a range of PDMS stiffnesses. Perhaps this is due to filament geometry or the cells eventually succumb to the surrounding pressures during invasion and lyse. Initial experiments using haploid and tetraploid strains that were kindly provided by Judith Berman's lab suggests geometry plays a role in invasive ability. In these strains, ploidy appears to affect filament diameter with the tetraploid having wider than normal filaments and haploids are slightly narrower. Initial results showed that the haploid seemed to invade less efficiently than the diploid wild-type or the haploid.

During the process of invasion, it might be proposed that the cells are under constant stress due to the mechanical force of invasion. I sought to address this possibility by using stress reporters to quantify if invasion causes stress on the cells. I used the osmolarity stress marker Hog1 and the cell wall stress marker Pkc1 (Andrews and Stark, 2000; Day and Quinn 2019). Using osmotic shock as a control experiment I found that during osmotic stress Hog1localizes to the nucleus, as has been shown previously, while Pkc1, which normally localizes to the filament tip, re-localizes along the sides of the filament (Appendix Figure

2A,B). During invasive growth neither Hog1 or Pkc1 showed altered localization (Appendix Figure 2C-F). This provides evidence that cells during invasive growth are not under stress; this is similar to what has been previously shown that fission yeast growing under mechanical force do not show indications of cell stress (Minc et al., 2009). Another interesting possible effect of invasive growth is an effect on cytoplasmic crowding, or rheology. This is an interesting question that should be addressed. I have done preliminary work which shows effects of cytoplasmic crowding during drug treatment and during the yeast to hyphae transition using particle tracking of fluorescently genetically encoded monomeric nanoparticles (GEMs) (Delarue et al., 2018), which I optimized for use in *C. albicans* (Appendix Figure 3). It would be interesting to observe the effects on cytoplasmic crowding during invasive growth as well.

Another interesting observation that was made during this work was that the Spitzenkörper appears to be altered during burst-out events (see appendix figure 4). During the rare occurrence of a burst-out event, I also observed several instances where there was a transient increase in the Spitzenkörper intensity, observed by Sec4, and this consistently appeared just after the breakthrough occurred.

II – The composition and function of the *C. albicans* Spitzenkörper

It has been known for some time that the *C. albicans* hyphae have a Spitzenkörper, which is a feature of filamentous fungi, and this structure clearly contains a population of vesicles (Crampin et al., 2005; Jones and Sudbery, 2010; Li et al., 2007; Silva et al., 2019; Weiner et al., 2019). Recently, this structure was studied by perturbing polarized growth through optogenetic recruitment of Cdc42•GTP over the plasma membrane (Silva et al., 2019). Although, there is little known about the type of vesicles that are present in the structure and what the effects are to cells when this structure is continually altered. Previous

studies showed evidence that the population was at least largely secretory vesicles. Previous deletion of the gene encoding the Spitzenkörper localized formin *BNI1* resulted in no detectable Spitzenkörper formation (Li et al., 2005), making it difficult to study an altered Spitzenkörper. However, other work has been done on altering the Spitzenkörper through actin cable disruption using cytochalasin A (Crampin et al., 2005), latrunculin A (Crampin et al., 2005; Weiner et al., 2019) and through optogenetic delocalization (Silva et al., 2019). In the last study the Spitzenkörper appeared to be a robust structure that stayed intact, despite altered dynamics and cellular localization (Silva et al., 2019). Lastly, a *SEC3* mutant has been used to perturb the tip structure and leads to unfocused growth, shown by electron microscopy, and tip bulging after initial germ tube formation (Li et al., 2007; Weiner et al., 2019).

Here, I have presented work that explores the composition of the Spitzenkörper and, more importantly, its function *in vivo* using loss of function mutants (*mlc1*) as well as altering its stability and distribution. There are four main conclusions from my work: 1) the Spitzenkörper is comprised essentially of secretory vesicles; 2) the Spitzenkörper is critical for maintaining cell size and growth rate, specifically perturbing the Spitzenkörper increases filament diameter and increase the range of growth rates observed in a population; 3) there is a strong link between filament diameter and its extension rate, with a linear relationship between these two; 4) there does not appear to be a link between Spitzenkörper size and cell morphology, *i.e.* filament diameter or its extension rate.

I show that the Spitzenkörper in wild-type hyphae consists of ~100 secretory vesicles which is similar to the number vesicle determined by electron microscopy (Weiner et al., 2019), although somewhat higher. Previously it was shown that the Spitzenkörper can be labeled with FM4-64, which requires endocytosis for its uptake (Crampin et al., 2005; Zeng et al., 2012). However, it has been shown in *S. cerevisiae* (Bhave et al., 2014), filamentous

fungi (Fischer-Parton et al., 2000; Hernández-González et al., 2018) and, more recently, in *C. albicans* (Ghugtyal et al., 2015) that this lipophilic dye first travels to the Golgi *via* the endocytic network, where it then buds off in post Golgi vesicles targeted to the plasma membrane (*via* the Spitzenkörper).

Although the numbers of vesicles determined by electron microcopy are within the range of the number secretory vesicles, I determined by fluorescence microscopy, there is certainly a shift in the number from ~60 to what I estimate at ~100. There are several possible explanations for this difference. Firstly, the number of vesicles determined by EM may be an under estimation due to fixation affect, *i.e.* some destruction of some vesicles. Secondly, my estimation by fluorescence microscopy could be an overestimation due the fact that signals considered to be from secretory vesicles encompass a range of sizes, such that the signal of some vesicles or clusters are not fully captured, meaning that the average signal per vesicle is actually higher. Finally, the discrepancy could be due to differences in the numbers of cells sampled.

I was able to show that from the first time that a cluster of secretory vesicles is observed on the cell cortex its intensity is constant over time. Interestingly, and consistent with our previous studies (Silva et al., 2019), a vesicle cluster is typically observed prior to germ tube emergence. The results of altering the Spitzenkörper suggests that focusing vesicle traffic to a restricted, unique location is important for a constant filament morphology in a population of cells. Below I will discuss three questions related to the main aspects of this work.

III – Function of Mlc1 and its role in the Spitzenkörper

Interestingly *mlc1* deletion cells were multinucleated, reminiscent of filamentous fungi that have more than one nucleus (Gladfelter, 2006). We speculate this could be due to a

uncoupling of nuclear and cellular division, and I would need to examine in further detail time acquisitions to determine if the cell division is delayed or lacking. In addition, *mlc1* deletion mutants had a ~two-fold increase in filament diameter. Although the average extension rate for these cells was not substantially different from the wild-type, there was a strong correlation between extension rate and diameter. This suggests that in the wider cells with a substantially increased diameter there is likely a significant increase in vesicle incorporation into the tip to compensate for the increased geometry. In *S. cerevisiae*, Mlc1 is essential and plays a role in the regulation of secretory vesicle traffic to the site of cytokinesis and to the bud tip through an association with the myosin motor proteins Myo1 and Myo2 respectively (Luo et al., 2004; Pennestri et al., 2007; Stevens and Davis, 1998). Mlc1 is recruited to the cytokinetic ring, where it in turn recruits the IQGAP-like protein Iqg1 for actomyosin ring contraction and Myo1 to regulate the traffic of material for cytokinetic ring closure (Boyne et al., 2000; Feng et al., 2015; Luo et al., 2004; Shannon and Li, 2000).

We speculate that in *C. albicans* Mlc1 plays a role in regulating vesicle traffic from the Spitzenkörper by focusing or directing delivery to a restricted region of the filament tip. As we know from EM studies that secretory vesicles are within a diameter distance from the plasma membrane, it is possible that the size, shape and number of vesicles in the Spitzenkörper play, in part, a role in the location of vesicle fusion (also dictated by Sec3) and flux of vesicles, *i.e.* a greater area where vesicles are adjacent to the plasma membrane, which could mean a larger area for fusion and, hence, an increased flux. Without Mlc1 there is an increase in the rate of vesicle flux to the apex that is also less focused, leading to wider filaments with relatively constant extension rates. Consistent with this idea, the total intensity of the Spitzenkörper as observed with mSc-Sec4 is increased, while the overall area of the cluster remained unchanged. However, it would be critical to measure the region of the Spitzenkörper that is adjacent to the plasma membrane as this could increase without an

overall area increase. Nonetheless, the two-dimensional shape of the Spitzenkörper is not affected, arguing against this possibility. My results suggest there is an increase in the packing density of secretory vesicles in the Spitzenkörper, *i.e.* an increased population of vesicles in the cluster at a given time or alternatively an increase in the Sec4 level per vesicle, hence overall in the Spitzenkörper. This observed increase in Spitzenkörper intensity could be due to a lag in the initiation of traffic out of the Spitzenkörper. It is possible that initially, when the Spitzenkörper is forming, vesicles build up in a cluster and, for a specific amount of time, the Spitzenkörper increases in size as there are less vesicles leaving the Spitzenkörper, which subsequently increases.

Using the single vesicle intensity value and a normalization based on Spitzenkörper intensity, I estimated that there is roughly twice as many secretory vesicles in this mutant compared to the wild-type cells, assuming that the Sec4 per vesicle level is constant. This could be addressed by examining the average Sec4 signal in what appear to be vesicles, *i.e.* resolution limited signals. Additionally, it is possible that the altered growth rate results in an altered cell wall, hence explaining the sensitivity to cell wall perturbants and antifungal drugs, such as caspofungin (Mazu et al., 2016; Sorgo et al., 2011).

I also observed that the population of these mutants is highly variable in almost all aspects. It appears that Mlc1 not only regulates the flux of vesicles to the filament tip but also regulates the uniformity of this flux. However, if these two processes were linked, then only one would need to be altered for both to be affected. A large variation in budding cell size and shape was also observed. Importantly, the budding cell size had a significant positive correlation with filament diameter. It appears that the hyphal filament width is set by budding cell axis perpendicular to germ tube emergence and hence a wider budding cell leads to a wider filament. This would suggest that if polarity were altered in the budding cells, even slightly, it would result in wider filaments. It is interesting to note that the blastospore area

correlates linearly with the filament diameter, *i.e.* r^2 with r. One possibility is the critical parameter in the blastospore (which was the mother cell) is the radius of curvature, as this could dictate the size of the polarity cluster. Hence a mother cell that is large would have a larger radius of curvature and, hence, a larger polarity cluster would be maintained and lead to wider filaments.

It is likely that once the filament diameter is initially determined, it is maintained by feedback loops that maintain the region of vesicle fusion and the filament diameter. This process is likely regulated by Sec3 and Cdc42; the clustering of both on the plasma membrane of the apex is probably affected by the zone of secretory vesicle fusion. It would be important to investigate the distribution of both of these proteins in this mutant. Additionally, endocytosis regions have been shown to contain the region of exocytosis and disruptions in the endocytic containment results in a wider polarity axis (Jose et al., 2013). Although I do not see displaced endocytosis sites, it did appear that these sites were less intense, suggesting endocytosis might be decreased for the *mlc1* mutant. This would need additional investigation to address fully this notion.

IV – Mis-targeting the Spitzenkörper

Using a constitutively synthetic interaction, between the Mlc1 Spitzenkörper component fused to a GFP Nanobody and GFP targeted to the plasma membrane, I was able to alter the distribution of the Spitzenkörper. Given the proximity of the Spitzenkörper and the plasma membrane, it is not possible to resolve the two compartments spatially; however, in this mutant, the Spitzenkörper was less circular and had a large two-dimensional area. This resulted in a substantial increase in hyphal diameter, similar to that observed in the *mlc1* deletion mutant. In contrast to the *mlc1* deletion mutant, the average filament extension rate of this mutant was also increased. These results are similar to what has been previously

reported in *S. pombe* strains with a GNB decorated PM and GFP labeled v-SNARE protein Syb1 (Abenza et al., 2015). These effects are dominant as there is a wild-type copy of *MLC1* present, and I have not observed any defects with the *MLC1* heterozygote. By examining the GFP channel it is apparent that plasma membrane is re-localized,; however, we can't distinguish whether this is due to the Spitzenkörper or the plasma membrane.

I speculate that the wider diameter of these filaments is due to the broadened region of secretory vesicle fusion. The Spitzenkörper is perhaps associated with a larger region of the filament tip due to a change in shape or anchoring, which in turn spreads out new membrane insertion, resulting in a wider filament. This is a similar, in some respects, to that observed in the *mlc1*Δ/Δ mutant. Here extension rate is also increased, and I speculate again that an increased region of vesicle fusion with the plasma membrane leads ultimately to the spreading out of Cdc42 and Sec3. If this were true, it could result in more fusion at the same time, for example like the analogy that with three separate lines to three separate doors, more people can enter the room as opposed to three lines going through one door. Again, with this mis-targeted mutant, there remains a strong linear dependence between extension rate and diameter as well as an increase in variation of filament diameter and extension rate with a population.

V – Stabilizing the Spitzenkörper

The other perturbation of the Spitzenkörper involved a constitutive interaction between two Spitzenkörper components, Mlc1 and Sec4. Analysis of the Spitzenkörper Sec4 dynamics by FRAP confirmed that there was a significant increase in the Sec4 immobile population, indicating that the Spitzenkörper was stabilized. The exchange rate, *i.e.* $t_{½}$ for recovery did not change, consistent with the notion that the rate of vesicles into the Spitzenkörper (as well as that going out, as the size remains constant) was unchanged in this

mutant. This SPK-stabilized strain had an increased amount of Sec4, with an unchanged size and shape, suggestive of increased packing. Compared to the wild-type and PM-targeted mutant, the diameter was intermediate, while the extension was identical to the wild-type, similar to the situation with the *mlc1* deletion mutant. Interestingly, there was substantially less variation in the filament diameter with this SPK-stabilized strain compared to the deletion mutant as well as the PM-targeted strain. However, the extension rate was still quite variable.

Irrespective of the method to perturb the Spitzenkörper, there is a clear and strong dependence of extension on filament diameter. I speculate that this also exists in the wild-type; however, the range of diameters is very small, limiting measurement precision due to light resolution limits and pixel size. In any case the wild-type strains fall on the linear fit of filament extension rate versus diameter. This suggests that there is a link between diameter and secretory vesicle flux, *i.e.* new membrane addition and, as indicated above, may be due to the fact that with a focused and restricted zone of fusion, spatial constraints limit extension rate and when this extended (spread out) increased fusion can occur. This assumes that exocyst components, such as Sec3 and SNARES, are not limiting, or that the cell can compensate such as in the case of wider filament.

VI – Heterogeneity within populations

A common underlying theme in this work is a consistent heterogeneity within all measurements of a sample of single cells within a population. Often, we are comparing sample populations using mean averages and statistical significance between conditions; however, an often-overlooked aspect is the variation within each population, and how that may compare between conditions. In our investigation on the mechanical forces during invasive growth, we often observed variation within conditions: for example, extension rates

clearly decrease as a function of stiffness. However, within each condition, there may be subpopulations of cells with greater or decreased invasive growth ability, leading to a reasonable amount of spread within each condition. We observed what we referred to as 'escaper cells', which were cells that were able to invade substrate stiffnesses beyond the threshold of the population of cells. This variation is also clearly increased, for example with extension rates in Spitzenkörper perturbed mutants.

I have compiled the variation of several parameters from the Spitzenkörper perturbation study (Appendix Figure 4). The variation parameter used here is the coefficient of variation, which is a normalization of the variation by dividing the standard deviation by the mean. Doing this allows one to directly compare variation between conditions that would not be comparable by standard deviation due to the difference in scales. Here, it can be seen that the variation for the *mlc1*Δ/Δ mutant is substantially and consistently larger than the control strains (Appendix Figure 4A). A similar trend is seen in the GNB perturbed strains, with the SPK-stabilized strain showing the largest variation (Appendix Figure 4B).

This interest in variation has increased in recent years, particularly in the context of population heteroresistance to antifungal drug treatments not only in *C. albicans* but also other pathogenic fungi such as *C. glabrata, Cryptococcus neoformans, Cryptococcus gatti,* and *Aspergillus Fumigatus* (Ben-Ami et al., 2016; Bleichrodt et al., 2020; Rosenberg et al., 2018; Stone et al., 2019). I feel this topic of population variation could be an important aspect to research in more detail in the context of filamentous growth of *C. albicans* particularly because I have shown here that some perturbations to cellular processes may amplify what is normally a small amount of variation, which allows us to study this variation in greater detail. Some questions that arise in this context are: Does heterogeneity in invasive ability play a significant role in host infection? What leads to heterogeneity in size with *mlc1*Δ/Δ? Is there a

mechanism that allows some cells (‘escapers’) to survive and infect the host better, which could be useful drug targets?

VII – Conclusions and future prospects

Here I have presented two lines of work, both of which have a main goal of better understanding the mechanisms of polarized growth in the human fungal pathogen *C. albicans*. In the first we investigated how the mechanical forces and substrate stiffness affect the invasive capability of *C. albicans*. We first found a stiffness threshold where the fungus is no longer able to invade. Upon studying invasive growth compared to surface growth, we found that under the mechanical forces of invasion, cells undergo morphological changes in which they have an increased diameter and a reduction in cell compartment length. Additionally, invasive cells have a reduced extension rate that was used to determine the effective turgor pressure of this organism. We found that cell polarity was affected by resistive forces by an increase in active Cdc42 concentration in the filament apex but not an altered distribution. In contrast active Rho1 became less polarized during invasion. Lastly, we showed that the observed morphological changes were due to mechanical compressive force and not due to a widening of the growth site since the tip diameter did not increase over time, whereas subapical compartments did increase in diameter over the time of invasion.

With this work we developed a unique method of studying how mechanical resistive force affects cells. There are several ways this method could be used to study various aspects of the invasive growth of *C. albicans*, as this process is important for its ability to invade host tissues. As we developed this method to allow for live-cell imaging of fluorescently labeled cells, it would be interesting to screen available secretory pathway markers for possible alterations in localization or dynamics, also cytoplasmic crowding can be quantified using GEM mobility analysis. I have initiated some of this work by imaging invading cells with

labels such as mSc-Sec4, Abp1-mCh, mSc-LifeAct, GFP-Mlc1. There is some evidence that mSc-Sec4 signal transiently increases just after bursting out from PDMS into a chamber (*i.e.* change in resistive force); however, this will need additional examples in order to validate this phenomenon (see Appendix Figure 3).

Along a similar line, this method could be used to study if lipid distributions, such as PI(4)P or PI(4,5)P_2, are altered during invasive growth, as thus far this has been studied in non-invasive conditions (Ghugtyal et al., 2015; Vernay et al., 2012). There are also many possibilities in chamber shapes and designs that could be fabricated at various stiffnesses, which would allow one to test many aspects of *C. albicans* invasive growth. Lastly, this method also could be adapted for assays (as I used for the *mlc1*Δ/Δ mutant) or screening purposes, either looking for mutations or drug candidates that prevent invasive growth from occurring.

The second body of work revolves around the composition and perturbation of the Spitzenkörper. I showed that the Spitzenkörper is composed entirely of secretory vesicles of which the population number strongly correlates with the volume of the structure, suggesting a constant packing density. I also showed through three different perturbations that the Spitzenkörper functions to regulate the morphology and growth rate of hyphae and likely *vice versa*. I speculate this occurs through regulating the focus of growth to a small region in the tip, similar to what has been proposed in the vesicle supply center model. Any disruptions in this focus lead to altered and highly variable cell morphologies, growth rates, and Spitzenkörper shape and composition.

The mutant and alterations through GFP-GNB interaction presented here are an example of how to study the function of a cellular component or process. There are several aspects of the *mlc1*Δ/Δ mutant that could become future lines of research. This mutant appears to be multinucleated, defective in cell division in filaments (despite septin

localization still occurring), and more prone to lysis; however, *mlc1*Δ/Δ is still able to form long true hyphae and even undergoes filament branching after an extended growth period. It would be worthwhile to study additional aspects of this mutant, such as active Cdc42 localization, actin distribution, and localization of other secretory pathway components including the exocyst Sec3 and Golgi and ER distribution. Also, since this mutant appears to be prone to lysis, it would be intriguing to determine if this is due to an alteration in the cell wall, or perhaps there is improper regulation of turgor pressure that leads to overly inflated cells. Lastly, the GNB molecule has been used in other organisms (Abenza et al., 2015; Rothbauer et al., 2008; Schornack et al., 2009) and having it now as a tool to use for altering protein localization is novel in *C. albicans* research and will open up new ways of studying this organism.

Overall, this work provides novel insights into aspects of invasive growth and the role of the Spitzenkörper in regulation of cell growth and morphology in the human fungal pathogen *C. albicans.* Both of these aspects are important for successful host infection, and the information learned here may provide novel mechanisms to target for development in a quest to better treat this major human fungal pathogen.

Materials & Methods

I – Growth conditions

Strains were grown in rich (yeast extract peptone dextrose) media at 30°C, and hyphal inductions were performed at 37°C in 50% FCS and 50% YEPD+Uri. Strains used are derivatives of the BWP17 strain background and are explained in detail below. They can also be found in Table 1.

II – Plate assays

Invasive growth on FCS plates

Overnight cultures were back diluted to an $O.D._{600}$ of 0.1 and incubated at 30°C, shaking until $O.D._{600}$ of 0.6-0.8 was achieved. Using a 96 well microtiter plate, cultures were diluted to $O.D._{600}$ of 0.1 in the first well and serially diluted to $1x10^{-4}$. Each of the five dilutions were spotted (7 µl) on 50% FCS plates (50% YEPD+URI, 50% FCS, 1% agar). Plates were incubated at 30°C and imaged daily from day 3-6.

Antifungal and cell wall perturbant susceptibility

Spotting was performed in the same manner as with FCS plates. Plates were incubated at 30°C and imaged daily from day 1-5. The concentration of molecules was used as indicated.

III – Plasmid constructions

Primers used in the construction of plasmids can be found in Table 2, and the plasmids constructed can be found in Table 3.

pFA-CamScarlet and pFA-CamiRFP670 plasmids

The nucleotide sequences for the monomeric red fluorescent protein CamScarlet (Bindels et al., 2016) and the far-red fluorescent protein CamiRFP670 (Shcherbakova et al.,

2016) were all codon optimized for *C. albicans* and commercially synthesized (Baseclear, Netherlands for CamiRFP670 and GenScript, USA for CamScarlet). The synthesized fluorescent protein genes CamScarlet and CamiRFP670 were PCR amplified with primers containing a unique 5' PstI site and a GAGAGA linker sequence, and a unique 3' AscI site (Primers GA3CamScarPstIp, CamScarletmAscI, CamiRFP670PstIp and CamiRFP670AscIm). The genes were ligated into the pFA-GFP-*URA3* plasmid (Gola et al., 2003) to generate the pFA-CamScarlet-*URA3* and pFA-miRFP760-*URA3*. The *URA3* marker from pFA-CamiRFP670-*URA3* was swapped for the *CdHis1* marker from pFA-GFP-*CdHIS1* (Schaub et al., 2006) using unique AscI and PstI restriction sites. These plasmids were used with primers containing the standard S1-GFP and S2 sequences for use with pFA plasmids (Gola et al., 2003; Schaub et al., 2006).

pFA-mScarletx3-*URA3*

A cassette was commercially synthesized containing two tandem CamScarlet genes with a 5'XhoI site and GGsGGS linker, separated by a XmaI site and GSGSGS linker, and a 3' AscI site. This cassette was provided to us in a pUC57 backbone (BaseClear, Netherlands). Each of the two CamScarlet genes was altered in nucleotide sequence with conserved codons to prevent recombination effects. The mScarletx3 cassette was generated by PCR, amplifying CamScarlet from pUC57-CamScarlet with primers 1 and 3. Amplified fragments were digested with PstI and XhoI restriction enzymes, and column purified. The fragment was ligated into a pUC57-CamScarletx2 plasmid, which was digested with PstI and XhoI, and column purified. This resulted in a pUC57-CamScarletx3 plasmid. The CamScarletx3 fragment was digested out from pUC57-CamScarletx3 with PstI and AcsI restriction enzymes, and then ligated into a PstI and AscI digested pFA-GFP-*URA3* backbone (Gola et al., 2003) that was gel purified to remove the GFPγ fragment. This resulted in the pFA-CamScarletx3-*URA3* plasmid.

pFA-CaPfV-GFP plasmid set (40nm GEM)

The CaPfV gene, which encodes a genetically encoded monomeric (GEM) nanoparticle (Delarue et al., 2018), was codon optimized for *C. albicans* and commercially synthesized (BaseClear, Netherlands). The synthesized CaPfV gene was cloned from the pUC57 vector into the pFA-GFPγ-*URA3* plasmid using PstI sites, resulting in the pFA-CaPfV-GFPγ-*URA3* plasmid. The *URA3* marker was exchanged for *CdHIS1*, as described above. This plasmid was used as a template to PCR amplify the CaPfV-GFPγ-*URA3* cassette for genomic knock-in that would be expressed under the *TEF1p* promotor by using the primers pair TEF1p-pfVp and TEF1KIxFP_S2.

pFA-GNB plasmids

The GFP nanobody (GNB) gene (Rothbauer et al., 2006) was codon optimized for *C. albicans* and commercially synthesized (BaseClear, Netherlands). The synthesized CaGNB gene was cloned from the pUC57 vector into the pFA-GFPγ-*URA3* plasmid using PstI and AscI sites, which resulted in the pFA-CaGNB-*URA3* plasmid. The *URA3* marker was exchanged for *CdHIS1* and *ARG4*, as previously described. In the *URA3* version, the CamiRFP670 gene was PCR amplified with the forward sense primer CaiRFPpPstI, which adds a PstI restriction site to the 5' end and the reverse sense primer CaiRFPm-GSlink-PstI_noStop to introduce a GSGSGS linker between the CamiRFP670 gene and the CaGNB gene, and a PstI restriction site on the 3' end. The gene for CamiRFP670 was cloned in front of the CaGNB gene using a single PstI site. This resulted in the plasmid pFA-CamiRFP670-CaGNB-*URA3.* This plasmid was used to C-terminally tag *MLC1* with the construct -CamiRFP670-CaGNB-*URA3* using the forward sense primer CaMLC1_S1miRFP670p and the reverse sense primer CaMLC1mFA.

Plasmids for plasma membrane labeling

The pEXP*ARG4-ACT1*p-CamScarlet-Ct_{Rac1}-*ADH1t* was generated as follows. The synthesized CamScarlet gene was PCR amplified with primers containing a unique 5' RsrII

site (CamScarletFwdRsrII) and a 3' Ct_{Rac1} plasma membrane targeting moiety followed by a unique MluI site (yemChmCtRacMluI). The fragment was ligated into the pEXP*ARG4-ACT1p*-CRIB-mCherry-*Ct_{Rac1}-ADH1t* (Silva et al., 2019), resulting in pEXP*ARG4-ACT1p*-CamScarlet-*Ct_{Rac1}-ADH1t*. The genes for the fluorescent proteins CamiRFP670 and GFPγ were PCR amplified with the primer pairs CamiRFP670pRsrII and CamiRFP670CtRacmMluI for CamiRFP670, and GFPgpRsrII and CaGFPymCtRacMluI for GFPγ, and ligated into pEXPARG4-ACT1p-CamScarlet-Ct_{Rac1}-ADH1t resulting in pEXPARG4-ACT1p-CamiRFP670-Ct_{Rac1}-ADH1t and pEXPARG4-ACT1p-GFPγ-Ct_{Rac1}-ADH1t. The plasmids were integrated at the RP10 locus after linearization with the StuI restriction enzyme.

The pDUP5-ADH1p-CamScarlet-Ct_{rac1}-ACT1t plasmid was generated by PCR amplification of CamScarlet with a unique 5' AscI site and a 3' CtRac1 followed by a unique MluI site (primernucleotides CamScarletAscIp and yemChmCtRacMluI) and cloned into pDUP5-ADH1p-CibN-Ct_{Rac1}-ACT1t (Silva et al., 2019). The fragment used for integration was released from the pDUP3/5 plasmids by digestion NgoMIV for integration at the NEUT5L locus.

***SEC4* plasmids**

The pEXPARG-*SEC4p1311*-CamScarlet-*Sec4* plasmid was constructed by PCR amplification of the *SEC4* ORF using the primers CaSec4pAscI and CaSec4mMluI, and inserted using AscI and MluI restriction sites. The codon optimized CamScarlet was added by PCR amplification using the primers CamScarletFwdRsrII and CamScarletmAscI, and inserted using RsrII and AscI sites. The 1311 bp *SEC4* promoter was added by PCR amplification with the primers CaSec4P1311pNotI and CaSec4PmRsrII, and inserted using NotI and RsrII restriction sites (Silva et al., 2019).

The *SEC4p*1311-CamScarlet-*SEC4* cassette was cloned into pGEMURA (Wilson et al., 1999) using unique NotI and SalI restriction sites, resulting in pGEM*URA-SEC4*p1311-

CamScarlet-*SEC4*. The CamScarlet was exchanged for GFPγ by using RsrII and AscI restrictions sites. The gene for GFPγ was PCR amplified using the primers GFPgpRsrII and CaGFPymAscI. These plasmids were linearized with BglII that cuts within *SEC4*p1311 and integrated at the *SEC4* locus. Additionally, for some strains, the cassette was PCR amplified using the primers CaSec4KIpURAmScar and CaSec4m1139 and then transformed into cells for replacement of genomic *SEC4* with the fluorescently tagged copy.

pEA *MLC1p-MLC1-MLC1t* complementation vector

The *MLC1* gene with 1kb upstream and downstream (3479 bases) was PCR amplified from genomic DNA using the primers MLC1pup1000XhoI and MLC1m2479NotI, which include unique 5' XhoI and 3' NotI restriction sites. This cassette was ligated into the pEA-p*ARF3ARF3* plasmid (Labbaoui et al., 2017) that was digested with XhoI and NotI, and purified to generate the pEA-*MLC1p-MLC1-MLC1t* plasmid. The sequence of the *MLC1* ORF was confirmed by sequencing the plasmid using the primers MLC1mup177 and MLC1p1006. This plasmid was digested with StuI for integration at the *RP10* locus.

IV – Yeast transformation

Electroporation

Genetic manipulations were performed using electroporation as a standard protocol. For this, overnight cultures were back-diluted 1:10 in 10 ml of YEPD+Uri, and cells were incubated, shaking at 30°C for 4-5 hr. To prepare cells for electroporation, cultures were centrifuged and resuspended in sterile diH_2O, 0.1 M lithium acetate, 10 mM Tris, and 1 mM EDTA; and incubated, shaking at 30°C for 45 min. 25 mM dithiothreitol (DTT) was then added, and cells were incubated for an additional 15 min. After incubation, cells were washed twice with ice-cold diH_2O (40 ml then 25 ml) and once with cold 1 M sorbitol (5 ml). They were then resuspended in 40 µl of cold 1 M sorbitol per electroporation and kept on ice.

For the electroporation, 40 µl of prepared cells were placed in electroporation cuvettes (Cell Projects, 0.2 mm electrode gap) with 5µg of DNA (5-10µl of DNA in diH_2O). DNA used for electroporation was prepared by isopropanol precipitation for PCR product cassettes and by column purification for digested plasmid cassettes. Cells were electroporated at 18 kV to achieve a time constant between 5 and 6 msec (Eppendorf electroporator 2510). After electroporation, cells were removed from cuvettes by suspending them in 1 ml of 1 M sorbitol. Cells were pelleted by centrifugation and the supernatant was removed. The cells were resuspended in LM2 media and then plated on selective plates. For nourseothricin (NAT) selection, cells were resuspended in YEPD+Uri media and incubated at 30ºC for 4 hr prior to plating on YEPD+Uri+NAT plates (200µg/ml NAT). For hygromycin (HYG) selection, cells were resuspended in YEPD+Uri media and incubated at 30ºC for 5 hr prior to plating on YEPD+Uri+HYG plates (1 mg/ml HYG).

V – Strains

Fluorescently labeled strains

Strains were fluorescently labeled by either C-terminal knock-in tagging or by integration of a cassette on an integrative plasmid. For C-terminal knock-in tagging, primers containing 50-100 bp of sequence homology to the 3' end of the ORF being tagged were used to integrate the fluorescent tag in frame just before the stop codon. (Primers used for this are listed in Table 2, under the section titled AFP tagging KI primers.) Cassettes that are in the pEXP*ARG4* backbone were linearized with the StuI restriction enzyme for integration into the *RP10* locus. The backbones pDUP3 and pDUP5 were digested with NgoMIV to release the cassette to be integrated in the *NEU5L* locus. The *SEC4* containing pGEM plasmids were designed to be digested with BglII to linearize the plasmid for integration in the *SEC4* promotor

region or PCR amplification of the *SEC4*p1311mScarlet-*SEC4-ADH1t* cassette using the already stated primers, which are listed in Table 2.

MLC1 deletion mutant

Knockout cassettes were generated using the primers CaMLC1pKO and CaMLC1mKO, which contain 100 and 105 bases of homology that are respectively upstream and downstream of the *MLC1* open reading frame in addition to S1 and S2 primer sites for amplifying knockout cassettes from the pFA knockout plasmid set (Gola et al., 2003; Schaub et al., 2006).

The *mlc1*Δ/Δ strain, which contains CamScarlet-Sec4, was generated as follows. The heterozygote was made by knocking out one copy of *MLC1* with the *SAT1* dominant selection marker. Then the BglII digested pGEM *URA3* CamScarlet-*SEC4* plasmid was integrated into the *SEC4* locus. Lastly, the second copy of *MLC1* was deleted using the *CdHIS1* auxotrophic marker. This resulted in the *mlc1*Δ/Δ;CamScarlet-*SEC4* mutant strain. Additional double mutants were generated from the initial heterozygote using *URA3* or *HygB* markers in three additional independent transformations. Mutants were confirmed by PCR using genomic DNA prepared from transformants grown overnight in liquid media. The primer pair CaMLC1pup303 and CaMLC1m85 was used for confirming the absence of the *MLC1* ORF. The primer pair CaMLC1pup303 combined with CaSATm240, or CaUra3minus, CdHis1m93 or CaHygm416, was used to confirm the presence of the *SAT1*, *URA3*, *CdHIS1*, or *HygB* genes respectively.

The *mlc*-/- strains with *NOP1*-GFP, *CDC10*-GFP, and *ABP1*-GFP were generated as follows. The fluorescent tags were introduced into the *mlc1*+/Δ;CamScarlet-*SEC4* strain using the pFA-GFPγ-*ARG4* and the primer sets: CaNop1KI_S1 and CaNop1KI_S2 for *NOP1* tagging, CaCdc10pFA and CaCdc10mFA for *CDC10*, and caAbp1xFP_S1 and caAbp1xFP_S2 for *ABP1*. This resulted in the strains *mlc1*+/Δ;CamScarlet-*SEC4;NOP1*-

GFP, *mlc1+/*Δ;CamScarlet-*SEC4;CDC10*-GFP, and *mlc1+/*Δ;CamScarlet-*SEC4;ABP1*-GFP. The second copy of *MLC1* was knocked out with *HIS1* from the pFA-HIS1 to generate *mlc1*Δ/Δ;CamScarlet-*SEC4;NOP1*-GFP, *mlc1*Δ/Δ;CamScarlet-*SEC4;CDC10*-GFP, and *mlc1*Δ/Δ;CamScarlet-*SEC4;ABP1*-GFP. These mutants were indistinguishable from the original mutant by microscopy and were verified by their inability to form invasive filamentous growth when spotted on FCS plates after 6 days of growth.

Mlc1-miR-CaGNB strains

The miR-CaGNB tag was PCR amplified from pFA-CamiRFP670-CaGNB-*URA3* using the forward sense primer CaMLC1_S1miRFP670p and the reverse sense primer CaMLC1mFA. It was then transformed into the wildtype auxotrophic BWP17 background, resulting in the *MLC1*-miR-CaGNB strain background. Next, pGFP-*SEC4*-utr was introduced by BglII digestion or pEXP*ARG4*-GFPγ-Ct_{Rac1} was introduced by StuI digestion. This resulted in the strains *MLC1*-miR-CaGNB;GFP-*SEC4* (SPK stabilized strain) and *MLC1*-miR-CaGNB;GFPγ-Ct_{Rac1} (PM Targeted strain).

VI – Microfabrication

Thin layer

Microchambers were fabricated using standard soft-lithography methods (Minc et al., 2009; Whitesides et al., 2001). Chambers were 5 μm deep and 10 μm in diameter with 15 μm spacing between them. The overall thickness of the microchamber preparations was approximately 150 μm. PDMS microchambers of varying stiffness were generated by varying the ratios of polymer and crosslinker (Sylgard 184; Dow Corning). Mixtures of polymer and crosslinker were spin coated (Laurell Technologies corporation) on molds (5 sec 100 rpm followed by 50 sec 500 rpm) to achieve ~150 μm thickness and then cured for 1 hr at 60ºC.

Thick 10:1 PDMS frames were then placed on top of the partially cured chambers, which were baked for an additional 2 hr at 90°C in order to peel the thin chambers off the mold.

Thick layer

The same microchamber molds were used as above. PDMS microchambers of varying stiffness were generated by varying the ratios of polymer and crosslinker (Sylgard 184; Dow Corning). Mixtures of polymer and crosslinker were degassed by centrifugation at 3200 rpm for 2 min (LaFratta, 2010). The degassed polymer-crosslinker mixtures were poured on to molds and cured overnight at 60°C. After curing, PDMS was slowly removed from the molds and stored dry until use.

VII – PDMS microscopy sample preparation

PDMS microchambers were activated by plasma treatment (Harrick Plasma Cleaner) for 14 sec at 500 mTorr on low setting and submerged in DH2O until usage. Prior to usage, PDMS samples were dried with nitrogen gas, treated with poly-D-lysine (1 mg/ml), and subsequently treated with concanavalin A (0.4 mg/ml). Each sample was incubated for 20 min and then dried with a stream of nitrogen gas. Exponentially growing cells were mixed with FCS media (75% FCS, 0.6 × minimal media and 2% dextrose), spotted onto the microchambers and sealed with a coverslip. Typically, cells on PDMS microchambers were incubated for ~ 1 hr at 37°C to initiate filamentation prior to microscopy.

VIII – Microscopy

All imaging was carried out in the iBV PRISM microscopy platform.

FCS + agarose pad preparation

FCS + agarose pads for use in live-cell time-lapse imaging were prepared as follows. Pads were composed of 75% FCS, 2% agar, and SC media. Exponentially growing cells were

first mixed with 50% FCS then added to the pads and covered with a No. 1.5 cover slip. Typically, cells were incubated on the pads for 30 min prior to microscopy.

Spinning disk confocal

Spinning disk confocal experiments were done on an inverted IX81 Olympus microscope (Olympus Corporation of the Americas, Center Valley, Pa). The microscope was equipped with a motorized XY stage (Prior scientific, Cambridge, UK), a Yokogawa CSU-X1 confocal head (Yokogawa Electric Corporation, Tokyo, Japan), and a sensitive iXON DU-897-BV EMCCD camera (Andor technology, Belfast, UK). The laser lines used were a 488 nm (DPSS), 561 nm (DPSS), or 640 nm (Diode) (Andor technology, Belfast, UK). The objective used was a UPLSAPO 60X oil 1.35 NA, a UPLSAPO 60X water 1.2 NA, or a UPLSAPO 100X oil 1.4 NA. Z stacks of 0.4 µm, 0.5 µm, or 0.2 µm were acquired using a piezo stage NanoScan Z100 (Prior scientific, Cambridge, UK). The 37°C atmosphere was controlled by an incubator box, an air heating system and an air pump system (Okolab, Ottaviano, Italy). The system was controlled using MetaMorph software version 7.8.8.0 (Molecular Devices, Sunnyvale, CA, USA).

For colocalization experiments, samples were illuminated simultaneously with 488 nm and 561 nm laser lines. The emission signal was split using a red-green dichroic placed within an Andor TuCam two-camera adaptor (Andor technology, Belfast, UK). Each channel was captured simultaneously by a separate iXON DU-897-BV EMCCD camera (Andor technology, Belfast, UK) into one 1024x512 image. Images were split and organized into hyper-stacks for image analysis.

Spinning disk confocal with photo manipulation and pseudo-TIRF imaging

Spinning disk confocal experiments that combined photomanipulation, as with the ablation during invasion experiments, were carried out on a Nikon Ti eclipse inverted microscope (Nikon France S.A.S., Champigny-sur-Marne, France) that was equipped with an

iXON life 888 camera (Andor technology, Belfast, UK). The laser illumination used was a 405 nm diode, a 488 nm diode, a 561 nm diode, or a 642 nm diode. The objective used a 100x CFI-APO-TIRF oil NA 1.49. Photomanipulation was controlled with an iLas2 scan head (Roper scientific, Evry, France) using a 405 nm diode, a 488 nm diode, a 561 nm diode, or a 642 nm diode. Multi-position acquisitions were done using a motorized XY stage (Nikon France S.A.S., Champigny-sur-Marne, France). Image acquisition was controlled by Metamorph software version 7.10.1.161 (Molecular Devices, Sunnyvale, CA, USA) and supplemented with iLAS2 software for photomanipulation. Temperature conditions of 37^{o}C were controlled by an incubator chamber (Okolab, Ottaviano, Italy).

Lysis of PDMS invading cells

Lysing of PDMS invading cells used the on-the-fly spot mode and 405 nm laser set to 100%. A before image was taken first and then the cell was lysed by repeated laser pulses (typically 2-5) at the edge of the cell or cell tip. Finally, an after image was acquired.

Rapid framerate GEM acquisition

Rapid frame rate time-lapse of GEMs displacement experiments were carried out in TIRF mode without the spinning disk in the light path. The illumination light was bent within the near-TIRF range. Images were collected in stream mode, allowing for the fastest possible imaging and set with an exposure time of 10 msec for 200-300 images depending on the experiment.

Scanning confocal with photomanipulation

FRAP experiments were carried out on an inverted Axio Observer Z1 stand (Carl Zeiss Microscopy GmbH, Jena, Germany) equipped with a Zeiss 880 confocal head, using a Plan Apo 63X oil 1.4. The lasers used were a 488 nm argon, a 561 nm DPSS, or HeNe 633 nm. Images were acquired using two descanned PMTs, a descanned GaAsP, and an external PMT for transmission. The system was controlled using Zen software version 14.0.19.201 (Carl

Zeiss Microscopy GmbH, Jena, Germany). Temperature conditions of 37ºC were controlled by an incubator chamber.

FRAP was performed by creating a circular ROI that encompassed the Spitzenkörper. The acquisition was done with a 256x256 frame with a scan time of 629.14 msec with averaging of 4 per line, unidirectional scanning and a bit depth of 12-bit. The zoom was set to achieve a pixel size of 0.18 µm. Images were acquired with a 488 nm or 561 nm laser, set to 0.66 or 0.02 respectively, using a maximum pin hole size of 601µm. Signals were acquired using the GaAsP detector set to range 492-533 nm for the green channel and 588-630nm for the red channel. Bleach was performed with 488 nm and 561 nm laser lines using a power of 0.8 or 0.5 respectively. Bleach was performed after 5 initial images and was done with 5 iterations using an alternative pixel dwell time of 16.38 µsec for the green channel only. After the bleach an additional 95 images (~94 sec) were acquired to track the recovery of the signal.

Widefield

For widefield images, acquisitions were performed on an inverted ZEISS Axio Observer Z1 microscope (Zeiss, Jena, Germany) equipped with Zeiss 63X Plan-Apo DICIII oil 1.4 NA and Zeiss 100X Plan-NeoFluar DICIII oil 1.3 NA objectives. Images were acquired with a monochrome EMCCD iXON+897 camera (Andor, Belfast, UK) or Neo scMOS camera (Andor, Belfast, UK) controlled with Metamorph 7.8 software (Molecular Devices, Sunnyvale, CA). Temperature conditions of 37ºC were controlled by an incubator chamber.

Deconvolution

Deconvolution of image z-stacks was carried out using Huygens professional software version 18.04 (Scientific-Volume Imaging). Images were deconvolved using the appropriate settings for the microscope and excitation source used. The signal to noise setting was 10, and the background detection was set to auto unless otherwise stated.

IX – Analysis

Morphology and extension rates

Image analysis for extension rate, compartment and tip diameter, and active Rho GTPase polarization was carried out with Fiji (version 1.51) (Schindelin et al., 2012). For determination of the extension rate, the lengths of the filaments (mother cell neck to filament tip) were determined over time using plasma membrane fluorescence signal. For the *mlc1* mutants, the CamScarlet-Sec4 signal was used. Extension rate values are from the slope of a line fit to length values over minimally a 1 hr acquisition (> 12 time points). For liquid extension rates, cells induced with 50% FCS at 37ºC were fixed every 30 min, and average cell lengths for each time point (0 - 90 min) were used. Compartment lengths were measured using the edge-to-edge fluorescence signal between two formed septa. Only invasive compartments that were entirely within the PDMS were used for analyses. Active Cdc42 and Rho1 polarization was determined using a fixed size ROI to quantitate the signal intensity at the tip and in a subapical region. The ratio of tip to subapical signal was averaged over the time-lapse, and the mean for invasive cells was normalized to the mean ratio for non-invasive cells. The percentage of cells undergoing subapical bending within a chamber and filament buckling within PDMS was assessed using DIC images. For the determination of errors from values derived from multiple measurements, classical error propagation was carried out (Bevington and Robinson, 2003). Statistical significance was determined with Student's t-test.

DIC representation

For representation of three-dimensional DIC images, an algorithm was applied to image z-stacks using a custom developed Matlab program, called InFocus, inspired from Extended Depth of Field plugin (Forster et al., 2004). The program extracts the local contrast per channel from any three-dimensional multi-channel acquisition. From these maps, it determines the Z of highest contrast per pixel from one or a combination of channels and then extracts a

smoothened plane to get a two-dimensional multichannel image. Parameters can be adapted through the Graphical User Interface.

Tip curvature

For quantitation of filament tip curvature over time, we developed another Matlab program, called TipCurve, with an intuitive interface dedicated for morphological analyses along the major axis of filamentous cells. For such analyses, three-dimensional images were converted into two-dimensional images by sum projection. Similar to the HyphalPolarity program (Silva et al., 2019), a backbone was extracted from images over time as well as the cell contour. By specifically extracting the tip first, the extremity of the backbone subtracted by the tip radius was estimated. The local curvature was then estimated only along the tip (either -45° to +45° or -90° to 90°) from the curvilinear function f(s) extracted from the cell contour.

$$C(s) = \frac{1}{R(s)} = \frac{f''(s)}{(f'(s))^2}$$

The distribution of active Cdc42 and Rho1 at the filament tip was determined by TipCurve. For these analyses, images that had a polarized fluorescent signal along with a uniform cytoplasmic signal were used. The latter were used to identify the cell and extract the backbone. Then an additive projection was done to get kymograph curves per time point and per fluorescence channel. To estimate the distribution of intensity at the tip of Cdc42 and Rho1, we fitted the kymograph to estimate x_{imax}, the distance of maximum intensity from the tip, and the decay of intensity above x_{imax} as an exponential function.

Analysis of the Spitzenkörper

Quantification of the number of secretory vesicles in the Spitzenkörper by CamScarlet-Sec4 intensity was done by using z-stack images of live filaments expressing CamScarlet-Sec4 with z-step intervals of 0.2 µm. Image z-stacks were deconvolved and analyzed using Volocity software version 6.3. Particles and clusters of CamScarlet-Sec4 were identified by intensity

using 5.5 standard deviations above the mean. An average intensity for single particles of Sec4 was calculated as these were assumed to be single vesicles. The intensity of the Spitzenkörper cluster was divided by the average single vesicle intensity to estimate the number of vesicles in the identified Spitzenkörper cluster. Spitzenkörper vesicle population numbers were comparative to a previous study that counted vesicle numbers by serial section transmission electron microscopy (Weiner et al., 2019). For the two-dimensional analysis of the Spitzenkörper, image stacks were acquired by the same method. Image z-stacks were deconvolved and then sum projected. The sum projected images were uploaded into the Volocity program for analysis. The Spitzenkörper structure was identified by standard deviations above the mean using 8 standard deviations for CamScarlet-Sec4 and 25 standard deviations for GFP-Sec4. All parameters reported were calculated by Volocity. The shape factor formulas are:

$$\text{Shape Factor (2D)} = 4\pi\frac{A}{P^2} \qquad \text{Shape Factor (3D)} = \frac{\pi^{\frac{1}{3}}(6V_0)^{\frac{2}{3}}}{A_0}$$

A is the area, P is the perimeter, and V is the volume. The closer the value is to 1, the closer the object is to a perfect circle or sphere respectively.

GEM diffusion analysis

Quantification of GEM diffusions by particle tracking was carried out as follows. Rapid frame rate images of GEM particles in cells were analyzed with the Mosaic Particle Tracker plugin for Fiji (Sbalzarini and Koumoutsakos, 2005). The parameters used in the Particle Tracker were a radius of 3, a cutoff of 0, a percentile of 0.5-2—this was adjusted based on background levels per experiment. Additionally, the link range was set to 1, the displacement was set to 5, and the Brownian diffusion model was used. The output in the form of X and Y coordinates for particle tracks was analyzed cumulatively per condition using a custom made Matlab program, QuantTrack. This program analyzes the mean squared displacements (MSD)

for each track in a condition to calculate the effective diffusion coefficient. The program fits curve to the mean ensemble MSDs and calculates the slope of the curve and the sigma or plateau.

FRAP analysis

FRAP analysis was performed by measuring the intensity of the bleach site (bleach), another location within the cell (inside), and outside the cell (bkgd) at each time point of the bleach time series. The inside signal was used to fit an exponential decay bleaching curve (BC). The bleach signal was corrected for bleaching using the following formula:

$$\text{Bleach Corr}_t = \frac{bleach_t - bkgd_t}{BC_t}$$

The Bleach Corr values were normalized to the maximum prebleach (first 5 time points) Bleach Corr value.

X – Gene Sequences

CamScarlet
ATGGTTTCAAAAGGTGAAGCTGTTATTAAAGAATTTATGAGATTTAAAGTTCAT ATGGAAGGTTCAATGAATGGTCATGAATTTGAAATTGAAGGTGAAGGTGAAGG TAGACCATATGAAGGTACTCAAACTGCTAAATTAAAAGTTACTAAAGGTGGTC CATTACCATTTTCATGGGATATTTTATCACCACAATTTATGTATGGTTCAAGAG CTTTTACTAAACATCCAGCTGATATTCCAGATTATTATAAACAATCATTTCCAG AAGGTTTTAAATGGGAAAGAGTTATGAATTTTGAAGATGGTGGTGCTGTTACT GTTACTCAAGATACTTCATTAGAAGATGGTACTTTAATTTATAAAGTTAAATTA AGAGGTACTAATTTTCCACCAGATGGTCCAGTTATGCAAAAAAAAACTATGGG TTGGGAAGCTTCAACTGAAAGATTATATCCAGAAGATGGTGTTTTAAAAGGTG ATATTAAAATGGCTTTAAGATTAAAAGATGGTGGTAGATATTTAGCTGATTTTA AAACTACTTATAAAGCTAAAAAACCAGTTCAAATGCCAGGTGCTTATAATGTT GATAGAAAATTAGATATTACTTCACATAATGAAGATTATACTGTTGTTGAACA ATATGAAAGATCAGAAGGTAGACATTCAACTGGTGGTATGGATGAATTATATA AATAA

CamiRFP670
ATGGTTGCTGGTCATGCTTCAGGTTCACCAGCTTTTGGTACTGCTTCACATTCA AATTGTGAACATGAAGAAATTCATTTAGCTGGTTCAATTCAACCACATGGTGCT TTATTAGTTGTTTCAGAACATGATCATAGAGTTATTCAAGCTTCAGCTAATGCT GCTGAATTTTTAAATTTAGGTTCAGTTTTAGGTGTTCCATTAGCTGAAATTGAT GGTGATTTATTAATTAAAATTTTACCACATTTAGATCCAACTGCTGAAGGTATG CCAGTTGCTGTTAGATGTAGAATTGGTAATCCATCAACTGAATATTGTGGTTTA ATGCATAGACCACCAGAAGGTGGTTTAATTATTGAATTAGAAAGAGCTGGTCC ATCAATTGATTTATCAGGTACTTTAGCTCCAGCTTTAGAAAGAATTAGAACTGC

TGGTTCATTAAGAGCTTTATGTGATGATACTGTTTTATTATTTCAACAATGTACT
GGTTATGATAGAGTTATGGTTTATAGATTTGATGAACAAGGTCATGGTTTAGTT
TTTTCAGAATGTCATGTTCCAGGTTTAGAATCATATTTTGGTAATAGATATCCA
TCATCAACTGTTCCACAAATGGCTAGACAATTATATGTTAGACAAAGAGTTAG
AGTTTTAGTTGATGTTACTTATCAACCAGTTCCATTAGAACCAAGATTATCACC
ATTAACTGGTAGAGATTTAGATATGTCAGGTTGTTTTTTAAGATCAATGTCACC
ATGTCATTTACAATTTTTAAAAGATATGGGTGTTAGAGCTACTTTAGCTGTTTC
ATTAGTTGTTGGTGGTAAATTATGGGGTTTAGTTGTTTGTCATCATTATTTACCA
AGATTTATTAGATTTGAATTAAGAGCTATTTGTAAAAGATTAGCTGAAAGAAT
TGCTACTAGAATTACTGCTTTAGAATCATAA

CamScarletx3

ATGGTTTCAAAAGGTGAAGCTGTTATTAAAGAATTTATGAGATTTAAAGTTCAT
ATGGAAGGTTCAATGAATGGTCATGAATTTGAAATTGAAGGTGAAGGTGAAGG
TAGACCATATGAAGGTACTCAAACTGCTAAATTAAAAGTTACTAAAGGTGGTC
CATTACCATTTTCATGGGATATTTTATCACCACAATTTATGTATGGTTCAAGAG
CTTTTACTAAACATCCAGCTGATATTCCAGATTATTATAAACAATCATTTCCAG
AAGGTTTTAAATGGGAAAGAGTTATGAATTTTGAAGATGGTGGTGCTGTTACT
GTTACTCAAGATACTTCATTAGAAGATGGTACTTTAATTTATAAAGTTAAATTA
AGAGGTACTAATTTTCCACCAGATGGTCCAGTTATGCAAAAAAAAACTATGGG
TTGGGAAGCTTCAACTGAAAGATTATATCCAGAAGATGGTGTTTTAAAAGGTG
ATATTAAAATGGCTTTAAGATTAAAAGATGGTGGTAGATATTTAGCTGATTTTA
AAACTACTTATAAAGCTAAAAAACCAGTTCAAATGCCAGGTGCTTATAATGTT
GATAGAAAATTAGATATTACTTCACATAATGAAGATTATACTGTTGTTGAACA
ATATGAAAGATCAGAAGGTAGACATTCAACTGGTGGTATGGATGAATTATATA
AACTCGAGGGAGGTTCAGGAGGCAGCGTGTCCAAAGGTGAGGCCGTTATTAA
AGAGTTCATGCGTTTCAAAGTACACATGGAAGGCTCAATGAATGGTCACGAGT
TTGAGATTGAGGGGGAAGGGGAAGGTAGGCCCTATGAGGGTACGCAAACCGC
AAAACTAAAGGTCACGAAAGGAGGGCCTCTACCGTTTAGTTGGGACATCCTTT
CTCCTCAGTTCATGTATGGCCTGCGCGCGTTCACGAAACATCCTGCGGACATTC
CAGATTATTATAAGCAGTCTTTTCCGGAGGGTTTCAAATGGGAAAGAGTCATG
AATTTTGAGGACGGTGGAGCTGTAACGGTCACTCAGGACACCAGCCTTGAAGA
TGGCACTCTTATCTACAAAGTAAAACTACGCGGAACGAACTTTCCTCCAGACG
GACCTGTCATGCAGAAGAAAACAATGGGATGGGAGGCTAGTACAGAGAGATT
ATATCCAGAAGATGGTGTGTTAAAAGGAGATATTAAGATGGCTCTACGGTTGA
AGGATGGTGGGCGGTACCTTGCAGATTTTAAGACCACGTACAAGGCCAAGAAG
CCCGTACAGATGCCCGGCGCGTACAATGTAGACCGTAAATTAGACATAACCTC
CCACAACGAGGACTATACTGTTGTCGAACAATACGAACGGTCAGAGGGCCGAC
ATCTGACTGGTGGTATGGATGAATTGTACAAGGGTAGCGGCAGCGGTAGCCCC
GGGGTCTCGAAAGGTGAAGCAGTTATCAAGGAGTTCATGCGATTTAAGGTTCA
CATGGAAGGATCAATGAATGGTCATGAGTTTGAAATTGAAGGCGAGGGTGAA
GGTCGCCCTTATGAAGGCACTCAGACTGCAAAGTTAAAGGTTACGAAAGGTGG
GCCTCTTCCGTTTTCTTGGGATATTTTAAGCCCCCAGTTCATGTATGGAAGTCG
TGCATTTACCAAGCATCCAGCTGATATTCCAGATTACTATAAACAATCCTTTCC
CGAAGGTTTTAAGTGGGAACGTGTCATGAATTTTGAAGATGGCGGTGCTGTTA
CTGTTACACAAGATACATCTCTTGAGGACGGTACTTTAATCTATAAAGTCAAAC
TCCGTGGCACAAATTTTCCGCCTGATGGCCCTGTCATGCAGAAGAAGACCATG
GGCTGGGAAGCTAGTACAGAAAGGCTCTACCCAGAAGACGGAGTACTAAAAG
GAGACATTAAAATGGCATTACGTCTCAAAGATGGTGGTCGCTATCTAGCTGAC
TTCAAAACTACTTATAAGGCTAAAAAGCCTGTTCAAATGCCTGGCGCATATAA

TGTTGACCGTAAATTAGATATCACTCTGCACAACGAAGATTATACGGTAGTTG
AGCAATACGAACGCTCTGAGGGTCGCCATTCAACCGGTGGAATGGATGAATTA
TATAAGTAA

CaPfV

ATGTTATCAATTAATCCAACTTTAATTAATAGAGATAAACCATATACTAAAGA
AGAATTAATGGAAATTTTAAGATTAGCTATTATTGCTGAATTAGATGCTATTAA
TTTATATGAACAAATGGCTAGATATTCAGAAGATGAAAATGTTAGAAAAATTT
TATTAGATGTTGCTAGAGAAGAAAAAGCTCATGTTGGTGAATTTATGGCTTTAT
TATTAAATTTAGATCCAGAACAAGTTACTGAATTAAAAGGTGGTTTTGAAGAA
GTTAAAGAATTAACTGGTATTGAAGCTCATATTAATGATAATAAAAAAGAAGA
ATCAAATGTTGAATATTTTGAAAAATTAAGATCAGCTTTATTAGATGGTGTTAA
TAAAGGTAGATCATTATTAAAACATTTACCAGTTACTAGAATTGAAGGTCAAT
CATTTAGAGTTGATATTATTAAATTTGAAGATGGTGTTAGAGTTGTTAAACAAG
AATATAAACCAATTCCATTATTAAAAAAAAAATTTTATGTTGGTATTAGAGAA
TTAAATGATGGTACTTATGATGTTTCAATTGCTACTAAAGCTGGTGAATTATTA
GTTAAAGATGAAGAATCATTAGTTATTAGAGAAATTTTATCAACTGAAGGTAT
TAAAAAAATGAAATTATCATCATGGGATAATCCAGAAGAAGCTTTAAATGATT
TAATGAATGCTTTACAAGAAGCTTCAAATGCTTCAGCTGGTCCATTTGGTTTAA
TTATTAATCCAAAAAGATATGCTAAATTATTAAAAATTTATGAAAAATCAGGT
AAAATGTTAGTTGAAGTTTTAAAAGAAATTTTTAGAGGTGGTATTATTGTTACT
TTAAATATTGATGAAAATAAAGTTATTATTTTTGCTAATACTCCAGCTGTTTTA
GATGTTGTTGTTGGTCAAGATGTTACTTTACAAGAATTAGGTCCAGAAGGTGAT
GATGTTGCTTTTTTAGTTTCAGAAGCTATTGGTATTAGAATTAAAAATCCAGAA
GCTATGTTGTTTTAGAATGGTAA

CaGNB

ATGGCTGATGTTCAATTAGTTGAATCAGGTGGTGCTTTAGTTCAACCAGGTGGT
CATTAAGATTATCATGTGCTGCTTCAGGTTTTCCAGTTAATAGATATTCAATGA
GATGGTATAGACAAGCTCCAGGTAAAGAAAGAGAATGGGTTGCTGGTATGTCA
TCAGCTGGTGATAGATCATCATATGAAGATTCAGTTAAAGGTAGATTTACTATT
TCAAGAGATGATGCTAGAAATACTGTTTATTTACAAATGAATTCATTAAAACC
AGAAGATACTGCTGTTTATTATTGTAATGTTAATGTTGGTTTTGAATATTGGGG
TCAAGGTACTCAAGTTACTGTTTCATCAGGTAGATAA

Table 1: Strains

Strain	Genotype	reference
BWP17	*ura3Δ::λimm434/ura3Δ::λimm434 his1Δ::hisG/his1Δ::his arg4::hisG/arg4Δ::hisG*	Wilson et al. 1999
PY173	*ade2Δ::hisG/ade2Δ::hisG ura3Δ::λimm434/ura3Δ::λimm434 his1Δ::hisG/his1Δ::hisG arg4Δ::hisG/arg4Δ::hisG ENO1/eno1::ENO1-tetR ScHAP4AD- 3×HA-ADE2*	Vernay et al. 2012
PY2165	BWP17 with *RP10::ARG4-ACT1p-GFP-RID-ADH1t*	Corvest et al. 2013
PY2263	BWP17 with *RP10::ARG4-ACT1p-CRIB-GFP-ADH1t*	Corvest et al. 2013
PY2705	BWP17 THE1 with *sec4Δ::HIS1/SEC4*	
PY3113	BWP17 with *RP10::ARG4-ADH1p-GFP-CtRac1-ACT1t*	This study
PY4405	BWP17 with *RP10::ARG4-ACT1p-mScarletCtRac1-ADH1t*	This Study
PY4483	BWP17 with *RP10::ARG4-ACT1p-miRFP670CtRac1-ADH1t*	This Study
PY4501	BWP17 *RP10::ARG4-GFP-SEC4*	This Study
PY4524	BWP17 *RP10::ARG4-mScarlet-SEC4*	This Study
PY4538	PY4524 with *MLC1/MLC1::HIS1 MLC1-GFPγ*	This Study
PY4554	PY2705 with *sec4Δ::HIS1/SEC4::URA3.SEC4P.mScarlet.SEC4*	This Study
PY4687	BWP17 with *mlc1Δ::SAT1/ MLC1*	This Study
PY4709	BWP17 *SEC4/SEC4::URA3 GFPγ-SEC4*	This Study
PY4809	PY4709 with *MLC1/MLC1::CdHIS1 MLC1-miRFP670*	This Study
PY4861	*ura3Δ::λ imm434/ura3Δ::λ imm434 his1::hisG/HIS1::his1::hisG arg4::hisG/URA3::ARG4::arg4::hisG*	Bassilana et al. 2003
PY4887	BWP17 with *RP10::ARG4-ACT1p-GFPγCtRac1-ADH1t*	This Study
PY4914	PY4805 *MLC1/MLC1::HIS1 MLC1-miRFP670*	This Study
PY5018	PY4687 with *SEC4::URA3.SEC4P.mScarlet.SEC4/SEC4*	This Study
PY5127	PY4489 with *NEUT5L::URA3-ADH1p-mScarlet-CtRac1-ACT1t*	This study
PY5184	PY2263 with *ADH1p::mScarlet-URA3*	This study
PY5224	BWP17 with *bni1Δ::ARG4/bni1Δ::HIS1*	Li et al. 2005
PY5304	BWP17 *TEF1p::PfV-GFPγ-CdHIS1*	This Study
PY5385	BWP17 with *MLC1/MLC1::URA3 MLC1-miRFP670-GNB*	This Study
PY5405	PY5385 with *RP10::ARG4-GFP-SEC4*	This Study
PY5409	PY5385 with *GFPγ-CtRac1*	This Study
PY5234	PY4887 with *HOG1/HOG1:: URA3 HOG1-mScarlet(3x)*	This Study
PY5250	PY4887 with *PKC1/PKC1::URA3 PKC1-mScarlet(3x)*	This Study
PY5433	BWP17 with *SEC4/SEC4::URA3 mScarlet-SEC4*	This Study
PY5435	PY5224 with *SEC4/SEC4::URA3 mScarlet-SEC4*	This Study
PY5451	PY5018 with *mlc1Δ::SAT1/ mlc1Δ::CdHis1*	This Study
PY5556	PY5304 with *RP10::ARG4-ACT1p-mScarletCtRac1-ADH1t*	This Study
PY5661	PY5451 with *RP10::ARG4-MLC1pMLC1MLC1t*	This Study
PY5713	PY5018 with *CDC10/CDC10::ARG4 CDC10-GFPγ*	This Study
PY5716	PY5018 with *NOP1/NOP1-GFPγ*	This Study
PY5717	PY5713 with *mlc1Δ::SAT1/ mlc1Δ::CdHis1*	This Study
PY5720	PY5716 with *mlc1Δ::SAT1/ mlc1Δ::CdHis1*	This Study
PY5755	PY 5018 with *ABP1/ABP1:: ARG4 ABP1-GFPγ*	This Study
PY5764	PY 5755 with *mlc1Δ::SAT1/ mlc1Δ::CdHis1*	This Study
PY5831	PY5409 with *SEC4/SEC4::URA3 mScarlet-SEC4*	This Study

Table 2: Oligos used

Name	Sequence
CamScarletFwdRsrII	ctcgcggtccgcggaccgATGGTTTCAAAAGGTGAAG
yemChmCtRacMluI	cttctagtatacgcgtcttataatatagtacatttttagctctcttaatttttctttttcttTTTATATAATTCATCCATACCACC
GA3CamScarPstIp	gtactgcagGGTGCTGGCGCAGGTGCTgtttcaaaaggtgaagctg
CamScarletmAscI	cggcgcgccTTTATATAATTCATCCATACCACC
CamScar.mXhoI	ctccctcgagTTTATATAATTCATCCATACC
CamiRFP670pRsrII	ctcgcggtccgcggaccgATGGTTGCTGGTCATGCTTCAGG
CamiRFP670CtRacmMluI	cttctagtatacgcgtcttataatatagtacatttttagctctcttaatttttctttttcttGATTCTAAAGCAGTAATTCTAG
CamiRFP670PstIp	gtactgcagGGTGCTGGCGCAGGTGCTgttgctggtcatgcttcagg
CamiRFP670AscIm	cgcggcgcgccTTATGATTCTAAAGCAGTAATTC
GFPgpRsrII	acgcggaccgATGTCTAAAGGTGAAGAATTATTCACTGG
CaGFPymAscI	cggcgcgccTTTGTACAATTCATCCATACC
GFPgpRsrII	acgcggaccgATGTCTAAAGGTGAAGAATTATTCACTGG
CaGFPymCtRacMluI	cttctagtatacgcgtcttataatatagtacatttttagctctcttaatttttctttttcttTTTGTACAATTCATCCATACC
CaSec4P1311pNotI	GTAGACGCGGCCGCaaagctgttaaattggaaaatccaaag
CaSec4PmRsrII	cgatcgCGGTCCGCGGACCGggatgaattgttaatacttag
CaSec4KIpURAmScar	GTTGGCAAGTTCTCAAGCTGGTTATTTAGAAGTCATGCCTTTGACTTTATCTTCTCACG ATGAGAATTTTGCTTGGTTGAAACAGAAGGATGATGGTACCgggcccgacgtcgcatgctc
CaSec4m1139	GGTGGTTATAAATGAAGGG
CaSec4pAscI	aaaggcgcgccgATGAGCGGTAAAGGAACATC
CaSec4mMluI	atcacgcgtaCTAGCAACAGTTATTCTTTGC
CaMLC1pKO	CTGTCACTGATAGATTATGTAGGCTTCACTAGTTGCATTGTGCAGGGTAAACTTTTTTT TTGTCTGATCCCAAAAGAGTAGTTTGTTTACATTTTTTCTGgaagcttcgtacgctgcaggtc
CaMLC1mKO	GTTACTTTTCCTCTCTTACTCTCTCTCTTTTCATTGGCATATATTACTCTCCAAAGTAACT TATCAAGTACTACATAAAACTTCAAATAAACGGTATCCAATTCGtctgatatcatcgatgaattcgag
MLC1pup1000XhoI	GTCTGTctcgagTAACTGTCCAATTTGATTCTTTGGC
MLC1m2479NotI	ACgcggccgcACCGAACAAGCTAAAACCTTAGGTGC
CaMLC1m85	gcaaatgcatctctgtaggtc
CaMLC1pup303	CTGTTTGTTCTGGTCTCCTG
MLC1mup177	GAGTACTTTGGTTGCGTC
MLC1p1006	TCATGATCGTTGCTGGTGTC
CaADH1KIxFP_S1	ccagaattatttttttttcatcagtttaacaacaacaaacgttattgtcatacaacaacaacaacaaatacaaaaacaattatgGGTGCTGG CGCA GGTGCT
CaADH1KIxFP_S2	ctgggtaatccttgtagactaattgaccaccattggtatcaaagacaacggctttttgagttttgggatttgttcagacatTCTGATATCAT CGATGAATTCGAG
TEF1p-PfVp	aaagaaaaaaaaatttttccctcgtcatcttgatttttacttcttcttcttcttcttttttccttttcttcacacattatagtcataatcaatcATGTTATC AA TTAATCCAAC
TEF1KIxFP_S2	CCACCACACTTGTAAATTAAGTGACCGGTGGTAGTAGATTTACCGGAATCGACGTGA CCAATAACAACAACGTTAACGTGAGTTTTTTCTTTACCCATtctgatatcatcgatgaattcg
CaSATm240	gggcagtgcacacactac
caUra3minus	TGTTACGAATCAATGGCACTAC
CdHis1m93	ACCGCTCAATAAGCTGCA
CaHygm416	gttattgcgtacacgacctgg
caAbp1xFP_S1	TGTTGAAATCGAATTTGTTGACGATGATTGGTGGCAAGGAAAACATTCCAAGACAGG AGAAGTCGGATTGTTCCCTGCTAACTATGTTGTCTTGAATGAGggtgctggcgcaggtgcttc
caAbp1xFP_S2	CAATTTATCTTTTCTTTGTATTTATATTATAGATTCATATAAAAAAAAAACGAATATTG TTTATACTAAATtctgatatcatcgatgaattcgag
CaCdc10pFA	caatcaaaccaagatttgaagaacacctctggtgtgccaaatgctcctatgttccaatcaactacaggtactgctgctgctagaGGTGCTG GCG CAGGTGCTTC

CaCdc10mFA	CGCGTTTTGCTTTTCAACAAACACACAAAAGAAGAGGAATACAAAAAAGTAAAATCACA TTATATCAATAACAAACctgatatcatcgatgaattcgag
CaHOG1xFP_S1	GTTGGTGTGGCAAATGAAACTGAGGGTTCCGAACAACCAGACCTGCAAGTGGAGCA AAACAACTTGGATTCCGCCAACGGAGCTggtgctggcgcaggtgct
CaHOG1xFP_S2	CAAACTTAATAATGTAAAGTTAATAGTAATAGTAATACATATTTCACTTTTAAATTTA TTTCTATAATTGCTAGCTTGTATTTTTGAAGATTAtctgatatcatcgatgaattcgag
CaPKC1xFP_S1	GAAACACCAAGATTGACACCAGTGGAAACAGTTCTTACTTCTGAAATGCAAGAACA GTTTAGAGGGTTCTCGCATATATCTGACAATGCAACGATTggtgctggcgcaggtgct
CaPKC1xFP_S2	GTACATAGATGAATATACATATTATACGGATGTGTGTATGTTCTGCCATCCTCCTTTTT ATAAAAATATTATTATTATATATCTACTTTAATCAtctgatatcatcgatgaattcgag
CaMLC1pFA	GATGAGTTATTAAAAGGGGTCAATGTAACTTCTGATGGAAATGTGGATTATGTTGAATT TGTCAAATCAATTTTAGACCAAGGTGCTGGCGCAGGTGCTTC
CaMLC1mFA	CGAACAAGACTATACAATAACTATAATTTGTAAAACTTGTAGTATATATATTTCAATGGT TAATTGTAAATTTTCTTTTATTCTGATATCATCGATGAATTCGAG
CaNop1KI_S1	GAGAAGTCCAAAAATTGAGAGAAGAAAGAATTAAACCATTGGAACAATTGACCTTGGA ACCTTATGAAAGAGACCATTGTATTGTTGTTGGTAGATACATGAGAAGCGGAATAAAGA AAggtgctggcgcaggtgcttc
CaNop1KI_S2	CCAGTGTTTCCAAAATTTTCATTCATTCTTTATTTTTTTTTAGTTTTCAATAATCAAATGTA TTAATCCTATTGTACAAAATATTTTTATTTAAAATTTAGAGTATCCCAAAATAACCTAATt ctgatatcatcgatgaattcgag

Table 3: Plasmids

Plasmid	Reference
pFA-*SAT1*	Schaub *et al*. 2006
pFA-*CdHIS1*	Schaub *et al*. 2006
pFA-*GFP-URA3*	Gola *et al.* 2003
pFA-*GFP-CdHIS1*	Schaub *et al*. 2006
pFA-*GFPγ-HIS1*	Zhang and Konopka 2010 Euk. Cell
pFA-*GFPγ-ARG4*	Zhang and Konopka 2010 Euk. Cell
pFA-*mScarlet-URA3*	This Study
pFA-*mScarletx3-URA3*	This Study
pFA-*miRFP760-URA3*	This Study
pFA-*miRFP760-CdHis1*	This Study
pFA-*PfV-GFPγ-URA3*	This Study
pFA-*PfV-GFPγ-CdHis1*	This Study
pFA-*miRFP670-GNB-URA3*	This Study
pEXP*ARG4-ACT1p-CRIB-mCherry-CtRac1-ADH1t*	Silva et al. 2019
pEXP*ARG-SEC4p-mScarlet-Sec4*	This Study
pEXP*ARG4-Sec4p1311-mScarlet-Sec4-ADH1t*	This Study
pEXP*ARG4-ACT1p-mScarlet-Ct$_{Rac1}$-ADH1t*	This Study
pEXP*ARG4-ACT1p-miRFP670-Ct$_{Rac1}$-ADH1t*	This Study
pEXP*ARG4-ACT1p-GFPγ-Ct$_{Rac1}$-ADH1t*	This Study
pEXPARG4-*MLC1p-MLC1-MLC1t*	This Study
p*ARF3ARF3*	Labbaoui *et al* 2017
pGEM*URA*	Wilson *et al.* 1999
pGEM*URA-SEC4p1311-mScarlet-SEC4*	This Study
pGEM-*URA-SEC4p1311-GFPγ-SEC4*	This Study
pDUB5	Gerami-Nejad et al., 2013
pDUP5-*ADH1p-CibN-Ct$_{Rac1}$-ACT1t*	Silva *et al.* 2019
pDUB5-*ADH1p-mScarlet-Ct$_{rac1}$-ACT1t*	This Study

Table 4: Materials

REAGENT or RESOURCE	SOURCE	IDENTIFIER
Chemicals		
Concanavalin A	Merck Millipore	Cat# 234567-1GM
Fetal bovine serum	Dutscher	Cat# P30-8500-500ml
Paraformaldehyde	Electorn Microscopy Sciences	Cat# RT 15710-16%
SYLGARD 184 Silicone Elastomer Kit	Dow	1673921
Poly-D-lysine hydrobromide	Sigma-Aldrich	P6407-5MG
Software		
ImageJ version 1.53 software	National Institutes of Health	ImageJ
Huygens Professional software version 18.04	Scientific-Volume Imaging	Huygens Professional
Volocity Software version 6.3	PerkinElmer	Volocity
MATLAB version 2019 software	MathWorks	MathWorks
GraphPad Prism 8 software	GraphPad	Prism
MetaMorph version 7.8.8.0 software	Molecular Devices	MetaMorph

Appendix Figures

Appendix Figure 1: **Invasively growing cells are under mechanical compressive force.** Using a UV laser, for photomanipulation, on maximum intensity, cells were lysed during PDMS invasion to measure the difference in buckling angles when the internal cell pressure is released. A) The buckling angle is increased after lysis, indicating cells are under mechanical force. Before and after representative image of a lysed invading cell. The tip compartment and mother cell compartment were lysed, and the middle compartment was left intact. The buckling angle was measure before and after lysis with an increase of ~ 15 degrees. Images are from sum projections. Magenta lines represent the angles that were measured. B) A quantification of buckling angle percent change for several cells lysed on 1 or both sides of the compartment that was measured. Surface cells were also lysed on both sides and measured as a control. This data shows that invading cells are growing against mechanical compressive force and complements the observation that upon bursting out, the buckling angle is also relaxed.

Appendix Figure 1

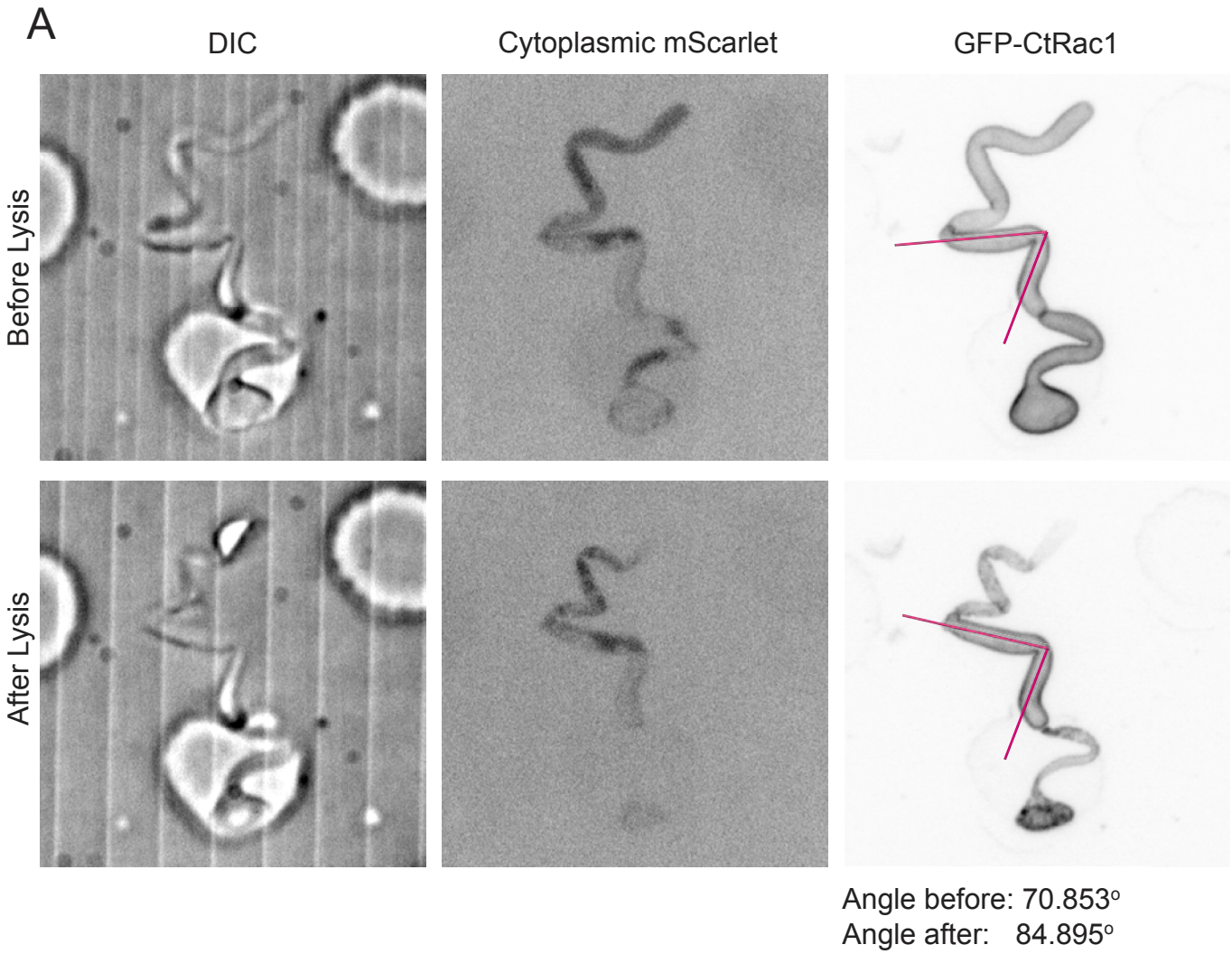

Appendix Figure 2: **Cells undergoing invasive growth do not appear have constant osmotic or cell wall stress.** I used the Hog1 and Pkc1 as reporters for osmotic and cell wall stress respectively (Andrews and Stark, 2000; Day and Quinn, 2019). A control experiment was done by osmotically shocking cells with 2 M sorbitol and immediately imaging. A) Hog1 labels the nucleus after sorbitol treatment. Representative max projected images are shown with or without sorbitol treatment. B) Invasive growth does not affect Hog1 localization. Representative max projected images of invasive and surface cells are shown. C) Quantification of nuclear signals from sorbitol treatment and invasive growth. D) Pkc1 delocalizes along the filament after sorbitol treatment. Pkc1 normally localized to the filament tip. After sorbitol treatment, Pkc1 re-localized along the length of the filament. Representative max projected images of cells treated, or untreated, with sorbitol. E) Invasive growth does not affect Pck1 localization. During invasive growth Pkc1 remained localized to the filament tip. F) Quantification of Pkc1 localization. Quantification is a mean of 3 background subtracted cross-section intensity measurements along the length of the filament. There is a clear increase in the sorbitol treatment but not during invasive growth. This data indicates that invasive growth does not impose osmotic or cell wall stress on the cells.

Appendix Figure 2

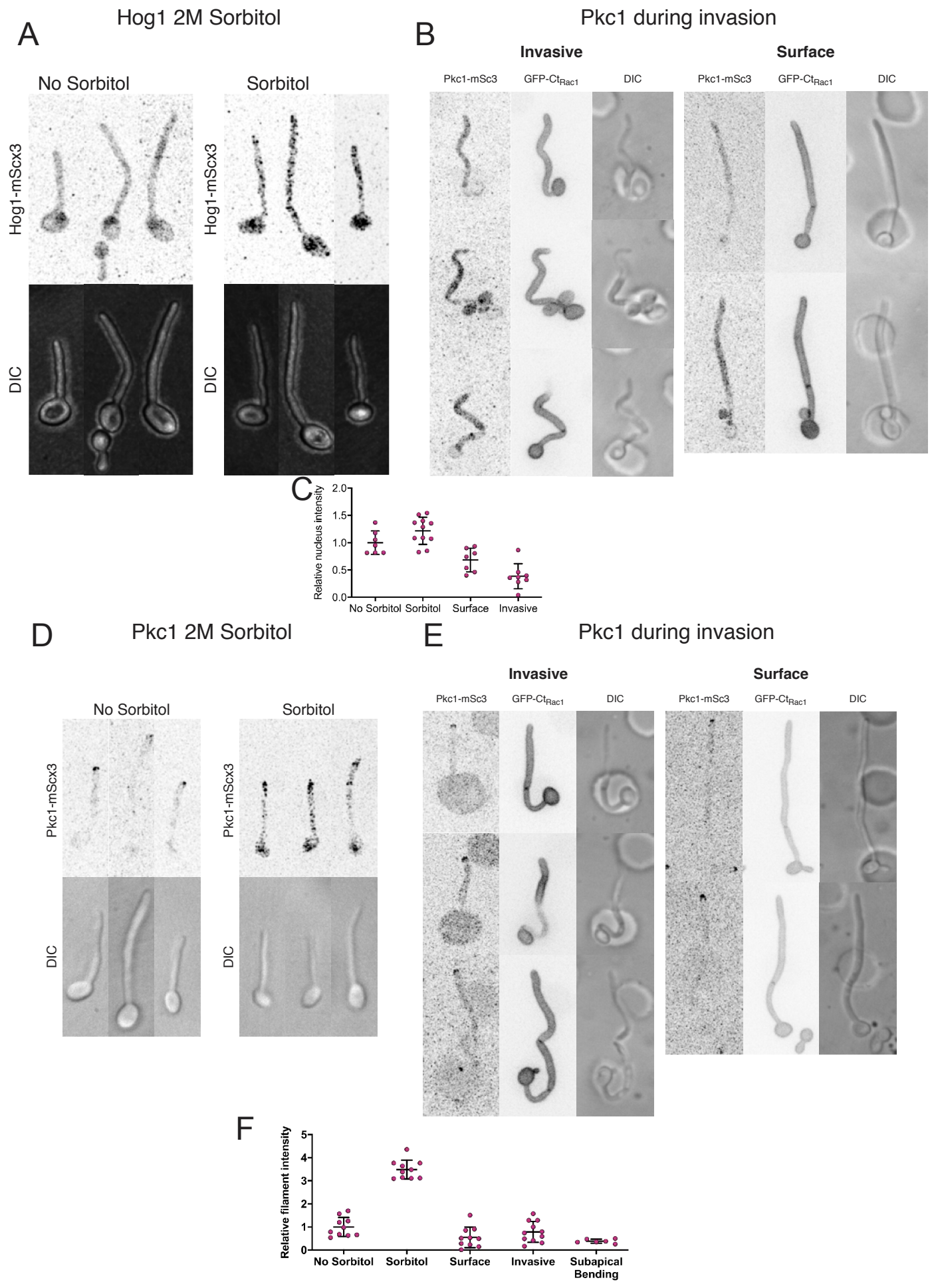

Appendix Figure 3: **Cytoplasmic crowding in filamentous cells and during drug treatment.** A) Cytoplasmic crowding is measured by particle tracking of fluorescently labeled and self-assembling genetically encoded monomeric nanoparticles (GEMs). Representative images are color coded time projections of GEM particles in filaments (left) and budding cells (right). Images of short exposure time (~10 ms) are taken sequentially for ~20-30 sec (200-300 images). GEM particles are tracked using particle tracking software, and the tracks are quantified for mean squared displacements and coefficient of diffusions. B) Cytoplasmic mobility is increased in longer filaments. Cells were treated with FCS for 60 min or 90 min and the effects on cytoplasmic mobility were quantified. Quantification of mean squared displacements (left graph) and cumulative frequency distributions of effective diffusion coefficients (right graph). C) Drug treatments affect cytoplasmic mobility. Cells were treated with caspofungin or fluconazole and the effects on cytoplasmic mobility were quantified after 4 hr and 8 hr of growth under drug exposure. Quantification of mean squared displacements (left graph) and cumulative frequency distributions of effective diffusion coefficients (right graph). D) A table of mean effective diffusion coefficients and their ratios to the untreated budding control.

These are preliminary results which I have acquired and analyzed. Future work could look into how invasion affects mobility as well as investigating population heterogeneity during drug treatments and how this might correspond with survival or susceptibility to drugs.

Appendix Figure 3

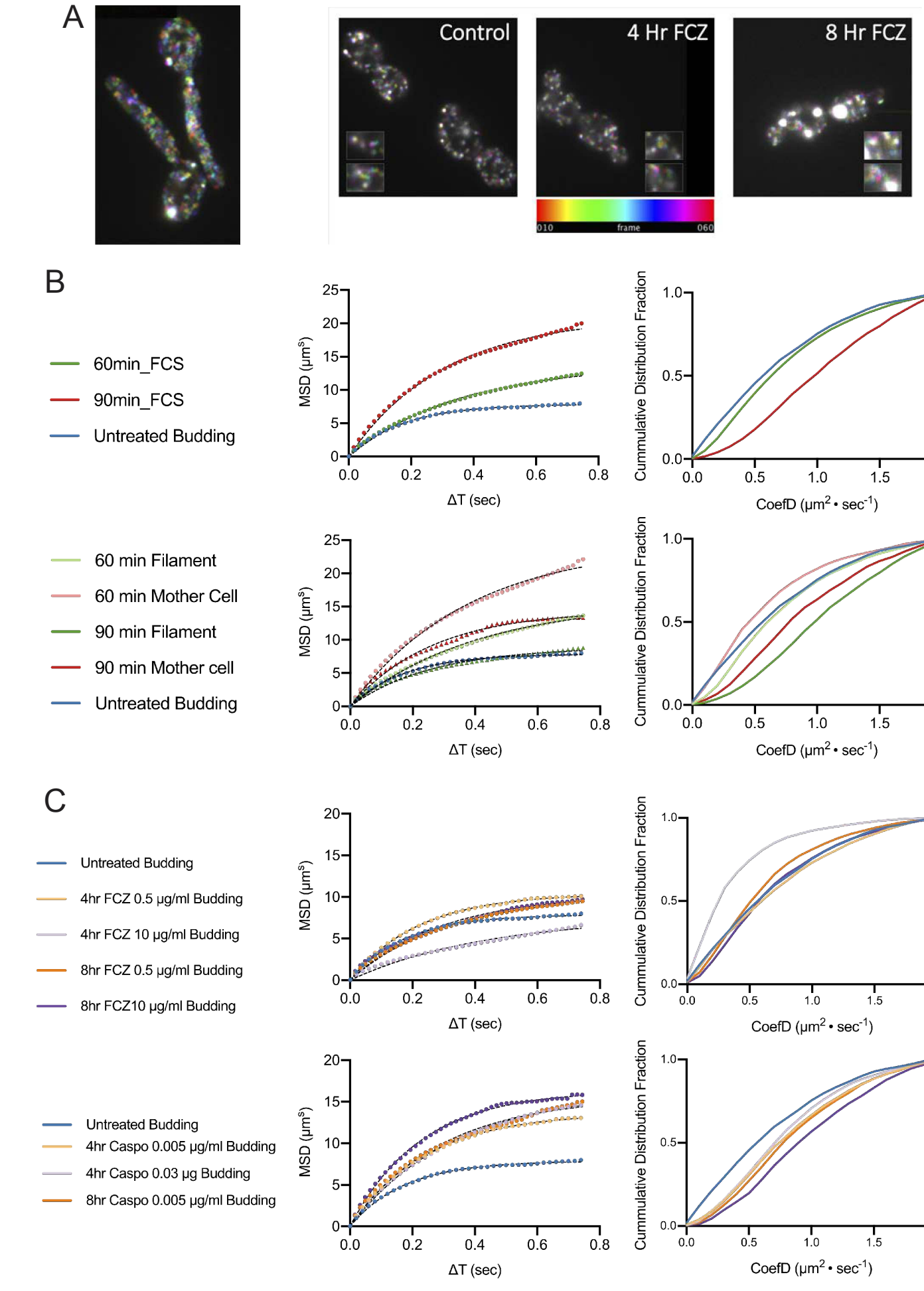

Appendix Figure 3 Continued

D

		Mean D_{eff}	Ratio to Budding
Control	Untreated Budding	0.82 ± 0.65	
FCS Treatment			
60 min	Whole Cell	0.91 ± 0.66	1.11
	Filament	0.89 ± 0.65	1.09
	Mother cell	0.74 ± 0.64	0.83
90 min	Whole Cell	1.30 ± 0.71	1.58
	Filament	1.28 ± 0.67	1.56
	Mother cell	1.07 ± 0.67	1.30
Drug Treatments			
4hr	FCZ 0.5 µg/ml	0.89 ± 0.66	1.08
	FCZ 10 µg/ml	0.47 ± 0.50	0.57
	Caspo 0.005 µg/ml	1.01 ± 0.66	1.23
	Caspo 0.03 µg/ml	0.97 ± 0.64	1.18
8 hr	FCZ 0.5 µg/ml	0.75 ± 0.58	0.91
	FCZ 10 µg/ml	0.83 ± 0.62	1.01
	Caspo 0.005 µg/ml	1.04 ± 0.65	1.27
	Caspo 0.03 µg/ml	1.24 ± 0.72	1.51

Appendix Figure 4: **The Spitzenkörper is altered during invasive growth.** A) A representative time lapse of a Spitzenkörper alteration during a burst-out from growth within PDMS into a chamber. Images are sum projections of 21 x 0.4 µm z-stacks. Images were acquired every 5 min. Increase in Sec4 intensity is indicated by the white arrowhead, and the diameter of the well is indicated by dotted yellow circle. Top panel is a zoom of the tip in mSc-Sec4 channel only. Bottom panel is DIC transmission. Red line indicates where burst-out occurs. B) Quantification of mSc-Sec4 intensity and well diameter. Well diameter was measured at point of entry by the filament tip. mSc-Sec4 tip intensity is normalized to the PM signal at the same location. Red line indicates where burst-out occurs. C) Signal intensity for surface cells is stable over time. Average of 10 cells over 80 min of surface growth. mSc-Sec4 tip intensity is normalized to the PM signal at the same location. Error bars are standard deviations. D) Three additional examples of mS-Sec4 intensity increases at burst out events.

I invested a significant amount of time in attempting to quantify effects to the Spitzenkörper during invasive growth. I found that during burst-out events that result in dramatic microchamber deformation and snap-back there was an alteration in the Sec4 intensity at the filament tip. This alteration is observed through a transient increase in Sec4 intensity, which consistently occurs just after the burst-out. Unfortunately, these burst-out events were quite rare events; therefore, I was unable to acquire sufficient examples to appropriately quantify this. Here, I have shown four examples of this occurrence; I have quantified a total of 10 examples of this phenomenon out of 1000s of cells imaged during many time-lapses.

Appendix Figure 4

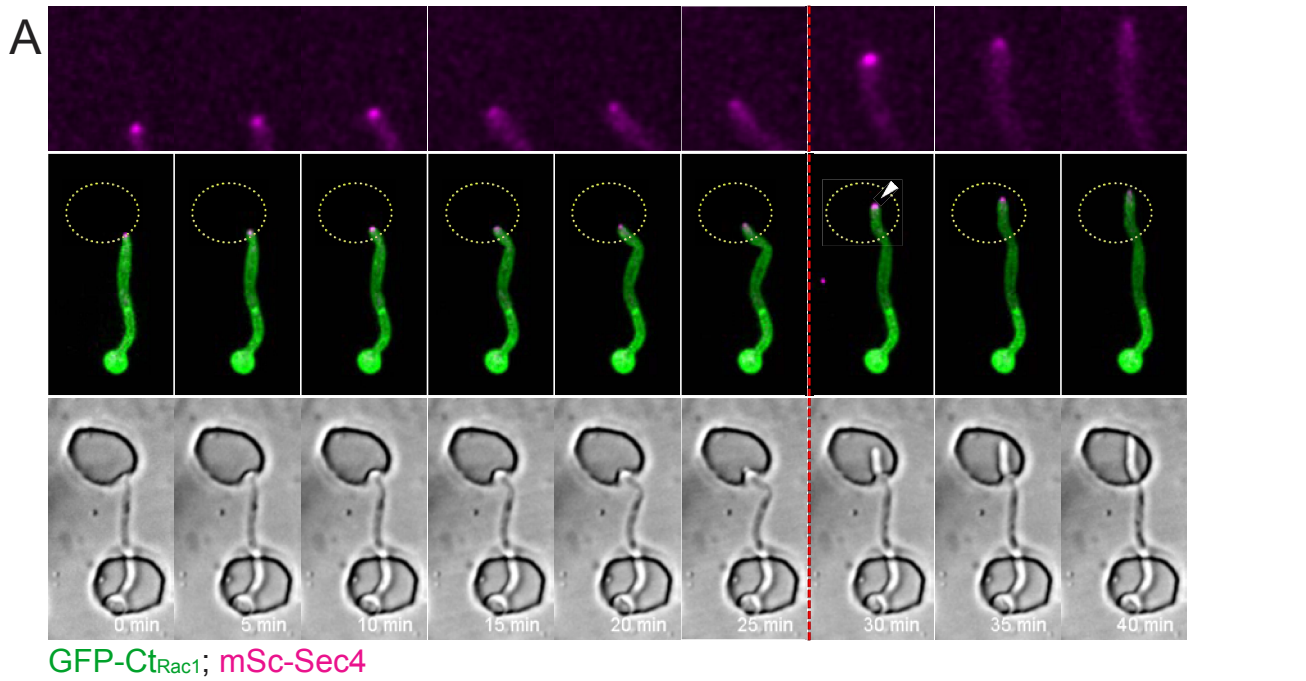

Appendix Figure 5: **Spitzenkörper alterations lead to population variability.** When the Spitzenkörper is altered there is a substantial increase in the variation of several parameters. I quantified this variation between conditions by dividing the standard deviation by the mean, also known as (A) the coefficient of variation. B) Cells lacking *MLC1* are highly variable. Heatmap of coefficient of variation values for four parameters measured. Values are normalized to the mean of the *mlc1*+/Δ and *mlc1*Δ/Δ+*MLC1* strains. The normalized values used for the heatmap are in the table below. C) Altering the distribution and stability of the Spitzenkörper results in increased variability. Heatmap of coefficient of variation values for four parameters measured. Values are normalized to the wild-type. The normalized values used for the heatmap are in the table below.

Appendix Figure 5

A

Coeffiecient of variation = Standard Deviation/Mean

B

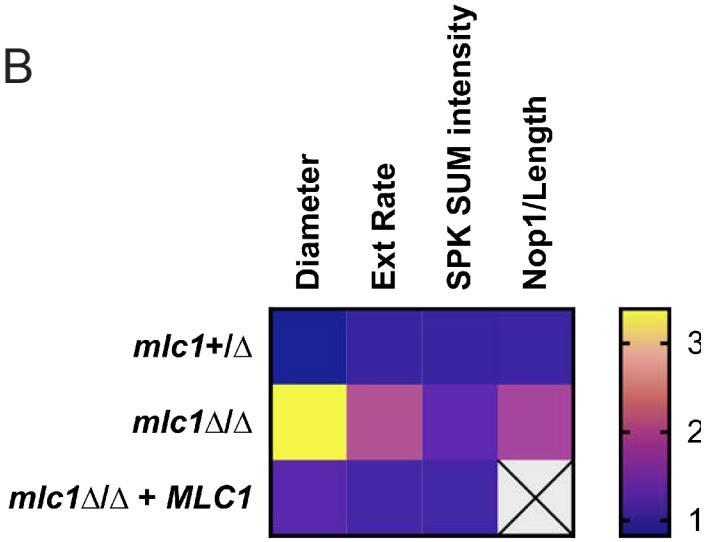

	Diameter	Ext Rate	SPK SUM intensity	Nop1 Ratio
mlc1 +/Δ	0.83	0.96	0.97	1.00
mlc1 Δ/Δ	3.39	1.98	1.23	1.85
mlc1 Δ/Δ + *MLC1*	1.17	1.04	1.03	

C

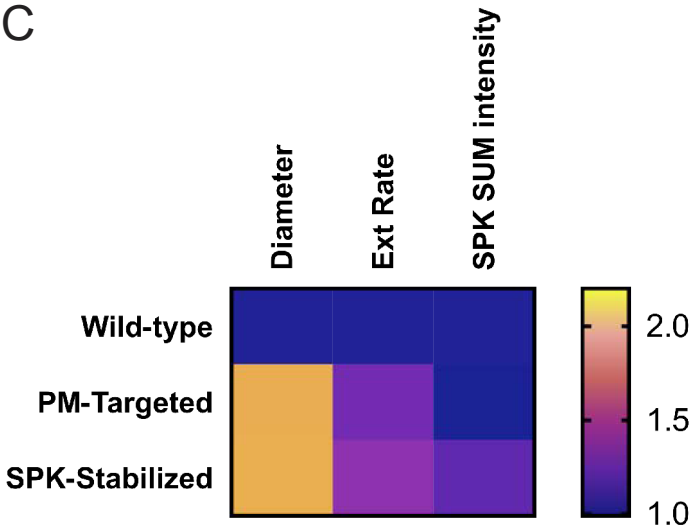

	Diameter	Ext Rate	SPK SUM intensity
Wild-type	1.00	1.00	1.00
PM-Targeted	1.93	1.25	0.99
SPK-Stabilized	1.94	1.36	1.18

References

Abenza, J. F., Couturier, E., Dodgson, J., Dickmann, J., Chessel, A., Dumais, J., & Carazo Salas, R. E. (2015). Wall mechanics and exocytosis define the shape of growth domains in fission yeast. *Nature Communications*, *6*. https://doi.org/10.1038/ncomms9400

Allert, S., Förster, T. M., Svensson, C. M., Richardson, J. P., Pawlik, T., Hebecker, B., Rudolphi, S., Juraschitz, M., Schaller, M., Blagojevic, M., Morschhäuser, J., Figge, M. T., Jacobsen, I. D., Naglik, J. R., Kasper, L., Mogavero, S., & Hube, B. (2018). Candida albicans-induced epithelial damage mediates translocation through intestinal barriers. *MBio*, *9*(3), 1–20. https://doi.org/10.1128/mBio.00915-18

Altenburg, T., Goldenbogen, B., Uhlendorf, J., & Klipp, E. (2019). Osmolyte homeostasis controls single-cell growth rate and maximum cell size of Saccharomyces cerevisiae. *Npj Systems Biology and Applications*, *5*(1). https://doi.org/10.1038/s41540-019-0111-6

Amberg, D. C., Zahner, J. E., Mulholland, J. W., Pringle, J. R., & Botstein, D. (1997). Aip3p/Bud6p, a yeast actin-interacting protein that is involved in morphogenesis and the selection of bipolar budding sites. *Molecular Biology of the Cell*, *8*(4), 729–753. https://doi.org/10.1091/mbc.8.4.729

Araujo-Bazán, L., Peñalva, M. A., & Espeso, E. A. (2008). Preferential localization of the endocytic internalization machinery to hyphal tips underlies polarization of the actin cytoskeleton in Aspergillus nidulans. *Molecular Microbiology*, *67*(4), 891–905. https://doi.org/10.1111/j.1365-2958.2007.06102.x

Arkowitz, R.A. (2009, August). Chemical gradients and chemotropism in yeast. *Cold Spring Harbor Perspectives in Biology*. https://doi.org/10.1101/cshperspect.a001958

Arkowitz, R.A., & Bassilana, M. (2011). Polarized growth in fungi: symmetry breaking and hyphal formation. *Seminars in Cell and Developmental Biology*, *22*(8), 806–815. https://doi.org/10.1016/j.semcdb.2011.08.010

Arkowitz, R.A., & Bassilana, M. (2014). Rho GTPase-phosphatidylinositol phosphate interplay in fungal cell polarity. *Biochemical Society Transactions*, *42*(1), 206–211. https://doi.org/10.1042/bst20130226

Arkowitz, R.A., & Bassilana, M. (2019). Recent advances in understanding Candida albicans hyphal growth. *F1000Research*, *8*(May), 700. https://doi.org/10.12688/f1000research.18546.1

Atilgan, E., Magidson, V., Khodjakov, A., & Chang, F. (2015). Morphogenesis of the fission yeast cell through cell wall expansion. *Current Biology*, *25*(16), 2150–2157. https://doi.org/10.1016/j.cub.2015.06.059

Baba, M., Baba, N., Ohsumi, Y., Kanaya, K., & Osumi, M. (1989). Three-dimensional analysis of morphogenesis induced by mating pheromone alpha factor in Saccharomyces cerevisiae. *Journal of Cell Science*, *94 (Pt 2)*, 207–216.

Bar-Yosef, H., Gildor, T., Ramírez-Zavala, B., Schmauch, C., Weissman, Z., Pinsky, M., Naddaf, R., Morschhäuser, J., Arkowitz, R. A., & Kornitzer, D. (2018). A global analysis of kinase function in Candida albicans hyphal morphogenesis reveals a role for the endocytosis regulator Akl1. *Frontiers in Cellular and Infection Microbiology*, *8*, 17. https://doi.org/10.3389/fcimb.2018.00017

Bartnicki-Garcia, S., Hergert, F., & Gierz, G. (1989). Computer simulation of fungal morphogenesis and the mathematical basis for hyphal (tip) growth. *Protoplasma*, *153*, 46–57. https://doi.org/10.1007/BF01322464

Bartnicki-Garcia, S., Bartnicki, D. D., Gierz, G., López-Franco, R., Bracker, C. E., Lopez-Franco, R., & Bracker, C. E. (1995). Evidence that Spitzenkörper behavior determines the shape of a fungal hypha: a test of the hyphoid model. *Experimental Mycology*, *19*(2), 153–159. https://doi.org/10.1006/emyc.1995.1017

Bartnicki-Garcia, S., Bracker, C. E., Gierz, G., López-Franco, R., & Haisheng, L. (2000). Mapping the growth of fungal hyphae: orthogonal cell wall expansion during tip growth and the role of turgor. *Biophysical Journal*, *79*(5), 2382–2390. https://doi.org/10.1016/S0006-3495(00)76483-6

Bassilana, M., Blyth, J., & Arkowitz, R. A. (2003). Cdc24, the GDP-GTP exchange factor for Cdc42, is required for invasive hyphal growth of Candida albicans. *Eukaryotic Cell*, *2*(1), 9–18. https://doi.org/10.1128/EC.2.1.9-18.2003

Bassilana, M., Hopkins, J., & Arkowitz, R. A. (2005). Regulation of the Cdc42/Cdc24 GTPase module during Candida albicans hyphal growth. *Eukaryotic Cell*, *4*(3), 588–603. https://doi.org/10.1128/EC.4.3.588–603.2005

Bassilana, M., Puerner, C., & Arkowitz, R. A. (2020). External signal–mediated polarized growth in fungi. *Current Opinion in Cell Biology*, *62*, 150–158. https://doi.org/10.1016/j.ceb.2019.11.001

Bastmeyer, M., Deising, H. B., & Bechinger, C. (2002). Force exertion in fungal infection. *Annual Review of Biophysics and Biomolecular Structure*, *31*, 321–341. https://doi.org/10.1146/annurev.biophys.31.091701.170951

Ben-Ami, R., Zimmerman, O., Finn, T., Amit, S., Novikov, A., Wertheimer, N., Lurie-Weinberger, M., & Berman, J. (2016). Heteroresistance to fluconazole is a continuously distributed phenotype among candida glabrata clinical strains associated with in vivo persistence. *MBio*, *7*(4), 1–12. https://doi.org/10.1128/mBio.00655-16

Bender, A., & Pringle, J. R. (1991). Use of a screen for synthetic lethal and multicopy suppressee mutants to identify two new genes involved in morphogenesis in Saccharomyces cerevisiae. *Molecular and Cellular Biology*, *11*(3), 1295–1305. https://doi.org/10.1128/mcb.11.3.1295

Bendezú, F. O., & Martin, S. G. (2013). Cdc42 explores the cell periphery for mate selection in fission yeast. *Current Biology*, *23*(1), 42–47. https://doi.org/10.1016/j.cub.2012.10.042

Bertin, A., McMurray, M. A., Thai, L., Garcia, G., 3rd, Votin, V., Grob, P., Allyn, T., Thorner, J., & Nogales, E. (2010). Phosphatidylinositol-4,5-bisphosphate promotes budding yeast septin filament assembly and organization. *Journal of Molecular Biology*, *404*(4), 711–731. https://doi.org/10.1016/j.jmb.2010.10.002

Bevington, P., & Robinson, D. (2003). *Data reduction and error analysis for the physical sciences* (University of California: McGraw-Hill Education).

Bhave, M., Papanikou, E., Iyer, P., Pandya, K., Jain, B. K., Ganguly, A., Sharma, C., Pawar, K., Austin, J., Day, K. J., Rossanese, O. W., Glick, B. S., & Bhattacharyya, D. (2014). Golgi enlargement in Arf-depleted yeast cells is due to altered dynamics of cisternal maturation. *Journal of Cell Science*, *127*(1), 250–257. https://doi.org/10.1242/jcs.140996

Bindels, D. S., Haarbosch, L., van Weeren, L., Postma, M., Wiese, K. E., Mastop, M., Aumonier, S., Gotthard, G., Royant, A., Hink, M. A., & Gadella, T. W., Jr (2017). mScarlet: a bright monomeric red fluorescent protein for cellular imaging. *Nature methods*, *14*(1), 53–56. https://doi.org/10.1038/nmeth.4074

Bishop, A., Lane, R., Beniston, R., Chapa-Y-Lazo, B., Smythe, C., & Sudbery, P. (2010). Hyphal growth in Candida albicans requires the phosphorylation of Sec2 by the Cdc28-Ccn1/Hgc1 kinase. *The EMBO Journal*, *29*(17), 2930–2942. https://doi.org/10.1038/emboj.2010.158

Bleichrodt, R. J., Foster, P., Howell, G., Latgé, J. P., & Read, N. D. (2020). Cell wall composition heterogeneity between single cells in aspergillus fumigatus leads to heterogeneous behavior during antifungal treatment and phagocytosis. *MBio*, *11*(3), 1–15. https://doi.org/10.1128/mBio.03015-19

Bonhomme, J., Chauvel, M., Goyard, S., Roux, P., Rossignol, T., & D'Enfert, C. (2011). Contribution of the glycolytic flux and hypoxia adaptation to efficient biofilm formation by Candida albicans. *Molecular Microbiology*, *80*(4), 995–1013. https://doi.org/10.1111/j.1365-2958.2011.07626.x

Bose, I., Irazoqui, J. E., Moskow, J. J., Bardes, E. S., Zyla, T. R., & Lew, D. J. (2001). Assembly of scaffold-mediated complexes containing Cdc42p, the exchange factor Cdc24p, and the effector Cla4p required for cell cycle-regulated phosphorylation of Cdc24p. *Journal of Biological Chemistry*, *276*(10), 7176–7186. https://doi.org/10.1074/jbc.M010546200

Bourett, T. M., & Howard, R. J. (1991). Ultrastructural immunolocalization of actin in a fungus. *Protoplasma*, *163*, 199–202.

Bowser, R., & Novick, P. (1991). Sec15 protein, an essential component of the exocytotic apparatis, is associated with the plasma membrane and with a soluble 19.5S particle. *Journal of Cell Biology*, *112*(6), 1117–1131. https://doi.org/10.1083/jcb.112.6.1117

Boyd, C., Hughes, T., Pypaert, M., & Novick, P. (2004). Vesicles carry most exocyst subunits to exocytic sites marked by the remaining two subunits, Sec3p and Exo70p. *Journal of Cell Biology*, *167*(5), 889–901. https://doi.org/10.1083/jcb.200408124

Boyne, J. R., Yosuf, H. M., Bieganowski, P., Brenner, C., & Price, C. (2000). Yeast myosin light chain, Mlc1p, interacts with both IQGAP and class II myosin to effect cytokinesis. *Journal of Cell Science*, *113 Pt 24*, 4533–4543. http://www.ncbi.nlm.nih.gov/pubmed/11082046

Brand, A., Vacharaksa, A., Bendel, C., Norton, J., Haynes, P., Henry-Stanley, M., Wells, C., Ross, K., Gow, N. A., & Gale, C. A. (2008). An internal polarity landmark is important for externally induced hyphal behaviors in Candida albicans. *Eukaryotic Cell*, *7*(4), 712–720. https://doi.org/10.1128/EC.00453-07

Braun, B. R., & Johnson, A. D. (2000). TUP1, CPH1 and EFG1 make independent contributions to filamentation in Candida albicans. *Genetics*, *155*(1), 57–67.

Brunswick, H. (1924). Untersuchungen uber geschlechts und kernverhaltnisse bei der Hymenomyzete gattung Coprinus. *Botanische Abhandlugen*, *5*.

Buller, A. H. R. (1931). *Researches on fungi Vol. 4, Vol. 4,*. London; New York: Longmans Green and Co.

Butty, A. C., Perrinjaquet, N., Petit, A., Jaquenoud, M., Segall, J. E., Hofmann, K., Zwahlen, C., & Peter, M. (2002). A positive feedback loop stabilizes the guanine-nucleotide exchange factor Cdc24 at sites of polarization. *The EMBO Journal*, *21*(7), 1565–1576. https://doi.org/10.1093/emboj/21.7.1565

Caballero-Lima, D., Kaneva, I. N., Watton, S. P., Sudbery, P. E., & Craven, C. J. (2013). The spatial distribution of the exocyst and actin cortical patches is sufficient to organize hyphal tip growth. *Eukaryotic Cell*, *12*(7), 998–1008. https://doi.org/10.1128/EC.00085-13

Caballero-Lima, D., & Sudbery, P. E. (2014). In Candida albicans, phosphorylation of Exo84 by Cdk1-Hgc1 is necessary for efficient hyphal extension. *Molecular Biology of the Cell*, *25*(7), 1097–1110. https://doi.org/10.1091/mbc.E13-11-0688

Cassone, A., Kerridge, D., & Gale, E. F. (1979). Ultrastructural changes in the cell wall of Candida albicans following cessation of growth and their possible relationship to the development of polyene resistance. *Journal of General Microbiology*, *110*(2), 339–349. https://doi.org/10.1099/00221287-110-2-339

Castro, D. G., & Martin, S. G. (2018). Differential GAP requirement for Cdc42-GTP polarization during proliferation and sexual reproduction. *Journal of Cell Biology*, *217*(12), 4215–4229. https://doi.org/https://doi.org/10.1083/jcb.201806016 4215

Chang, E. C., Barr, M., Wang, Y., Jung, V., Xu, H. P., & Wigler, M. H. (1994). Cooperative interaction of S. pombe proteins required for mating and morphogenesis. *Cell*, *79*(1), 131–141. https://doi.org/10.1016/0092-8674(94)90406-5

Chang, F. (2017). Forces that shape fission yeast cells. *Molecular Biology of the Cell*, *28*(14), 1819–1824. https://doi.org/10.1091/mbc.E16-09-0671

Chant, J., & Herskowitz, I. (1991). Genetic control of bud site selection in yeast by a set of gene products that constitute a morphogenetic pathway. *Cell*, *65–7*(1203–12). https://doi.org/10.1016/0092-8674(91)90015-Q

Chen, H., Zhou, X., Ren, B., & Cheng, L. (2020). The regulation of hyphae growth in Candida albicans. *Virulence*, *11*(1), 337-348 https://doi.org/10.1080/21505594.2020.1748930

Cleary, I. A., Reinhard, S. M., Lazzell, A. L., Monteagudo, C., Thomas, D. P., Lopez-Ribot, J. L., & Saville, S. P. (2016). Examination of the pathogenic potential of Candida albicans filamentous cells in an animal model of haematogenously disseminated candidiasis. *FEMS Yeast Research*, *16*(2), 1–10. https://doi.org/10.1093/femsyr/fow011

Clemente-Blanco, A., González-Novo, A., Machín, F., Caballero-Lima, D., Aragón, L., Sánchez, M., de Aldana, C. R., Jiménez, J., & Correa-Bordes, J. (2006). The Cdc14p phosphatase affects late cell-cycle events and morphogenesis in Candida albicans. *Journal of Cell Science*, *119*(6), 1130–1143. https://doi.org/10.1242/jcs.02820

Corvest, V., Bogliolo, S., Follette, P., Arkowitz, R. A., & Bassilana, M. (2013). Spatiotemporal regulation of Rho1 and Cdc42 activity during Candida albicans filamentous growth. *Molecular Microbiology*, *89*(4), 626–648. https://doi.org/10.1111/mmi.12302

Court, H., & Sudbery, P. (2007). Regulation of Cdc42 GTPase activity in the formation of hyphae in Candida albicans. *Molecular Biology of the Cell*, *18*(1), 265–281.

Crampin, H., Finley, K., Gerami-Nejad, M., Court, H., Gale, C., Berman, J., & Sudbery, P. (2005). Candida albicans hyphae have a Spitzenkörper that is distinct from the polarisome found in yeast and pseudohyphae. *Journal of Cell Science*, *118*(13), 2935–2947. https://doi.org/10.1242/jcs.02414

Davì, V., Tanimoto, H., Ershov, D., Haupt, A., De Belly, H., Le Borgne, R., Couturier, E., Boudaoud, A., & Minc, N. (2018). Mechanosensation dynamically coordinates polar growth and cell wall assembly to promote cell survival. *Developmental Cell*, *45*(2), 170-182.e7. https://doi.org/10.1016/j.devcel.2018.03.022

Davis-Hanna, A., Piispanen, A. E., Stateva, L. I., & Hogan, D. A. (2008). Farnesol and dodecanol effects on the Candida albicans Ras1-cAMP signalling pathway and the regulation of morphogenesis. *Molecular Microbiology*, *67*(1), 47–62. https://doi.org/10.1111/j.1365-2958.2007.06013.x

Delarue, M., Brittingham, G. P., Pfeffer, S., Surovtsev, I. V., Pinglay, S., Kennedy, K. J., Schaffer, M., Gutierrez, J. I., Sang, D., Poterewicz, G., Chung, J. K., Plitzko, J. M., Groves, J. T., Jacobs-Wagner, C., Engel, B. D., & Holt, L. J. (2018). mTORC1 controls phase separation and the biophysical properties of the cytoplasm by tuning crowding. *Cell*, *174*(2), 338–349.e20. https://doi.org/10.1016/j.cell.2018.05.042

Desai, J. V., Bruno, V. M., Ganguly, S., Stamper, R. J., Mitchell, K. F., Solis, N., Hill, E. M., Xu, W., Filler, S. G., Andes, D. R., Fanning, S., Lanni, F., & Mitchell, A. P. (2013). Regulatory role of glycerol in Candida albicans biofilm formation. *mBio*, *4*(2), e00637-12. https://doi.org/10.1128/mBio.00637-12

Desai, J. V., Cheng, S., Ying, T., Nguyen, M. H., Clancy, C. J., Lanni, F., & Mitchell, A. P. (2015). Coordination of Candida albicans invasion and infection functions by phosphoglycerol phosphatase Rhr2. *Pathogens*, *4*(3), 573–589. https://doi.org/10.3390/pathogens4030573

Endo, M., Shirouzu, M., & Yokoyama, S. (2003). The Cdc42 binding and scaffolding activities of the fission yeast adaptor protein Scd2. *Journal of Biological Chemistry*, *278*(2), 843–852. https://doi.org/10.1074/jbc.M209714200

Epp, E., Nazarova, E., Regan, H., Douglas, L. M., Konopka, J. B., Vogel, J., & Whiteway, M. (2013). Clathrin- and arp2/3-independent endocytosis in the fungal pathogen Candida albicans. *mBio*, *4*(5), e00476--13. https://doi.org/10.1128/mBio.00476-13

Epp, J. A., & Chant, J. (1997). An IQGAP-related protein controls actin-ring formation and cytokinesis in yeast. *Current biology : CB*, *7*(12), 921–929. https://doi.org/10.1016/S0960-9822(06)00411-8

Etienne-Manneville, S. (2004). Cdc42 - the centre of polarity. *Journal of Cell Science*, *117*(Pt 8), 1291–1300. https://doi.org/10.1242/jcs.01115

Fairn, G. D., Hermansson, M., Somerharju, P., & Grinstein, S. (2011). Phosphatidylserine is polarized and required for proper Cdc42 localization and for development of cell polarity. *Nature Cell Biology*, *13*(12), 1424–1430. https://doi.org/10.1038/ncb2351

Fang, H. M., & Wang, Y. (2006). RA domain-mediated interaction of Cdc35 with Ras1 is essential for increasing cellular cAMP level for Candida albicans hyphal development. *Molecular Microbiology*, *61*(2), 484–496. https://doi.org/10.1111/j.1365-2958.2006.05248.x

Feng, Z., Okada, S., Cai, G., Zhou, B., & Bi, E. (2015). Myosin-II heavy chain and formin mediate the targeting of myosin essential light chain to the division site before and during cytokinesis. *Molecular Biology of the Cell*, *26*(7), 1211–1224. https://doi.org/10.1091/mbc.E14-09-1363

Fischer-Parton, S., Parton, R. M., Hickey, P. C., Dijksterhuis, J., Atkinson, H. A., & Read, N. D. (2000). Confocal microscopy of FM4-64 as a tool for analysing endocytosis and vesicle trafficking in living fungal hyphae. *Journal of Microscopy*, *198*(3), 246–259. https://doi.org/10.1046/j.1365-2818.2000.00708.x

Fisher, K. E., & Roberson, R. W. (2016). Hyphal tip cytoplasmic organization in four zygomycetous fungi. *Mycologia*, *108*(3), 533–542. https://doi.org/10.3852/15-226

Fisher, K. E., Romberger, I., Lowry, D., Shange, P., & Roberson, R. W. (2018). Hyphal tip growth and cytoplasmic characters of Conidiobolus coronatus (Zoopagomycota, Entomophthoromycotina). *Mycologia*, *110*(1), 31–38. https://doi.org/10.1080/00275514.2017.1403808

Forster, B., Van De Ville, D., Berent, J., Sage, D., & Unser, M. (2004). Complex wavelets for extended depth-of-field: a new method for the fusion of multichannel microscopy images. *Microscopy research and technique*, *65*(1-2), 33–42. https://doi.org/10.1002/jemt.20092

Garrenton, L. S., Stefan, C. J., McMurray, M. A., Emr, S. D., & Thorner, J. (2010). Pheromone-induced anisotropy in yeast plasma membrane phosphatidylinositol- 4,5-bisphosphate distribution is required for MAPK signaling. *Proceedings of the National Academy of Sciences of the United States of America*, *107*(26), 11805–11810. https://doi.org/10.1073/pnas.1005817107

Garrenton, L. S., Young, S. L., & Thorner, J. (2006). Function of the MAPK scaffold protein, Ste5, requires a cryptic PH domain. *Genes and Development*, *20*(14), 1946–1958. https://doi.org/10.1101/gad.1413706

Ghugtyal, V., Garcia-Rodas, R., Seminara, A., Schaub, S. S., Bassilana, M., & Arkowitz, R. A. (2015). Phosphatidylinositol-4-phosphate-dependent membrane traffic is critical for fungal filamentous growth. *Proceedings of the National Academy of Sciences of the United States of America*, *112*(28), 8644–8649. https://doi.org/10.1073/pnas.1504259112

Gierz, G., & Bartnicki-Garcia, S. (2001). A three-dimensional model of fungal morphogenesis based on the vesicle supply center concept. *Journal of Theoretical Biology*, *208*(2), 151–164. https://doi.org/10.1006/jtbi.2000.2209

Girbardt, M. (1957). Der Spitzenkörper von Polystictus versicolor (L.). *Planta*, *50*(1), 47–59. https://doi.org/10.1007/BF01912343

Girbardt, M. (1969). Die Ultrastruktur der Apikalregion von Pilzhyphen. *Protoplasma*, *67*, 413–441. https://doi.org/10.1007/BF01254905

Gladfelter, A. S. (2006). Nuclear anarchy: asynchronous mitosis in multinucleated fungal hyphae. *Current Opinion in Microbiology*, *9*(6), 547–552. https://doi.org/10.1016/j.mib.2006.09.002

Gola, S., Martin, R., Walther, A., Dünkler, A., & Wendland, J. (2003). New modules for PCR-based gene targeting in Candida albicans: rapid and efficient gene targeting using 100 bp of flanking homology region. *Yeast (Chichester, England)*, *20*(16), 1339–1347. https://doi.org/10.1002/yea.1044

Goldenbogen, B., Giese, W., Hemmen, M., Uhlendorf, J., Herrmann, A., & Klipp, E. (2016). Dynamics of cell wall elasticity pattern shapes the cell during yeast mating morphogenesis. *Open Biology*, *6*(9), 160136. https://doi.org/10.1098/rsob.160136

González-Novo, A., Correa-Bordes, J., Labrador, L., Sánchez, M., Vázquez de Aldana, C. R., & Jiménez, J. (2008). Sep7 is essential to modify septin ring dynamics and inhibit cell separation during Candida albicans hyphal growth. *Molecular Biology of the Cell*, *19*(April), 1509–1518. https://doi.org/10.1091/mbc.E07

Goryachev, A. B., & Leda, M. (2017). Many roads to symmetry breaking: molecular mechanisms and theoretical models of yeast cell polarity. *Molecular Biology of the Cell*, *28*(3), 370–380. https://doi.org/10.1091/mbc.E16-10-0739

Goyer, M., Loiselet, A., Bon, F., L'Ollivier, C., Laue, M., Holland, G., Bonnin, A., & Dalle, F. (2016). Intestinal cell tight junctions limit invasion of Candida albicans through active penetration and endocytosis in the early stages of the interaction of the fungus with the intestinal barrier. *PLoS ONE*, *11*(3), 1–19. https://doi.org/10.1371/journal.pone.0149159

Graziano, B. R., Yu, H. Y., Alioto, S. L., Eskin, J. A., Ydenberg, C. A., Waterman, D. P., Garabedian, M., & Goode, B. L. (2014). The F-BAR protein Hof1 tunes formin activity to sculpt actin cables during polarized growth. *Molecular Biology of the Cell*, *25*(11), 1730–1743. https://doi.org/10.1091/mbc.E14-03-0850

Grove, S. N., & Bracker, C. E. (1970). Protoplasmic organization of hyphal tips among fungi: vesicles and Spitzenkörper. *Journal of Bacteriology*, *104*(2), 989–1009.

Guillas, I., Vernay, A., Vitagliano, J. J., & Arkowitz, R. A. (2013). Phosphatidylinositol 4,5-bisphosphate is required for invasive growth in Saccharomyces cerevisiae. *Journal of Cell Science*, *126*(16), 3602–3614. https://doi.org/10.1242/jcs.122606

Guo, P. P., Yong, J. Y. A., Wang, Y. M., & Li, C. R. (2016). Sec15 links bud site selection to polarised cell growth and exocytosis in Candida albicans. *Scientific Reports*, *6*(May), 26464. https://doi.org/10.1038/srep26464

Guo, W., Grant, A., & Novick, P. (1999). Exo84p is an exocyst protein essential for secretion. *Journal of Biological Chemistry*, *274*(33), 23558–23564. https://doi.org/10.1074/jbc.274.33.23558

Hall, R. A., Turner, K. J., Chaloupka, J., Cottier, F., De Sordi, L., Sanglard, D., Levin, L. R., Buck, J., & Mühlschlegel, F. A. (2011). The quorum-sensing molecules farnesol/homoserine lactone and dodecanol operate via distinct modes of action in Candida albicans. *Eukaryotic Cell*, *10*(8), 1034–1042. https://doi.org/10.1128/EC.05060-11

Harris, S. D., Read, N. D., Roberson, R. W., Shaw, B., Seiler, S., Plamann, M., & Momany, M. (2005). Polarisome meets spitzenkörper: microscopy, genetics, and genomics converge. *Eukaryotic Cell*, *4*(2), 225–229. https://doi.org/10.1128/EC.4.2.225-229.2005

Haupt, A., Ershov, D., & Minc, N. (2018). A positive feedback between growth and polarity provides directional persistency and flexibility to the process of tip growth. *Current Biology*, *28*(20), 3342-3351.e3. https://doi.org/10.1016/j.cub.2018.09.022

Haupt, A., & Minc, N. (2017). Gradients of phosphatidylserine contribute to plasma membrane charge localization and cell polarity in fission yeast. *Molecular Biology of the Cell*, *28*, 210–220. https://doi.org/10.1091/mbc.E16-06-0353

Hazan, I., & Liu, H. (2002). Hyphal tip-associated localization of Cdc42 is F-actin dependent in Candida albican. *Eukaryotic Cell*, *11*(6), 856–864. https://doi.org/10.1128/EC.1.6.856-864.2002

Hazan, I., Sepulveda-Becerra, M., & Liu, H. (2002). Hyphal elongation is regulated independently of cell cycle in Candida albicans. *Molecular Biology of the Cell*, *13*(1), 134–145. https://doi.org/10.1091/mbc.01

He, B., Xi, F., Zhang, X., Zhang, J., & Guo, W. (2007). Exo70 interacts with phospholipids and mediates the targeting of the exocyst to the plasma membrane. *The EMBO Journal*, *26*(18), 4053–4065. https://doi.org/10.1038/sj.emboj.7601834

Hernández-González, M., Bravo-Plaza, I., Pinar, M., de Los Ríos, V., Arst, H. N., & Peñalva, M. A. (2018). Endocytic recycling via the TGN underlies the polarized hyphal mode of life. *PLoS Genetics*, *14*(4), e1007291. https://doi.org/10.1371/journal.pgen.1007291

Howard, R. J. (1981). Ultrastructural analysis of hyphal tip cell growth in fungi: Spitzenkörper, cytoskeleton and endomembranes after freeze-substitution. *Journal of Cell Science*, *48*, 89–103.

Howard, R. J., Ferrari, M. A., Roach, D. H., & Money, N. P. (1991). Penetration of hard substrates by a fungus employing enormous turgor pressures. *Proceedings of the National Academy of Sciences of the United States of America*, *88*(24), 11281–11284. https://doi.org/10.1073/pnas.88.24.11281

Howard, R. J., & Valent, B. (1996). Breaking and entering: host penetration by the fungal rice blast pathogen Magnaporthe grisea. *Annual Review of Microbiology*, *50*(1), 491–512. https://doi.org/10.1146/annurev.micro.50.1.491

Irazoqui, J. E., Gladfelter, A. S., & Lew, D. J. (2003). Scaffold-mediated symmetry breaking by Cdc42p. *Nature Cell Biology*, *5*(12), 1062–1070. https://doi.org/10.1038/ncb1068

Ito, T., Matsui, Y., Ago, T., Ota, K., & Sumimoto, H. (2001). Novel modular domain PB1 recognizes pc motif to mediate functional protein-protein interactions. *The EMBO Journal*, *20*(15), 3938–3946. https://doi.org/10.1093/emboj/20.15.3938

Jedd, G., & Pieuchot, L. (2012, December). Multiple modes for gatekeeping at fungal cell-to-cell channels. *Molecular Microbiology*, *86*(6), 1291–1294. https://doi.org/10.1111/mmi.12074

Johnson, D. I. (1999). Cdc42: An essential Rho-type GTPase controlling eukaryotic cell polarity. *Microbiology and Molecular Biology Reviews*, *63*(1), 54–105.

Johnson, D. I., & Pringle, J. R. (1990). Molecular characterization of Cdc42, a Saccharomyces cerevisiae gene involved in the development of cell polarity. *Journal of Cell Biology*, *111*(1), 143–152.

Johnson, J. M., Jin, M., & Lew, D. J. (2011). Symmetry breaking and the establishment of cell polarity in budding yeast. *Current Opinion in Genetics & Development*, *21*(6), 740–746.

Jones, L. A., & Sudbery, P. E. (2010). Spitzenkörper, exocyst, and polarisome components in Candida albicans hyphae show different patterns of localization and have distinct dynamic properties. *Eukaryotic Cell*, *9*(10), 1455–1465. https://doi.org/10.1128/EC.00109-10

Jong, J. C. de, McCormack, B. J., Smirnoff, N., & Talbot, N. J. (Department of B. S. U. of E. W. S. L. P. R. E. E.-4QG (United K. (1997). Glycerol generates turgor in rice blast. *Nature (London) (United Kingdom)*.

Jose, M., Tollis, S., Nair, D., Sibarita, J. B., & McCusker, D. (2013). Robust polarity establishment occurs via an endocytosis-based cortical corralling mechanis. *Journal of Cell Biology*, *200*(4), 407–418. https://doi.org/10.1083/jcb.201206081

Julien, J.-D., & Boudaoud, A. (2018). Elongation and shape changes in organisms with cell walls: a dialogue between experiments and models. *The Cell Surface*, *1*(February), 34–42. https://doi.org/10.1016/j.tcsw.2018.04.001

Kadosh, D., & Johnson, A. D. (2005). Induction of the Candida albicans filamentous growth program by relief of transcriptional repression: a genome-wide analysis. *Molecular Biology of the Cell*, *16*(6), 2903–2912.

Kelly, F. D., & Nurse, P. (2011). Spatial control of Cdc42 activation determines cell width in fission yeast. *Molecular Biology of the Cell*, *22*(20), 3801–3811. https://doi.org/10.1091/mbc.E11-01-0057

Knafler, H. C., Rooij, I. I. S., Walker, L. A., Lee, K. K., Gow, N. A. R., & Ayscough, K. R. (2019). AP-2-Dependent endocytic recycling of the chitin synthase Chs3 regulates polarized growth in Candida albicans. *mBio*, *10*(2), e02421-18. https://doi.org/10.1128/mBio.02421-18

Knapp, B. D., Odermatt, P., Rojas, E. R., Cheng, W., He, X., Huang, K. C., & Chang, F. (2019). Decoupling of rates of protein synthesis from cell expansion leads to supergrowth. *Cell Systems*, *9*(5), 434-445.e6. https://doi.org/10.1016/j.cels.2019.10.001

Köhli, M., Galati, V., Boudier, K., Robertson, R. W., & Philippsen, P. (2008). Growth-speed-correlated localization of exocyst and polarisome components in growth zones of Ashbya gossypii hyphal tips. *Journal of Cell Science*, *121*(Pt23), 3878–3889. https://doi.org/10.1242/jcs.033852

Kornitzer, D. (2019). Regulation of Candida albicans hyphal morphogenesis by endogenous signals. *Journal of Fungi*, *5*(1). https://doi.org/10.3390/jof5010021

Kozubowski, L., Saito, K., Johnson, J. M., Howell, A. S., Zyla, T. R., & Lew, D. J. (2008). Symmetry-breaking polarization driven by a Cdc42p GEF–PAK complex. *Current Biology*, *18*(22), 1719–1726. https://doi.org/10.1016/j.cub.2008.09.060

Kullberg, B. J., & Arendrup, M. C. (2015). Invasive candidiasis. *New England Journal of Medicine*, *373*(15), 1445–1456. https://doi.org/10.1056/NEJMra1315399

Labbaoui, H., Bogliolo, S., Ghugtyal, V., Solis, N. V., Filler, S. G., Arkowitz, R. A., & Bassilana, M. (2017). Role of Arf GTPases in fungal morphogenesis and virulence. *PLoS Pathogens*, *13*(2), 1–24. https://doi.org/10.1371/journal.ppat.1006205

LaFratta, C.N. (2010). *Degas PDMS in two minutes*. Royal Society of Chemistry. https://blogs.rsc.org/chipsandtips/2010/08/17/degas-pdms-in-two-minutes/?doing_wp_cron=1598564545.1718978881835937500000

Lang, C., Grava, S., Finlayson, M., Trimble, R., Philippsen, P., & Jaspersen, S. L. (2010). Structural mutants of the spindle pole body cause distinct alteration of cytoplasmic microtubules and nuclear dynamics in multinucleated hyphae. *Molecular Biology of the Cell*, *21*, 753–766. https://doi.org/10.1091/mbc.E09

Lang, C., Grava, S., van den hoorn, T., Trimble, R., Philippsen, P., & Jaspersen, S. L. (2010). Mobility, microtubule nucleation and structure of microtubule-organizing centers in multinucleated hyphae of Ashbya gossypii. *Molecular Biology of the Cell*, *21*, 18–28. https://doi.org/10.1091/mbc.E09

Leberer, E., Harcus, D., Broadbent, I. D., Clark, K. L., Dignard, D., Ziegelbauer, K., Schmidt, A., Gow, N. A., Brown, A. J., & Thomas, D. Y. (1996). Signal transduction through homologs of the Ste20p and Ste7p protein kinases can trigger hyphal formation in the pathogenic fungus Candida albicans. *Proceedings of the National Academy of Sciences USA*, *93*(23), 13217–13222. https://doi.org/10.1073/pnas.93.23.13217

Lew, R. R. (2011). How does a hypha grow? The biophysics of pressurized growth in fungi. *Nature Reviews Microbiology*, *9*, 509–518. https://doi.org/10.1038/nrmicro2591

Li, C. R., Lee, R. T. H., Wang, Y. M., Zheng, X. De, & Wang, Y. (2007). Candida albicans hyphal morphogenesis occurs in Sec3p-independent and Sec3p-dependent phases separated by septin ring formation. *Journal of Cell Science*, *120*(11), 1898–1907. https://doi.org/10.1242/jcs.002931

Li, C. R., Wang, Y. M., De Zheng, X., Liang, H. Y., Tang, J. C., & Wang, Y. (2005). The formin family protein CaBni1p has a role in cell polarity control during both yeast and hyphal growth in Candida albicans. *Journal of Cell Science*, *118*(Pt 12), 2637–2648. https://doi.org/10.1242/jcs.02393

Lippincott, J., & Li, R. (1998). Sequential assembly of myosin II, an IQGAP-like protein, and filamentous actin to a ring structure involved in budding yeast cytokinesis. *The Journal of cell biology*, *140*(2), 355–366. https://doi.org/10.1083/jcb.140.2.355

Liu, H. P., Kohler, J., Fink, G. R., Köhler, J. R., & Fink, G. R. (1994). Suppression of hyphal formation in Candida albicans by mutation of a STE12 homolog. *Science*, *266*(5191), 1723–1726. https://doi.org/10.1126/science.7992058

Lo, H.-J., Köhler, J. R., Didomenico, B., Loebenberg, D., Cacciapuoti, A., & Fink, G. R. (1997). Nonfilamentous C. albicans mutants are avirulent. *Cell*, *90*(5), 939–949. https://doi.org/10.1016/S0092-8674(00)80358-X

López-Franco, R., Bartnicki-Garcia, S., & Bracker, C. E. (1994). Pulsed growth of fungal hyphal tips. *Proceedings of the National Academy of Sciences of the United States of America*, *91*(25), 12228–12232. https://doi.org/10.1073/pnas.91.25.12228

Luo, J., Vallen, E. A., Dravis, C., Tcheperegine, S. E., Drees, B., & Bi, E. (2004). Identification and functional analysis of the essential and regulatory light chains of the only type II myosin Myo1p in Saccharomyces cerevisiae. *Journal of Cell Biology*, *165*(6), 843–855. https://doi.org/10.1083/jcb.200401040

Martin, R., Hellwig, D., Schaub, Y., Bauer, J., Walther, A., & Wendland, J. (2007). Functional analysis of Candida albicans genes whose Saccharomyces cerevisiae homologues are involved in endocytosis. *Yeast*, *24*(6), 511–522. https://doi.org/10.1002/yea.1489

Martin, S. G. (2015). Spontaneous cell polarization: feedback control of Cdc42 GTPase breaks cellular symmetry. *Bioessays*, *37*(11), 1193–1201. https://doi.org/10.1002/bies.201500077

Martin, S. G., & Arkowitz, R. A. (2014). Cell polarization in budding and fission yeasts. *FEMS Microbiology Reviews*, *38*(2), 228–253. https://doi.org/10.1111/1574-6976.12055

Martin, S. W., & Konopka, J. B. (2004). Lipid raft polarization contributes to hyphal growth in Candida albicans. *Eukaryotic Cell*, *3*(3), 675–684. https://doi.org/10.1128/EC.3.3.675-684.2004

Martínez-Núñez, L., & Riquelme, M. (2015). Role of BGT-1 and BGT-2, two predicted GPI-anchored glycoside hydrolases/glycosyltransferases, in cell wall remodeling in Neurospora crassa. *Fungal Genetics and Biology*, *85*, 58–70. https://doi.org/10.1016/j.fgb.2015.11.001

Mazu, T. K., Bricker, B. A., Flores-Rozas, H., & Ablordeppy, S. Y. (2016). The mechanistic targets of antifungal agents: an overview. *Mini Review Medical Chemistry*, *16*(7), 555–578. https://doi.org/10.2174/1389557516666160118112103

McCarty, T. P., & Pappas, P. G. (2016). Invasive candidiasis. *Infectious Disease Clinics of North America*, *30*(1), 103–124. https://doi.org/10.1016/j.idc.2015.10.013

Meca, J., Massoni‐Laporte, A., Martinez, D., Sartorel, E., Loquet, A., Habenstein, B., & McCusker, D. (2019). Avidity‐driven polarity establishment via multivalent lipid–GTPase module interactions. *The EMBO Journal*, *38*(3), e99652. https://doi.org/10.15252/embj.201899652

Mendgen, K., Hahn, M., & Deising, H. (1996). Morphogenesis and mechanisms of penetration by plant pathogenic fungi. *Annual Review of Phytopathology*, *34*(1), 367–386. https://doi.org/10.1146/annurev.phyto.34.1.367

Minc, N., Boudaoud, A., & Chang, F. (2009). Mechanical forces of fission yeast growth. *Current Biology*, *19*(13), 1096–1101. https://doi.org/10.1016/j.cub.2009.05.031

Moyes, D. L., Richardson, J. P., & Naglik, J. R. (2015). Candida albicans-epithelial interactions and pathogenicity mechanisms: scratching the surface. *Virulence*, *6*(4), 338–346. https://doi.org/10.1080/21505594.2015.1012981

Moyes, D. L., Wilson, D., Richardson, J. P., Mogavero, S., Tang, S. X., Wernecke, J., Höfs, S., Gratacap, R. L., Robbins, J., Runglall, M., Murciano, C., Blagojevic, M., Thavaraj, S., Förster, T. M., Hebecker, B., Kasper, L., Vizcay, G., Iancu, S. I., Kichik, N., Häder, A., … Naglik, J. R. (2016). Candidalysin is a fungal peptide toxin critical for mucosal infection. *Nature*, *532*(7597), 64–68. https://doi.org/10.1038/nature17625

Murad, A. M., Leng, P., Straffon, M., Wishart, J., Macaskill, S., MacCallum, D., Schnell, N., Talibi, D., Marechal, D., Tekaia, F., d'Enfert, C., Gaillardin, C., Odds, F. C., & Brown, A. J. (2001). Nrg1 represses yeast–hypha morphogenesis and hypha–specific gene expression in Candida albicans. *The EMBO Journal*, *20*(17), 4742–4752. https://doi.org/10.1093/emboj/20.17.4742

Naglik, J. R., Moyes, D. L., Wächtler, B., & Hube, B. (2011). Candida albicans interactions with epithelial cells and mucosal immunity. *Microbes and Infection*, *13*(12–13), 963–976. https://doi.org/10.1016/j.micinf.2011.06.009

Nantel, A., Dignard, D., Bachewich, C., Harcus, D., Marcil, A., Bouin, A. P., Sensen, C. W., Hogues, H., van het Hoog, M., Gordon, P., Rigby, T., Benoit, F., Tessier, D. C., Thomas, D. Y., & Whiteway, M. (2002). Transcription profiling of Candida albicans cells undergoing the yeast-to-hyphal transition. *Molecular Biology of the Cell*, *13*(October), 3452–3465. https://doi.org/10.1091/mbc.E02

Novick, P., Medkova, M., Dong, G., Hutagalung, A., Reinisch, K., & Grosshans, B. (2006). Interactions between Rabs, tethers, SNAREs and their regulators in exocytosis. *Biochemical Society Transactions*, *34*(5), 683–686. https://doi.org/10.1042/BST0340683

Odds, F. C. (1984). Demonstration of a septal pore in budding candida albicans yeast cells. *Medical Mycology*, *22*(6), 505–507. https://doi.org/10.1080/00362178485380791

Orlando, K., Zhang, J., Zhang, X., Yue, P., Chiang, T., Bi, E., & Guo, W. (2008). Regulation of Gic2 localization and function by phosphatidylinositol 4,5-bisphosphate during the establishment of cell polarity in budding yeast. *Journal of Biological Chemistry*, *283*(21), 14205–14212. https://doi.org/10.1074/jbc.M708178200

Ortiz, D., Medkova, M., Walch-Solimena, C., & Novick, P. (2002). Ypt32 recruits the Sec4p guanine nucleotide exchange factor, Sec2p, to secretory vesicles; evidence for a Rab cascade in yeast. *The Journal of cell biology*, *157*(6), 1005–1015. https://doi.org/10.1083/jcb.200201003

Ozbudak, E. M., Becskei, A., & van Oudenaarden, A. (2005). A system of counteracting feedback loops regulates Cdc42p activity during spontaneous cell polarization. *Developmental Cell*, *9*(4), 565–571. https://doi.org/10.1016/j.devcel.2005.08.014

Pappas, P. G., Lionakis, M. S., Arendrup, M. C., Ostrosky-Zeichner, L., & Kullberg, B. J. (2018). Invasive candidiasis. *Nature Reviews Disease Primers*, *4*(May), 1–20. https://doi.org/10.1038/nrdp.2018.26

Park, H. O., & Bi, E. (2007). Central roles of small GTPases in the development of cell polarity in yeast and beyond. *Microbiology and Molecular Biology Reviews*, *71*(1), 48–96. https://doi.org/10.1128/MMBR.00028-06

Peñalva, M. Á. (2010, December 1). Endocytosis in filamentous fungi: Cinderella gets her reward. *Current Opinion in Microbiology*. Elsevier Current Trends. https://doi.org/10.1016/j.mib.2010.09.005

Pennestri, M., Melino, S., Contessa, G. M., Casavola, E. C., Paci, M., Ragnini-Wilson, A., & Cicero, D. O. (2007). Structural basis for the interaction of the myosin light chain Mlc1p with the myosin V Myo2p IQ motifs. *Journal of Biological Chemistry*, *282*(1), 667–679. https://doi.org/10.1074/jbc.M607016200

Peterson, J., Zheng, Y., Bender, L., Myers, A., Cerione, R., & Bender, A. (1994). Interactions between the bud emergence proteins Bem1p and Bem2p and Rho- type GTPases in yeast. *Journal of Cell Biology*, *127*(5), 1395–1406. https://doi.org/10.1083/jcb.127.5.1395

Pieuchot, L., Lai, J., Loh, R. A., Leong, F. Y., Chiam, K. H., Stajich, J., & Jedd, G. (2015). Cellular subcompartments through cytoplasmic streaming. *Developmental Cell*, *34*(4), 410–420. https://doi.org/10.1016/j.devcel.2015.07.017

Pinar, M., Pantazopoulou, A., Arst, H. N., & Peñalva, M. A. (2013). Acute inactivation of the Aspergillus nidulans Golgi membrane fusion machinery: correlation of apical extension arrest and tip swelling with cisternal disorganization. *Molecular Microbiology*, *89*(2), 228–248. https://doi.org/10.1111/mmi.12280

Puerner, C., Kukhaleishvili, N., Thomson, D., Schaub, S., Noblin, X., Seminara, A., Bassilana, M., Arkowitz, RA. (2020). Mechanical force-induced morphology changes in a human fungal pathogen. *BMC Biology*, 18:122. https://doi.org/10.1186/s12915-020-00833-0

Quindós, G. (2014). Epidemiology of candidaemia and invasive candidiasis. A changing face. *Revista Iberoamericana de Micologia*, *31*(1), 42–48. https://doi.org/10.1016/j.riam.2013.10.001

Rapali, P., Mitteau, R., Braun, C., Massoni-Laporte, A., Ünlü, C., Bataille, L., Arramon, F. S., Gygi, S. P., & McCusker, D. (2017). Scaffold-mediated gating of Cdc42 signalling flux. *eLife*, *6*. https://doi.org/10.7554/eLife.25257

Revilla-Guarinos, M. T., Martín-García, R., Villar-Tajadura, M. A., Estravís, M., Coll, P. M., & Pérez, P. (2016). Rga6 is a fission yeast Rho GAP involved in Cdc42 regulation of polarized growth. *Molecular Biology of the Cell*, *27*(9), 1524–1535. https://doi.org/10.1091/mbc.e15-12-0818

Reynaga-Peña, C. G., Gierz, G., & Bartnicki-Garcia, S. (1997). Analysis of the role of the Spitzenkörper in fungal morphogenesis by computer simulation of apical branching in Aspergillus niger. *Proceedings of the National Academy of Sciences of the United States of America*, *94*(17), 9096–9101. https://doi.org/10.1073/pnas.94.17.9096

Rico-Ramírez, A. M., Roberson, R. W., & Riquelme, M. (2018). Imaging the secretory compartments involved in the intracellular traffic of CHS-4, a class IV chitin synthase, in Neurospora crassa. *Fungal Genetics and Biology*, *117*(March), 30–42. https://doi.org/10.1016/j.fgb.2018.03.006

Rida, P. C. G., Nishikawa, A., Won, G. Y., & Dean, N. (2006). Yeast-to-hyphal transition triggers formin-dependent Golgi localization to the growing tip in Candida albicans. *Molecular Biology of the Cell*, *17*, 4364–4378. https://doi.org/10.1091/mbc.E06

Riga, A., Castiglioni, V. G., & Boxem, M. (2020). New insights into apical-basal polarization in epithelia. *Current Opinion in Cell Biology*, *62*, 1–8. https://doi.org/10.1016/j.ceb.2019.07.017

Riquelme, M., Aguirre, J., Bartnicki-García, S., Braus, G. H., Feldbrügge, M., Fleig, U., Hansberg, W., Herrera-Estrella, A., Kämper, J., Kück, U., Mouriño-Pérez, R. R., Takeshita, N., & Fischer, R. (2018). Fungal morphogenesis, from the polarized growth of hyphae to complex reproduction and infection structures. *Microbiology and Molecular Biology Reviews*, *82*(2), 1–47. https://doi.org/10.1128/mmbr.00068-17

Riquelme, Meritxell, Bartnicki-García, S., González-Prieto, J. M., Sánchez-León, E., Verdín-Ramos, J. A., Beltrán-Aguilar, A., & Freitag, M. (2007). Spitzenkörper localization and intracellular traffic of green fluorescent protein-labeled CHS-3 and CHS-6 chitin synthases in living hyphae of Neurospora crassa. *Eukaryotic Cell*, *6*(10), 1853–1864. https://doi.org/10.1128/EC.00088-07

Riquelme, M, Reynaga-Pena, C. G., Gierz, G., & Bartnicki-Garcia, S. (1998). What determines growth direction in fungal hyphae? *Fungal Genetics and Biology*, *24*, 101–109. https://doi.org/10.1006/fgbi.1998.1074

Riquelme, M., Roberson, R. W., McDaniel, D. P., & Bartnicki-García, S. (2002). The effects of ropy-1 mutation on cytoplasmic organization and intracellular motility in mature hyphae of Neurospora crassa. *Fungal Genetics and Biology*, *37*(2), 171–179. https://doi.org/10.1016/S1087-1845(02)00506-6

Riquelme, M., & Sánchez-León, E. (2014). The Spitzenkörper: A choreographer of fungal growth and morphogenesis. *Current Opinion in Microbiology*, *20*, 27–33. https://doi.org/10.1016/j.mib.2014.04.003

Roberson, R. W., Saucedo, E., Maclean, D., Propster, J., Unger, B., Oneil, T. A., Parvanehgohar, K., Cavanaugh, C., & Lowry, D. (2011). The hyphal tip structure of Basidiobolus sp.: a zygomycete fungus of uncertain phylogeny. *Fungal Biology*, *115*(6), 485–492. https://doi.org/10.1016/j.funbio.2011.02.012

Rocha, C. R., Schröppel, K., Harcus, D., Marcil, A., Dignard, D., Taylor, B. N., Thomas, D. Y., Whiteway, M., & Leberer, E. (2001). Signaling through adenylyl cyclase is essential for hyphal growth and virulence in the pathogenic fungus Candida albicans. *Molecular Biology of the Cell*, *12*(11), 3631–3643. https://doi.org/10.1091/mbc.12.11.3631

Rosenberg, A., Ene, I. V., Bibi, M., Zakin, S., Segal, E. S., Ziv, N., Dahan, A. M., Colombo, A. L., Bennett, R. J., & Berman, J. (2018). Antifungal tolerance is a subpopulation effect distinct from resistance and is associated with persistent candidemia. *Nature Communications*, *9*(1). https://doi.org/10.1038/s41467-018-04926-x

Rothbauer, U., Zolghadr, K., Muyldermans, S., Schepers, A., Cardoso, M. C., & Leonhardt, H. (2008). A versatile nanotrap for biochemical and functional studies with fluorescent fusion proteins. *Molecular and Cellular Proteomics*, *7*(2), 282–289. https://doi.org/10.1074/mcp.M700342-MCP200

Rothbauer, U., Zolghadr, K., Tillib, S., Nowak, D., Schermelleh, L., Gahl, A., Backmann, N., Conrath, K., Muyldermans, S., Cardoso, M. C., & Leonhardt, H. (2006). Targeting and tracing antigens in live cells with fluorescent nanobodies. *Nature methods*, *3*(11), 887–889. https://doi.org/10.1038/nmeth953

Ryder, L. S., Dagdas, Y. F., Kershaw, M. J., Venkataraman, C., Madzvamuse, A., Yan, X., Cruz-Mireles, N., Soanes, D. M., Oses-Ruiz, M., Styles, V., Sklenar, J., Menke, F., & Talbot, N. J. (2019). A sensor kinase controls turgor-driven plant infection by the rice blast fungus. *Nature*, *574*(7778), 423–427. https://doi.org/10.1038/s41586-019-1637-x

Sartorel, E., Ünlü, C., Jose, M., Massoni-Laporte, A., Meca, J., Sibarita, J. B., & McCusker, D. (2018). Phosphatidylserine and GTPase activation control Cdc42 nanoclustering to counter dissipative diffusion. *Molecular Biology of the Cell*, *29*(11), 1299–1310. https://doi.org/10.1091/mbc.E18-01-0051

Saville, S. P., Lazzell, A. L., Bryant, A. P., Fretzen, A., Monreal, A., Solberg, E. O., Monteagudo, C., Lopez-Ribot, J. L., & Milne, G. T. (2006). Inhibition of filamentation can be used to treat disseminated candidiasis. *Antimicrobial Agents and Chemotherapy*, *50*(10), 3312–3316. https://doi.org/10.1128/AAC.00628-06

Saville, S. P., Lazzell, A. L., Monteagudo, C., & Lopez-ribot, J. L. (2003). Engineered control of cell morphology in vivo reveals distinct roles for yeast and filamentous forms of Candida albicans during infection. *Eukaryotic Cell*, *2*(5), 1053–1060. https://doi.org/10.1128/EC.2.5.1053

Schaber, J., Adrover, M. A., Eriksson, E., Pelet, S., Petelenz-Kurdziel, E., Klein, D., Posas, F., Goksör, M., Peter, M., Hohmann, S., & Klipp, E. (2010). Biophysical properties of Saccharomyces cerevisiae and their relationship with HOG pathway activation. *European Biophysics Journal*, *39*(11), 1547–1556. https://doi.org/10.1007/s00249-010-0612-0

Schindelin, J., Arganda-Carreras, I., Frise, E., Kaynig, V., Longair, M., Pietzsch, T., Preibisch, S., Rueden, C., Saalfeld, S., Schmid, B., Tinevez, J. Y., White, D. J.,

Hartenstein, V., Eliceiri, K., Tomancak, P., & Cardona, A. (2012). Fiji: an open-source platform for biological-image analysis. *Nature methods*, *9*(7), 676–682. https://doi.org/10.1038/nmeth.2019

Schmied, C., Stamataki, E., & Tomancak, P. (2014). Open-source solutions for SPIMage processing. *Methods in Cell Biology*, *123*, 505–529. https://doi.org/10.1016/B978-0-12-420138-5.00027-6

Schornack, S., Fuchs, R., Huitema, E., Rothbauer, U., Lipka, V., & Kamoun, S. (2009). Protein mislocalization in plant cells using a GFP-binding chromobody. *Plant Journal*, *60*(4), 744–754. https://doi.org/10.1111/j.1365-313X.2009.03982.x

Shannon, K. B., & Li, R. (1999). The multiple roles of Cyk1p in the assembly and function of the actomyosin ring in budding yeast. *Molecular Biology of the Cell*, *10*(2), 283–296. https://doi.org/10.1091/mbc.10.2.283

Shannon, K. B., & Li, R. (2000). A myosin light chain mediates the localization of the budding yeast IQGAP-like protein during contractile ring formation. *Current Biology*, *10*(12), 727–730. https://doi.org/10.1016/S0960-9822(00)00539-X

Sheu, Y. J., Santos, B., Fortin, N., Costigan, C., & Snyder, M. (1998). Spa2p interacts with cell polarity proteins and signaling components involved in yeast cell morphogenesis. *Molecular and Cellular Biology*, *18*(7), 4053–4069. https://doi.org/10.1128/MCB.18.7.4053

Shcherbakova, D. M., Baloban, M., Emelyanov, A. V., Brenowitz, M., Guo, P., & Verkhusha, V. V. (2016). Bright monomeric near-infrared fluorescent proteins as tags and biosensors for multiscale imaging. *Nature communications*, *7*, 12405. https://doi.org/10.1038/ncomms12405

Silva, P. M., Puerner, C., Seminara, A., Bassilana, M., & Arkowitz, R. A. (2019). Secretory vesicle clustering in fungal filamentous cells does not require directional growth. *Cell Reports*, *28*(8), 2231-2245.e5. https://doi.org/10.1016/j.celrep.2019.07.062

Singh, P., Das, A., & Li, R. (2017). Investigating symmetry breaking in yeast: from seeing to understanding. *Methods in Cell Biology*, *139*, 23–50. https://doi.org/10.1016/bs.mcb.2016.12.001

Sorgo, A. G., Heilmann, C. J., Dekker, H. L., Bekker, M., Brul, S., de Koster, C. G., de Koning, L. J., & Klis, F. M. (2011). Effects of fluconazole on the secretome, the wall proteome, and wall integrity of the clinical fungus candida albicans. *Eukaryotic Cell*, *10*(8), 1071–1081. https://doi.org/10.1128/EC.05011-11

Stevens, R. C., & Davis, T. N. (1998). Mlc1p is a light chain for the unconventional myosin Myo2p in Saccharomyces cerevisiae. *Journal of Cell Biology*, *142*(3), 711–722. https://doi.org/10.1083/jcb.142.3.711

Stoldt, V. R., Sonneborn, A., Leuker, C. E., & Ernst, J. F. (1997). Efg1p, an essential regulator of morphogenesis of the human pathogen Candida albicans, is a member of a conserved class of bHLH proteins regulating morphogenetic processes in fungi. *The EMBO Journal*, *16*(8), 1982–1991. https://doi.org/10.1093/emboj/16.8.1982

Stone, N. R. H., Rhodes, J., Fisher, M. C., Mfinanga, S., Kivuyo, S., Rugemalila, J., Segal, E. S., Needleman, L., Molloy, S. F., Kwon-Chung, J., Harrison, T. S., Hope, W., Berman, J., & Bicanic, T. (2019). Dynamic ploidy changes drive fluconazole resistance in human cryptococcal meningitis. *Journal of Clinical Investigation*, *129*(3), 999–1014. https://doi.org/10.1172/JCI124516

Sudbery, P. E. (2011). Growth of Candida albicans hyphae. *Nature Reviews. Microbiology*, *9*(10), 737–748. https://doi.org/10.1038/nrmicro2636

Sudbery, P. (2011). Fluorescent proteins illuminate the structure and function of the hyphal tip apparatus. *Fungal Genetics and Biology*, *48*(9), 849–857. https://doi.org/10.1016/j.fgb.2011.02.004

Takahashi, S., & Pryciak, P. M. (2007). Identification of novel membrane-binding domains in multiple yeast Cdc42 effectors. *Molecular Biology of the Cell*, *18*(12), 4945–4956. https://doi.org/10.1091/mbc.E07

Takeshita, N. (2016). Coordinated process of polarized growth in filamentous fungi. *Bioscience, Biotechnology and Biochemistry*, *80*(9), 1693–1699. https://doi.org/10.1080/09168451.2016.1179092

Takeshita, N. (2018). Oscillatory fungal cell growth. *Fungal Genetics and Biology*, *110*(December), 10–14. https://doi.org/10.1016/j.fgb.2017.12.002

Takeshita, N., Evangelinos, M., Zhou, L., Serizawa, T., Somera-Fajardo, R. A., Lu, L., Takaya, N., Nienhaus, G. U., & Fischer, R. (2017). Pulses of Ca^{2+} coordinate actin assembly and exocytosis for stepwise cell extension. *Proceedings of the National Academy of Sciences of the United States of America*, *114*(22), 5701–5706. https://doi.org/10.1073/pnas.1700204114

TerBush, D. R., Maurice, T., Roth, D., & Novick, P. (1996). The exocyst is a multiprotein complex required for exocytosis in Saccharomyces cerevisiae. *The EMBO Journal*, *15*(23), 6483–6494. https://doi.org/10.1002/j.1460-2075.1996.tb01039.x

TerBush, D. R., & Novick, P. (1995). Sec6, Sec8, and Sec15 are components of a multisubunit complex which localizes to small bud tips in Saccharomyces cerevisiae. *Journal of Cell Biology*, *130*(2), 299–312. https://doi.org/10.1083/jcb.130.2.299

Thomson, D. D., Wehmeier, S., Byfield, F. J., Janmey, P. A., Caballero-Lima, D., Crossley, A., & Brand, A. C. (2015). Contact-induced apical asymmetry drives the thigmotropic responses of Candida albicans hyphae. *Cellular Microbiology*, *17*(3), 342–354. https://doi.org/10.1111/cmi.12369

Tian, C., Wu, Y., & Johnsson, N. (2014). Stepwise and cooperative assembly of a cytokinetic core complex in Saccharomyces cerevisiae. *Journal of Cell Science*, *127*(16), 3614–3624. https://doi.org/10.1242/jcs.153429

Ushinsky, S. C., Harcus, D., Ash, J., Dignard, D., Marcil, A., Morchhauser, J., Thomas, D. Y., Whiteway, M., & Leberer, E. (2002). CDC42 is required for polarized growth in human pathogen Candida albicans. *Eukaryotic Cell*, *1*(1), 95–104. https://doi.org/10.1128/EC.1.1.95-104.2002

Van den Ackerveken, G. F. J. M., Dunn, R. M., Cozijnsen, A. J., Vossen, J. P. M. J., Van den Broek, H. W. J., & De Wit, P. J. G. M. (1994). Nitrogen limitation induces expression of the avirulence gene avr9 in the tomato pathogen Cladosporium fulvum. *MGG Molecular & General Genetics*, *243*(3), 277–285. https://doi.org/10.1007/BF00301063

VandenBerg, A. L., Ibrahim, A. S., Edwards, J. E., Toenjes, K. A., & Johnson, D. I. (2004). Cdc42p GTPase regulates the budded-to-hyphal-form transition and expression of hypha-specific transcripts in Candida albicans. *Eukaryotic Cell*, *3*(3), 724–734. https://doi.org/10.1128/EC.3.3.724-734.2004

Vargas, M. M., Aronson, J. M., & Roberson, R. W. (1993). The cytoplasmic organization of

hyphal tip cells in the fungus Allomyces macrogynus. *Protoplasma*, *176*(1–2), 43–52. https://doi.org/10.1007/BF01378938

Vauchelles, R., Stalder, D., Botton, T., Arkowitz, R. A., & Bassilana, M. (2010). Rac1 dynamics in the human opportunistic fungal pathogen Candida albicans. *PloS one*, *5*(10), e15400. https://doi.org/10.1371/journal.pone.0015400

Verdín, J., Bartnicki-Garcia, S., & Riquelme, M. (2009). Functional stratification of the Spitzenkörper of Neurospora crassa. *Molecular Microbiology*, *74*(5), 1044–1053. https://doi.org/10.1111/j.1365-2958.2009.06917.x

Vernay, A., Schaub, S., Guillas, I., Bassilana, M., & Arkowitz, R. A. (2012). A steep phosphoinositide bis-phosphate gradient forms during fungal filamentous growth. *Journal of Cell Biology*, *198*(4), 711–730. https://doi.org/10.1083/jcb.201203099

Wächtler, B., Citiulo, F., Jablonowski, N., Förster, S., Dalle, F., Schaller, M., Wilson, D., & Hube, B. (2012). Candida albicans-epithelial interactions: dissecting the roles of active penetration, induced endocytosis and host factors on the infection process. *PLoS ONE*, *7*(5). https://doi.org/10.1371/journal.pone.0036952

Wakade, R., Labbaoui, H., Stalder, D., Arkowitz, R. A., & Bassilana, M. (2017). Overexpression of YPT6 restores invasive filamentous growth and secretory vesicle clustering in a Candida albicans arl1 mutant. *Small GTPases*, 1–7. https://doi.org/10.1080/21541248.2017.1378157

Wang, A., Raniga, P. P., Lane, S., Lu, Y., & Liu, H. (2009). Hyphal chain formation in Candida albicans: Cdc28-Hgc1 phosphorylation of Efg1 represses cell separation genes. *Molecular and Cellular Biology*, *29*(16), 4406–4416. https://doi.org/10.1128/mcb.01502-08

Wang, H., Huang, Z. X., Au Yong, J. Y., Zou, H., Zeng, G., Gao, J., Wang, Y., Wong, A. H., & Wang, Y. (2016). CDK phosphorylates the polarisome scaffold Spa2 to maintain its localization at the site of cell growth. *Molecular Microbiology*, *101*(2), 250–264. https://doi.org/10.1111/mmi.13386

Weiner, A., Orange, F., Lacas-Gervais, S., Rechav, K., Ghugtyal, V., Bassilana, M., & Arkowitz, R. A. (2019). On-site secretory vesicle delivery drives filamentous growth in the fungal pathogen Candida albicans. *Cellular Microbiology*, *21*(e12963). https://doi.org/10.1111/cmi.12963

Whitesides, G. M., Ostuni, E., Takayama, S., Jiang, X., & Ingber, D. E. (2001). Soft lithography in biology and biochemistry. *Annual review of biomedical engineering*, *3*, 335–373. https://doi.org/10.1146/annurev.bioeng.3.1.335

Wiederkehr, A., Du, Y., Pypaert, M., Ferro-Novick, S., & Novick, P. (2003). Sec3p is needed for the spatial regulation of secretion and for the inheritance of the cortical endoplasmic reticulum. *Molecular Biology of the Cell*, *14*(12), 4770–4782. https://doi.org/10.1091/mbc.E03-04-0229

Wild, A. C., Yu, J. W., Lemmon, M. A., & Blumer, K. J. (2004). The p21-activated protein kinase-related kinase Cla4 is a coincidence detector of signaling by Cdc42 and phosphatidylinositol 4-phosphate. *Journal of Biological Chemistry*, *279*(17), 17101–17110. https://doi.org/10.1074/jbc.M314035200

Wilson, R. A., & Talbot, N. J. (2009). Under pressure: investigating the biology of plant infection by Magnaporthe oryzae. *Nature Reviews Microbiology*, *7*(3), 185–195. https://doi.org/10.1038/nrmicro2032

Wilson, R. B., Davis, D., & Mitchell, A. P. (1999). Rapid hypothesis testing with Candida albicans through gene disruption with short homology regions. *Journal of bacteriology*, *181*(6), 1868–1874. https://doi.org/10.1128/JB.181.6.1868-1874.1999

Winters, M. J., & Pryciak, P. M. (2005). Interaction with the SH3 domain protein Bem1 regulates signaling by the Saccharomyces cerevisiae p21-activated kinase Ste20. *Molecular and Cellular Biology*, *25*(6), 2177–2190. https://doi.org/10.1128/mcb.25.6.2177-2190.2005

Woods, B., Kuo, C. C., Wu, C. F., Zyla, T. R., & Lew, D. J. (2015). Polarity establishment requires localized activation of Cdc42. *Journal of Cell Biology*, *211*(1), 19–26. https://doi.org/10.1083/jcb.201506108

Woods, B., & Lew, D. J. (2017). Polarity establishment by Cdc42: key roles for positive feedback and differential mobility. *Small GTPases*, *10*(2), 130–137. https://doi.org/10.1080/21541248.2016.1275370

Xie, Y., Sun, J., Han, X., Turšić-Wunder, A., Toh, J., Hong, W., Gao, Y. G., & Miao, Y. (2019). Polarisome scaffolder Spa2-mediated macromolecular condensation of Aip5 for actin polymerization. *Nature Communications*, *10*(1). https://doi.org/10.1038/s41467-019-13125-1

Xu, X. L., Lee, R. T., Fang, H. M., Wang, Y. M., Li, R., Zou, H., Zhu, Y., & Wang, Y. (2008). Bacterial peptidoglycan triggers Candida albicans hyphal growth by directly activating the adenylyl cyclase Cyr1p. *Cell Host and Microbe*, *4*(1), 28–39. https://doi.org/10.1016/j.chom.2008.05.014

Yamaguchi, Y., Ota, K., & Ito, T. (2007). A novel Cdc42-interacting domain of the yeast polarity establishment protein Bem1: implications for modulation of mating pheromone signaling. *Journal of Biological Chemistry*, *282*(1), 29–38. https://doi.org/10.1074/jbc.M609308200

Zeng, G., Wang, Y. M., & Wang, Y. (2012). Cdc28-Cln3 phosphorylation of Sla1 regulates actin patch dynamics in different modes of fungal growth. *Molecular Biology of the Cell*, *23*(17), 3485–3497. https://doi.org/10.1091/mbc.E12-03-0231

Zhang, J., Tan, K., Wu, X., Chen, G., Sun, J., Reck-Peterson, S. L., Hammer, J. A., 3rd, & Xiang, X. (2011). Aspergillus myosin-v supports polarized growth in the absence of microtubule-based transport. *PLoS ONE*, *6*(12), e28575. https://doi.org/10.1371/journal.pone.0028575

Zhang, X., Orlando, K., He, B., Xi, F., Zhang, J., Zajac, A., & Guo, W. (2008). Membrane association and functional regulation of Sec3 by phospholipids and Cdc42. *Journal of Cell Biology*, *180*(1), 145–158. https://doi.org/10.1083/jcb.200704128

Zheng, P., Nguyen, T. A., Wong, J. Y., Lee, M., Nguyen, T. A., Fan, J. S., Yang, D., & Jedd, G. (2020). Spitzenkörper assembly mechanisms reveal conserved features of fungal and metazoan polarity scaffolds. *Nature Communications*, *11*(1), 1–13. https://doi.org/10.1038/s41467-020-16712-9

Zheng, X., Lee, R. T. H., Wang, Y. M., Lin, Q. S., & Wang, Y. (2007). Phosphorylation of Rga2, a Cdc42 GAP, by CDK/Hgc1 is crucial for Candida albicans hyphal growth. *The EMBO Journal*, *26*(16), 3760–3769. https://doi.org/10.1038/sj.emboj.7601814

Zheng, X., Wang, Y., & Wang, Y. (2004). Hgc1, a novel hypha-specific G1 cyclin-related protein regulates Candida albicans hyphal morphogenesis. *The EMBO Journal*, *23*(8), 1845–1856. https://doi.org/10.1038/sj.emboj.7600195

Zhu, W., Phan, Q. T., Boontheung, P., Solis, N. V., Loo, J. A., & Filler, S. G. (2012). EGFR and HER2 receptor kinase signaling mediate epithelial cell invasion by Candida albicans during oropharyngeal infection. *Proceedings of the National Academy of Sciences*, *109*(35), 14194–14199. https://doi.org/10.1073/PNAS.1117676109

Ziman, M., O'Brien, J. M., Ouellette, L. A., Church, W. R., & Johnson, D. I. (1991). Mutational analysis of CDC42Sc, a Saccharomyces cerevisiae gene that encodes a putative GTP-binding protein involved in the control of cell polarity. *Molecular and Cellular Biology*, *11*(7), 3537–3544. https://doi.org/10.1128/mcb.11.7.3537